Design-to-Resource (DTR) using SMC Turbine Adaptive Strategy

Design Process of Low Temperature Organic Rankine Cycle (LT-ORC)

A thesis submitted in partial fulfilment of the requirements for the

Degree

Of Doctor of Philosophy in Mechanical Engineering

in the University of Canterbury

by Choon Seng Wong

University of Canterbury

2015

Supervisors

Prof. Susan Krumdieck	Senior Thesis Supervisor, University of Canterbury, NZ
Dr. Sid Becker	Thesis Co-Supervisor, University of Canterbury, NZ
Dr. Nicholas Baines	Thesis Supervisory Committee Member/ Technical Consultant, NREC Concepts, UK

Special Acknowledgement to the following people in supporting the research project and development of this thesis.

Assoc. Prof. Mark Jermy	University of Canterbury, NZ
Assoc. Prof. Mathieu Sellier	University of Canterbury, NZ
Dr. Don Clucas	University of Canterbury, NZ
Dr. Boaz Habib	Heavy Engineering Research Association, NZ
Jevon Priestly	Allied Industrial Engineering, NZ

UC ORC Research Teams:

David Meyer, Leighton Taylor, Michael Southon, Ariff Ghazali

This author is funded by Heavy Engineering Educational & Research Foundation (HEERF) in supporting this research project.

Contents

Abstract ____ *7*

1.0 Introduction ____ *9*

1.1 The Problem ____ **10**

1.2 Standard Design-to-Resource approach ____ **11**

1.3 Design-to-Resource approach for low temperature ORC ____ **14**

1.4 The Contribution ____ **16**

1.4 SMC Adaptive Strategy ____ **19**

1.5 Challenges in development of the SMC-DTR ____ **20**

1.6 Thesis Layout ____ **21**

1.7 References ____ **23**

Background ____ *25*

2.0 Literature Review ____ *25*

2.1 Background of Organic Rankine Cycle ____ **27**

2.2 Selection of Working Fluid for ORC ____ **32**

2.3 Industrial ORC Technology: A brief summary ____ **39**

2.4 State of the Art of ORC Turbines and Expanders ____ **43**

2.5 References ____ **53**

3.0 Thermodynamic Cycle Model ____ *63*

3.1 Thermodynamic Analysis of an Organic Rankine Cycle ____ **65**

3.1.1 Pre-heater and Evaporator Analysis ____ 66

3.1.2 Turbine Analysis ____ 66

3.1.3 Condenser Analysis ____ 67

3.1.4 Pump Analysis ____ 67

3.1.5 Cycle Analysis ____ 68

3.1.6 Numerical Model ____ 69

3.2 Cycle Design Approach and Example ____ **71**

3.3 References 77

3.4 References 77

4.0 Define Turbine Specification ***78***

4.1 Introduction 80

4.2 Calculation of Shaft Speed and Turbine Diameter 82

4.3 Calculation of Number of Stages 83

4.4 Case Studies for Turbine/Expander Selection 86

4.5 Conclusion 88

4.6 References 89

Investigative Study ***90***

5.0 Preliminary Design of Radial Inflow Turbine ***90***

5.1 Introduction 93

5.2 Standard Preliminary Design Approach 95

5.2.1 Preliminary Design 96

5.2.2 Thermo-physical and Thermodynamic Properties 99

5.2.3 Perfect Gas Model 99

5.2.4 Real Gas Model 101

5.2.5 Nozzle and Rotor Design 104

5.2.6 Turbine Loss Model 106

5.2.7 Validation of Turbine Empirical Loss Model 110

5.2.8 Optimization of Objective Function 111

5.2.9 Numerical Mathematical Model 112

5.3 Case Study for Low-Temperature Geothermal Brine 113

5.4 Conclusion 120

5.5 References 121

Components of the SMC Adaptive Strategy ***123***

6.0 Meanline Analysis of Radial Inflow Turbine ***123***

6.1 Introduction 125

6.2 Turbine Loss Model 127

6.3 Validation of Turbine Empirical Loss Model 131

6.4 References 133

7.0 CFD Analysis of Radial Inflow Turbine *134*

7.1 Introduction 136

7.2 CFD Methodology 138

7.2.1 Generation of Solid Models 139

7.2.2 Meshing 141

7.2.3 Details of Modelling the Physics 144

7.2.4 Solver 148

7.3 Grid Independence Study 149

7.4 Validation of the CFD Model 151

7.5 Conclusion 152

7.6 References 153

8.0 Similarity Analysis *154*

8.1 Introduction 156

8.2 Methodology 158

8.2.1 Similarity Analysis 159

8.2.2 Scaling Approach for Different Compressible Fluids 160

8.2.3 Evaluation of Aerodynamic Performance using CFD Analysis 161

8.3 Result 163

8.4 Discussion 169

8.5 Conclusion 178

8.6 References 179

Application of the SMC-DTR Approaches *181*

9.0 Application of the SMC-DTR using Meanline Analysis *181*

9.1 Introduction 183

9.2 Application of the SMC-DTR approach in a waste heat recovery (WHR) system 186

9.2.1 Heat source and heat sink: 186

9.2.2 Cycle design and fluid selection: 186

9.2.3 Define turbine specification: 187
9.2.4 Matching existing turbines: 188
9.2.5 Design of Nozzle Vanes: 189
9.2.6 Application of the SMC adaptive strategy 191
9.2.6 Mechanical design and system integration: 196
9.3 Conclusion 201
9.4 References 202
10.0 Application of the SMC-DTR using CFD Analysis on Turbine with Fix Nozzle Vane 204
10.1 Introduction 206
10.2 Application of the SMC-DTR Approach to Design an Air-Cooled Binary Plant 209
10.2.1 Heat source and heat sink 210
10.2.2 Cycle design and fluid selection 211
10.2.3 Define turbine specification: 212
10.2.4 Matching existing turbines: 213
10.2.5 Application of the SMC Adaptive Strategy 213
10.3 Conclusion 225
10.4 References 227
11.0 Application of the SMC-DTR using CFD Analysis on Turbine with Variable Nozzle Vane 228
11.1 Introduction 230
11.2 Test Subject – Automotive Turbocharger with Variable Nozzle Vanes 232
11.3 Performance Optimization using Variable Nozzle Vanes 233
11.4 Application of the SMC-DTR Approach in Heat Source with Variable Mass Flow 241
11.4.1 ORC System 241
11.4.2 Application of the SMC Adaptive Strategy 243
11.5 Discussion – Performance Evaluation of Variable Nozzle Vanes 247
11.6 Conclusion 251
11.7 References 252
12.0 Conclusion 253
12.1 Summary 254

12.1.1 Background 254
12.1.2 Investigative Study 255
12.1.3 Components of the SMC Adaptive Strategy 255
12.1.4 Application of the SMC-DTR Approaches 257
12.2 Perspectives 260

Abstract

Low grade heat source has a huge amount of power generation potential from the industrial waste heat, and the untapped low temperature geothermal reservoirs. A suitable turbine for these heat resources is usually not available from the market. A turbine can be designed and developed but it requires the knowledge based engineering (KBE) in the turbine technology with high engineering development cost. It is not cost effective to follow the conventional turbine design and development pattern for each set of working fluid and operating condition for ORC system. Another solution is to select and adapt the off-the-shelf turbines for the given heat resources. The objective of this thesis is to define and develop the design-to-resource (DTR) methodology coupled with the SMC turbine adaptive strategy, named SMC-DTR approach. . The SMC strategy consists of three different analysis techniques; similarity analysis, meanline analysis, and computational fluid dynamics (CFD) method, to analyse the turbine performance for application and working fluid different from the original design. This strategy allows the design and optimization of an ORC system for low temperature resources by adapting the off-the-shelf radial inflow turbines for various heat resource condition.

The SMC-DTR approach was applied in three different resources condition. The numerical study shows that the off-the-shelf radial inflow turbines are feasible to be adapted as ORC turbines but the turbine efficiency would deteriorate. The performance of automotive turbocharges deteriorates up to 20% whereas the gas turbine performance changes up to 10% if the working fluid is changed from air to refrigerants, including R134a, R245fa, and isobutane. Most of the off-the-shelf turbines are designed for sub-sonic expansion. If they are used for supersonic expansion, the turbine efficiency deteriorates when the expansion ratio increases. The rotor blade passage chokes, and the flow accelerates downstream of the rotor throat. This leads to the high swirl angle at the turbine outlet and high turbine loss in term of kinetic energy, which is reflected in the low turbine efficiency.

The application of the SMC-DTR approach also shows that a radial inflow turbine with fixed nozzle vanes can be selected and adapted for two different resource condition: constant heat source and heat sink condition, and constant heat source condition with varying heat sink temperature. The turbine efficiency and the thermal efficiency of the thermodynamic cycle

change up to 2% when the heat sink temperature changes from 10 to 23°C. However, a radial turbine with fixed nozzle vanes is not suitable for the heat source with varying flow rate. If the mass flow is reduced by 25% off the design value, the turbine performance and the thermodynamic cycle performance drop significantly. A variable nozzle turbine has to be selected for adaptation for the heat source with varying mass flow for optimal performance.

The thesis also evaluated the suitability of off-the-shelf turbines as ORC turbine and proposed a number of design changes. Automotive turbochargers and gas turbines cannot be applied directly as the ORC turbines since they are originally designed for air. A mechanical system design has to be performed to be used with refrigerants.

1.0 Introduction

This chapter describes the key contribution from this thesis work, provides the context of the contribution in the field, and gives the thesis organization. Geothermal energy is a promising low-carbon energy resource. The major technical barrier to expanded power generation from low-temperature resources is the lack of available expansion machines (or turbines). There is a growing body of literature describing thermodynamic cycle analysis, organic working fluids and component design for organic Rankine cycle (ORC) energy converters. If it was possible to simply order an expansion machine or a turbine for a given mass flow, expansion ratio and working fluid from a manufacturer, then the plant development cost would be the only barrier. Many of the early experimental sub-MW ORC researchers used positive displacement devices such as scrolls and screws. There are many developmental challenges and limitations with positive displacement machines, but they pale in comparison to the work of developing a turbine. The axial steam turbine is the work-horse of power generation, and large-scale geothermal power systems rely on commercially developed axial turbines for both flash steam plant, and binary ORC plant. The axial turbine is scalable and versatile, but its application is limited in the small scale and low-temperature range.

It is possible to develop a radial turbine for a given application through the standard R&D process. However, the cost of developing one turbine for one condition and one working fluid is far in excess of research funding available in New Zealand. The strategy explored in this thesis is to analyse and adapt existing radial inflow turbines for an organic working fluid and pressure ratio for the thermodynamic cycle best suited to a particular resource. The strategy would utilize the radial turbine for a different application and working fluid than the original design. The key contribution in this thesis is the development and demonstration of the turbine analysis strategy for the SMC turbine adaptation approach. The SMC approach makes strategic use of Similarity, Meanline and Computational Fluid Dynamics analyses, and is integrated to the proposed design-to-resource (DTR) method for low temperature resources to form SMC-DTR approach.

1.1 The Problem

A geothermal resource can be exploited by matching the resource to an existing power conversion system (such as Ormat Energy Convertor) [1], or by designing a power conversion system based on the given resource. Power conversion units are commercially available for high temperature resources; steam-based Rankine cycle from General Electric (GE) and an organic Rankine cycle using n-Pentane as working fluid from Ormat [1]. The commercially available systems have been developed over many years, specifically with one working fluid and one turbine design that can be scaled to different power range by increasing the number of stages. The problem is the large amount of research funding and development time needed to develop ORC systems based on other working fluids for use in lower temperature ranges. It is not practical to follow the historical pattern of research and experimental development, particularly in New Zealand with limited research funding support for fundamental Mechanical Engineering science that would be needed for development of a radial turbine for an organic working fluid. This thesis proposes a way to explore the possible adaptation of existing turbines to ORC applications using the modern turbine design and analysis tools.

1.2 Standard Design-to-Resource approach

The low temperature resources require a design of the energy conversion system that is different to the high temperature resources in two aspects:

1) Organic Rankine cycle has a higher thermal efficiency than a conventional steam-based Rankine cycle for low temperature resources [2]. However, the energy conversion system has to be designed and handled with care as all organic working fluids are costly and either flammable, toxic or having high greenhouse gas potential [3].
2) Multi-stage axial turbine is commonly used for steam Rankine cycle with high resource temperature [4]. However, different types of turbines are better match for the pressure ratio and working fluid for the low temperature resources, such as radial inflow turbine [5-8], radial outflow turbine [9], scroll expander [10], and screw expander [11, 12].

An organic Rankine cycle for low temperature resources can be designed and developed using the standard design-to-resource (DTR) approach, as illustrated in Figure 1.1. A thermodynamic model of an organic Rankine cycle is designed based on the given heat resource and heat sink condition, by applying rules for heat exchanger pinch-points, degree of superheat, maximum pressure, and critical temperature of the working fluid. A parametric study is performed to select the optimal working fluid for maximum cycle efficiency. The type of the system components are selected to match the heat transfer requirements and pump conditions. The individual components would need to be designed, developed, and tested in the OEC system. All the components (heat exchangers and turbine) are assembled and a field test is performed.

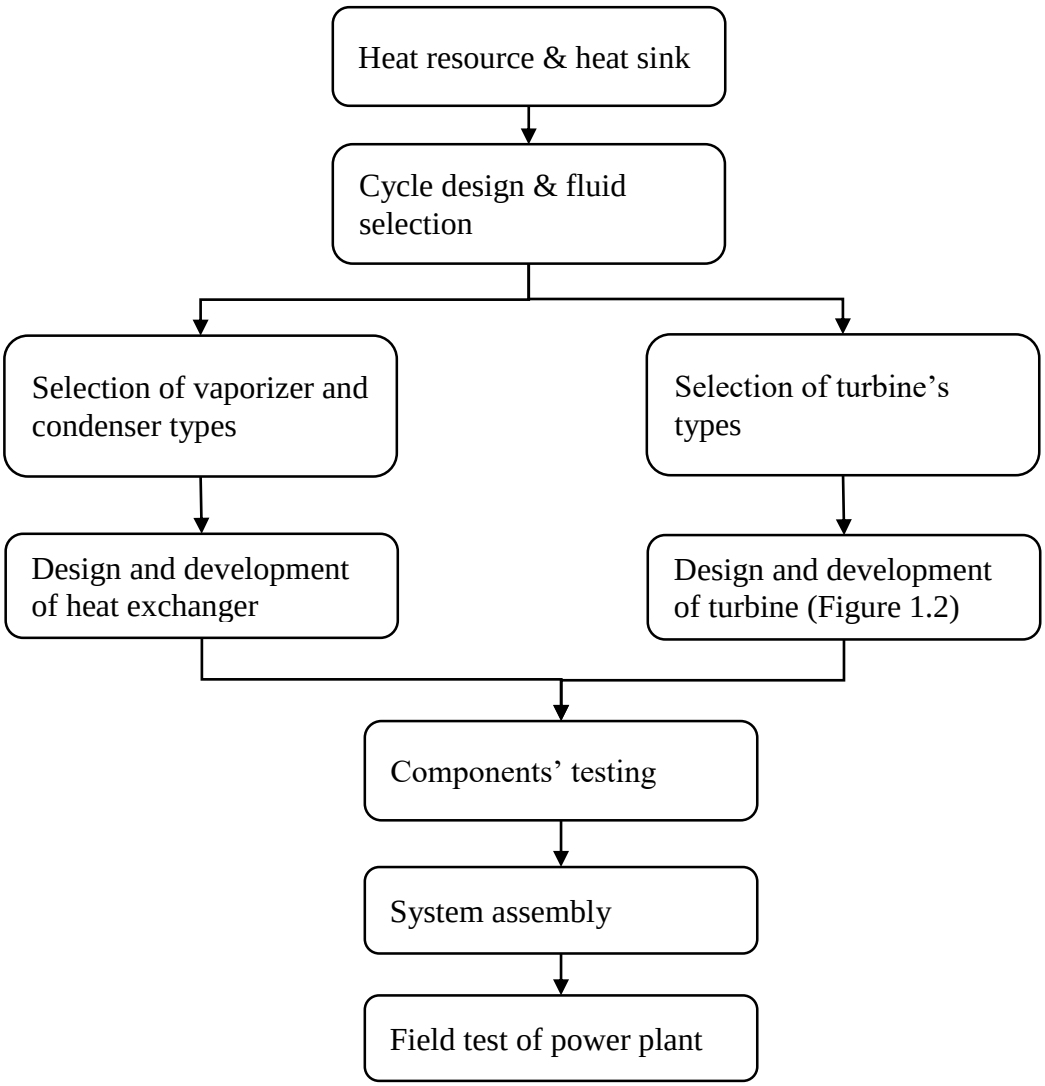

Figure 1.1: Standard DTR approach for low temperature resources

The standard DTR approach for commercial development of low temperature resources would only be successful if turbines were available in the market for the working fluids used in the binary power plant. The conventional turbine design and development approach is illustrated in Figure 1.2 [13]. An iterative cycle of in-depth engineering design and analysis steps are required. Preliminary design means matching the available pressure drop, mass flow, and inlet and exit enthalpies to the desired turbine speed and turbine principal geometry to achieve the best efficiency. The detailed design investigations include aerodynamic design of blade profile, finite element analysis (FEA) on structural integrity of the blade, computational fluid dynamics (CFD) analysis on aerodynamic performance, rotor-dynamic analysis, and system integration of turbine and auxiliary components. The resulting turbomachine design is then embodied by manufacture of prototype, and laboratory testing. The testing results feed

back into the design and the design cycle proceeds with the objective of improving the design of the next generation of turbines.

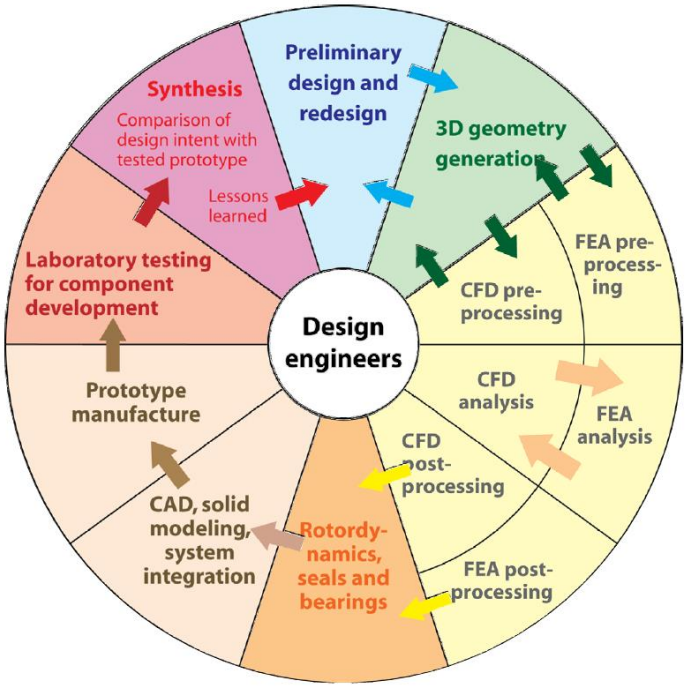

Figure 1.2: Standard turbine design and development approach [13]

Each step of the process requires in-depth engineering knowledge and experience, also known as knowledge-based engineering (KBE). Jet engines for airliners and steam turbines for power plants continue to undergo research and development cycles to improve efficiency and reliability. Mass-manufactured turbomachines in consumer products like vacuum cleaners, fans and pumps also require KBE and investment in R&D to achieve cost targets. The thing that all of the conventional turbomachines have in common, is that they represent further development of existing turbines for the same working fluid under similar working conditions. The challenge for ORC development is the lack of this existing platform for expander technology using organic fluids for power generation. Ormat is a successful geothermal power plant developer because they have essentially built up their own KBE and axial turbine design platform for pentane. Ormat can then design the Ormat energy converter (OEC) unit to suit a range of high temperature resource situations. Thus, the conventional DTR approach is to use an existing design platform and scale the size of the existing technology to optimize a given resource.

1.3 Design-to-Resource approach for low temperature ORC

The design and development of a turbine for low temperature resources with low potential power output entails a high investment cost, and a high capital cost per kilowatt hour, attributed to the complexity of the aforementioned process and low amount of power generation. Thus, low temperature ORC (LTORC) developers have focused on using turbomachine technology developed for refrigerants. Given the lower generation potential of LTORC, leveraging an existing technology is a logical approach.

a. Scroll compressors have been adapted as scroll expanders for micro-scale ORC system with potential power output of a few kilowatts [14-19].
b. The feasibility of adapting different positive displacement machines have been studied, including vane expander and piston expander (reported in a review by Bao [20]) using organic working fluids for power conversion system less than 100 kW.
c. A refrigeration system has been re-purposed by replacing the centrifugal impeller with a radial inflow turbine, and changing the working fluid from R245fa to R134a to match the heat source condition [21-23].
d. A turbocharger using air as working medium has been re-purposed as an ORC turbine using organic working medium [24], but no details are found regarding the adaptation strategy and the turbine performance.

Among these adaptive solutions, the conversion of scroll compressors into scroll expanders allows the development of the small scale power conversion units with potential power output up to 30 kW [25]. The conversion of other positive displacement machines such as the vane expander and piston expander results in a low turbine efficiency of less than 70% [20], and the converted machines are limited to small power conversion units with less than a few hundred kilowatts. The repurposing of a refrigeration system can reduce the investment cost but a turbine has to be designed using the conventional turbine design and analysis approach [21]. The repurposing of a turbocharger as an ORC turbine using different working fluid is an interesting concept. This approach reduces the investment cost and allows the design and build of energy conversion units without necessitating a strong KBE in turbine technology. However, the one known project was reported by Barber Nichols for a US Military project, and no details were available regarding the adaptation process, analysis strategy, and the performance of the adapted turbines.

The gap to be filled by the work in this thesis is the lack of strategy to analyse and adapt existing radial inflow turbines for working fluid and application different from the original design. In this thesis, the existing turbines investigated are commercially available off-the-shelf turbines which do not require custom manufacturer. The selection of a suitable turbine from the existing turbines is carried out to match the resource condition or to match the cycle design. The adaptation of the turbine is defined as the utilization of turbine nozzle and rotor, and modification of mechanical system design (re-design the casing, re-design the lubrication system, and re-select the bearing) for a different working fluid and application. The turbine adaptation approach covers only one type of turbine, a radial inflow air or gas turbine. Other types of turbines, such as axial turbine, radial outflow turbine, and positive displacement machines are not considered in this thesis research, but could also be investigated using the proposed adaptation approach. The radial inflow turbine is selected as the core subject of the adaptation approach for the following reasons:

a. Radial inflow turbine is suitable for energy conversion units with a wide range of potential power output, from a few kilowatts to a few megawatts [25].
b. Radial inflow turbine is suitable for low temperature resources with a lower system pressure ratio than high temperature resources.
c. Radial inflow turbine shows a higher isentropic efficiency than positive displacement machines.
d. Radial inflow turbine is relatively simple to manufacture and assemble compared to the multi-stage axial turbine.
e. Radial inflow turbines are commercially available in different geometry and size as automotive turbochargers and micro gas turbines with a lower price tag, compared to commercially available steam turbines.

The strategy of the turbine adaptation approach and the questions to be addressed are presented in detail in the subsequent section.

1.4 The Contribution

The contribution of this thesis is engineering gap for adaptation of existing radial inflow turbines for working fluid different from the original design. Up to the time of writing this thesis, no open literature was found regarding the analysis and adaptation of existing turbines to different working fluids (except the publications by the author). The turbine analysis strategy is named the SMC adaptation strategy, where S refers to similarity analysis, M refers to meanline analysis, and C refers to computational fluid dynamic (CFD) analysis. The SMC approach is needed because the standard approach is not possible given research investment constraints. The SMC turbine adaptation strategy forms the backbone of the new iterative LTORC design-to-resource (DTR) method developed in this thesis. The new DTR method with integrated SMC analysis is named SMC-DTR, and illustrated in Figure 1.3.

The SMC-DTR turbine adaptation approach includes:

a. Define turbine specification.
b. Matching existing turbines to the heat resources
c. SMC adaptive strategy
d. Mechanical design and system integration
e. Laboratory testing

The SMC adaptive strategy allows the engineers to study the performance of existing turbines for the working fluid determined from the cycle design, and match the turbines to different resources. If the turbine efficiency using the working fluid from the cycle design does not fall within an acceptable range, the calculation process is repeated using another working fluid or another turbine, as shown in Figure 1.3. Only the process enclosed in the dotted box is presented in this thesis. The differences between the new DTR and the standard DTR approach are presented in Table 1.1.

Table 1.1: Differences between the standard DTR and new DTR methods

	Standard DTR approach	**New DTR approach**
Turbine development strategy	Turbine is designed using the turbine design wheel in Figure 1.2.	Existing radial gas turbine is selected and adapted to the cycle design.
Numerical calculation	Forward analysis. The turbine is designed based on the working fluid.	Iterative analysis. Different turbines can be analysed using the SMC approach for different working fluid to optimize the cycle performance.

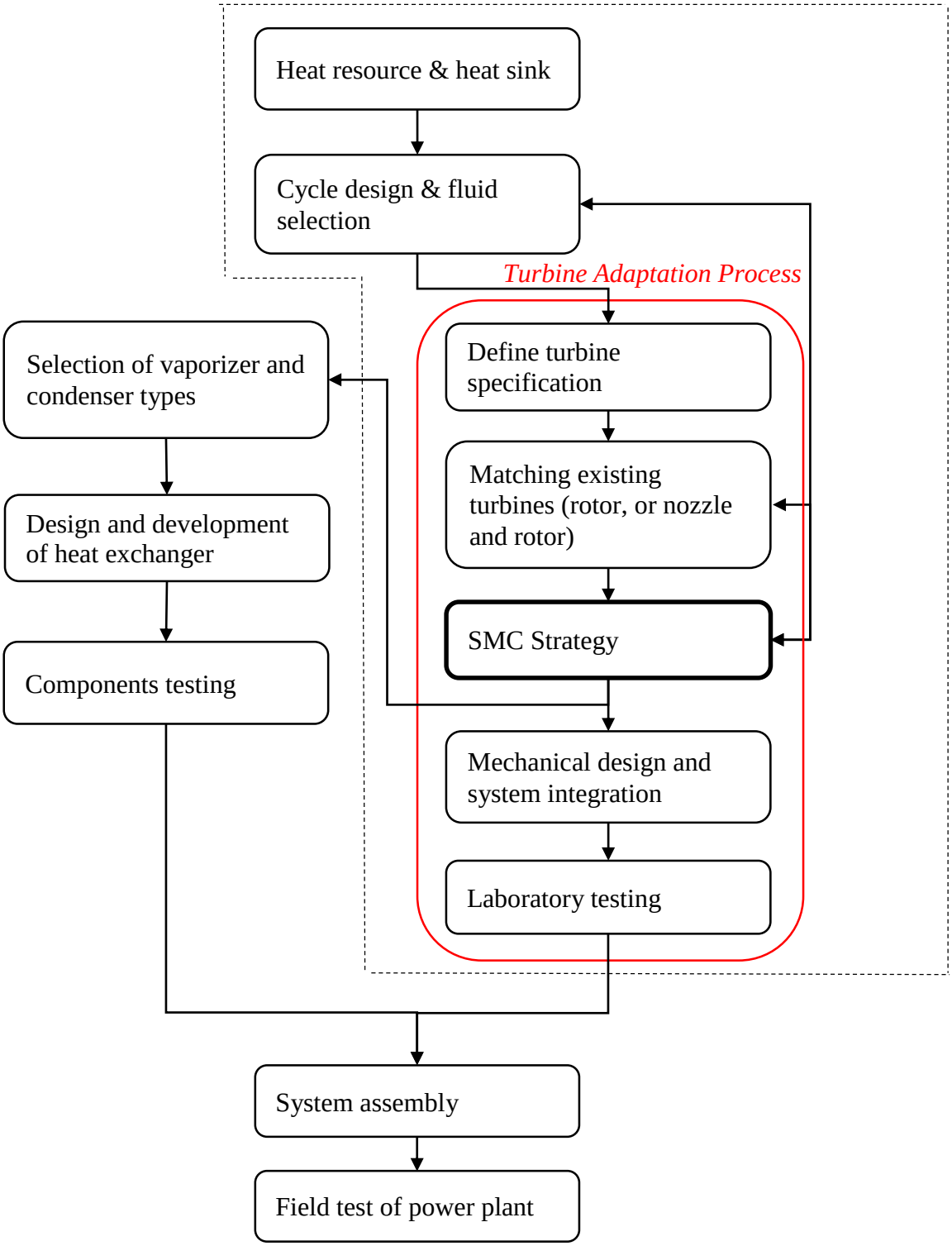

Figure 1.3: SMC-DTR approach for low temperature resources

1.4 SMC Adaptive Strategy

The SMC adaptive strategy involves three turbine analysis techniques; similarity analysis, meanline analysis, and CFD analysis. The SMC strategy is unique because the turbine performance is investigated using the most relevant and informative analysis for the given situation. The similarity analysis is performed only if the turbine performance map is available. If the turbine performance map is not available, the meanline analysis is performed. The turbine efficiency using the selected working fluid is evaluated using either the similarity analysis or the meanline analysis. If the turbine efficiency does not fall into an acceptable range, the working fluid can be re-selected from the cycle design, or the turbine can be re-selected. The CFD analysis is performed if the efficiency of the selected turbine is acceptable, or there is only one available turbine. The decision flow chart of the SMC approach is illustrated in Figure 1.4.

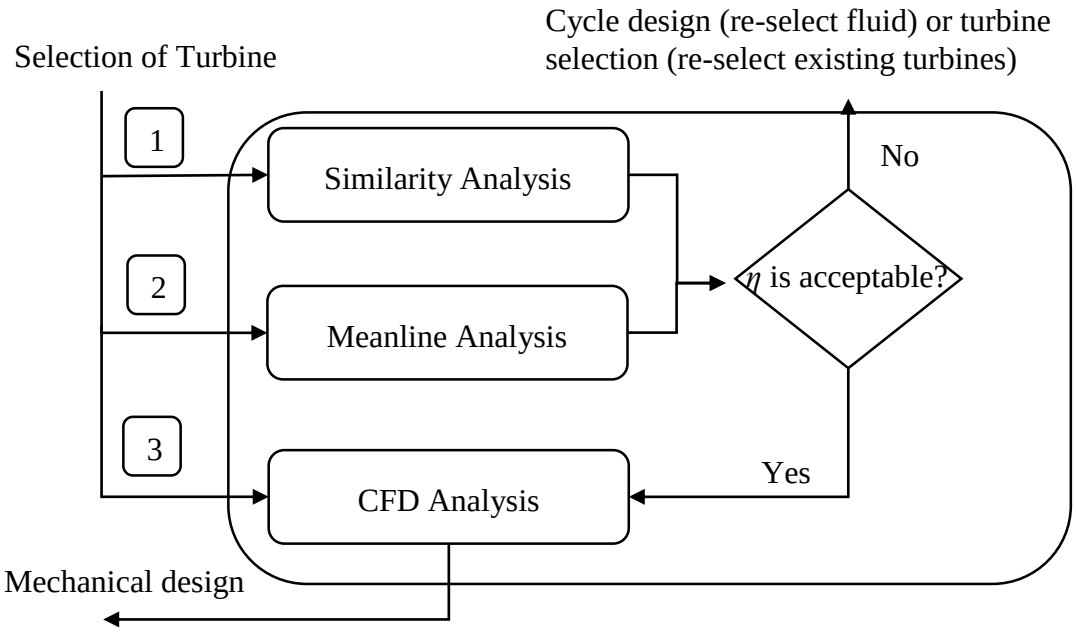

1: Turbine performance map (using air as working medium) is available.
2: Turbine performance map is not available.
3: Only one existing turbine is available.

Figure 1.4: SMC analysis approach

1.5 Challenges in development of the SMC-DTR

A number of research works are required to address the following issues in order to complete the SMC-DTR approach.

a. A turbine is typically designed for a specific set of working fluid and operating condition. Is it feasible to adapt existing gas turbines for organic working fluid?
b. What components of a radial gas turbine can be retained and what components have to be re-designed if the working fluid is changed from air to organic working fluid, such as isobutane or R245fa?
c. A turbine preliminary design approach can be used to select an existing turbine with the closest dimension and geometry to the design output from the preliminary design. The turbine preliminary design approach has been developed using ideal gas law assuming constant isobaric specific heat [26], before the work of this thesis is performed. What is the difference in the design output from the preliminary design approach using different gas models (ideal gas and real gas model)?
d. Similarity analysis can scale a turbine from one operating condition to another, and scale a turbine for different turbine diameter if the working fluid is the same [27]. However, similarity analysis cannot scale a turbine from one working fluid to another, especially if the working fluid is compressible. What is the appropriate assumption or approach to perform the similarity analysis for different working fluid?
e. How to optimize the cycle performance using the adapted turbines if the resource condition is changing?

The aforementioned challenges were successfully investigated in this thesis. The main components of the SMC analysis approach were investigated and applied separately for each case study, in order to exhibit the feasibility of the components as standalone analysis approaches.

1.6 Thesis Layout

The aim of this thesis is to develop the SMC-DTR approach for low temperature resources with different resources' behaviour, and the main contribution of this thesis is to develop the key component, SMC analysis approach.

Background

Chapter 2 presents the literature review of organic Rankine cycle (ORC) as the key technology in energy conversion units for low temperature resources. The literature review covers the background of ORC, selection of working fluid, development of the industrial ORC units, and state of the art of turbines and expanders.

Chapter 3 presents the numerical calculation of the standard thermodynamic modelling of the ORC system using Engineering Equation Solver (EES), an essential component of the SMC-DTR approach. This component is coupled to the SMC adaptive strategy to optimize the cycle performance. This component allows the engineers to select the working fluid and determine the turbine operating condition for maximum system performance.

Chapter 4 presents the standard approach to define the turbine specification: calculating the shaft speed, turbine wheel diameter, and number of stage using a standard turbine specific speed-specific diameter performance chart.

Investigative Study

Chapter 5 presents the radial inflow turbine preliminary design method. This component allows the users to match existing turbines to the cycle design with different working fluid. The turbine designed using ideal gas model (with constant specific heat) and real gas model are compared.

Components of the SMC Approach

Chapter 6 presents the meanline analysis of radial inflow turbine and the model validation.

Chapter 7 presents the CFD method in analysing a radial inflow turbine using ANSYS Turbomachinery software. An industrial gas turbine is presented to validate the CFD model.

Chapter 8 presents the similarity analysis approach to scale a turbine from air (behaves as ideal gas) to organic working fluid (behaves as real gas). Three different variable parameter sets are established and investigated, known as perfect gas approach, variable pressure ratio approach, and constant specific speed approach. The most feasible and accurate approach are selected and applied in the similarity analysis component in the SMC approach. An industrial gas turbine is selected as the test subject in this chapter. A correction chart is developed to extend the application of the selected approach for different pressure ratio.

Application of SMC-DTR approach

Chapter 9 presents the application of the SMC-DTR approach for two nozzle-less automotive turbochargers without the turbine performance map in designing the ORC system. This chapter presents the cycle design and fluid section, calculation of the turbine specification, meanline analysis of the SMC adaptive strategy, and the mechanical system design to adapt the automotive turbochargers into ORC turbines.

Chapter 10 presents the application of a radial gas turbine with fixed nozzle vanes using the SMC-DTR approach for a resource condition with constant heat source condition and varying heat sink temperature. The CFD analysis of the SMC adaptive strategy is applied to evaluate the turbine performance, and the flow field across the turbine blade passage was compared for different working fluids.

Chapter 11 presents the application of a variable nozzle turbocharger using the SMC-DTR approach for a resource condition with constant heat sink temperature and varying heat source flow rate. The first section presents the investigate study to optimize the turbine performance using variable nozzle vanes. The second section demonstrates the application of the SMC-DTR approach to optimize the cycle performance. The third section discusses the losses within the variable nozzle vanes at different vane angle.

Conclusion

Chapter 12 presents the summary and the implications of the lessons from each section, and the author's perspective of this research work.

1.7 References

1. Nasir, P., et al., *Utilization of Turbine Waste Heat to Generate Electric Power at Neptune Plant.* 2004.
2. Vankeirsbilck, I., et al., *Organic rankine cycle as efficient alternative to steam cycle for small scale power generation.* Proceedings of 8 th International Conference on Heat Transfer, Fluid Mechanics and Thermodynamics, Pointe Aux Piments (Mauritius), 2011.
3. Chen, H., D.Y. Goswami, and E.K. Stefanakos, *A review of thermodynamic cycles and working fluids for the conversion of low-grade heat.* Renewable and Sustainable Energy Reviews, 2010. **14**(9): p. 3059-3067.
4. Meher-Homji, C.B. *'The Historical Evolution of Turbomachinery*. in *Proceedings of the 29th Turbomachinery Symposium, Texas A&M University, Houston, TX*. 2000.
5. Clemente, S., et al., *Bottoming organic Rankine cycle for a small scale gas turbine: A comparison of different solutions.* Applied Energy, 2013. **106**: p. 355-364.
6. Agahi, R. *Application of an Inflow Radial Turbine in a Geothermal Organic Rankine Cycle Power Plant*. in *35th New Zealand Geothermal Workshop*. 2013. Rotorua, New Zealand.
7. Ventura, C., et al., *Preliminary Design and Performance Estimation of Radial Inflow Turbines: An Automated Approach.* Journal of Fluids Engineering-Transactions of the Asme, 2012. **134**(3).
8. Marcuccilli, F. and D. Thiolet. *Optimizing Binary Cycles Thanks to Radial Inflow Turbines*. in *Proceedings world geothermal congress*. 2010. Bali, Indonesia.
9. EXERGY *Radial Outflow Turbine*.
10. Song, P., et al., *A review of scroll expanders for organic Rankine cycle systems.* Applied Thermal Engineering, 2013(0).
11. Smith, I.K., et al., *Steam as the working fluid for power recovery from exhaust gases by means of screw expanders.* Proceedings of the Institution of Mechanical Engineers Part E-Journal of Process Mechanical Engineering, 2011. **225**(E2): p. 117-125.
12. Smith, I.K., N. Stosic, and A. Kovacevic, *Screw expanders increase output and decrease the cost of geothermal binary power plant systems.* Proc. Of the Geothermal Resources Council Annual Meeting, Reno, Nevada-USA, September, 2005: p. 25-28.
13. Baines, N. *ENGR408-ENME 627-S1 Special Topic in Engineering: Turbomachinery*. 2014.
14. Declaye, S., et al., *Experimental study on an open-drive scroll expander integrated into an ORC (Organic Rankine Cycle) system with R245fa as working fluid.* Energy, 2013. **55**: p. 173-183.

15. Lemort, V., S. Declaye, and S. Quoilin, *Experimental characterization of a hermetic scroll expander for use in a micro-scale Rankine cycle.* Proceedings of the Institution of Mechanical Engineers. Part A, Journal of power and energy, 2012. **226**(1): p. 126.

16. Oralli, E., *Conversion of a Scroll Compressor to an Expander for Organic Rankine Cycle: Modeling and Analysis*. 2010, University of Ontario Institute of Technology (Canada): Canada.

17. Harada, K.J., *Development of a small scale scroll expander*. 2010.

18. Mathias, J.A., et al., *Experimental Testing of Gerotor and Scroll Expanders Used in, and Energetic and Exergetic Modeling of an Organic Rankine Cycle.* Journal of Energy Resources Technology-Transactions of the Asme, 2009. **131**(1).

19. Lemort, V. and S. Quoilin, *Designing scroll expanders for use in heat recovery Rankine cycles*, in *International Conference on Compressors and Their Systems*. 2009. p. 2010.

20. Bao, J. and L. Zhao, *A review of working fluid and expander selections for organic Rankine cycle.* Renewable and Sustainable Energy Reviews, 2013. **24**: p. 325-342.

21. Brasz, J.J. and B.P. Biederman, *Power generation with a centrifugal compressor*. 2010, Google Patents.

22. Brasz, J.J. and B.P. Biederman, *Turbine with vaned nozzles*. 2007, Google Patents.

23. Biederman, J.J.B.B.P., *Organic Rankine Cycle Waste Heat Applications* 2002, Carrier Corporation: US.

24. Buerki, T., et al., *Use of a Turbocharger and Waste Heat Conversion System*. 2010, EP Patent 2,092,165.

25. Quoilin, S., S. Declaye, and V. Lemort, *Expansion Machine and fluid selection for the Organic Rankine Cycle.* 2010.

26. Moustapha, H., et al., *Axial and Radial Turbines*. 2003: Concepts Eti.

27. Japikse, D. and N.C. Baines, *Introduction to turbomachinery*. 1995: Concepts ETI.

Background

2.0 Literature Review

The aim of this thesis is to present the SMC-DTR approach for low temperature resources, and the main contribution of this thesis is to develop the key component, SMC adaptive strategy. This chapter presents a background study of Organic Rankine cycle, choice of working fluids, industrial development of ORC technologies, and the current state of the art of turbines and expanders in the ORC application. The aim of this chapter is to present a background information on the current technology and development of ORC from research perspective and industrial development. The working fluid is one of the key components to be selected to optimize the system performance of ORC. An extensive study has been performed by a number of researchers and the result from their researches was compiled in this chapter. The literature review reveals that R245fa is the most recommended working fluid for an optimal ORC system. The later part of this chapter presents a comprehensive literature review on different turbines and expanders technologies for ORC, including axial turbine, radial inflow turbine, radial outflow turbine, scroll expander, screw expander, and other positive displacement machines. This literature review introduces the current design and development of turbines and expanders for low temperature ORC system. This review also reinstates the engineering gap that was presented in the previous chapter: lack of strategy to analyse and adapt an existing turbine for different working fluid.

2.1 Background of Organic Rankine Cycle

Different thermodynamic cycles have been developed to convert potential energy and internal energy of fuel or natural heat sources into something useful, such as electricity, domestic water heating, and mechanical drive. The increasing demand for electricity in urban development has led to constant improvement in the thermodynamic cycle. 67.2% of the world electricity production in year 2010 was contributed by power plants burning fossil fuel [1], indicating that the steam Rankine cycle is the backbone of the power generation. The maximum achievable efficiency is 35% for a sub-critical steam plant, 40% for a super-critical steam plant, 45% for an ultra-super-critical steam plant, and 50% for an advanced ultra-super-critical steam plant [2]. The energy supply system using fossil fuels has to be phased out gradually and replaced by different alternative renewable energy conversion systems. Among the alternatives, geothermal energy utilizing Organic Rankine Cycle (abbreviated to ORC) shows a very good reliability with simple cycle design and minimal engineering components.

Conventional Rankine cycle is a thermodynamic cycle using steam as working fluid with four main components: feed pump, turbine or expansion machine, evaporator, and condenser. The basic principle of the conventional Rankine cycle is described briefly:

- Heat transfer occurs between the heat source and the steam within the evaporator.
- The high temperature and high pressure steam is then expanded across the turbine to the condenser pressure, where the fluid energy is transferred to drive the turbine and the generator to generate electricity.
- The low temperature/pressure steam is cooled down from saturated steam to sub-cooled region (water).
- The water is pumped from the condensation pressure to the evaporation pressure, before the water is evaporated in the evaporator. The thermodynamic cycle is repeated.

In an ideal thermodynamic cycle, the heat transfer across the condenser and the evaporator is reversible and isobaric, and the compression and expansion processes are isentropic and reversible, as illustrated in Figure 2.1.

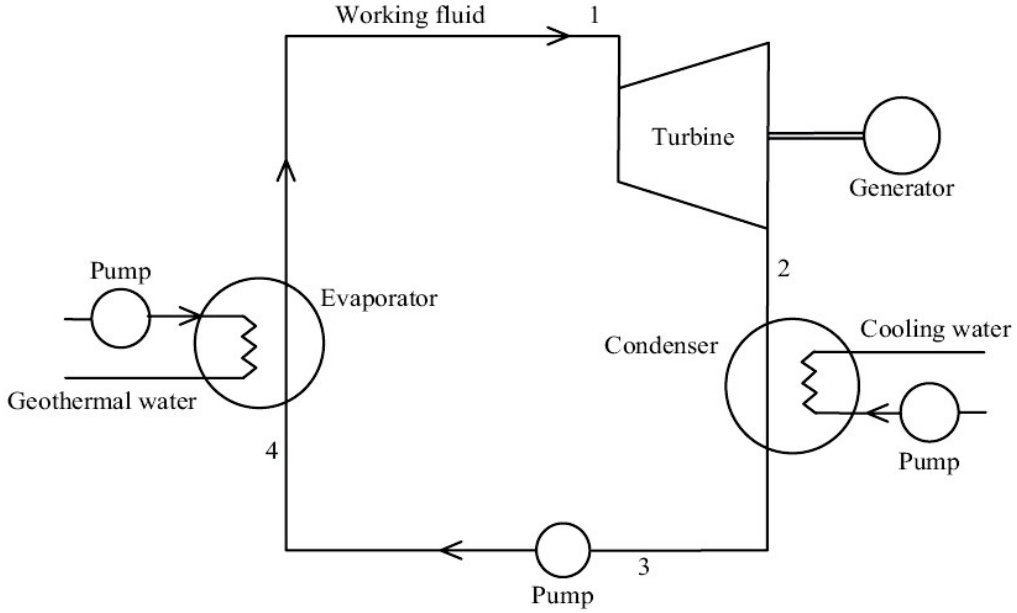

(a)

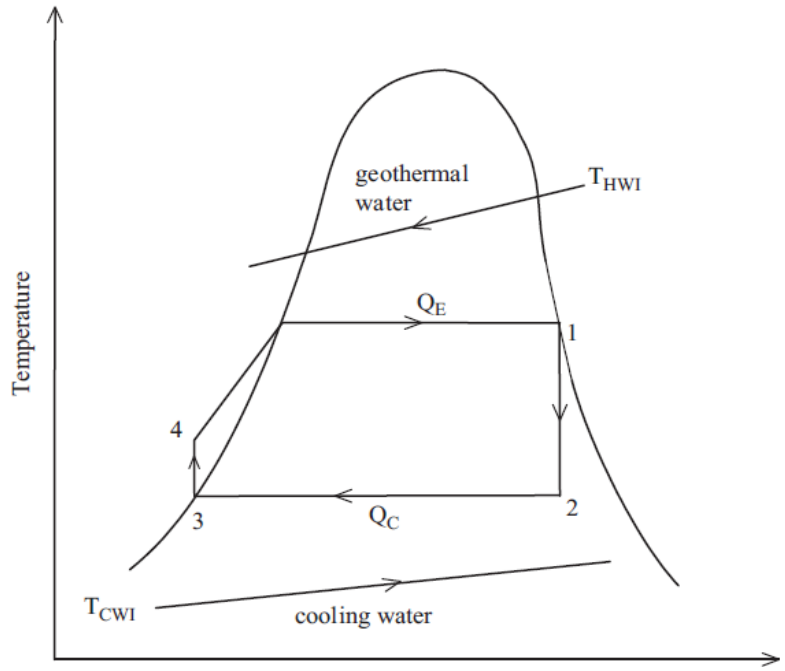

(b)

Figure 2.1: Schematic diagram (a) and (b) temperature-entropy diagram of a simple Rankine cycle [3]

The conventional Rankine cycle using steam is, however, not suitable to extract energy from a low temperature heat source. A numerical comparison between steam and a number of refrigerants (Toluene, n-Pentane, solkatherm, OMTS, HMDS and cyclopentane) in Rankine cycle shows that the Rankine cycle using refrigerants exhibits a higher cycle efficiency than using water [4]. Water (and steam) is not a cost effective solution when the heat sink of the Rankine cycle is close to ambient temperature from a thermodynamic standpoint. A low condensation pressure smaller than 0.1 bar is required, implying a high specific volume of steam with large turbine rotors and large condensers. The very low condensation pressure also implies the high expansion ratio across the turbine, and a multi-stage turbine is usually required for maximum cycle efficiency [5]. Water is classified as wet fluid, in which a certain amount of superheat is required to avoid the excessive formation of droplets at the end of the expansion process [6]. Large turbine rotors with multiple stages configuration, large condenser, and high temperature-resistant materials, incurs a high capital cost for material, manufacturing, and assembly. All these issues have led to the popularity of ORC system in the low temperature heat source application.

ORC is similar to the convetional Rankine cycle with different working medium instead of steam. A number of different configurations are evolved from a simple ORC system, including Kalina cycle, super-critical ORC system, and ORC system with recuperator. Kalina cycle is more complicated than a simple ORC system, with many extra features to maximize the cycle performance with the ammonia-water mixture, such as re-heat, re-generative heating, super-critical pressure and dual pressure configurations [7]. A comparison study was performed between a Kalina cycle and a simple ORC system from a thermodynamic standpoint [8]. Kalina cycle and ORC system produce very similar amount of electric power (at 1,600 kW) but Kalina cycle requires a much higher system pressure at 100 bar, as compared to the low system pressure of about 10 bar for ORC system [8]. Super-critical ORC system is another form of ORC system with the evaporation temperature higher than the critical temperature of the chosen working medium. The main advantage of a super-critical ORC system is higher power output, thermal efficiency, and Carnot cycle efficiency as compared to a sub-critical ORC system, due to the higher temperature of the heat input [9]. The enthalpy drop in a super-critical ORC system is higher which yields a higher amount of useful power, compared to a sub-critical ORC system with the same turbine inlet temperature, as illustrated in Figure 2.2. The temperature glide of the super-critical fluid allows a better thermal match with the heat source temperature within the evaporator, than the fluid below the critical point, as shown in

Figure 2.3. A better thermal match yields a minimal amount of entropy generation with less irreversibility, increasing the exergy efficiency of the thermodynamic cycle.

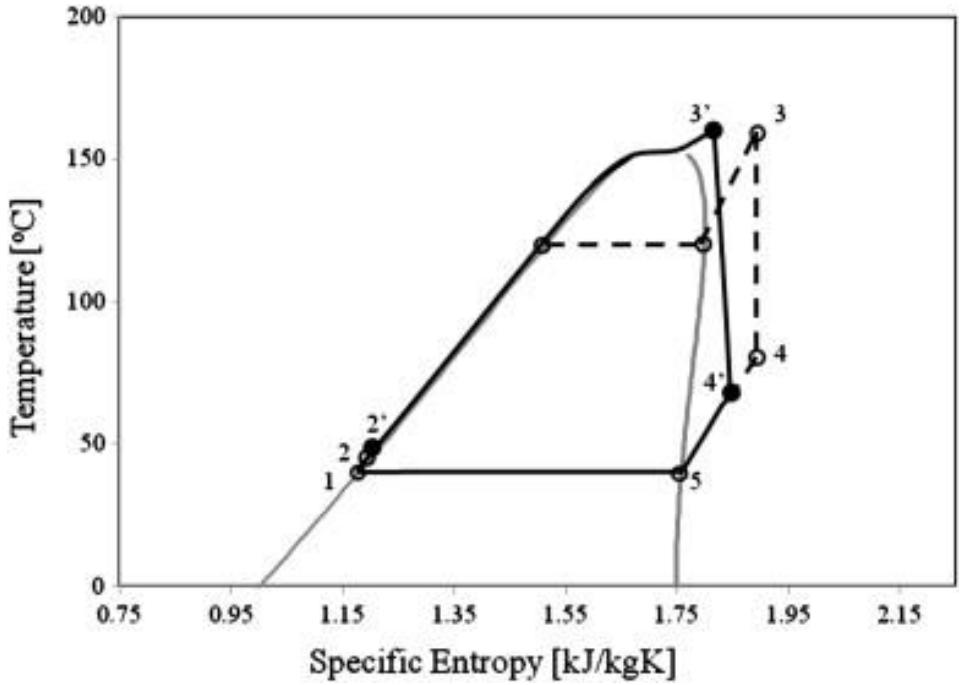

Figure 2.2: Comparison of a sub-critical and a super-critical ORC system using R245fa [10]

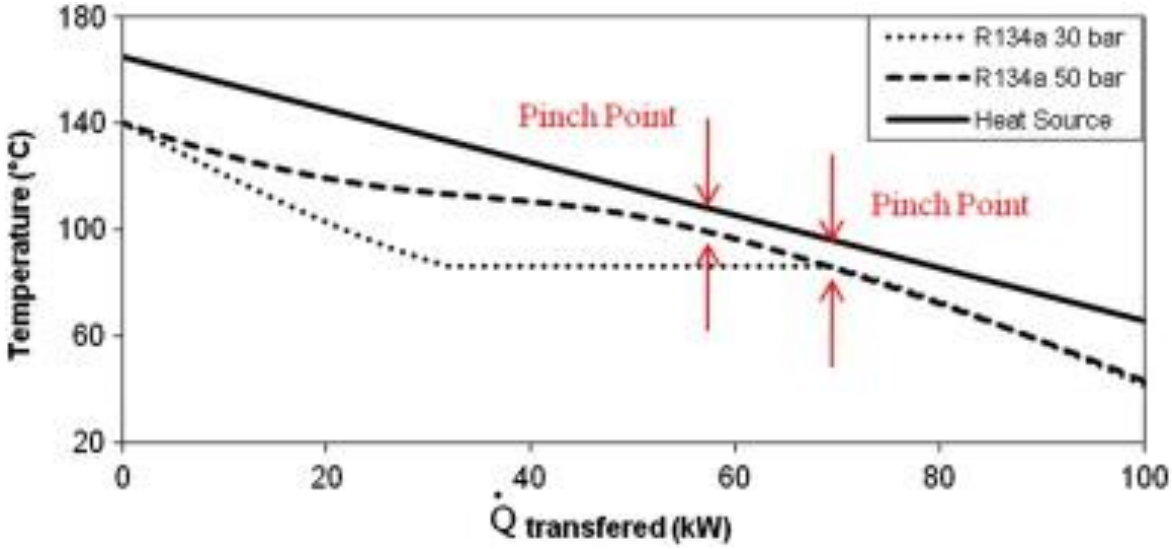

Figure 2.3: Comparison of thermal-glide between a sub-critical and a super-critical ORC system using R134a [10]

The current state-of-arts in super-critical system includes the optimization of the cycle performance with different working fluid with different approaches, interaction between the

fluid properties and cycle performance, different applications of super-critical cycle, and the application of zeotropic mixtures [11]. However, the application of super-critical cycle is still limited as some organic working fluid tend to decompose at high temperature [6]. R245fa might decompose over 250˚C and produce hydrofluoric acid and carbonyl halides [6]. The high pressure specification for super-critical ORC requires high pressure-resistant materials for the piping construction and advanced sealing techniques to avoid the leakage of refrigerants into the atmosphere.

2.2 Selection of Working Fluid for ORC

Selection of suitable working fluid would determine the maximum achievable cycle efficiency and installed cost of the ORC system. A suitable working fluid has to be determined in a preliminary cycle design phase to provide an estimation in system's cost and system performance to the site owner. The thermodynamic properties of the organic working fluid are briefly discussed, and the corresponding effects on the ORC system are presented.

Type of working fluid based on saturation vapour curve

The organic working fluids are categorized by the gradient of the saturation curve in a temperature-entropy (T-s) diagram [12], as shown in Figure 2.4. There are three types of working fluid, namely wet fluid, dry fluid and isentropic fluid. Wet fluid is characterized with a negative gradient in a T-s diagram, such as water and ammonia. A minimum amount of superheat is required at the turbine inlet to avoid the formation of droplets during the expansion process within the expansion machines. The droplets would impinge on the surface of the rotating parts of a positive displacement machines or blade surface of a turbine, causing the cavitation effects and surface damage. An excessively high degree of superheat would, however, reduce the overall cycle efficiency. Compromise is required to maintain the cycle efficiency within an acceptable range without sacrificing the life cycle of the turbine. A common practise in steam plant application is to maintain the minimum dryness fraction above 85% without having an excessive amount of superheat at the turbine inlet [13]. The application of the wet fluid requires frequent maintenance and overhaul of the turbines.

Dry fluid and wet fluid are better candidates for ORC application without the concern of condensation along the expansion process. Dry fluid is characterized by the positive gradient in the T-s diagram. Superheat is not recommended when dry fluid is used as the overall cycle efficiency would be reduced [14]. If superheat is applied in dry fluid at the turbine inlet, there would be a larger amount of superheat at the turbine outlet. A larger heating load is required to apply the superheat and a larger amount of cooling load is required to cool the working fluid to sub-cooled state, hence reducing the thermal efficiency of the overall cycle. An isentropic fluid is defined with the close-to-vertical line type of gradient in the T-s diagram such as R245fa [6]. Isentropic fluid allows the expansion process along the vertical lines in the T-s diagram, without any condensation. The isentropic fluid is superior compared to the dry fluid as the ORC working fluid since the isentropic fluid is not excessively superheated at the turbine outlet, in

which the cooling load requirement of the condenser is lesser compared to the application of dry fluid.

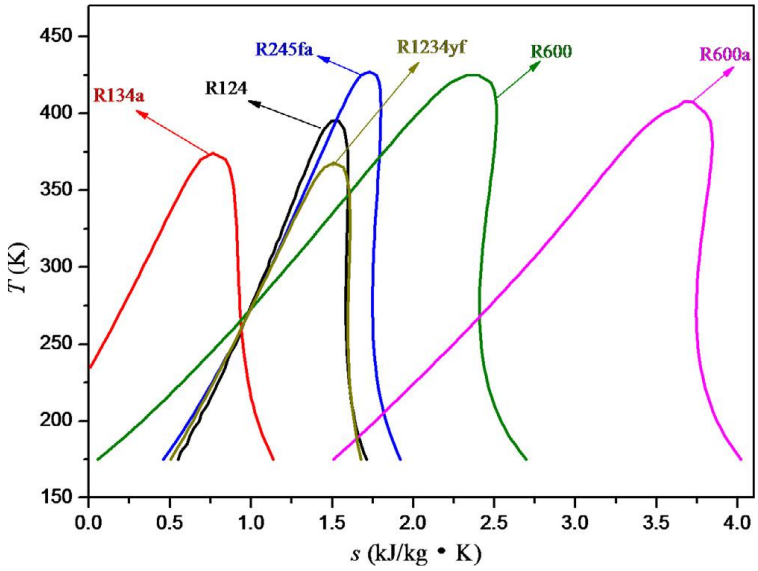

Figure 2.4: Temperature-entropy (T-s) diagram of working fluid [15]

Boiling point, freezing point and critical point

The thermodynamics properties of the selected fluid were found to have certain type of correlations with the thermal efficiency of the ORC. The impact of the boiling temperature of the working fluid was studied numerically by Mago [16] using different dry fluid, such as R113, R123, R245ca and iso-butane. The study reveals that the optimal performance of the ORC system was achieved by the fluid with highest boiling point. The result does not agree with the study by Aljundi, which demonstrates that the optimal working fluid is not necessary the working fluid with the highest boiling point [17]. However, a numerical study by Saleh has validated the hypothesis that the fluid from the same family with the highest boiling point contribute to the highest ORC thermal efficiency [18]. The correlation between the critical temperature of the working fluid, expansion ratio across the turbine, and the condensing temperature has been discussed [13]. A study by Bruno [19] shows that the working fluid with higher critical temperature result in higher thermal efficiency. The finding is supported by a study by Wang, in which the ORC system efficiency decreases when the working fluid with smaller critical temperature were applied in waste heat recovery application [20]. The freezing point of the fluid does not have direct correlation with the ORC performance. The freezing

point of the selected fluid has to be lower than the cycle lowest operating temperature to avoid choking the condenser.

Compatibility and stability

Organic working fluids usually undergo deterioration and decomposition when the temperature is much higher than the critical point. Hence, the application in super-critical region with very high operating temperature has to be taken care of [12]. Organic working fluid usually exhibits different types of non-favourable properties, such as high flammability in n-Pentane and toxicity in ammonia. An ideal fluid would be non-corrosive, non-toxic, non-flammable, non-fouling and compatible with the plant design and plant material. ASHRAE refrigerant safety classification can be used to indicate the safety level of the fluid [6].

Environmental impact

The main parameters for the consideration of the environmental effects are ozone depletion potential (ODP), global warming potential (GWP), atmospheric lifetime (ALT), flammability (F) and toxicity (C). Some of the working fluid have been phased out by Montreal Protocol such as R-11, R-12, R-113, R-114, R-115 and others will potentially be phased out at 2020 and 2030 such as R-21, R-22, R-123, R-124, R141b [6]. The fluid in consideration for the ORC system should exclude the soon-to-be-phased-out fluid.

Molecular weight

The molecular weight of the working fluid shows a direct correlation with the turbine efficiency. Harinck et al. reported that the organic working fluid with higher molecular weight is preferable for better turbine efficiency [21]. A study by Stijepovic et al. [22] shows that the increase in molecular weight increases the size parameter, thus increasing the turbine efficiency, based on equation (2.1). The size parameter, *SP*, was first derived mathematically by Macchi [23] using the correlation of specific speed and specific diameter, which was further simplified by Stijepovic as a function of molar mass, *F*, molecular weight, *M*, density at the turbine exit, ρ, and isentropic drop across the turbine stage at the given pressure ratio, Δh_{is}.

$$SP = \frac{\sqrt{F \bullet M / \rho}}{\Delta h_{is}^{0.25}} \tag{13.1}$$

Though the molecular weight has a positive effect on the turbine performance, evaporator and condenser with higher heat transfer area are required to compensate the increase in the specific

volume of the fluid in vapour form [13]. The effect of the molecular weight on the other turbine performance index such as work output and pressure ratio has not been investigated.

Latent heat, density and specific heat

High vaporization latent heat, high density and low specific heat are favourable for the ORC performance and turbine design. High vaporization latent heat allows most of the heat transfer within the evaporator and minimizes the need of super-heating [24]. Low liquid specific heat allows the minimal pump power requirement [25]. A study by Bao, however, shows that there is no direct correlation between the specific work of the liquid and the pump power requirement [13]. High density fluid is favourable to allow the installation of smaller size of turbines and heat exchangers units as evaporator and condensers for the similar power output.

Quantitative Screening Parameters for the Working Fluid

This quantitative method is proposed by Kuo [12] to evaluate the optimal fluid for the ORC system from the standpoint of the cycle performance. Two parameters have been proposed, namely Jacob number and Figure of Merit. Jacob number serves as a screening indicator for different working fluid while figure of merit can be used for screening of the same fluid under different operating conditions. Kuo et al. [12] found that lower Jacob number and figure of merit result in higher system thermal efficiency. Jacob number is defined as the ratio of sensible heat transfer and latent heat of evaporation.

$$Ja = \frac{C_p \Delta T}{h_{fg}} \tag{13.2}$$

$$FOM = Ja^{0.1} \frac{T_{cond}}{T_{evap}}^{0.8} \tag{13.3}$$

Where C_p is specific heat at constant pressure, h_{fg} is latent heat of evaporation, FOM is figure of merit, Ja is Jacob number, T_{evap} is evaporating temperature, T_{cond} is condensing temperature, and ΔT is the difference of evaporating temperature and condensing temperature of the thermodynamic cycle.

Summary of Proposed Working Fluid for ORC based on Current State-of-Art

Selection of optimal working fluid for the ORC system using different objective functions, such as cycle performance, exergy efficiency, and heat-exchange areas, has been performed extensively for the past decades, in both numerical simulation and experimental validations. Different types of application have different optimal working fluid. Research in working fluid selection with corresponding field application is compiled in Table 2.1. **Among the working fluids, the most recommended fluid for ORC is R245fa, followed by R236ea and benzene for sub-critical ORC system.**

Table 2.1: Recommended fluid from the past research with different screening criteria

Authors	**Application**	**Cycle**	**Cond. Temp (^{0}C)**	**Evap. Temp (^{0}C)**	**Considered Fluid**	**Recommended fluid (Efficiency / Net Power Output/cost per kWh)**
Guo et al. (2011) [9, 26]	Geothermal	subcritical ORC	35	90 *	27 fluid	R236ea, E170, R600, R141b
		trans-critical	25	80 - 120 *	Natural and conventional fluid	R125, R32, R143a
		trans-critical	25	>100 *		R218, R143a, R32
Wang et al. (2011) [27]	Waste Heat Recovery	Sub-critical	27 - 87	0.2 - 2 Mpa	R245fa, R245ca, R236ea, R141b, R123, R114, R113, R11, Butane	R245fa, R245ca (environmental friendly) and R113, R123, R11, R141b (high performance)
Vankeirsbilck et al. (2011) [4]	Waste Heat Recovery	Sub-critical	40	120-350*	R245fa, Toluene, (cyclo)-pentane, Solkatherm, 2 silicone oils (MM and MDM), OMTS, HDMS	Toluene, OMTS, HMDS, cyclo-pentane
Rayegan and Tao (2011) [28]	Solar	Sub-critical	25	130	Refrigerants and non-refrigerants (117 fluid)	refrigerant (R245fa, R245ca), non-refrigerant (Acetone, Benzene)
				85		refrigerant (R245fa, R245ca, E134), non-refrigerant (Cyclohexane, Benzene)
Kuo, Hsu, Cliohang, Wang (2011) [12]	Not specified (50kW)	Sub-critical	45	108	R123, R236fa, R245fa, R600, n-Pentane	R123 followed by n-Pentane, R245fa, R600, R236fa
Aljundi (2011)	n/a	n/a	30	50-140	RC-138,R227ea, R113, isobutane, n-butane, n-hexane, isopentane, neo-pentane, R245fa, R236ea, C5F12, R235fa	n-hexane
Papadopoulos et al. (2010) [25]	n/a	Sub-critical	n/a	n/a	Hydrocarbons, Hydrofluorocarbons, conventional fluid	R611
Mikielewicz and Mikielewicz (2010)	CHP	n/a	50	170	R365mfc, Heptane, Pentane, R12, R141b, Ethanol	Ethanol

Fankam et al. (2009)	Solar	Sub-critical	35	60 - 100	Refrigerants	R125a, R600, R290
Tchanche et al. (2009)	Solar	n/a	35	60-100	Refrigeratns	R152a, R600, R290
Facao (2009)	Solar	n/a	45	120 / 230	Water, n-Pentane, HFE7100, Cyclohexane, Toluene, R245fa, n-dodecane, iso-butane	n-dodecane
Dai (2009) [29]	Waste heat recovery	n/a	25	145*	Water, ammonia, butane, isobutane, R11, R123, R141b, R236ea, R245ca, R113	R236ea
Desai (2009) [30]	Waste heat recovery	n/a	40	120	Alcanes, Benzene, R113, R123, R141b, R236ea, R245ca, R245fa, R365mfc, Toluene	Toluene, Benzene
Gu (2009)	Waste heat recovery	n/a	50	80-220	R600a, R245fa, R123, R113	R113 and R123
Saleh et al. (2007)	Geothermal	Sub-critical	30	100	Alkanes, fluorinated alkanes, ethers and fluorinated ethers	RE134, RE245, R600, R245fa, R245ca, R601
Drescher and Bruggemann (2007)	Biosmass CHP	n/a	90*	250 - 350 *	ButylBenzene, Propylbenzene, Ethylbenzene, Toluene, OMTS	Alkyl Benzenes
Hettiarachchia et al. (2007) [3]	geothermal	Sub-critical	30*	70-90	Ammonia, n-Pentane, R123, PF5050	Ammonia
Lemort et al. (2007)	Waste Heat Recovery	Sub-critical	35	60-100	R245fa, R123, R134a, n-Pentane	R123, n-Pentane
Borsukiewicz-Gozdur and Nowak (2007)	Geothermal	Sub-critical	25	80-115	propylene, R227ea, RC318, R236fa, ibutane, R245fa	Propylene, R227ea, R245fa
El Chammas and Clodic (2005)	Waste Heat Recovery (Internal Combustion Engine)	n/a	55 (100 for water)	60 - 150 (150 - 260 for water)	Water, R123, isopentane, R245ca, R245fa, butane, isobutene, R152a	Water, R245ca and Iso-pentane
Maizza and Maizza [24]	n/a	Sub-critical	35-60	80-110	Unconventional working fluid	R123, R124

** indicate temp of heat source/heat sink **the table is extended from [31] and [32]*

2.3 Industrial ORC Technology: A brief summary

ORMAT has commercialized the ORC system and manufactured small power units in Massachusetts in early 1970 [33]. The company has ventured into geothermal application, installing the first ORMAT Energy Convertor (OEC) in Wabuska facility outside of Yerington,, Nevada in 1984. ORMAT has then expanded the business worldwide with over 626 MW geothermal plants, and over 1,750 MW of installed OEC capacity in year 2014 [33]. Turboden is another leading company in development and production of ORC technology, based in Italy and founded by Mario Gaia, Professor of Energy at the Politecnico di Milano [34]. Turboden manufactures ORC units from 300 kW for combined heat and power (CHP) application in early 1980 [35]. Turboden has expanded the business and developed the off-the-shelf ORC units between 300 kW and 10 MW [34]. Both ORMAT and Turboden are the pioneers of the commercial ORC products with their extensive experiences in the field over decades. Figure 1.6 shows the number of the ORC sites and the power distributions of the ORC sites installed by a number of ORC companies. ORMAT has the largest installed capacities whereas Turboden has the most number of sites in the market. The figure also shows a number of ORC manufacturers, including Tri-O-Gen, UTC Power, BNI, Electratherm, and etc. A market analysis on the commercial ORC technologies was performed and the current ORC manufacturers and suppliers with their corresponding technologies were presented in Table 2.2.

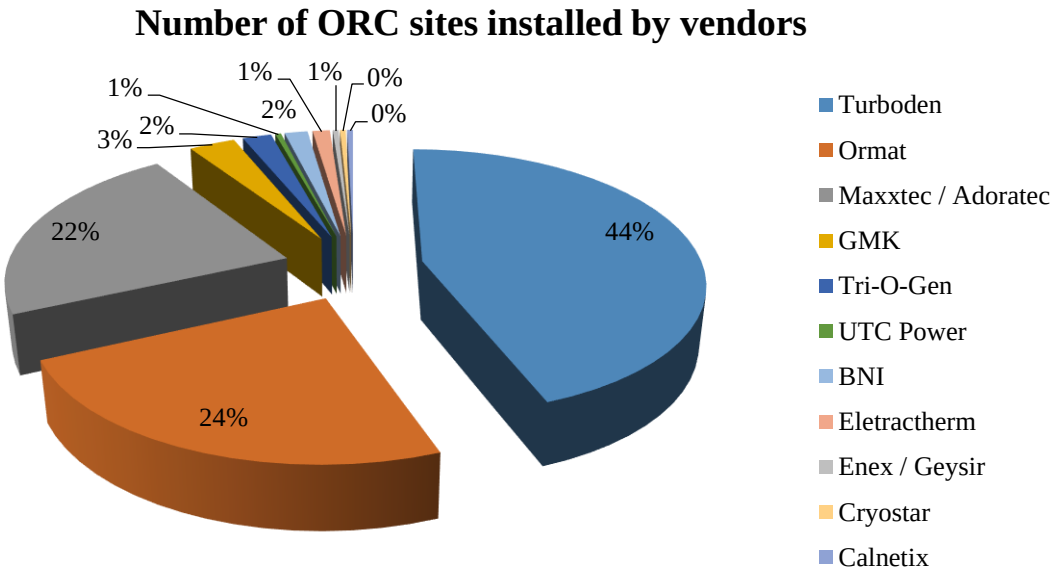

(a)

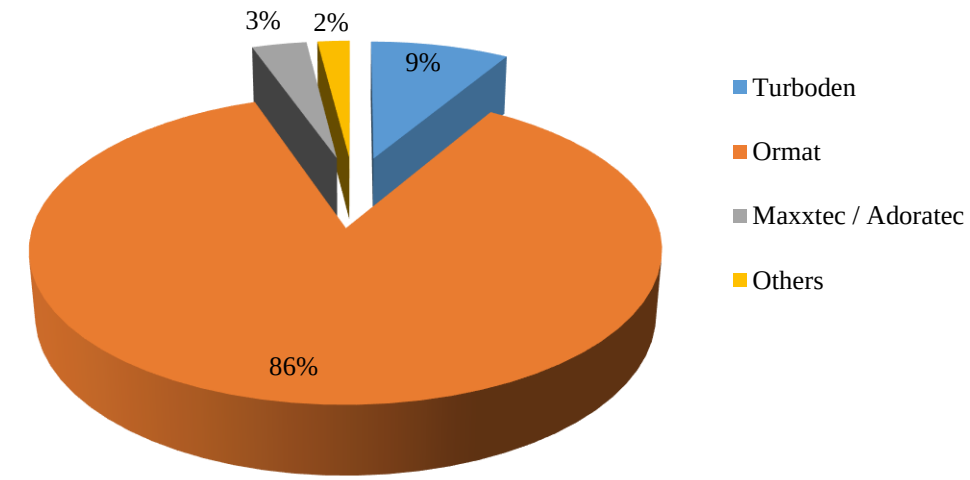

(b)

Figure 2.5: (a) The sites installed and b) the total power distributions by the major ORC manufacturers [36]

Table 2.2: Summary of some ORC manufacturers with the corresponding technology and products

Suppliers	Types of Heat Source	Heat Source Temp.	Heat Carrier	Thermal Input (kW)	Power Output	Units	Technology
Ormat	Geothermal Heat Recovery Solar	Low - High	Geothermal fluid/steam	n/a	250 kW to 20 MW (200 kWe to 72 MWe)	OEC (Custom-made)	Fluid: n-pentane
Turboden (UTC)	Biomass	in300/out240	Thermal Oil	3340 to 12020	643 kW to 2304 Kw	TD6CHP - TD22CHP	n/a
		in310/out210	Thermal Oil	4155 to 13075	1 MW to 3 MW	TURBODEN 12 HRS & TURBODEN 24 HRS	n/a
	Heat Recovery	240 - 310	Exhaust gas, refineries hot streams, jacket cooling water of engines, condensing organic fluid	2.5 MW to 50 MW	600 Kw to 10 MW	TURBODEN 6/7HR - TURBODEN 50 to 100 HR	Fluid: OMTS, Solkatherm Axial Turbines
		in310/out210		4155 to 13075	1 MW to 3 MW	TURBODEN 12 HRS & TURBODEN 32 HRS	n/a
	Geothermal	Min 91 degree C	Hot water/steam	n/a	280 kW	PureCycle® power system	n/a
					1.5 MW	n/a	n/a
Infinity Turbine ®	Heat Recovery	Below 100 degree C (>80 degree C)	Compressed air, steam, water, etc.	n/a	5kW-10kW, 50,250 kW	IT50, IT10, IT250, Itmine or Itxr	Fluid: R134a Radial Turboexpander
GE Energy	Heat Recovery	in143/out127	Pressurized Hot Water,saturated steam, gas	980 kW	125 kW	Clean Cycle™ 125	
Maxxtec / Adoratec	Biomass	320/245	Thermal Oil	1650 kW to 12970 kW	300 kW to 2400 kW	AD300 TF-plus - AD2400TF-plus	Fluid : OMTS
GMK	Heat Recovery	300 degree C	Thermal Oil	3.5 - 10.0 MW	0.5 - 5.0 MW	INDUCAL®	3000 rpm multi-stage axial turbines (KKK)

							Fluid: GL160 (GMK patented)
	Biomass	350 degree C	Thermal Oil	3.5 - 10.0 MW	0.5 - 2.0 MW	ECOCAL®	n/a
	Geothermal	100 °C up to 250 °C	Thermal waters	3.5 - 125.0 MW	0.5 - 15.0 MW	GEOCAL®	n/a
TRI-O-GEN	Heat Recovery	> 350 degree C	Toluene (direct exposed to heat source)	450 - 900 kWth	60 - 165 kWe	Tri-O-Gen ORC	Turbo Expander
Calnetix Technologies	Heat Recovery	n/a	n/a	n/a	125 kW	Thermapower™ Organic Rankine Cycle (ORC) Modules	n/a
ElectraTherm	Heat Recovery	88 °C -116°C	Other Liquid Waste Heat Sources	n/a	18 - 65 kWe	Series 4000 Green Machine	Twin Screw Expander
	Solar		Hot Water Heat Source				
	Biomass		Thermal Oils				
	Geothermal		Hot Water Heat Source				
Cryostar	Geothermal	100 – 400 °C	n/a	n/a	1.5 MW (France)/ 3.3MW (Germany)	n/a	Radial Inflow Turbine Fluid: R245fa, R134a
koehler-ziegler	Waste Heat	90 – 200 °C	n/a	n/a	50 – 200 kWe	n/a	Fluid: Hydrocarbons Steam Turbine (screw expander)
Free Power	Waste Heat	180 – 225 °C	n/a	n/a	n/a	FP85, FP 100, FP 120	n/a

Note: The table is compiled from [31] and further extended from the official website from the relevant companies

2.4 State of the Art of ORC Turbines and Expanders

The expander is the most important component in a thermodynamic cycle producing the useful power in the form of rotating shaft. The expander technologies have two different categories, turbo-expanders and positive displacement machines. The turbo-expander operates by continuous injection of fluid into the turbine without any flow interruption; while the positive displacement machine operates by injection of a specific amount of fluid, followed by fluid expansion and discharge to the downstream component to complete a revolution. Turbo-expanders are commonly applied in large scale power generation systems, aerospace applications in driving the compressors for the airplane, diesel-driven micro gas turbines, and turbocharging technologies [37]. Positive displacement machines are commonly used in refrigeration and air conditioning industry as compressors and pumps [38].

Different turbine and expander technologies are showcased in Table 2.3. Some turbines and expanders are supplied as standalone units and some are supplied as part of the commercial ORC units. The radial inflow turbine is, by far the most popular technology in the commercial ORC units, based on Table 2.3. An axial turbine is limited to ORC applications with high mass flow and high power output. The radial inflow turbine is however, more sensitive to the design conditions than the axial turbine, as shown in the performance curve in the work by Dixon [39]. Positive displacement machines, such as the scroll expander, are gaining an enormous interest in recent years, due to the simplicity in design and the capability to be coupled directly to standard 50/60 Hz generators. A huge amount of research has been conducted by adapting existing scroll compressors from automotive and refrigeration applications for small scale ORC systems.

Table 2.3: Market available turbines and expanders for commercial ORC units with corresponding working fluid

Suppliers	Expander Types	Application	Power Range (kW)	Rotational Speed (rev/min)	Working medium	References
NREC Concepts	Axial Turbine	G, W, B	150 - 330	20,000	R112, R113, R114, R134a, R236fa, R245fa	[40]
ORMAT	Axial Turbine	G	250 - 20,000	*Not provided*	n-Pentane	[41]
GMK	Axial Turbine	G, W, B	500 - 5,000	3,000 and 20,000	GL160, WL220	[42], [43]
Ener-G-rotors	gerotors	W	40 - 60	3,000 - 3,600	Steam	[44]
Green Turbine	*Not provided*	S	1.2 - 15	26,000 - 30,000	Steam	[45]

COGEN Microsystems	Piston expander	W, CHP	< 20	*Not provided*	*Not provided*	[46]
Infinity Turbine	Radial inflow turbine	G, W	10 - 250	3,600	R245fa, R134a	[47]
Verdicorp	Radial inflow turbine	W	20 - 115	Up to 45,000	R245fa	[48]
Tri-O-Gen	Radial inflow turbine	W, B	60 - 165	25,000	Toluene	[43], [49]
GE Energy	Radial inflow turbine	W	125	26,500	R245fa	[43], [50]
Zuccato-Energia	Radial inflow turbine	W	50, 150	15,000	R245fa	[51]
Cryostar	Radial inflow turbine	W, CHP	500 - 15,000	6,000 - 33,000	*Not provided*	[52]
Atlas Copco	Radial inflow turbine/ Axial Turbine	G, W	200 - 25,000	14,000*	Isobutane *	[53]
Turboden	Radial inflow turbine/ Axial Turbine	G, W, B, CHP	200 - 15,000	*Not provided*	R134a, Steam	[34], [54]
Exergy	Radial outflow turbine	G, W, B	400 - 5,500	3,000	Steam	[55]
Exa-Energie	Screw expander	W, CHP	15 - 150	3,000 - 3,600	R245fa, R134a, Toluene	[56]
Electra-Therm	Screw expander	W, CHP, B	35 - 110	3,000 - 3,600	R245fa	[43]
Air Squared	Scroll expander	W	1 - 10	3,000 - 3,600	R245fa	[52]
ENEFTECH	Scroll expander	W, CHP	5 - 30	3,000	R245fa	[57]
Icenova Engineering	Scroll expander	W	15, 30	3,000 - 3,600	R245fa	[56]

The design and development of expansion machines for ORC system involves a number of research in different fields, including modelling improvement in the cycle preliminary design phase, application of more accurate equations of state (EoS) to model the real gas effects, advanced improvement in design and analysis of axial and radial turbines, and evaluation of the feasibility of different positive displacement machines, such as scroll expander, screw expander, vane expander, and piston expander. An ORC system has to be modelled to determine the optimal cycle configuration and working fluid for the best cycle performance before conducting a detailed design analysis on the system components. A number of assumptions is usually made to reduce the computational efforts, including the constant efficiency of pump and turbine. One of the disadvantages of assuming the constant efficiency of the pump and the turbine is the system performance and the turbine performance cannot be

represented precisely at different operating condition. The turbine performance is very sensitive to the type of machines and the operating condition. Radial inflow turbine is more sensitive to the design point compared to axial turbine, in which the representation of the off-design performance of the radial inflow turbine would be deviated significantly from the actual condition if the performance is assumed constant [39]. Different turbine modelling approaches have been incorporated into the cycle preliminary design phase to improve the accuracy of the cycle model, as the following:

- the isentropic efficiency of the turbine has been modelled as a function of volumetric flow rate of the working fluid and enthalpy drop across the turbine [58],
- the isentropic efficiency has been modelled as a function of specific speed, volumetric expansion ratio, and the size parameter [59], and
- the turbine design and meanline analysis program has been coupled to the cycle design [60-62]

One of the innovations in current ORC technology is the application of scroll machines as the expanders to generate electricity in the range of a few kilowatts to thirty kilowatts. An initiative has been taken by a few researchers to convert the scroll compressors from automobile application and from refrigeration system into scroll expanders [63-67]. The conversion of the scroll compressors into scroll expanders is feasible with an acceptable range of isentropic efficiency for the expanders. Different types of industrial scroll compressors have been investigated and converted into expansion machines for ORC, with the maximum efficiency between 70 and 80% for hermetic refrigeration scroll compressors [68-71], 60 and 70% for open-drive automotive scroll compressors [72-74], 70 and 78% for scroll air compressors [66, 75, 76], and 80% for semi-hermetic automotive compressor [77]. Three different modelling techniques have been developed to study the steady state performance and the dynamic behaviour of the scroll expander, namely deterministic model, semi-empirical model, and empirical model. Deterministic model is the full mathematical model describing the dynamic motion of the scroll expander for the full revolution, coupled to the conservation of mass flow, leakage model, suction pressure and discharge pressure loss [78-80], and the heat transfer between the fluid, casing, and the atmosphere. The deterministic model is able to provide the information of the variation of mass flow with the rotation angle, under-expansion or over-expansion, and shaft power as a function of the shaft speed without conducting an experiment. Empirical model has been developed to correlate the operating parameters to the

performance parameters. Fundamental thermodynamics behaviour is, in most cases, ignored in the empirical model. Semi-empirical model has been developed by taking into account of the mass balance, pressure drop, expansion process, and heat balance of the scroll system. Eight model parameters were identified and the values were determined from the experimental measurements [66]. The semi-empirical model was then applied to investigate the mass flow and shaft power at different pressure ratio with maximum deviation of less than 5% [66]. One of the interesting experimental works for scroll expanders is the investigation of the breakdown of losses of a scroll expander [69]. The study shows that both the mechanical loss and the motor loss contribute to the low isentropic efficiency of the scroll expander, even at the optimal operating condition. Other than the adaptation of scroll compressors as scroll expanders, a design procedure, known as 8-dimensional planar curve framework, was adapted for the geometrical design of scroll expanders [81]. The method was demonstrated by designing a scroll geometry for a 3 kWe ORC system with maximum isentropic efficiency of 85% [81].

There are different positive displacement machines suitable for the application in an ORC system. Among the machines, screw expander is another popular technology with low flow and low power output less than 250 kWe. Screw expander is comprised of either a helical rotor or a pair of helical rotors with a casing. The volume between the rotors and the casing changes as a function of the rotational angle. The power is transferred from the expansion of the fluid to the rotor shafts by the pressure difference on the rotors, which changes with the fluid volume during the rotation [82].The technology of screw machine has been studied extensively by Smith [83-92] over 20 years in different applications with different modelling techniques, including thermodynamic analysis [84], full flow field study using computational fluid dynamics (CFD) [83] and fluid-solid interactions [93]. The main suppliers for screw machines for ORC application include Electratherm (twin screw expander), BEP Europe (mono screw machine), and Opcon (Lysholm expanders) [94]. The current research study of screw expander includes the development of an empirical-based model for expander's performance [95], experimental study of an ORC system using screw expander [96], preliminary testing of a screw expander by using a compressed air test rig [97], and evaluation of the performance of the screw expander was evaluated with different intake pressure [98] and different clearance between the rotors and the casing [99]. The screw expander technology has been evaluated using three-dimensional CFD model to study the performance of different designs under different pressure ratio [100] and evaluate the development of pressure distribution using single phase flow and two phase flow [101].

Ge-rotor, piston expander, and rotary vane expander are less popular than the scroll expander. A scroll expander and a ge-rotor were tested using R123 [70] at 3 kWe and 2 kWe with isentropic efficiency of 83% and 85%, respectively. A small ge-rotor with built-in volume ratio of 2 was tested with nominal power of 10 We with an isentropic efficiency of 11% [102]. The low isentropic efficiency is attributed to the large frictional force at small power, which could be improved for an optimal ORC unit. Ener-G-Rotors produces ge-rotors as commercial ORC expander units with nominal power of 40 and 60 kWe. Piston expander and rotary vane expander are potential ORC expansion machines with low isentropic efficiency [13]. A number of drawbacks in utilizing the piston expander as expansion machines were stated [13], including lubrication issues and poor breathing characteristics attributed to the high frictional losses across the valves. Two research prototype units of piston expander were tested using carbon dioxide as the working medium, with isentropic efficiency of 11% [103] and 62% [104]. A rotary vane expander (adapted from an air motor) was tested [105] using HFE7000 with a measured power of 860.7We and approximately 55% isentropic efficiency. A number of prototype research of the piston expander and vane expander was presented in Table 2.4. The application of these machines in the ORC application is limited due to the low isentropic efficiency of the piston expander and vane expander, attributed to the poor sealing, high leakage flow, and high frictional losses between the contacting surfaces. A high isentropic efficiency is usually favourable commercially to increase the energy return on investment (EROI), which further impedes the research development of these machines.

Table 2.4: The prototype research of reciprocating piston expander and rotary vane expander [13]

Researchers	Type of machines	Working fluid	Max. Isentropic efficiency (%)	Power (kW)	Pressure ratio
Baek et al. [106]	Reciprocating piston expander	CO2	10.5	24	2.1
Zhang et al. [107]	Reciprocating piston expander	CO2	62	-	2.4
Mohd et al. [108]	Rotary vane expander	R245fa	48	0.03	24
Yang et al. [109]	Rotary vane expander	CO2	23	-	-
Qiu et al. [105]	Rotary vane expander	HFE7000	55	1.7	2.1

The radial inflow turbine is the most popular solution for the ORC application, from a few kWe to a few MWe. An ORC expansion machine has to be able to handle the expansion of dense gas at high pressure ratio, with low flow rate and low enthalpy drop. A single stage

radial inflow turbine is more superior than a single stage axial turbine for the following reasons [110]:

- A radial inflow turbine can be optimized for different geothermal resources through minor changes.
- High turbine efficiency can be achieved for part-load condition using variable inlet guide vanes.
- The turbine blade profile is less sensitive to the deviation from manufacturing, compared to axial turbine.
- The blade structure is more robust under high blade loading with high density fluid.
- Radial inflow turbine shows a better rotor-dynamic stability and higher stiffness.

Different researches have been conducted extensively on the radial inflow turbine, prior to the development of the ORC technology, mainly in turbocharging and gas turbine sectors. The conventional design and development process of a radial inflow turbine is very intricate, and one of the design approaches has been proposed by Baines, as illustrated in Figure 2.6 [111]. The preliminary design stage uses the least computational effort with the highest efficiency improvement for the turbine design. The preliminary design process aims to provide the overall geometry of the turbine by calculating the velocity vector at the turbine inlet and the exit, and solve the law of conservation of mass, energy, and momentum to determine the mass flow rate and the thermodynamic conditions at each stations. A number of preliminary design approaches using meanline analysis has been developed about half a century ago [112-114]. The preliminary design approaches have been coupled to different optimization methods to provide the best geometry based on the weighted specifications as outlined by the designers. One of the evolutionary algorithms, known as Genetic Algorithm (GA), is commonly applied by a number of researchers [115-119]. Other optimization techniques have been coupled to the preliminary design phase, such as particle swarm optimization [120], multi-objective optimization [61], and DIRECT algorithm [60]. The preliminary design of radial turbine has been commonly implemented using the perfect gas assumption to reduce the computational effort but the thermodynamic properties of hydrocarbons or refrigerants in an ORC system do not agree well with the ideal gas law [21]. Hence, the fluid database has often been coupled to the preliminary design program to improve the accuracy of the turbine design model [121, 122]. Aerodynamic study on the turbine blade profile gains increased attention, especially for the ORC turbine due to the use of dense gas, with behaviour deviated significantly from the ideal gas law. Aerodynamic analysis was performed across the ORC turbine to investigate the unsteady

interaction between nozzle vanes and rotor blade for transonic flow [123] and the detailed analysis of shock wave patterns evolution within the blade passage [124]. Aerodynamic study was also conducted to model the supersonic flow within the blade passage of the nozzle vanes [125-127] to improve the nozzle design. One of the concerns of the ORC turbine is the turbine performance in different operating conditions, as the pressure ratio and mass flow rate of the ORC would fluctuate as a function of ambient temperature for a air-cooled geothermal binary plant [128]. The radial inflow turbine is very sensitive to the operating condition, compared to axial turbine [39]. The performance gain of the application of variable inlet guide vanes in an ORC turbine was investigated numerically [53] and experimentally [129] in a geothermal binary plant for a wide range of operating conditions.

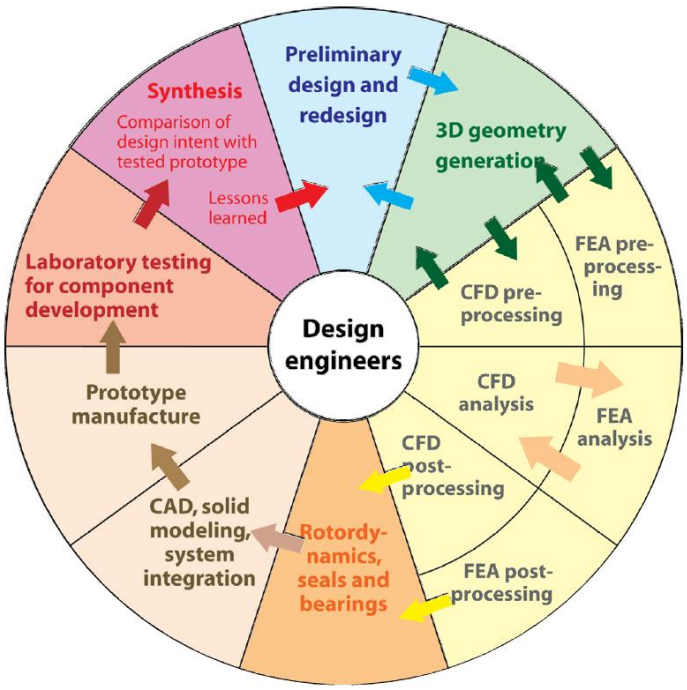

Figure 2.6: The design approach of turbine [111]

Radial outflow turbine is another innovative solution proposed and installed by EXERGY for geothermal, biomass and waste heat recovery application [130]. The gas flow is directed into the smaller wheel side and out from the turbine at the larger wheel side. The radial outflow turbine was reported to spin at low speed, with a large pressure ratio across multiple stages on a single disk. However, the radial outflow turbine tends to demonstrate a lower specific work output compared to an axial turbine and a radial inflow turbine with similar size [111]. An in-house design program for radial outflow turbine, known as *zTurbo* incorporating

the meanline analysis and optimization approach has been developed [131, 132]. The pressure field of the design outcome has been analysed and validated using an in-house through-flow solver, *TzFlow* [132]. The complex flow field in the radial outflow turbine was studied using ANSYS-CFX and the interaction between compressible flow effects on the blade profile design has been presented [133].

Axial turbine is a turbomachine for high flow rate and high pressure ratio. The axial turbine technology was developed over half a century ago in military and aerospace applications, which was then extended into the power generation application as steam turbine and gas turbine. Different empirical losses models were developed and validated for air and steam applications, including Ainley-Mathieson model [134], Craig-Cox model [135], Kacker-Okapuu model [136], and etc. The comparison between different empirical loss models for the ORC application [137] shows some discrepancies in the performance evaluation. A concept and design of an ORC cascade wind tunnel was proposed [138] with the aim to develop loss correlations of different aerofoil profile for ORC application. A commercial turbine design package, *AxStream,* incorporating the conventional design approach with real fluid database, was used to design a single stage axial turbine for R245fa with rated power of 250 kWe and estimated isentropic efficiency over 80% [139]. The axial flow configuration also allows the use of the multiple stage of axial turbines for high expansion ratio (up to 20:1 with a 4-stage configuration) with high isentropic efficiency [40]. Axial turbine, however, is not suitable for small system with low volumetric flow rate. A full admission axial turbine was designed for n-Pentane with rated power of 2 kWe [140]. The isentropic efficiency was found at 57% at the design point as compromise was required for a feasible design. A partial admission turbine was designed and tested for low flow application with measured isentropic efficiency of 53% [141].

The application of accurate gas model to predict the thermodynamic properties of the selected fluid is crucial in both turbine design and performance analysis. The adaptation of perfect gas model would yield large deviations up to 25% in density, sonic velocity, and total pressure loss, and 10% in Mach number, pressure and temperature distribution [142]. Another study by Lujan [143] shows that the maximum relative deviations using ideal gas equation are over 100% for pressure and heat capacity at constant volume, less than 70% for local speed of sound and heat capacity at constant pressure, and 50% for internal energy and enthalpy of the fluid. Though the deviation in the estimation of thermodynamic properties is significant, the distribution of thermodynamic properties in the flow field using ideal gas equation is similar to the flow field using real gas model [144]. A numerical study by Michele et al. [124] reports

that the use of perfect gas is not able to capture the working fluid behaviour across the whole expansion process accurately, but the behaviour within a single component (such as nozzle or rotor) was predicted successfully. A number of non-dimensional parameters deduced from similarity criterion was compared for a turbine using two different fluid, namely R245fa and air [145]. A large deviation in the non-dimensional parameters was found, and the error was attributed to the influence of the specific heat ratio [145]. The summary of the review of the current state-of-art of ORC expansion machine was illustrated by a fish bone diagram in Figure 2.7.

The current researches on the ORC turbine can generally be divided into two main categories: the adaptation of the positive displacement machines for the ORC application, and the improved numerical model to optimize the current turbine design and analysis in terms of steady and unsteady flow. The adaptation of the turbine from one working fluid into another is yet to be investigated or studied. Hence, the main contribution of this thesis is to fill in this engineering gap by presenting the SMC-DTR approach to design and optimize the ORC system to the resource condition by adapting the off-the-shelf turbines.

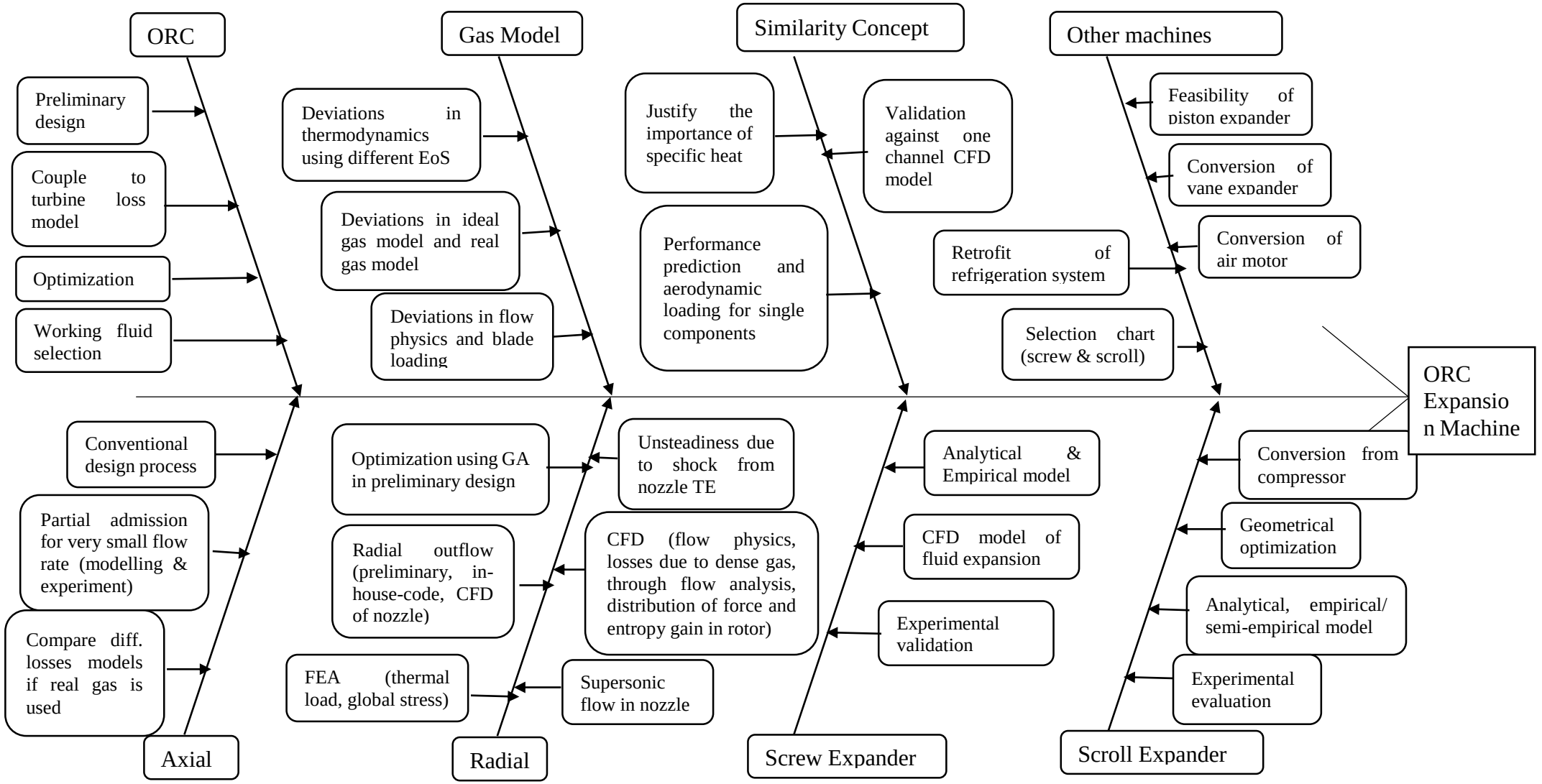

Figure 2.7: Current state-of-art of ORC expansion machines

2.5 References

1. Agency, I.E. *IEA Electricity Information 2012*. 2012.
2. *Overview of Existing Power Generation Turbine Designs*. 2000 - 2014, SoftInWay Incorporation.
3. Madhawa Hettiarachchi, H.D., et al., *Optimum design criteria for an Organic Rankine cycle using low-temperature geothermal heat sources.* Energy, 2007. **32**(9): p. 1698-1706.
4. Vankeirsbilck, I., et al., *Organic rankine cycle as efficient alternative to steam cycle for small scale power generation.* Proceedings of 8 th International Conference on Heat Transfer, Fluid Mechanics and Thermodynamics, Pointe Aux Piments (Mauritius), 2011.
5. Li, J., et al., *Energetic and exergetic investigation of an organic Rankine cycle at different heat source temperatures.* Energy, 2012. **38**(1): p. 85-95.
6. Chen, H., D.Y. Goswami, and E.K. Stefanakos, *A review of thermodynamic cycles and working fluids for the conversion of low-grade heat.* Renewable and Sustainable Energy Reviews, 2010. **14**(9): p. 3059-3067.
7. Zhang, X., M. He, and Y. Zhang, *A review of research on the Kalina cycle.* Renewable and Sustainable Energy Reviews, 2012. **16**(7): p. 5309-5318.
8. Bombarda, P., C.M. Invernizzi, and C. Pietra, *Heat recovery from Diesel engines: A thermodynamic comparison between Kalina and ORC cycles.* Applied Thermal Engineering, 2010. **30**(2–3): p. 212-219.
9. Guo, T., H. Wang, and S. Zhang, *Comparative analysis of natural and conventional working fluids for use in transcritical Rankine cycle using low-temperature geothermal source.* International Journal of Energy Research, 2011. **35**(6): p. 530-544.
10. Karellas, S., A. Schuster, and A.-D. Leontaritis, *Influence of supercritical ORC parameters on plate heat exchanger design.* Applied Thermal Engineering, 2012. **33–34**(0): p. 70-76.
11. Radulovic, J. and N.I. Beleno Castaneda, *On the potential of zeotropic mixtures in supercritical ORC powered by geothermal energy source.* Energy Conversion and Management, 2014. **88**(0): p. 365-371.
12. Kuo, C.-R., et al., *Analysis of a 50kW organic Rankine cycle system.* Energy, 2011. **36**(10): p. 5877-5885.
13. Bao, J. and L. Zhao, *A review of working fluid and expander selections for organic Rankine cycle.* Renewable and Sustainable Energy Reviews, 2013. **24**: p. 325-342.
14. Hung, T.C., T.Y. Shai, and S.K. Wang, *A review of organic rankine cycles (ORCs) for the recovery of low-grade waste heat.* Energy, 1997. **22**(7): p. 661-667.

15. Shu, G., et al., *Parametric and working fluid analysis of a dual-loop organic Rankine cycle (DORC) used in engine waste heat recovery.* Applied Energy, 2014. **113**(0): p. 1188-1198.

16. Mago, P.J., et al., *An examination of regenerative organic Rankine cycles using dry fluids.* Applied thermal engineering, 2008. **28**(8): p. 998-1007.

17. Aljundi, I.H., *Effect of dry hydrocarbons and critical point temperature on the efficiencies of organic Rankine cycle.* Renewable Energy, 2011. **36**(4): p. 1196-1202.

18. Saleh, B., et al., *Working fluids for low-temperature organic Rankine cycles.* Energy, 2007. **32**(7): p. 1210-1221.

19. Bruno, J.C., et al., *Modelling and optimisation of solar organic rankine cycle engines for reverse osmosis desalination.* Applied Thermal Engineering, 2008. **28**(17): p. 2212-2226.

20. Liu, B.T., K.H. Chien, and C.C. Wang, *Effect of working fluids on organic Rankine cycle for waste heat recovery.* Energy, 2004. **29**(8): p. 1207-1217.

21. Harinck, J., *Super-and Transcritical Fluid Expansions*, in *Mechanical, Maritime and Materials Engineering*. 2010, Delft University of Technology.

22. Stijepovic, M.Z., et al., *On the role of working fluid properties in Organic Rankine Cycle performance.* Applied Thermal Engineering, 2012. **36**: p. 406-413.

23. Macchi, E. and A. Perdichizzi, *Efficiency prediction for axial-flow turbines operating with nonconventional fluids.* ASME Journal of Engineering for Power, 1981. **103**: p. 718e24.

24. Maizza, V. and A. Maizza, *Working fluids in non-steady flows for waste energy recovery systems.* Applied Thermal Engineering, 1996. **16**(7): p. 579-590.

25. Papadopoulos, A.I., M. Stijepovic, and P. Linke, *On the systematic design and selection of optimal working fluids for Organic Rankine Cycles.* Applied Thermal Engineering, 2010. **30**(6-7): p. 760-769.

26. Guo, T., H. Wang, and S. Zhang, *Fluids and parameters optimization for a novel cogeneration system driven by low-temperature geothermal sources.* Energy, 2011.

27. Wang, E.H., et al., *Study of working fluid selection of organic Rankine cycle (ORC) for engine waste heat recovery.* Energy, 2011. **36**(5): p. 3406-3418.

28. Rayegan, R. and Y.X. Tao, *A procedure to select working fluids for Solar Organic Rankine Cycles (ORCs).* Renewable Energy, 2011. **36**(2): p. 659-670.

29. Dai, Y., J. Wang, and L. Gao, *Parametric optimization and comparative study of organic Rankine cycle (ORC) for low grade waste heat recovery.* Energy Conversion and Management, 2009. **50**(3): p. 576-582.

30. Desai, N.B. and S. Bandyopadhyay, *Process integration of organic Rankine cycle.* Energy, 2009. **34**(10): p. 1674-1686.

31. Quoilin, S. and V. Lemort. *Technological and economical survey of Organic Rankine Cycle systems*. in *5th European Conference Economis and Management of Energy in Industry*. 2009. Algarve, Portugal.

32. Quoilin, S., et al., *Thermo-economic optimization of waste heat recovery Organic Rankine Cycles.* Applied Thermal Engineering, 2011. **31**(14–15): p. 2885-2893.

33. Nordquist, J., *DOE's Quadrennial Energy Review Stakeholder Meeting*

Natural Gas Transmission, Storage & Distribution. 2014: Pittsburgh, PA.

34. [cited 2014 3rd Sept]; Available from: http://www.turboden.eu/en/home/index.php.

35. Bronicki, L. *Short review of the long history of ORC power systems*. in *2nd International Seminar on ORC Power Systems (ORC2013), Rotterdam, Oct*. 2013.

36. Enertime. *Markets and actors in Organic Rankine Cycle*. 2009 [cited 2012 15th June]; Available from: http://www.cycle-organique-rankine.com/market-markers.php#2.

37. Meher-Homji, C.B. *'The Historical Evolution of Turbomachinery*. in *Proceedings of the 29th Turbomachinery Symposium, Texas A&M University, Houston, TX*. 2000.

38. Hundy, G., A.R. Trott, and T. Welch, *Refrigeration and Air-conditioning*. 2008: Butterworth-Heinemann.

39. Dixon, S.L. and C. Hall, *Fluid Mechanics and Thermodynamics of Turbomachinery*. 2010, Butterworth-Heinemann: Burlington.

40. David Japikse, F.D.B., Maxwell Hurgin, Keith Patch. *Development of a 300 kWe Integrated Axial Turbine and Generator for ORC Applications*. in *2nd Internal Seminar on ORC Power Systems: Turbo Expanders II*. 2013. De Doelen, Rotterdam, The Netherlands: American Society of Mechanical Engineers (ASME).

41. Nasir, P., et al., *Utilization of Turbine Waste Heat to Generate Electric Power at Neptune Plant.* 2004.

42. GMK. [cited 2014 22nd Sept]; Available from: http://www.gmk.info/.

43. Quoilin, S., et al., *Techno-economic survey of Organic Rankine Cycle (ORC) systems.* Renewable and Sustainable Energy Reviews, 2013. **22**(0): p. 168-186.

44. Newell, M. [cited 2004 29th Aug]; Available from: http://www.ener-g-rotors.com/.

45. *Green Turbine*, in *Green Turbine*. Netherlands.

46. Microsystems, C. *How our Technology Works*. [cited 2014 22nd Sept]; Available from: http://www.cogenmicro.com/.

47. Giese, G. [cited 2014 20th Sept]; Available from: http://www.infinityturbine.com/ORC/.

48. Ron Conry, S.M., Randolph Dietzel, Joost Brasz. *The Verdicorp ORC Turbine*. in *1st International Seminar on ORC Power Systems*. 2011. Aula Conference Centre, TU Delft, The Netherlands.

49. Buijtenen, J.v. *Design, Development and Operation of the TRI-O-GEN ORC Power Unit*. in *1st International Seminar on ORC Power Systems*. 2011. Aula Conference Centre, TU Delft, The Netherlands.

50. Stephen F. Anderson, P.B.B., PE; Betty Riley *City of Klamath Falls, Oregon: Geothermal Power Plant Feasibility Study*. 2011.

51. Energia, Z. [cited 2014 25th Aug]; Available from: http://www.zuccatoenergia.it/.

52. [cited 2014 2nd Sept]; Available from: http://airsquared.com/products/expanders.

53. Agahi, R. and C. Spadacini. *Comparison between Variable and Fixed Geometry Turbine in Geothermal Power Plants*. in *Proceedings World Geothermal Congress*. 2010. Bali, Indonesia.

54. Holdmann, G., *The Chena Hot Springs 400kW geothermal power plant: experience gained during the first year of operation.* Chena Geothermal Power Plant Report, Chena Power Plant, Alaska, 2007: p. 1-9.

55. [cited 2014 12th Sept]; Available from: http://exergy-orc.com/.

56. Fredella, L., *Preliminary Study of a Network Micro-co-generative ORC System* in *Mechanical, Nuclear , Aviation and Metallurgical Engineering Department*. 2012 - 2013, Universit of Bologna: Italy. p. 133.

57. Qiu, G., H. Liu, and S. Riffat, *Expanders for micro-CHP systems with organic Rankine cycle.* Applied Thermal Engineering, 2011. **31**(16): p. 3301-3307.

58. Ghasemi, H., et al., *Modeling and optimization of a binary geothermal power plant.* Energy, 2013. **50**(0): p. 412-428.

59. Lazzaretto, A. and G. Manente, *A New Criterion to Optimize ORC Design Performance using Efficiency Correlations for Axial and Radial Turbines.* International Journal of Thermodynamics, 2014. **17**(3).

60. Rahbar, K., et al., *Modelling and optimization of organic Rankine cycle based on a small-scale radial inflow turbine.* Energy Conversion and Management, 2015. **91**: p. 186-198.

61. Persky, R., E. Sauret, and L. Ma. *Optimisation methods for coupled thermodynamic and 1D design of radial-inflow turbines*. in *ASME 2014 4th Joint US-European Fluids Engineering Division Summer Meeting collocated with the ASME 2014 12th International Conference on Nanochannels, Microchannels, and Minichannels*. 2014. American Society of Mechanical Engineers.

62. Wang, X., X. Liu, and C. Zhang, *Performance Analysis of Organic Rankine Cycle With Preliminary Design of Radial Turbo Expander for Binary-Cycle Geothermal Plants.* Journal of Engineering for Gas Turbines and Power, 2013. **135**(11): p. 111402-111402.

63. Quoilin, S., V. Lemort, and J. Lebrun, *Experimental study and modeling of an Organic Rankine Cycle using scroll expander.* Applied Energy, 2010. **87**(4): p. 1260-1268.

64. Oralli, E., *Conversion of a Scroll Compressor to an Expander for Organic Rankine Cycle: Modeling and Analysis*. 2010, University of Ontario Institute of Technology (Canada): Canada.

65. Harada, K.J., *Development of a small scale scroll expander*. 2010.

66. Lemort, V., et al., *Testing and modeling a scroll expander integrated into an Organic Rankine Cycle.* Applied Thermal Engineering, 2009. **29**(14-15): p. 3094-3102.

67. Lemort, V. and S. Quoilin, *Designing scroll expanders for use in heat recovery Rankine cycles*, in *International Conference on Compressors and Their Systems*. 2009. p. 2010.

68. Bracco, R., et al., *Experimental tests and modelization of a domestic-scale ORC (Organic Rankine Cycle).* Energy, 2013. **58**: p. 107-116.

69. Lemort, V., S. Declaye, and S. Quoilin, *Experimental characterization of a hermetic scroll expander for use in a micro-scale Rankine cycle.* Proceedings of the Institution of Mechanical Engineers. Part A, Journal of power and energy, 2012. **226**(1): p. 126.

70. Mathias, J.A., et al., *Experimental Testing of Gerotor and Scroll Expanders Used in, and Energetic and Exergetic Modeling of an Organic Rankine Cycle.* Journal of Energy Resources Technology-Transactions of the Asme, 2009. **131**(1).

71. Kane, M., et al., *Small hybrid solar power system.* Energy, 2003. **28**(14): p. 1427-1443.

72. Woodland, B.J., et al., *Experimental testing of an organic Rankine cycle with Scroll-type expander.* 2012.

73. Saitoh, T., N. Yamada, and S.-I. Wakashima, *Solar Rankine cycle system using scroll expander.* 2007.

74. Manolakos, D., et al., *Experimental evaluation of an autonomous low-temperature solar Rankine cycle system for reverse osmosis desalination.* Desalination, 2007. **203**(1): p. 366-374.

75. Declaye, S., et al., *Experimental study on an open-drive scroll expander integrated into an ORC (Organic Rankine Cycle) system with R245fa as working fluid.* Energy, 2013. **55**: p. 173-183.

76. Wang, H., R. Peterson, and T. Herron, *Experimental performance of a compliant scroll expander for an organic Rankine cycle.* Proceedings of the Institution of Mechanical Engineers, Part A: Journal of Power and Energy, 2009. **223**(7): p. 863.

77. Jradi, M., et al., *Micro-scale ORC-based combined heat and power system using a novel scroll expander.* International Journal of Low-Carbon Technologies, 2014: p. ctu012.

78. Wang, J., et al., *Mathematical modeling study of scroll air motors and energy efficiency analysis—part II.* Mechatronics, IEEE/ASME Transactions on, 2011. **16**(1): p. 122-132.

79. Guangbin, L., et al., *Simulation of the dynamic processes in a scroll expander-generator used for small-scale organic Rankine cycle system.* Proceedings of the

Institution of Mechanical Engineers Part a-Journal of Power and Energy, 2011. **225**(A1): p. 141-149.

80. Guangbin, L., et al., *Simulation and experiment research on wide ranging working process of scroll expander driven by compressed air.* Applied Thermal Engineering, 2010. **30**(14–15): p. 2073-2079.

81. Orosz, M.S., et al., *Geometric Design of Scroll Expanders Optimized for Small Organic Rankine Cycles.* Journal of Engineering for Gas Turbines and Power, 2013. **135**(4): p. 042303-042303.

82. Smith, I.K., et al., *Steam as the working fluid for power recovery from exhaust gases by means of screw expanders.* Proceedings of the Institution of Mechanical Engineers Part E-Journal of Process Mechanical Engineering, 2011. **225**(E2): p. 117-125.

83. Kovacevic, A., N. Stosic, and I. Smith, *Screw Compressors : Three Dimensional Computational Fluid Dynamics and Solid Fluid Interaction*. 2007, Springer: Dordrecht.

84. Stošić, N., I.K. Smith, and A. Kovačević, *Screw compressors: mathematical modelling and performance calculation*. 2005: Springer Verlag.

85. Smith, I.K., N. Stosic, and A. Kovacevic, *Screw expanders increase output and decrease the cost of geothermal binary power plant systems.* Proc. Of the Geothermal Resources Council Annual Meeting, Reno, Nevada-USA, September, 2005: p. 25-28.

86. Kovacevic, A., N. Stosic, and I.K. Smith, *A numerical study of fluid–solid interaction in screw compressors.* International Journal of Computer Applications in Technology, 2004. **21**(4): p. 148-158.

87. Stosic, N., I.K. Smith, and A. Kovacevic, *Optimization of screw compressor design.* 2002.

88. Smith, I. and N. Stosic, *Prospects for energy conversion efficiency improvements by the use of twin screw two-phase expanders.* Proc. of the 2nd International Heat Powered Cycles Conference, Paris-France, 2001.

89. Smith, I., et al., *Twin screw expanders in large chiller units.* Proceedings of International Conference on Industrial Compressors and their Systems, City University, London, 1999.

90. Stosic, N., et al., *The design of a twin-screw compressor based on a new rotor profile.* Journal of Engineering Design, 1997. **8**(4): p. 389-399.

91. Stosic, N. and K. Hanjalic, *Development and optimization of screw machines with a simulation model .1. Profile generation.* Journal of Fluids Engineering-Transactions of the Asme, 1997. **119**(3): p. 659-663.

92. Smith, I.K., N. Stosic, and C.A. Aldis, *Development of the trilateral flash cycle system .3. The design of high-efficiency two-phase screw expanders.* Proceedings of the Institution of Mechanical Engineers Part a-Journal of Power and Energy, 1996. **210**(1): p. 75-93.

93. Kovacevic, A., N. Stosic, and I. Smith, *Fluid-Solid Interaction In Screw Compressors.* 2002.

94. Vanslambrouck, B., et al., *Turn waste heat into electricity by using an Organic Rankine Cycle*, in *2nd European Conference on Polygeneration*. 2011: Tarragona, Spain. p. nn-mm.

95. Krishna Avadhanula, V. and C.-S. Lin, *Empirical Models for a Screw Expander Based on Experimental Data From Organic Rankine Cycle System Testing.* Journal of Engineering for Gas Turbines and Power, 2014. **136**(6): p. 062601-062601.

96. Sung-Wei, H., H.-W.D. Chiang, and Y. Chih-Wei, *Experimental Investigation of the Performance of a Hermetic Screw-Expander Organic Rankine Cycle.* Energies (19961073), 2014. **7**(9): p. 6172-6185.

97. Wang, W., et al., *Preliminary experimental study of single screw expander prototype.* Applied Thermal Engineering, 2011. **31**(17–18): p. 3684-3688.

98. He, W., et al., *Influence of intake pressure on the performance of single screw expander working with compressed air*. Applied Thermal Engineering, 2013. **51**(1–2): p. 662-669.

99. Wang, W., et al., *Experimental study on the performance of single screw expanders by gap adjustment.* Energy, 2013. **62**(0): p. 379-384.

100. Papes, I., J. Degroote, and J. Vierendeels. *3D CFD analysis of a twin screw expander for small scale ORC systems*. in *11th World Congress on Computational Mechanics (WCCM XI-2014).* 2014.

101. Xia, G.-d., et al., *Single-phase and two-phase flows through helical rectangular channels in single screw expander prototype.* Journal of Hydrodynamics, Ser. B, 2014. **26**(1): p. 114-121.

102. N. Yamada, M.W., A. Hoshi. *Experiment of Pumpless Organic Rankine-type Cycle fow Low-Temperature Waste Heat Recoevery*. in *ORC 2011 First International Seminar on ORC Power Systems*. 2011. TU Delft, The Netherlands.

103. Baek, J.S., E.A. Groll, and P.B. Lawless, *Piston-cylinder work producing expansion device in a transcritical carbon dioxide cycle. Part I: experimental investigation.* International Journal of Refrigeration, 2005. **28**(2): p. 141-151.

104. Zhang, B., et al., *Development of a double acting free piston expander for power recovery in transcritical CO2 cycle.* Applied Thermal Engineering, 2007. **27**(8–9): p. 1629-1636.

105. Qiu, G.Q., et al., *Experimental investigation of a biomass-fired ORC-based micro-CHP for domestic applications.* Fuel, 2012. **96**(1): p. 374-382.

106. Baek, J., E. Groll, and P. Lawless, *Piston-cylinder work producing expansion device in a transcritical carbon dioxide cycle. Part I: experimental investigation.* International Journal of Refrigeration, 2005. **28**(2): p. 141-151.

107. Zhang, B., et al., *Development of a double acting free piston expander for power recovery in transcritical CO 2 cycle.* Applied Thermal Engineering, 2007. **27**(8): p. 1629-1636.

108. Tahir, M.B.M., N. Yamada, and T. Hoshino, *Efficiency of compact organic Rankine cycle system with rotary-vane-type expander for low-temperature waste heat recovery.* 2010.

109. Yang, B., et al., *Experimental investigation on the internal working process of a CO 2 rotary vane expander.* Applied Thermal Engineering, 2009. **29**(11): p. 2289-2296.

110. Sauret, E. and A.S. Rowlands, *Candidate radial-inflow turbines and high-density working fluids for geothermal power systems.* Energy, 2011. **36**(7): p. 4460-4467.

111. Baines, N. *ENGR408-ENME 627-S1 Special Topic in Engineering: Turbomachinery*. 2014.

112. Whitfield, A., *The preliminary design of radial inflow turbines.* J. Turbomach, 1990. **112**: p. 50-57.

113. Glassman, A.J., *Computer program for preliminary design analysis of axial-flow turbines.* 1972.

114. Rohlik, H.E., *Analytical determination of radial inflow turbine design geometry for maximum efficiency*. 1968: National Aeronautics and Space Administration.

115. Pasquale, D., G. Persico, and S. Rebay, *Optimization of Turbomachinery Flow Surfaces Applying a CFD-Based Throughflow Method.* Journal of Turbomachinery, 2014. **136**(3): p. 031013.

116. Erbas, M., et al. *Design and optimization of a low temperature organic Rankine cycle and turbine*. in *ASME 2013 International Mechanical Engineering Congress and Exposition*. 2013. American Society of Mechanical Engineers.

117. Surekha, N., et al., *Optimization of Principal Dimensions of Radial Flow Gas Turbine Rotor Using Genetic Algorithm.* International Journal of Scientific and Engineering Research, 2012. **3**(12): p. 152-157.

118. Ebaid, M. and Q. Al-Hamdan, *Optimization techniques for designing an inward flow radial turbine rotor.* Proceedings of the Institution of Mechanical Engineers, Part A: Journal of Power and Energy, 2004. **218**(8): p. 655-668.

119. Surekha, N., et al., *Optimization of Principal Dimensions of Radial Flow Gas Turbine Rotor Using Genetic Algorithm.*

120. Tsalicoglou, I. and B. Phillipsen, *Design of Radial Turbine Meridional Profiles using Particle Swarm Optimization.* 2nd International Conference on Engineering Optimization, 2010.

121. Ventura, C., et al., *Preliminary Design and Performance Estimation of Radial Inflow Turbines: An Automated Approach.* Journal of Fluids Engineering-Transactions of the Asme, 2012. **134**(3).

122. Fiaschi, D., G. Manfrida, and F. Maraschiello, *Thermo-fluid dynamics preliminary design of turbo-expanders for ORC cycles.* Applied Energy, 2012. **97**: p. 601-608.

123. Wheeler, A.P. and J. Ong. *A Study of the Three-Dimensional Unsteady Real-Gas Flows Within a Transonic ORC Turbine*. in *ASME Turbo Expo 2014: Turbine Technical Conference and Exposition*. 2014. American Society of Mechanical Engineers.

124. Marconcini, M., et al., *Aerodynamic investigation of a high pressure ratio turbo-expander for organic Rankine cycle applications.* ASME paper No. GT2012-69409, 2012.

125. Persico, G., et al. *Aerodynamic Design and Analysis of Centrifugal Turbine Cascades*. in *ASME Turbo Expo 2013: Turbine Technical Conference and Exposition*. 2013. American Society of Mechanical Engineers.

126. Harinck, J., et al., *Computational Study of a High-Expansion Ratio Radial Organic Rankine Cycle Turbine Stator.* Journal of Engineering for Gas Turbines and Power, 2010. **132**(5): p. 054501-6.

127. Hoffren, J., et al., *Numerical simulation of real-gas flow in a supersonic turbine nozzle ring.* Journal of engineering for gas turbines and power, 2002. **124**(2): p. 395-403.

128. Kanoğlu, M. and Y.A. Çengel, *Improving the Performance of an Existing Air-Cooled Binary Geothermal Power Plant: A Case Study.* Journal of Energy Resources Technology, 1999. **121**(3): p. 196-202.

129. Agahi, R. *Application of an Inflow Radial Turbine in a Geothermal Organic Rankine Cycle Power Plant*. in *35th New Zealand Geothermal Workshop*. 2013. Rotorua, New Zealand.

130. EXERGY *Radial Outflow Turbine*.

131. Casati, E., et al., *Centrifugal Turbines for Mini-Organic Rankine Cycle Power Systems.* Journal of Engineering for Gas Turbines and Power, 2014. **136**(12): p. 122607.

132. Pini, M., et al., *Preliminary Design of a Centrifugal Turbine for Organic Rankine Cycle Applications.* Journal of Engineering for Gas Turbines and Power, 2013. **135**(4): p. 042312-042312.

133. Persico, G., et al., *AERODYNAMICS OF CENTRIFUGAL TURBINE CASCADES.* Journal of Engineering for Gas Turbines and Power, 2015.

134. Ainley, D. and G. Mathieson, *A method of performance estimation for axial-flow turbines*. 1951: Defense Technical Information Center.

135. Craig, H. and H. Cox, *Performance estimation of axial flow turbines.* Proceedings of the Institution of Mechanical Engineers, 1970. **185**(1): p. 407-424.

136. Kacker, S.C. and U. Okapuu, *A Mean Line Prediction Method for Axial Flow Turbine Efficiency.* Journal of Engineering for Power, 1982. **104**(1): p. 111-119.

137. Klonowicz, P., et al., *Significance of loss correlations in performance prediction of small scale, highly loaded turbine stages working in Organic Rankine Cycles.* Energy, 2014. **72**: p. 322-330.

138. Hasselmann, K., et al. *Performance Predictions of Axial Turbines for Organic Rankine Cycle (ORC) Applications Based on Measurements of the Flow Through Two-Dimensional Cascades of Blades*. in *ASME 2014 Power Conference*. 2014. American Society of Mechanical Engineers.

139. Moroz, L., et al. *Axial turbine flow path design for an organic Rankine cycle using R-245fa*. in *ASME Turbo Expo 2013: Turbine Technical Conference and Exposition*. 2013. American Society of Mechanical Engineers.

140. P., B.T. and H. S. *Design and Testing of n-Pentane Turbine for 2 kW Model of Binary Cycle Power Plant*. in *Proceedings World Geothermal Congress 2010*. 2010. Bali, Indonesia.

141. Klonowicz, P., et al., *Design and performance measurements of an organic vapour turbine.* Applied Thermal Engineering, 2014. **63**(1): p. 297-303.

142. Harinck, J., et al., *Influence of thermodynamic models in two-dimensional flow simulations of turboexpanders.* Journal of turbomachinery, 2010. **132**(1): p. 011001.

143. Luján, J.M., et al., *Model of the expansion process for R245fa in an Organic Rankine Cycle (ORC).* Applied Thermal Engineering, 2012. **40**(0): p. 248-257.

144. Zhang, L., et al. *The Influence of Real Gas Effects on ICE-ORC Turbine Flow Fields*. in *ASME Turbo Expo 2014: Turbine Technical Conference and Exposition*. 2014. American Society of Mechanical Engineers.

145. Zhang, L., et al. *The Influence of Working Fluid Characteristic Parameters on Turbine Performance for the Small Scale ORC System*. in *ASME 2013 Fluids Engineering Division Summer Meeting*. 2013. American Society of Mechanical Engineers.

146. Brasz, J.J. and B.P. Biederman, *Power generation with a centrifugal compressor*. 2010, Google Patents.

147. Brasz, J.J. and B.P. Biederman, *Turbine with vaned nozzles*. 2007, Google Patents.

148. Biederman, J.J.B.B.P., *Organic Rankine Cycle Waste Heat Applications* 2002, Carrier Corporation: US.

149. Buerki, T., et al., *Use of a Turbocharger and Waste Heat Conversion System*. 2010, EP Patent 2,092,165.

150. Anton, N. and W. Wiberg, *Aerodynamic design of a gas turbine rotor blade for the KTH test turbine.* ISRN LUTMDN/TMHP--13/5284--SE, 2013.

151. Japikse, D. and N.C. Baines, *Introduction to turbomachinery*. 1995: Concepts ETI.

152. Aungier, R.H., *Turbine aerodynamics: axial-flow and radial-inflow turbine design and analysis*. 2006: ASME Press.

3.0 Thermodynamic Cycle Model

The aim of this thesis is to present the SMC-DTR approach for low temperature resources, and the main contribution of this thesis is to develop the key component, SMC adaptive strategy. This chapter presents the thermodynamic cycle design and modelling of organic Rankine cycle. This component is one of the critical components in the SMC-DTR approach as it is coupled to the turbine matching and the SMC adaptive strategy to determine the optimal configuration of working fluid and existing turbine for optimal system performance. This thermodynamic cycle model is developed using Engineering Equation Solver (EES) and the mathematical equations are presented. A case study is presented, in which an ORC system is designed using the heat source condition of Rotokawa steam field (located in New Zealand) and the ambient air as the heat sink.

3.1 Thermodynamic Analysis of an Organic Rankine Cycle

ORC system plays an important role in extracting the heat energy from low grade heat source with minimal carbon emission into the atmosphere. In its simplest form, an ORC system comprises of four major components, which are feed pump, evaporator, turbine, and condenser. In this chapter, a simplified schematic of a basic binary geothermal plant using the concept of an ORC system is presented as a framework for the discussion of the thermodynamic analysis. P is pump, PW is production well of the geothermal reservoir, IW is injection well into the geothermal reservoir, E is evaporator, PH is pre-heater, C is condenser, CP is condensate pump (or feed pump), T is turbine, G is generator, and CW is cooling water. The flow direction of geothermal brine is represented by the path A-B-C, where the geothermal brine is pumped from the geothermal reservoir into the evaporator for heat-exchange into the ORC system, before being pumped into the well via the injection well at low energy state. Each station in the ORC circuit is represented with a numbering system; 1: evaporator outlet/turbine inlet, 2: turbine outlet/condenser inlet, 4: condenser outlet/pump inlet, 5: pump outlet/pre-heater inlet, 6: pre-heater outlet/evaporator inlet.

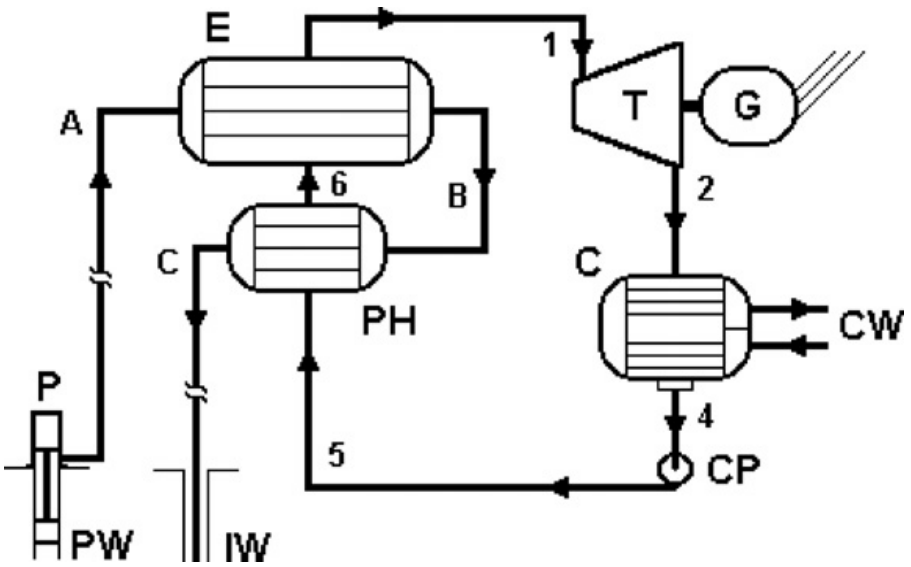

Figure 3.1: Schematic diagram of a binary geothermal plant [1]

3.1.1 Pre-heater and Evaporator Analysis

Heat transfer occurs within the evaporator and the pre-heater between the geothermal brine and the working fluid of the ORC circuit. The heat exchanger is assumed to be well-insulated, with no heat loss into the atmosphere. All the heat energy from the geothermal brine is transferred to the working fluid of the ORC circuit, without the heat gain by any solid components of the heat exchangers. The law of conservation of energy is applied on the evaporator and the pre-heater, and the thermodynamic system is governed by equations (3.1) and (3.2).

$$\dot{Q}_{evap} = \dot{m}_{brine}\left(h_a - h_b\right) = \dot{m}_{wf}\left(h_1 - h_6\right) \tag{14.1}$$

$$\dot{Q}_{PH} = \dot{m}_{brine}\left(h_b - h_c\right) = \dot{m}_{wf}\left(h_6 - h_5\right) \tag{14.2}$$

Where $\dot{m}_{brine}$ is the mass flow of the geothermal brine, $\dot{m}_{wf}$ is the mass flow of the working fluid of the ORC system, $\dot{Q}_{evap}$ is the heat transfer rate in the evaporator, $\dot{Q}_{PH}$ is the heat transfer rate in the pre-heater, h is the enthalpy, h_a is the enthalpy of brine into the evaporator, h_b is the enthalpy of brine out of evaporator or into the pre-heater, h_c is the enthalpy of brine out of the pre-heater. The total heat input from the geothermal brine is the sum of the heat transfer rate of the pre-heater and the evaporator. In some cases, a super-heater is installed to super-heat the working fluid and the heat transfer rate of the superheater has to be included.

$$\dot{Q}_H = \dot{Q}_{evap} + \dot{Q}_{PH} = \dot{m}_{brine}\left(h_a - h_c\right) = \dot{m}_{wf}\left(h_1 - h_5\right) \tag{14.3}$$

Where $\dot{Q}_H$ is the total heat transfer rate from the heat source (geothermal brine) into the working fluid of the ORC system.

3.1.2 Turbine Analysis

The performance of a turbine is represented by total-to-static isentropic efficiency and the work output, as shown in the equations below.

$$\eta_{ts} = \frac{h_1 - h_2}{h_1 - h_{2s}} \tag{14.4}$$

$$\dot{W}_{turbine} = \eta_{ts} \dot{m}_{wf} \left(h_1 - h_{2s} \right) \tag{14.5}$$

Where η_{ts} is the total-to-static isentropic efficiency of the turbine, $\dot{W}_{turbine}$ is work output of the turbine, $\dot{m}_{wf}$ is the mass flow of the working fluid, h_1 is the enthalpy at the turbine inlet, h_2 is the enthalpy at the turbine outlet, and h_{2s} is the isentropic enthalpy at the turbine outlet.

There is a number of ways to model the isentropic efficiency of the turbine. One common way is to assume a constant value for the isentropic efficiency, typically between 80 and 90%. The isentropic efficiency can be modelled more accurately, by using a turbine performance chart as a function of volumetric expansion ratio and size parameter [2], or using a numerical correlation as a function ratio of enthalpy drop and ratio of volumetric flow rate [3].

3.1.3 Condenser Analysis

The thermodynamic analysis model of a condenser is similar to an evaporator. There are two common fluid as the heat sink: water and air. The heat transfer between the heat sink and the working fluid is assumed to be ideal, without any heat loss to the atmosphere or heat gain by the pipelines, as governed by equation (3.6).

$$\dot{Q}_{cond} = \dot{m}_{cw} \left(h_{cw,inlet} - h_{cw,exit} \right) = \dot{m}_{wf} \left(h_2 - h_4 \right) \tag{14.6}$$

Where $\dot{Q}_{cond}$ is the heat rate required to be rejected by the condenser into the atmosphere, $\dot{m}_{cw}$ is the mass flow of the cooling medium (either water or air), $h_{cw,inlet}$ and $h_{cw,exit}$ are the enthalpy of the cooling medium at the inlet and exit of the condenser, respectively, h_2 is the enthalpy at the condenser inlet, and h_4 is the enthalpy at the condenser outlet.

3.1.4 Pump Analysis

The main parameters for the pump are the isentropic efficiency and the pump power requirement. The performance parameters of the pump are represented by equations (3.7) and (3.8).

$$\eta_{pump} = \frac{h_{5s} - h_4}{h_5 - h_4} \tag{14.7}$$

$$\dot{W}_{pump} = \dot{m}_{wf}\left(h_{5s} - h_4\right) \Big/ \eta_{pump} \tag{14.8}$$

Where η_{pump} is the isentropic efficiency of the pump, $\dot{W}_{pump}$ is the pump power requirement, and h_{5s} is the isentropic enthalpy at the pump outlet, assuming an isentropic compression process across the pump.

3.1.5 Cycle Analysis

The performance of the overall cycle can be evaluated using the First Law and Second Law of thermodynamics. The thermal efficiency of the cycle is determined using the first law of thermodynamics and the exergy efficiency (sometimes known as utilization efficiency) is determined using the second law of thermodynamics. The thermal efficiency is defined as the ratio of the total work output to the total heat input.

$$\eta_{th} = \frac{\dot{W}_{net}}{\dot{Q}_H} = \frac{\dot{W}_{turbine} - \dot{W}_{pump} - \dot{W}_{auxiliary}}{\dot{Q}_H} \tag{14.9}$$

Where η_{th} is thermal efficiency, $\dot{W}_{net}$ is the net power output of the system, and $\dot{W}_{auxiliary}$ is the work requirement for auxiliary components, such as the fan of the air-cooled condenser or cooling tower.

The exergy efficiency is defined as the ratio of the total work output to the potential maximum power output of the system [1].

$$\eta_{II} = \frac{\dot{W}_{turbine} - \dot{W}_{pump} - \dot{W}_{auxiliary}}{\dot{W}_{\max}} = \frac{\dot{W}_{turbine} - \dot{W}_{pump} - \dot{W}_{auxiliary}}{\dot{m}_{brine}\left[\left(h_{reservoir} - h_0\right) - T_0\left(s_{reservoir} - s_0\right)\right]} \tag{14.10}$$

Where $h_{reservoir}$ is the enthalpy of the geothermal reservoir, $\dot{W}_{\max}$ is the potential maximum work output of the system, T_0 is the dead state temperature (the temperature is equivalent to local wet bulb temperature if a cooling tower is used as a heat sink, or local ambient temperature if an air-cooled condenser is employed), and h_0 and s_0 are the enthalpy and entropy at the dead state temperature.

3.1.6 Numerical Model

A number of commercially available software can be implemented to solve the mathematical equations of the aforementioned thermodynamic model, such as Engineering Equation Solver (EES), MATLAB, ASPEN, AxCycle, Cycle-Tempo, FORTRAN, and etc. MATLAB and FORTRAN provides high flexibility in setting up mathematical model for different thermodynamic cycle but the non-linear mathematical equations cannot be solved directly. ASPEN, AxCycle, and Cycle-Tempo are developed for thermodynamic cycle analysis with in-built fluid databases but the programs are lack of flexibility to be integrated with some user-defined mathematical models. Hence, EES was selected as the software:

1) is able to solve non-linear mathematical equations using the in-built numerical calculation schemes,
2) includes in-built multi-parameters equations of state and transport properties for a number of working fluids to determine the state and the property of the fluid of interest,
3) And allows the users to develop separate calculation modules and integrate the modules in a single platform for solving. Say, the thermodynamic analysis of the ORC system is developed in the main working platform, and the detailed analysis of each components are developed in modules, such as evaporator module, condenser, module, turbine module and pump module. This allows the performance estimation of each component with empirical model rather than the correlations chosen and set up by the software developers.

The thermodynamic model is developed in the EES platform, and the Jacobian matrix of the mathematical equations are calculated. The in-built back-tracking algorithm is employed to re-group the mathematical equations into blocks to reduce the number of equations to be solved simultaneously and reduce the computational effort in the solving process.

The thermodynamic properties of the working fluids are calculated by calling the in-built property function, such as temperature, pressure, or enthalpy. Two properties, such as temperature, pressure, enthalpy, entropy, or quality, have to be defined to fix the state of the working fluids. The appropriate property function is then called to determine the property of interest. For example, X=Enthalpy(R245fa, T=350, P=100) is called to determine the enthalpy of R245fa at temperature of 350K and pressure of 100kPa. The unit system can be re-defined to unit SI or metric using the option toolbox. The details of the multi-parameter equations of

states can be referred to the work by Span [4], and the back-tracking algorithm and the details of the numerical solving using Jacobian matrix and Newton's method can be referred to the works by Tarjan [5] and Klein [6], respectively. The overall calculation process is illustrated in Figure 3.2.

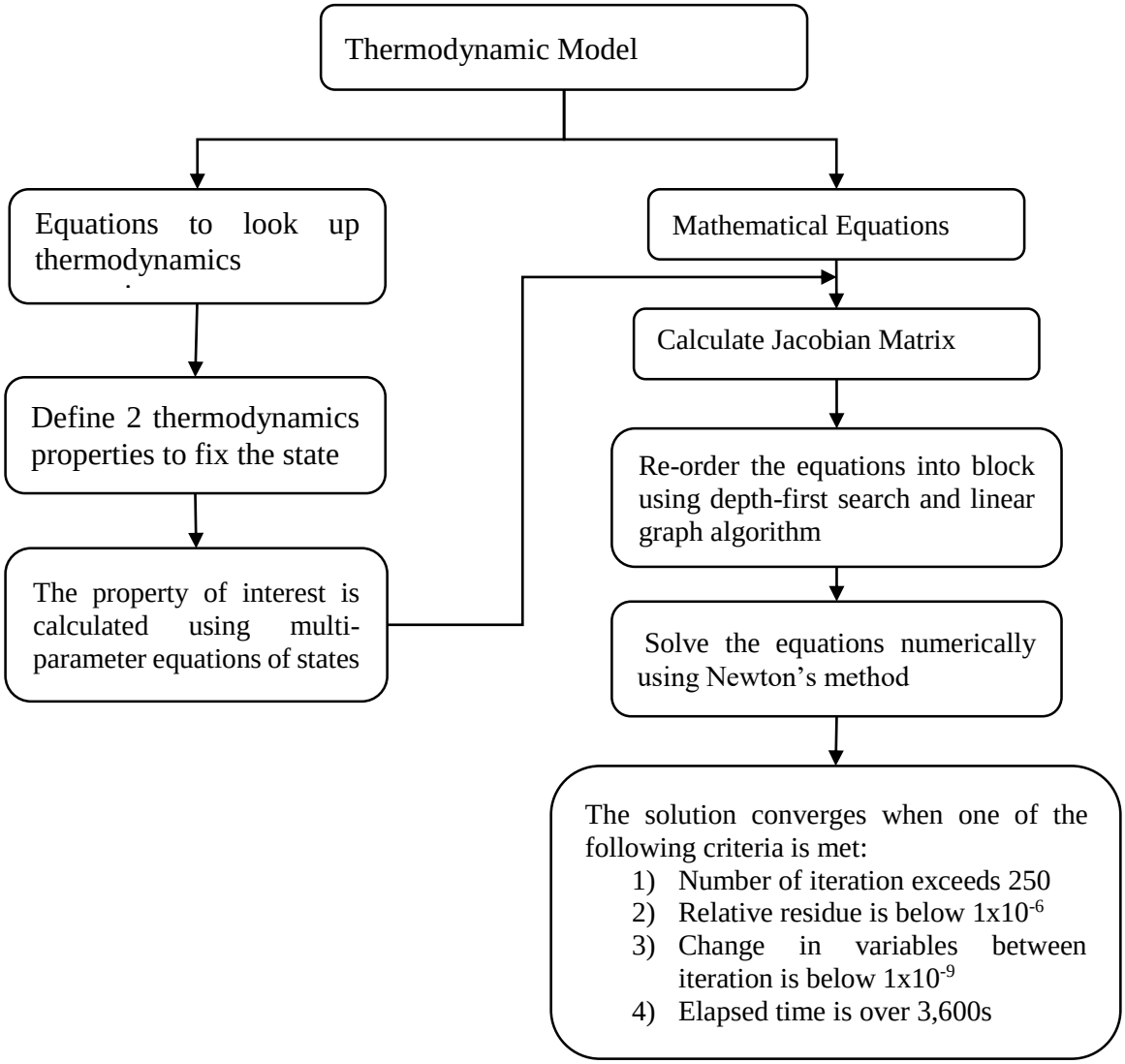

Figure 3.2: Calculation flow process in EES

3.2 Cycle Design Approach and Example

The thermodynamic modelling of the ORC system is developed using Engineering Equation Solver (EES) to determine the thermodynamic properties of each station and the performance parameters of the overall cycle. A number of working fluids was coupled to the thermodynamic model, including but not limited to R245fa, R134a, R123, R600, and R236fa, n-Pentane, isobutane, and ammonia. A number of assumptions was made in the thermodynamic model:

- A differential temperature of 6˚C at the pinch point of the condenser.
- Degree of sub-cooling: 0˚C
- Pump efficiency at 80%
- Generator efficiency at 95%
- No heat loss and no pressure drop across the heat exchangers and the piping
- All the heat energy from the heat source is transferred to the working fluid in the evaporator, and all the heat energy from the working fluid is transferred to the cooling medium in the condenser.

An example was set up for the following operating condition in Table 3.1 to demonstrate the modelling of the thermodynamic cycle, which would be used as the framework in the later section to investigate an air-cooled geothermal binary plant performance as a function of turbine performance and ambient air temperature. The plant design condition was defined and set as input in the rectangular box, as shown in Figure 3.3. A number of stations was defined,

- station 1: turbine inlet/evaporator outlet
- station 2: turbine outlet/condenser inlet
- station 3: at condensing temperature before the phase change begins
- station 4: pump inlet/condenser outlet where state of the fluid as saturated liquid
- station 5: pump outlet/evaporator inlet
- station 6: at evaporation temperature before the phase change begins

The thermodynamic properties at each station were calculated as system outputs, including temperature, pressure, enthalpy, entropy, and density. The system outputs also include the system performance, such as pump work requirement, turbine work output, cycle thermal efficiency, heat load in the evaporator, cooling load in the condenser, differential temperature at the pinch points, and the mass flow rate of the working fluids. The calculation process of the thermodynamic model was presented below.

Table 3.1: Design condition of a geothermal binary plant (similar to the design condition of Rotokawa steam field in New Zealand [7])

Heat source condition		
Working medium	-	Geothermal brine (modelled as water/steam)
Mass flow rate	kg/s	84.17
Inlet pressure	kPa	2400
Inlet temperature	°C	217.5
Injection well temperature	°C	150
Binary cycle		
Working medium	-	n-Pentane
Degree of superheat (turbine inlet)	°C	3
Turbine inlet temperature	°C	120
Heat sink condition		
Cooling mechanism	-	mechanical draft using air-cooled condenser
Cooling medium	-	air
Ambient temperature	°C	17

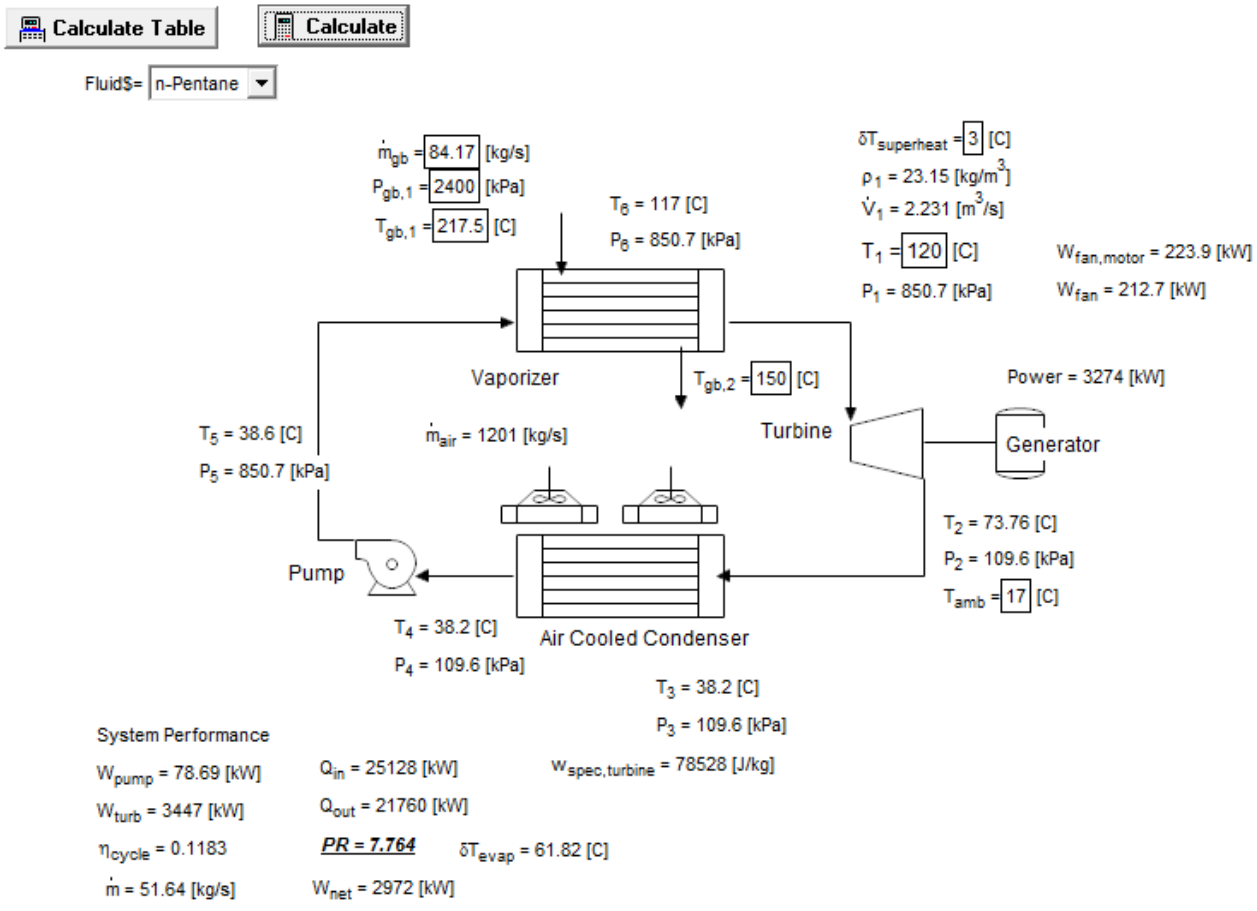

Figure 3.3: Graphical user interface of an ORC model developed by the author

Heat source:

The enthalpy of the heat source at the inlet and the outlet of the evaporator was determined by calling the in-built functions based on the given temperature and pressure. The geothermal brine was modelled as water/steam in this study. The heat rate absorbed by the working fluid from the geothermal brine was determined using equation (3.11).

$$\dot{Q}_H = \dot{m}_{gb}\left(h_{gb,1} - h_{gb,2}\right) \tag{14.11}$$

Where $\dot{m}_{gb}$ is the mass flow rate of brine, $\dot{Q}_H$ is the total heat rate transferred from the geothermal brine into the binary loop, and $h_{gb,1}$ and $h_{gb,2}$ are the enthalpy of brine at the evaporator inlet and outlet, respectively. All the heat energy was assumed to be transferred to the working fluid within the evaporator without losses into atmosphere or conduction losses into the piping. The mass flow rate of the working fluid in the binary loop (or the ORC system) was determined using equation (3.12).

$$\dot{m}_{wf} = \dot{Q}_H / (h_1 - h_5) \tag{14.12}$$

Where $\dot{m}_{wf}$ is the mass flow rate of the working fluid, and h_1 and h_5 are the enthalpy of the working fluid at the evaporator inlet and the outlet, respectively.

Pinch point at the evaporator:

The pinch point in the evaporator was determined at station 6 (refer to Figure 3.4). The energy balance between the geothermal brine and the working fluid at the pinch point allows the calculation of the pinch point of the geothermal brine. The enthalpy at the pinch point of the geothermal brine was determined using equation (3.13).

$$h_{gb,\,pinch} = h_{gb,1} - \frac{\dot{m}_{wf}\left(h_1 - h_6\right)}{\dot{m}_{gb}} \tag{14.13}$$

The temperature at the pinch point of the brine, $T_{gb,pinch}$ was determined using the in-built property function as a function of enthalpy and pressure. The pinch point temperature difference is set at 5˚C to ensure a feasible heat exchange within the evaporator.

$$\Delta T_{evap} = T_{evap} - T_{gb,\,pinch} \tag{14.14}$$

Where ΔT_{evap} is the pinch point temperature difference of the evaporator.

Heat sink:

The required heat to be rejected into the atmosphere was calculated using equation (3.6). The cooling load is equivalent to the required to be rejected into the atmosphere, assuming no loss of heat into the atmosphere and no heat gain by the piping. The required mass flow of the cooling air was determined using equation (3.15).

$$\dot{m}_{air} = \frac{\dot{Q}_{cond}}{C_{p,air}\left(T_{air,outlet} - T_{ambient}\right)} \tag{14.15}$$

Where $\dot{m}_{air}$ is the mass flow of the cooling air, $C_{p,air}$ is the isobaric specific heat of air, and $T_{air,outlet}$ is the outlet temperature of the cooling air, which was set at 35˚C in this example.

Pinch point at the condenser:

Pinch point at the condenser was determined at station 3 (refer to Figure 3.4). The energy balance equation was applied within the condenser, and the temperature of the cooling medium at the pinch point was determined using equation (3.16).

$$T_{cond,\text{pinch}} = \frac{\dot{m}_{wf}(h_3 - h_4)}{\dot{m}_{air} c_{p,air}} + T_{ambient} \tag{14.16}$$

Where $T_{cond,pinch}$ is the temperature of the cooling medium at the pinch point. The pinch point temperature difference of the condenser was set at 6˚C to allow feasible heat transfer between the cooling medium and the working fluid of the ORC system.

$$\Delta T_{cond} = T_{cond} - T_{cond,pinch} \tag{14.17}$$

Where T_{cond} is the condensation temperature of the working fluid within the binary loop (or the ORC system), and ΔT_{cond} is the pinch point temperature difference of the condenser.

Binary cycle (or Organic Rankine Cycle):

Station 1: The thermodynamic properties at the turbine inlet were determined by using the in-built property functions.

Station 2: The pressure ratio across the turbine was set up as the ratio of the evaporation pressure (station 6) and condensation pressure (station 3). The turbine isentropic efficiency was assumed 85%, and the enthalpy at the turbine outlet was determined using equation (3.4). The other properties of interest (density, entropy, etc.) were then determined using the in-built functions.

Station 3: The condensation temperature was determined using the aforementioned pinch point analysis, and the condensation pressure was determined as the saturation pressure of the working fluid at the condensation temperature. The enthalpy and the entropy were determined using the in-built functions at the saturated vapour state (where the quality is one).

Station 4: The condenser outlet was determined at the saturated liquid state where the quality of the working fluid is zero.

Station 5: The pump efficiency was assumed 80%, and equation (3.7) was used to determine the pump outlet condition given that the pump outlet pressure is the same as the evaporation pressure, assuming no pressure drop across the piping.

Station 6: The evaporation temperature was determined given the turbine inlet temperature and the degree of superheat. The other thermodynamic properties were then determined by calling the appropriate look-up functions, as discussed previously.

System performance:

The auxiliary power requirement includes the fan power in the air-cooled condenser. The fan motor power requirement was determined using equation (3.18).

$$\dot{W}_{fan} = \frac{\dot{V}_{air}\Delta p_{air}}{\eta_{fan}\eta_{motor}} \tag{14.18}$$

Where $\dot{V}_{air}$ volumetric flow rate of air, Δp_{air} is pressure drop of cooling air across the fan, η_{fan} is fan efficiency and η_{motor} is motor efficiency. The pressure drop of the air across the fan was assumed 170 Pa [8], the fan efficiency and the motor efficiency were assumed 80% and 95%, respectively.

The work output of the turbine was determined using equation (3.5), and the work requirement of the pump was calculated using equation (3.5). The thermal efficiency and exergy efficiency were calculated using equations (3.9) and (3.10). The system output was presented in Figure 3.3 and the temperature-entropy diagram was illustrated in Figure 3.4.

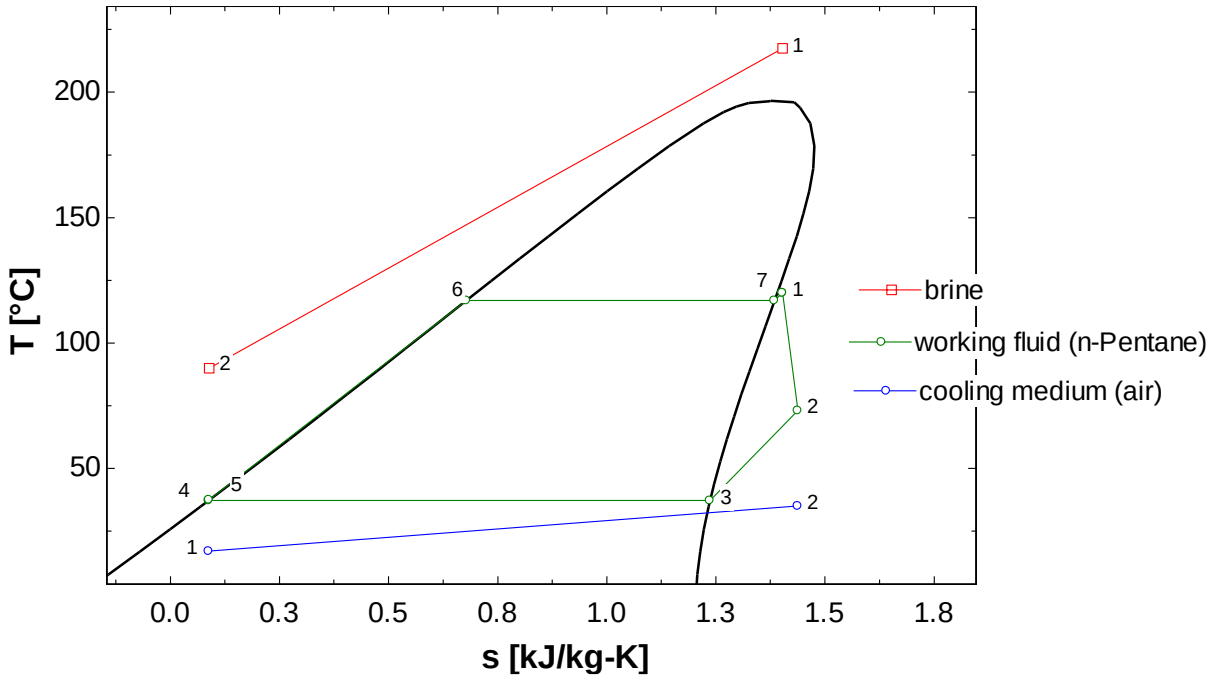

Figure 3.4: Temperature-entropy diagram of the binary plant model using n-Pentane

3.3 References

This section provides the fundamental thermodynamic modelling of the ORC system. This component is crucial in the SMC-DTR approach as this component is coupled to the SMC adaptive strategy to perform iterative calculations in order to determine the optimal configuration of the available turbines and the working fluid for optimal cycle performance.

3.4 References

1. DiPippo, R., *Geothermal power plants: principles, applications, case studies and environmental impact*. 2012: Butterworth-Heinemann.
2. Lazzaretto, A. and G. Manente, *A New Criterion to Optimize ORC Design Performance using Efficiency Correlations for Axial and Radial Turbines.* International Journal of Thermodynamics, 2014. **17**(3).
3. Ghasemi, H., et al., *Modeling and optimization of a binary geothermal power plant.* Energy, 2013. **50**(0): p. 412-428.
4. Span, R., *Multiparameter equations of state: an accurate source of thermodynamic property data*. 2000: Springer.
5. Tarjan, R., *Depth-first search and linear graph algorithms.* SIAM journal on computing, 1972. **1**(2): p. 146-160.
6. Klein, S.A. and G. Nellis, *Mastering EES*. 2013: F-Chart Software.
7. Legmann, H. and P. Sullivan. *The 30 MW Rotokawa I geothermal project five years of operation*. in *International Geothermal Conference*. 2003.
8. Lukawski, M., *Design and optimization of standardized organic Rankine cycle power plant for European conditions.* 2010.

4.0 Define Turbine Specification

The aim of this thesis is to present the SMC-DTR approach for low temperature resources, and the main contribution of this thesis is to develop the key component, SMC adaptive strategy. This chapter presents the approach to define the specification for radial inflow turbine: calculating the shaft speed, turbine wheel diameter, and number of stages using a standard turbine specific speed-specific diameter performance chart. Three screening criteria, namely tip speed, shaft speed, and relative Mach number at the turbine outlet were defined to calculate the number of stages. Four different case studies were presented and the specification of the radial inflow turbine was determined for the case studies. The case studies include a 1 kW ORC-B pilot plant installed in University of Canterbury, a planned bottoming cycle in Refining NZ, an ORMAT binary plant in Rotokawa geothermal field, and two installed commercial ORC units (known as PureCycle) in Chena hot spring.

4.1 Introduction

Once the thermodynamic cycle has been established, the type of turbine and expander has to be selected before the turbine specification is defined. The type of turbine and expander can be specified using the specific speed-specific diameter by Balje, as shown in Figure 4.1 [1]. This method is commonly used to select a suitable type of gas turbine, steam turbine and hydraulic turbine [2, 3]. Another turbine selection chart has been developed by Quoilin [4] to select the working fluid and the type of turbine for LT-ORC. The performance map is applicable for three different turbines: screw expander, scroll expander, and radial inflow turbines. However, the selection of the turbine type would not be presented in this thesis as the method does not form part of the SMC-DTR approach. The SMC-DTR approach in this thesis utilizes radial inflow turbine, and the reasons were presented in Chapter 1.

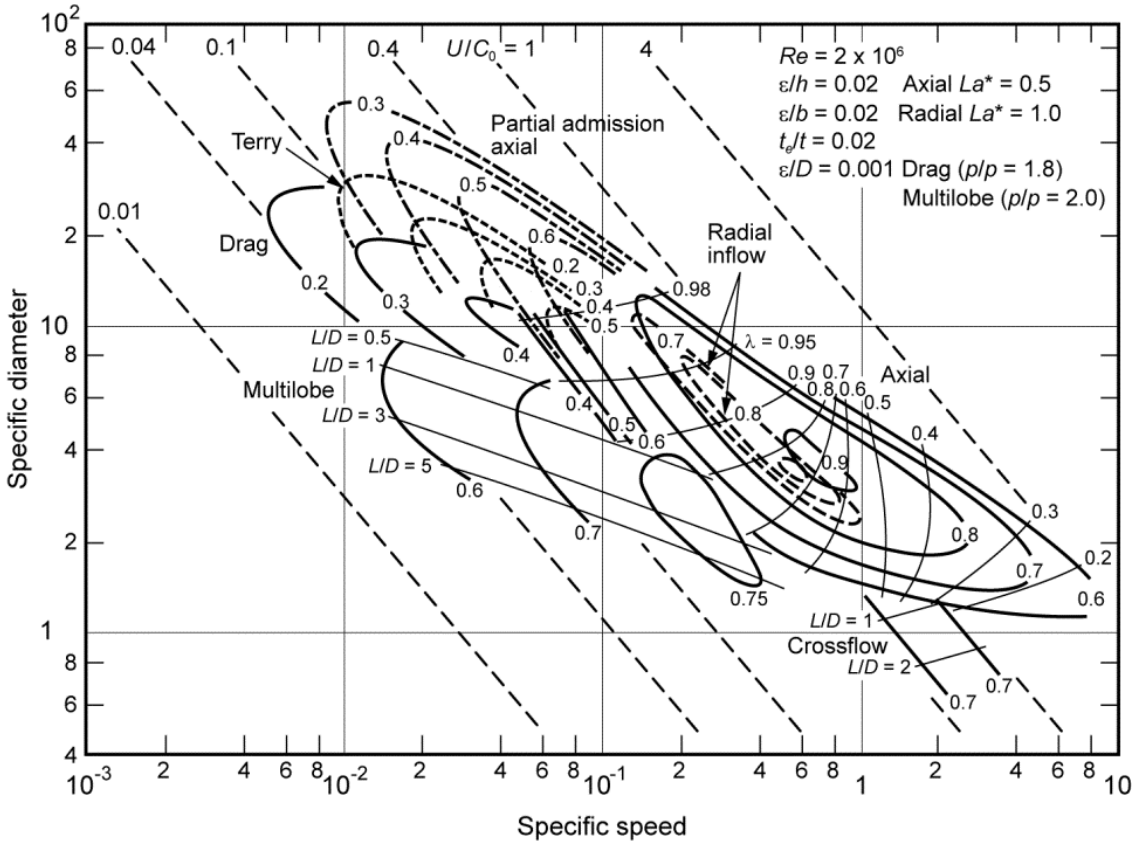

Figure 4.1: Turbine performance chart by Balje as a function of specific speed and specific diameter [1]

This chapter aims to present the approach to define the specification of radial inflow turbine for LT-ORC application by considering shaft speed, turbine tip speed, and relative Mach number at the turbine outlet. A relative Mach number less than one is recommended to

ensure a subsonic expansion across the turbine, as a supersonic flow would impose an additional shock loss during the expansion process [5], further reducing the isentropic efficiency of the turbine. A high shaft speed would impose high friction loss at the bearing and the coupling. A high shaft speed (equivalent to a high tip speed) also gives rise to a high centrifugal stress on the turbine rotor and shaft, increasing the fatigue stress and the failure probability. The specification of the radial inflow turbine was defined for four different case studies: a 1 kW ORC-B pilot plant installed in University of Canterbury, a planned bottoming cycle in Refining NZ, an ORMAT binary plant in Rotokawa geothermal field, and two installed commercial ORC units (known as PureCycle) in Chena hot spring.

4.2 Calculation of Shaft Speed and Turbine Diameter

The turbine shaft speed and the turbine diameter can be calculated using the specific speed-specific diameter turbine performance chart. The concept of specific speed has been introduced first in year 1903 [6] as an important parameter for turbine blade design. The concept was applied by Balje to correlate the turbine performance data as a function of specific speed and specific diameter, as illustrated in Figure 4.1. The concept of specific speed was then applied by Wood (reported in the work by Dixon [7]), Whitfield [8] and Baines [3] to correlate the efficiency of axial turbines and radial inflow turbines to specific speed. The specific speed is a non-dimensional parameter which is proportional to shaft speed and independent of turbine geometry, as shown in equation (4.1).

$$N_s = \frac{\omega \sqrt{\dot{m} / \rho_{exit}}}{\left(\Delta h_{isen}\right)^{0.75}} \tag{15.1}$$

Where N_s is the specific speed, ω is turbine shaft speed in rad/s, $\dot{m}$ is mass flow across the turbine stage, ρ_{exit} is fluid density evaluated at the turbine outlet, and Δh_{isen} is the isentropic enthalpy drop.

The specific diameter is another non-dimensional parameter which is dependent on the turbine geometry and independent of the shaft speed.

$$D_s = \frac{D\left(\Delta h_{isen}\right)^{0.25}}{\sqrt{m / \rho_{exit}}} \tag{15.2}$$

Where D_s is the specific diameter, and d is the turbine rotor diameter. The feasible operating range of specific speed and the corresponding specific diameter of radial inflow turbine is shown in Table 4.1. The turbine shaft speed and the rotor diameter can be determined using equations (4.1) and (4.2) once the specific speed and the specific diameter have been selected from Table 4.1.

Table 4.1: Optimal specific speed and the corresponding specific diameter for radial inflow turbine

Specific speed, Ns	Specific diameter, Ds	Potential maximum efficiency	Note
0.2	8	0.8	Feasible
0.5	4	0.9	Optimal
0.8	3	0.8	Feasible

4.3 Calculation of Number of Stages

The required pressure ratio determines the number of stages of turbine. A high pressure ratio across a turbine is favorable to generate a high amount of work output. However, if the pressure ratio is too high for the individual turbine stage, a supersonic expansion would occur within the turbine. The shock wave is formed and the isentropic efficiency of the turbine is compromised. If the design pressure ratio for the individual turbine stage is too low, the required number of stages would increase, and the system cost would escalate to an unacceptable value. A balance has to be achieved to obtain a high pressure ratio across each turbine stage and a minimal number of turbine stages with an acceptable range of isentropic efficiency.

The number of stages can be determined using the flow chart illustrated in Figure 4.3. A suitable value of pressure ratio (usually less than 5.0) is guessed. The specific speed and specific diameter are selected from Figure 4.1 or from Table 4.1. The turbine shaft speed, the turbine diameter and the tip speed are calculated. Tip speed is one of the important factors to determine the centrifugal loading on the turbine wheel. The centrifugal stress can be approximated using equation (4.3).

$$\sigma = K \rho_{material} U_{in}^{\ 2} \tag{15.3}$$

Where σ is centrifugal stress on the turbine rotor, K is the geometrical factor, $\rho_{material}$ is the density of the material of the turbine rotor, and U_{in} is rotor inlet tip speed. If the centrifugal stress is more than the yield strength of the selected material, the turbine blade would suffer structural failure and fatigue issue. A limiting turbine tip speed of 400 m/s is used in the calculation process.

The relative Mach number at the turbine outlet is then calculated. If the relative Mach number is over 1, a supersonic expansion would occur within the rotor blade passage, inducing the shock loss and reducing the isentropic efficiency of the turbine stage. The relative Mach number can be calculated using equation (4.4).

$$Ma_{rel,exit} = \frac{W_{exit}}{C_{critical}} \tag{15.4}$$

Where $Ma_{rel,exit}$ is the relative Mach number at the turbine outlet, W_{exit} is the relative flow velocity at the turbine outlet, and $C_{critical}$ is the local speed of sound at the turbine outlet. The relative flow velocity, W_{exit} is determined from a velocity triangle (shown in Figure 4.2), which

is commonly used in turbomachinery application to determine the vector of the bulk flow at the inlet and the outlet of the fluid machines. The following assumption are made to facilitate the calculation procedure:

- Zero swirl at the turbine outlet, where C_θ is 0 [7]
- Flow coefficient, ϕ is 0.2 based on the flow coefficient-loading coefficient chart compiled by Baines [9]
- Inlet to outlet radius ratio, r_r is chosen as 1.8 (usually in the range of 1.6 and 18) [7]

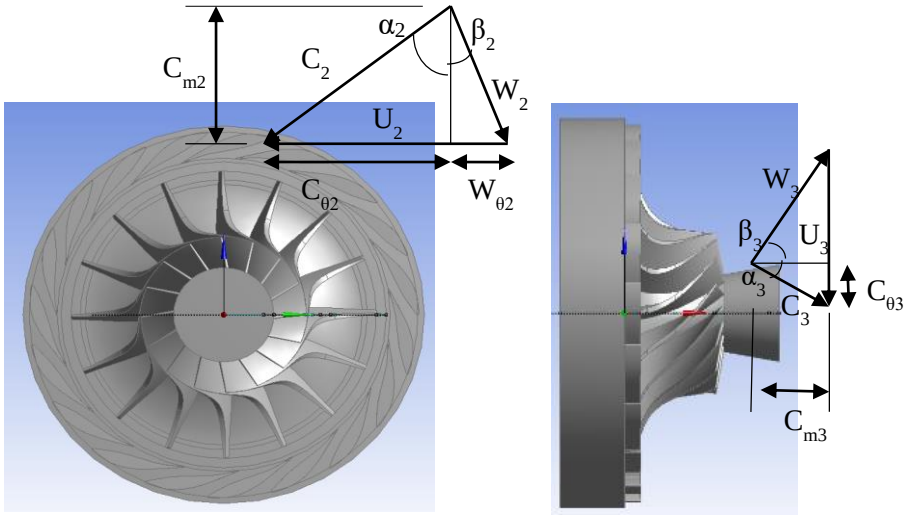

Figure 4.2: Velocity diagram at the rotor inlet and outlet

The relative flow velocity, W_{exit} is the simplified from the unknown variables of the velocity vectors, into the known variables, including the flow coefficient, and radius ratio, as stated in equation (4.5).

$$W_{exit}{}^2 = C_{m,exit}{}^2 + (C_{\theta,exit} - U_{exit})^2 = U_{in}{}^2\left[\phi^2 + (1/r_r)^2\right] = 0.35U_{in}{}^2 \quad (15.5)$$

Where C_m is absolute flow velocity in meridional plane across the turbine, C_θ is absolute tangential flow velocity, and the subscript *exit* is the turbine outlet. More information of the velocity triangle can be referred to a number of relevant texts [3, 7, 10]. The limiting value of relative Mach number is set at 0.95 to avoid the supersonic expansion within the blade passage. If the relative Mach number is over 0.95, the pressure ratio of the current stage is re-selected. The calculation is iterated until the total pressure ratio is equivalent to the required total pressure ratio of the system. The process flow of the calculation is illustrated in Figure 4.3.

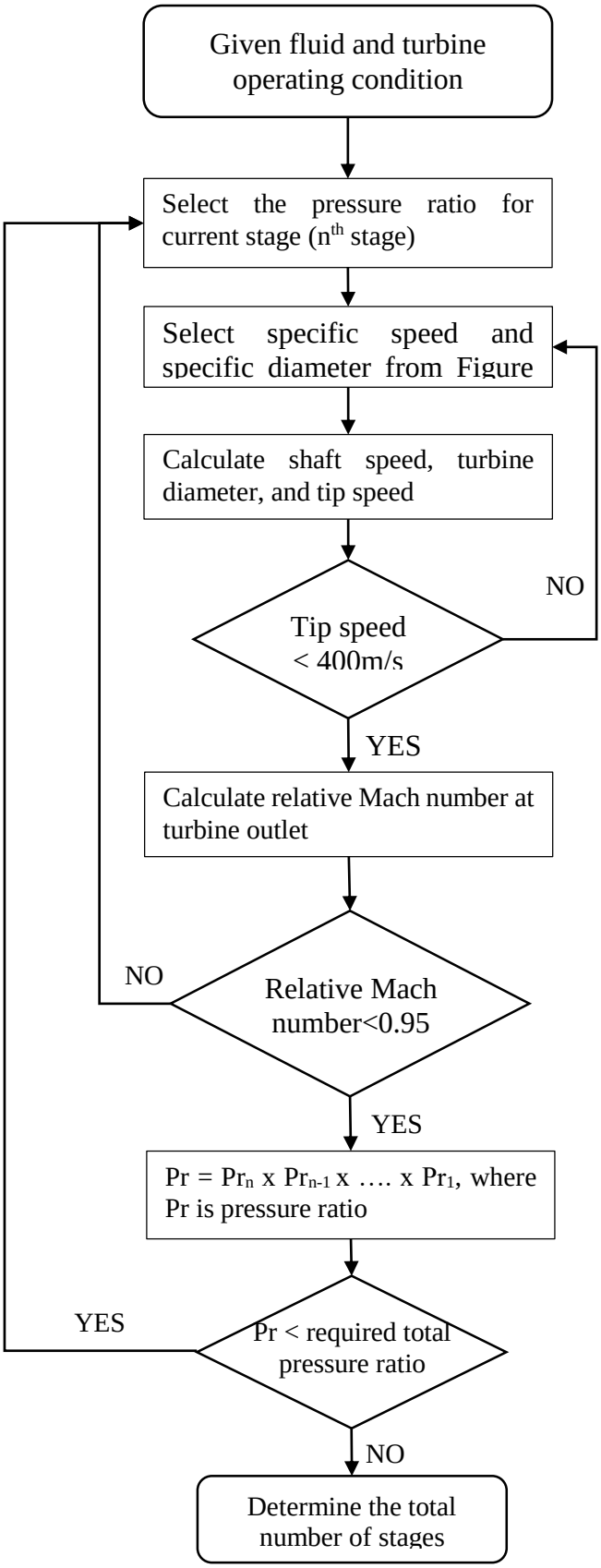

Figure 4.3: Flow chart calculating the number of stages for radial inflow turbine

4.4 Case Studies for Turbine/Expander Selection

The calculation process (Figure 4.3) was applied in four different case studies: 1 kW ORC-B pilot plant in University of Canterbury, a planned bottoming cycle in a refinery plant, a proposed binary plant for a high temperature steam field, and a binary plant for a low temperature geothermal hot spring. The heat source condition, cooling medium, and the operating condition of the corresponding ORC system were tabulated in Table 4.2. The 1 kW ORC-B pilot plant in University of Canterbury is a bottoming cycle of a 30 kW Capstone gas turbine, built by ORC research team between year 2013 and 2014 in University of Canterbury using a commercially available scroll expander from Air Squared supplier. The plant utilizes a non-conventional working fluid, a mixture of R365mfc and R245fa, to match the thermal curve of the exhaust gas from the gas turbine. The waste heat recovery system using the kerosene flow in Refinery plant in New Zealand is a conceptual study by ORC research team from University of Canterbury. The conceptual study aims to evaluate the feasibility of an ORC plant as a bottoming cycle in an existing chemical process plant. The Rotokawa steam field in New Zealand utilizes a hybrid plant configuration, with a combination of steam plants and binary plants as the bottoming cycles. The Chena hot spring in Alaska, United States utilizes a commercially available ORC unit, known as PureCycle from Pratt and Whitney (at the time of writing) to extract the low temperature heat energy.

The methodology, as outlined in Figure 4.3, was applied for different cases to determine the shaft speed, turbine diameter, turbine tip speed, and number of stages for different applications, and the result was tabulated in Table 4.3. The numerical model was applied in Microsoft Excel and the mathematical equations were solved. The calculated shaft speed of the turbine was compared to the actual rotational speed of the radial inflow turbine in Chena hot spring to validate the outlined method. The actual shaft speed of the radial inflow turbine in Chena hot spring is 13,500 rev/min whereas the optimal value based on the proposed method is 13,123 rev/min. Radial inflow turbine are not currently installed in the 1 kW ORC-B pilot plant due to the excessive shaft speed to achieve an acceptable turbine efficiency in a feasible range of specific speed.

Table 4.2: Resource characteristics and operating parameters for the ORC system

Application	*Waste heat recovery*	*Waste heat recovery [11]*	*High temperature geothermal [12]*	*Low temperature geothermal [13]*
Site	University Canterbury 1 kW ORC-B Pilot Plant, New Zealand	Refining NZ, New Zealand	Rotokawa Geothermal Field, New Zealand	Chena Hot spring, Alaska, US
Heat Source				
Heat source medium	Exhaust gas	Kerosene flow	Geothermal brine	Hot spring water
Heat source inlet temperature (°C)	300.0	115.0	217.5	73.3
Heat source outlet temperature (°C)	230.0	70.0	150.0	54.4
Mass flow (kg/s)	0.11	40.3	84.17	33.39
Heat sink				
Cooling medium	Water	Water	Air	Water/Air
Cooling medium temperature (°C)	15.50	24.00	12.00	4.44
ORC system				
Working medium	M1 (mixture of R365mfc and R245fa)	R245fa	n-Pentane	R134a
Mass flow (kg/s)	0.07	17.8	46.12[2]	12.17
Density at turbine outlet (kg/m3)	6.15	13.17	2.62[2]	20.84
Pressure ratio	11.0	3.0	17.62[2]	3.6
Enthalpy drop (kJ/kg)	34.30	17.13	112.25[2]	22.15
Turbine efficiency	0.85[1]	0.85[1]	0.97	0.8
Nominal Power (kW)	2.0	259.2	5,021.7	215.7

[1]The turbine efficiency was estimated at 85% for the subsequent analysis.
[2]The operating condition was estimated based on the given heat source condition and nominal power output of the turbo-generator unit, by using the energy balance formulae as described by DiPippo [14].

Table 4.3: Turbine specifications for the case studies

Site	University Canterbury 1 kW ORC-B Pilot Plant	Refining NZ	Rotokawa Geothermal Field	Chena Hot spring
Candidate 1				
Machine type	Radial inflow turbine			
N (rev/min)	145,791	6,902	5,736	**13,123**
Actual N (rev/min)	NIL	NIL	NIL	**13,500***
D (m)	0.029	0.39	0.68/0.98	0.24
U (m/s)	218.1	141.5	204/294	164.4
Ma_rel	0.8882	0.604	0.6/0.79	0.6515
Ns	0.5	0.5	0.35/0.65	0.5
Number of stages	1	1	2	1

*The calculated rotational speed from the aforementioned numerical model was compared to the actual rotational speed of the steam/binary plant.

4.5 Conclusion

The proposed method is one of the critical steps in the SMC-DTR approach to define the turbine specification. This method is validated and can be fed into the next component to design the optimal geometry of the turbine, before a suitable turbine can be selected from a pool of turbine options.

4.6 References

1. Balje, O.E., *Turbomachines: A Guide to Design Selection and Theory*. 1981: Wiley.
2. Kenneth, E. and P. Nichols, *How to select turbomachinery for your application.* Barber-Nichols Inc, 2012: p. 5-6.
3. Japikse, D. and N.C. Baines, *Introduction to turbomachinery*. 1995: Concepts ETI.
4. Quoilin, S., S. Declaye, and V. Lemort, *Expansion Machine and fluid selection for the Organic Rankine Cycle.* 2010.
5. Dahlquist, A.N., *Investigation of Losses Prediction Methods in 1D for Axial Gas Turbines*, in *Division of Thermal Power Engineering, Department of Energy Sciences*. 2008, Lund University: Sweden.
6. Meher-Homji, C.B. *'The Historical Evolution of Turbomachinery*. in *Proceedings of the 29th Turbomachinery Symposium, Texas A&M University, Houston, TX*. 2000.
7. Dixon, S.L. and C. Hall, *Fluid Mechanics and Thermodynamics of Turbomachinery*. 2010, Butterworth-Heinemann: Burlington.
8. Whitfield, A. and N.C. Baines, *Design of radial turbomachines.* 1990.
9. Chen, H. and N.C. Baines, *The aerodynamic loading of radial and mixed-flow turbines.* International Journal of Mechanical Sciences, 1994. **36**(1): p. 63-79.
10. Schobeiri, M., *Turbomachinery flow physics and dynamic performance*. 2005: Springer.
11. Jung, H.C., S. Krumdieck, and T. Vranjes, *Feasibility assessment of refinery waste heat-to-power conversion using an organic Rankine cycle.* Energy Conversion and Management, 2014. **77**(0): p. 396-407.
12. Legmann, H. and P. Sullivan. *The 30 MW Rotokawa I geothermal project five years of operation*. in *International Geothermal Conference*. 2003.
13. Aneke, M., B. Agnew, and C. Underwood, *Performance analysis of the Chena binary geothermal power plant.* Applied Thermal Engineering, 2011. **31**(10): p. 1825-1832.
14. DiPippo, R., *Geothermal power plants: principles, applications, case studies and environmental impact*. 2012: Butterworth-Heinemann.

Investigative Study

5.0 Preliminary Design of Radial Inflow Turbine

The aim of this thesis is to present the SMC-DTR approach for low temperature resources, and the main contribution of this thesis is to develop the key component, SMC analysis approach. One of the critical steps in the SMC-DTR approach is to match existing turbines to the cycle design with different working fluid. This step is accomplished by performing a preliminary design of radial inflow turbine based on the selected working fluid and the turbine specification from previous chapters. The preliminary design approach provides the optimal geometry of the radial inflow turbine for a given resource condition. A suitable turbine (similar to the optimal geometry) is then selected from a pool of off-the-shelf turbines, such as gas turbines and automotive turbochargers. The standard preliminary design approach assumes ideal gas behaviour and provides good design outcomes for gas turbines and turbochargers when the working medium is air, but the method is proven not suitable for real fluids [1]. For ORC working fluids, it is not known how the ideal gas assumption affects the preliminary design outcome. The previous research shows that the deviation of thermodynamic properties is up to 100% in terms of local speed of sound and Mach number for refrigerants such as R245fa [2].

In this chapter the standard preliminary design approach was developed using ideal and real gas behaviour and the results were compared and analysed. The turbine preliminary design and analysis was performed using two different gas models, which are ideal gas equations, and multi-parameters equations of states for real fluids. The ideal gas equations in this chapter assumes constant values of isobaric specific heat and specific heat ratio for all temperature. Three working fluids are selected, R134a, R245fa and n-Pentane as they are the common refrigerants in low temperature ORC system and geothermal binary plant.

The results show that the deviation in change in enthalpy across the turbine stage using ideal gas equations is significant up to 1,000% when the compressibility factor is further away from one. The shape of the velocity diagram is dependent on the selection of turbine performance parameters, such as flow coefficient and radius ratio, but the shape of the velocity diagram is not affected by the choice of the gas models. The application of the ideal gas model over-estimates the turbine rotational speed and flow velocity, and under-sizes the rotor wheel diameter. The over-estimation in the turbine rotational speed using the ideal gas model increases the enthalpy loss across the turbine significantly, to the extent that the loss is larger than the isentropic enthalpy drop across the turbine. The turbine operates as a pump and consumes power for operation instead of operating as a turbine. The study shows that the

turbine preliminary design using real gas model is a better option to design the radial inflow turbine or to match the existing turbines to the cycle design.

5.1 Introduction

The turbine design conditions are usually specified by a steady state model of a thermodynamic cycle for the chosen working fluid. Standard turbomachinery design methods are typically used to calculate turbine geometry for this steady state "design point" [3-5]. The ideal gas assumption is applied throughout the conventional 1-D turbine preliminary design and analysis process to reduce the computational effort. However, the properties of refrigerants and organic fluids deviate significantly from ideal gas behaviour. The ideal gas equations have been shown to result in an extremely large deviation, in the range of 18% up to over 100% in terms of Mach number, thermodynamic properties, fluid sound velocity and total pressure loss across the turbine [23-25]. There are a number of methods to estimate the real fluid properties in the numerical calculation process [25], which are

(a) interpolation and extrapolation of thermodynamic property data tables,
(b) application of simple polynomial functions to fit the data of the property data tables from approach (a),
(c) analytical method to calculate the primitive quantities and a numerical scheme to evaluate the derivatives of the primitive values, and
(d) analytical method to calculate both the primitive quantities and the derivative values

Method 4 has been shown to provide the highest accuracy results, followed by 3, 2 and 1 [25]. The first two methods result in lower accuracy attributed to errors in the data interpolation. Two common equations of states (EoS) for real fluids are Redlich-Kwong-Soave (RKS) equations and Peng Robinson (PR) equations. A study by Lujan showed that the RKS and PR equations exhibit deviations of 8% and 6% respectively from the specific energy across the range of interest for R245fa compared to the NIST fluid property database [23]. Harinck studied the deviation of an improved version of the PR model by Stryjek and Vera, known as PRSV cubic equation from a highly accurate multi-parameter equation of state (MPEoS) [25]. He considered three different fluids, which are steam, toluene and R245fa in his study. He found that adopting the PRSV model for toluene and R245fa results in 2% deviations and 4% deviations for steam in all the flow parameters. Lemmon and Roland have developed the equations of states for a number of fluids, including non-polar fluids (carbon monoxide, decane, neopentane, toluene, isopentane, isohexane, etc.) and polar fluids (R134a, R245fa, R41, acetone, etc.) using Helmholtz energy equations with the experimental data [6, 7]. The

equation of states is known as multi-parameter equations of states with 12 coefficients to fit the experimental data with the mathematical model.

The numerical calculation of the turbine preliminary design process and performance estimation has been implemented in the commercially available thermodynamic software, namely Engineering Equations Solver (EES), with in-built fluid properties database to model the behaviour of the real fluids. Some research were previously performed to improve the turbine preliminary design process by coupling the preliminary design with external fluid database [8]. The turbine preliminary design process has been integrated into ORC system design to optimize the overall cycle performance with a proper selection of turbine parameters and turbine geometry [9]. A turbine designed using perfect gas equations and tested using real fluids was shown by Kang [4]. A single stage radial turbine was designed using dry air as working fluid with a pressure ratio of 3.6 with isentropic efficiency of 75%. The prototype of the turbine was built and tested using R245fa for a pressure ratio between 2.5 and 2.8, with tested isentropic efficiency between 60 and 80% [4].

This chapter aims to present the radial inflow turbine preliminary design method to match the existing turbines to the cycle design. The conventional preliminary design method using ideal gas model might not be suitable to provide an optimal turbine design outcome. Therefore, this chapter compares the turbines designed using the ideal gas equations and multi-parameter equations of states. The deviation in the performance parameters for turbines designed using ideal gas equations and multi-parameter equations of states for real fluids is then correlated to the compressibility factor at the turbine inlet condition.

5.2 Standard Preliminary Design Approach

This section presents the preliminary design of the radial inflow turbine using 1) polytropic ideal gas equations, and 2) multi-parameter equations of states by integrating the turbine preliminary program to a fluid database. The turbine performance analysis was presented as enthalpy loss in terms of passage loss, incidence loss, exit kinetic energy loss, tip clearance loss, and windage loss. The turbine loss model was validated against a gas turbine using air and an ORC turbo-expander using R245fa at the operating condition close to the design condition. The numerical model was developed using Engineering Equation Solver (EES) as EES is able to solve non-linear mathematical equations using the in-built Newton's method algorithm, and the in-built fluid database can be integrated into the turbine design and analysis program for better thermodynamics accuracy in the modelling process. 3 different stations were defined: station 1, nozzle inlet; station 2, rotor inlet; station 3: rotor outlet. The turbine design and analysis method was presented assuming the absence of diffuser downstream of the rotor. The velocity diagram at the rotor inlet and outlet was illustrated in Figure 5.1, which was applied in the preliminary design process to develop the velocity diagram at different stations. C denotes absolute flow velocity, W relative flow velocity, U turbine tip speed, α absolute flow angle (also known as swirl angle), β relative flow angle, C_m absolute flow velocity projected onto meridional plane, and C_θ absolute flow velocity projected onto tangential direction.

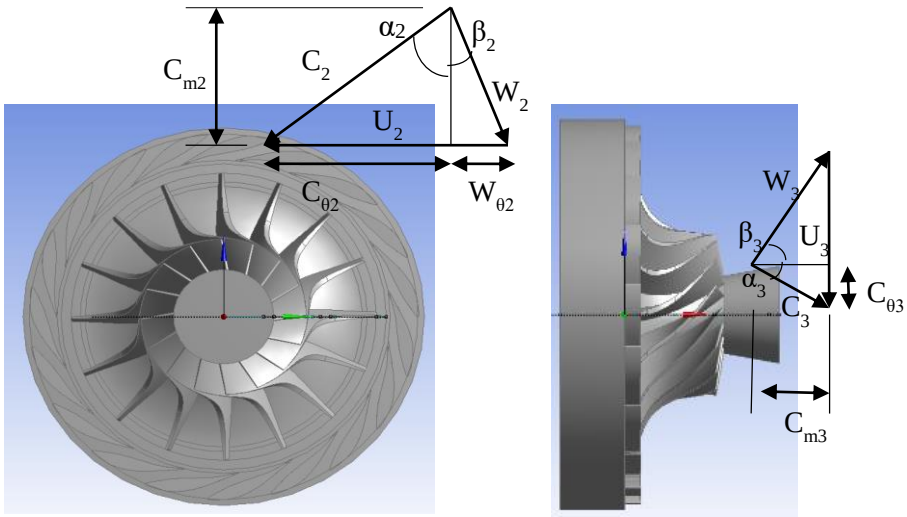

Figure 5.1: Velocity diagram at the rotor inlet and outlet

5.2.1 Preliminary Design

The preliminary design approach of radial inflow turbine is crucial in defining the optimal geometry of the turbine. A suitable turbine can then be selected from a pool of off-the-shelf turbines with the turbine geometry similar to the optimal geometry. The standard turbine preliminary design process has been discussed, improved and presented by a number of researchers [10-16] for the past few decades since the publication of the computational code of turbine preliminary design program as part of the NASA gas turbine program by Glassman [17].

The flow coefficient-stage loading coefficient correlation chart serves as a first step in the turbine preliminary design approach. The correlation between the flow coefficient and stage loading coefficient of radial section blades has been compiled by Baines using the actual test data of the radial inflow turbines [18]. Flow coefficient determines the swallowing capacity of the turbines whereas stage loading coefficient (sometimes known as work coefficient) determines the non-dimensional work output of the turbines. Flow coefficient, ϕ is the ratio of absolute flow velocity in the meridional plane, C_{m3}, to the rotor inlet tip speed, U_2.

$$\phi = \frac{C_{m3}}{U_2} \tag{16.1}$$

Stage loading coefficient, ψ is the ratio of total enthalpy drop across the turbine, Δh_0 to the squared to rotor inlet tip speed.

$$\psi = \frac{\Delta h_0}{U_2^{\,2}} = \frac{C_{\theta 2} - \varepsilon C_{\theta 3}}{U_2} \tag{16.2}$$

Where $C_{\theta 2}$ is the flow velocity in the tangential direction at the rotor inlet, and $C_{\theta 3}$ is the flow velocity in the tangential direction at the rotor outlet. This equation is simplified as a function of the flow velocity and rotor radius ratio, $\varepsilon = r_3/r_2$. The radius ratio was reported to be in the range of 0.4 to 0.75 for centrifugal compressors to achieve a high pressure ratio across the turbine stage [19].The radius ratio is limited below 0.7 to avoid excessive curvature of the rotor shroud [20].

The stage loading coefficient is selected between 0.9 and 1.0, and the flow coefficient is selected in the range of 0.2 and 0.3 to achieve optimal turbine efficiency. The stage loading coefficient-flow coefficient correlation chart is only valid for radial section blade with rotor outlet blade angle, β_{3b} at 0˚. If β_{3b} is greater than zero, the optimal stage loading coefficient is

increased and the maximum turbine efficiency is achieved at lower velocity ratio. Velocity ratio, υ is the ratio of rotor inlet tip speed to spouting velocity, C_s, which is defined as the flow velocity if the flow is expanded in the same total-to-static pressure ratio as the turbine stage in an ideal nozzle. The equation can be simplified to a function of rotor inlet tip speed and total-to-static enthalpy drop in an isentropic expansion process, $\Delta h_{ts,is}$.

$$\nu = \frac{U_2}{C_s} = \frac{U_2}{\sqrt{2\Delta h_{ts,is}}} \tag{16.3}$$

If β_{3b} is less than zero, the optimal stage loading coefficient is reduced and the maximum turbine efficiency is achieved at higher velocity ratio [21]. The subsequent turbine preliminary design process was presented assuming the radial section blades. The optimal velocity ratio is around 0.7 for radial section blades [14].

The specific work output of a turbine is determined using Euler turbomachinery equation.

$$\dot{W}_x = \Delta h_0 = U_2 C_{\theta 2} - U_3 C_{\theta 3} = U_2 C_{m2} \tan\alpha_2 - U_2 C_{m3} \tan\alpha_3 \tag{16.4}$$

Where $\dot{W}_x$ is the specific work output. The specific work output would increase if the turbine outlet swirl angle, α_3 is negative. However, the negative swirl angle at the rotor outlet increases the kinetic energy loss at the turbine outlet. The minimal kinetic energy loss at the rotor outlet occurs at zero swirl angle, in which the absolute flow velocity at the rotor outlet is minimal. The swirl angle, α_3 is set as zero for this preliminary design approach.

The turbine wheel diameter and the rotational speed can be determined using the specific speed-specific diameter performance chart in the previous chapter. The rotor inlet tip is calculated using equation (5.5), in which d_2 is the turbine wheel diameter, and N is the rotational speed in rad/sec. The rotor outlet tip speed is calculated given the radius ratio (which is set at 0.7).

$$U_2 = \frac{\pi d_2 N}{60} \tag{16.5}$$

$$U_3 = \varepsilon U_2 \tag{16.6}$$

The isentropic total-to-static enthalpy change, $\Delta h_{ts,is}$ can be deduced from the total-to-static pressure ratio, pr_{ts} specified as part of the requirement of turbine design condition.

$$\Delta h_{ts,is} = C_p T_{01}\left[1-\left(\frac{1}{pr_{ts}}\right)^{\left(k-1/k\right)}\right] \tag{16.7}$$

Where C_p is the isobaric heat capacity, T_{01} is stagnation temperature at the turbine inlet, and k is specific heat ratio.

The isentropic efficiency of the turbine stage is first guessed using the loading coefficient-flow coefficient performance chart compiled by Baines [18]. The actual enthalpy drop is then predicted using equation (5.8).

$$\Delta h_0 = \eta_{ts}\Delta h_{ts,is} \tag{16.8}$$

Where Δh_0 is the actual enthalpy drop across the turbine.

Rotor Exit:

The velocity diagram at the rotor exit is constructed. The absolute flow velocity in the meridional plane is calculated using equation (5.1) and the tip speed is determined from equation (5.6). The outlet swirl angle, α_3 is set as zero. The velocity vector and the flow angle in Figure 5.1 are calculated using equations (5.9) to (5.13).

$$C_3 = \frac{C_{m3}}{\cos\alpha_3} \tag{16.9}$$

$$C_{\theta 3} = C_{m3}\tan\alpha_3 \tag{16.10}$$

$$W_{\theta 3} = C_{\theta 3} - U_3 \tag{16.11}$$

$$W_3 = \sqrt{{C_{m3}}^2 + {W_{\theta 3}}^2} \tag{16.12}$$

$$\tan\beta_3 = \frac{W_{\theta 3}}{C_{m3}} \tag{16.13}$$

Rotor Inlet:

The velocity diagram at the rotor inlet is constructed. $C_{\theta 2}$ is calculated using the Euler turbomachinery equation in equation (5.4). The meridional velocity at the rotor inlet, C_{m2} is assumed to be the same as the meridional velocity at the rotor outlet, C_{m3}. The other velocity vectors and flow angle are calculated using equations (5.14) to (5.18).

$$W_{\theta 2} = C_{\theta 2} - U_2 \tag{16.14}$$

$$\tan \beta_2 = \frac{W_{\theta 2}}{C_{m2}} \tag{16.15}$$

$$C_2 = \sqrt{{C_{m2}}^2 + {C_{\theta 2}}^2} \tag{16.16}$$

$$\tan \alpha_2 = \frac{C_{\theta 2}}{C_{m2}} \tag{16.17}$$

$$W_2 = \sqrt{{C_{m2}}^2 + {W_{\theta 2}}^2} \tag{16.18}$$

5.2.2 Thermo-physical and Thermodynamic Properties

The calculation of the thermodynamic properties of the refrigerants is crucial in the design process. Polytropic ideal gas equations are usually employed for the design of conventional gas turbine and turbocharger as the polytropic ideal gas law can predict the thermodynamic properties of air accurately. The ideal gas law assumes constant isobaric specific heat and constant specific heat ratio for the range of temperature studied in this chapter.

The application of different working medium in ORC system, such as hydrocarbon and hydrofluorocarbon, requires real gas model to predict the thermodynamic properties accurately. The thermodynamic properties of the real gas can be determined from the original Redlich-Kwong equation [22] or the modified version of Redlich-Kwong equation [11]. In this study, the real gas fluid database from Engineering Equation Solver (EES) is integrated into the turbine preliminary design code developed by the author. The real fluid model in this study is based on the multi-parameter equation of states, which is described later.

5.2.3 Perfect Gas Model

The averaged specific heat ratio, k is determined given the turbine inlet and the isentropic outlet operating condition. The isobaric heat capacity, C_p is assumed constant throughout the expansion process and calculated using the equation below.

$$C_p = \frac{k}{k-1} R_{specific} \tag{16.19}$$

Where $R_{specific}$ is the specific gas constant for the working fluid.

The total enthalpy (or stagnation enthalpy) across the nozzle is conserved as no work is done in the nozzle. The total temperature across the nozzle is conserved since isobaric heat capacity is assumed constant across the expansion process. Static temperature, Mach number and relative Mach number are then calculated using equations (5.22) to (5.24). h_{01} denotes total enthalpy at nozzle inlet, h_{02} total enthalpy at rotor inlet, T_{01} total temperature at turbine inlet, T_{02} total temperature at rotor inlet, T_2 static temperature at rotor inlet, M_2 Mach number at rotor inlet, $M_{2,rel}$ relative Mach number at rotor inlet, and $c_{2,sound}$ local speed of sound.

$$h_{01} = h_{02} \tag{16.20}$$

$$T_{01} = T_{02} \tag{16.21}$$

$$T_2 = T_{02} - \frac{C_2^{\,2}}{2C_p} \tag{16.22}$$

$$M_2 = \frac{C_2}{c_{2,sound}} \tag{16.23}$$

$$M_{2,rel} = \frac{W_2}{c_{2,sound}} \tag{16.24}$$

$$c_{2,sound} = \sqrt{kRT_2} \tag{16.25}$$

The total pressure (or stagnation pressure) is not conserved across the nozzle due to the frictional losses between the fluid flow and the vane/casing surfaces. The total pressure loss coefficients have been measured in the range of 0.03 and 0.07 for nozzle vanes, and between 0.05 and 0.13 for the volute and nozzle combined [23]. A reasonable total pressure loss coefficient is estimated, and the total temperature, T_{02} and static temperature, T_2 are calculated by solving the non-linear mathematical equations (5.26) and (5.27) simultaneously.

$$K_s = \frac{p_{01} - p_{02}}{p_{02} - p_2} \tag{16.26}$$

$$\frac{p_2}{p_{02}} = \left(\frac{T_2}{T_{02}} \right)^{\frac{k}{k-1}} \tag{16.27}$$

The density at the rotor inlet, ρ_2 the effective flow area, $A_{2,eff}$ are calculated using the equations below.

$$\rho_2 = \frac{P_2}{RT_2} \tag{16.28}$$

$$A_{2,eff} = \frac{\dot{m}}{\rho_2 C_{m2}} \tag{16.29}$$

The losses within the vaneless zone between the nozzle vanes and the rotor is ignored in this study. The thermodynamic properties at the rotor outlet are calculated using equations (5.30) to (5.34). Mass conservation equation is applied to estimate the effective flow area at the turbine outlet, $A_{3,eff}$.

$$T_{03} = T_{01} - \frac{\Delta h_0}{C_p} \tag{16.30}$$

$$T_3 = T_{03} - \frac{C_3^2}{2C_p} \tag{16.31}$$

$$\frac{p_3}{p_{03}} = \left(\frac{T_3}{T_{03}}\right)^{\frac{k}{k-1}} \tag{16.32}$$

$$M_3 = \frac{C_3}{c_{3,sound}} \tag{16.33}$$

$$M_{3,rel} = \frac{W_3}{c_{3,sound}} \tag{16.34}$$

$$A_{3,eff} = \frac{m}{\rho_3 C_{m3}} \tag{16.35}$$

5.2.4 Real Gas Model

The thermodynamic properties of the real gas are calculated using multi-parameter equations of states in EES. The equation of state of real fluids are expressed in fundamental form explicit in the Helmholtz energy as a function of density and temperature. The Helmholtz energy is split into two terms, one to describe the behaviour of ideal gas at given density and temperature, and one to consider the residual behaviour of the real fluid [7], as shown in equation (5.36). The first term on the right hand side is the contribution from hypothetical ideal gas model, in which the internal energy of molecules are attributed to the translational,

rotational, vibrational, and intramolecular motion. The second term accounts for all intermolecular interactions. The residual Helmholtz energy is usually measured and determined from the experimental data due to the lack of physics model that can be fitted into the whole spectrum of real fluids.

$$a(\rho,T) = a^0(\rho,T) + a^r(\rho,T) \tag{16.36}$$

The functional form of Helmholtz energy is usually expressed in the dimensionless form, as a function of dimensionless density and temperature, where $\delta=\rho/\rho_c$ and $\tau=T_c/T$. α denotes dimensionless Helmholtz energy, ρ_C critical density, and T_c critical temperature.

$$\frac{a(\rho,T)}{RT} = \alpha(\delta,\tau) = \alpha^0(\delta,\tau) + \alpha^r(\delta,\tau) \tag{16.37}$$

The functional form of the residual of Helmholtz energy term is expressed in two different forms, one for polar fluids (R134a and R245fa), in equation (5.38), and one for non-polar fluids (n-Pentane and hydrocarbon), in equation (5.39). They both are represented by twelve coefficients, which have to be determined empirically. *e* is the exponential term, and the coefficients (n_1,n_2,….,n_{12}) for R134a, R245fa, and n-Pentane can be found by the works by Roland [7] and Eric [6], respectively.

$$\alpha^r(\delta,\tau) = n_1\delta\tau^{0.25} + n_2\delta\tau^{1.25} + n_3\delta\tau^{1.5} + n_4\delta^3\tau^{0.25} + n_5\delta^7\tau^{0.875} + n_6\delta\tau^{2.375}\,\mathrm{e}^{-\delta} + n_7\delta^2\tau^{2.0}\,\mathrm{e}^{-\delta}$$
$$+n_8\delta^5\tau^{2.125}\,\mathrm{e}^{-\delta} + n_9\delta\tau^{3.5}\,\mathrm{e}^{-\delta^2} + n_{10}\delta\tau^{6.5}\,\mathrm{e}^{-\delta^2} + n_{11}\delta^4\tau^{4.75}\,\mathrm{e}^{-\delta^2} + n_{12}\delta^2\tau^{12.5}\,\mathrm{e}^{-\delta^3}$$

(16.38)

$$\alpha^r(\delta,\tau) = n_1\delta\tau^{0.25} + n_2\delta\tau^{1.125} + n_3\delta\tau^{1.5} + n_4\delta^2\tau^{1.375} + n_5\delta^3\tau^{0.25} + n_6\delta^7\tau^{0.875} + n_7\delta^2\tau^{0.625}\,\mathrm{e}^{-\delta}$$
$$+n_8\delta^5\tau^{1.75}\,\mathrm{e}^{-\delta} + n_9\delta\tau^{3.625}\,\mathrm{e}^{-\delta^2} + n_{10}\delta^4\tau^{3.625}\,\mathrm{e}^{-\delta^2} + n_{11}\delta^3\tau^{14.5}\,\mathrm{e}^{-\delta^3} + n_{12}\delta^4\tau^{12.0}\,\mathrm{e}^{-\delta^3}$$

(16.39)

The thermodynamic properties, such as compressibility factor, internal energy, enthalpy, entropy, heat capacity, and speed of sound, can be determined as a function of the derivatives of Helmholtz energy, in which the full mathematical models can be found from the works by Span [7] and Eric [6].

The numerical model in the preliminary design phase is similar to the numerical model shown using polytropic ideal gas law, but most of the thermodynamic properties are determined as a function of enthalpy and entropy. The total enthalpy and entropy at the turbine inlet are determined using the total temperature and total pressure at the turbine inlet. The isentropic enthalpy at the turbine outlet, $h_{3,is}$ is determined as a function of total entropy at turbine inlet,

s_{01} and static pressure at the turbine outlet, p_3. The isentropic total-to-static enthalpy drop, $\Delta h_{ts,is}$ is determined using equation (5.43).

$$h_{01} = f(T_{01}, p_{01}) \tag{16.40}$$

$$s_{01} = f(T_{01}, p_{01}) \tag{16.41}$$

$$h_{3,is} = f(p_3, s_1) \tag{16.42}$$

$$\Delta h_{ts,is} = h_{01} - h_{3,is} \tag{16.43}$$

The total enthalpy across the nozzle is conserved, hence $h_{02}=h_{01}$, and the static enthalpy at the nozzle outlet is determined from equation (5.44). The nozzle loss coefficient, ξ_s is expressed in term of static enthalpy loss, as shown in equation (5.45). The nozzle enthalpy loss coefficient has been found between 0.05 and 0.15 by Benson as a function of corrected mass flow [24]. The overall stage performance, however, is insensitive to the nozzle loss coefficient in this range [12]. The isentropic enthalpy at the nozzle outlet, $h_{2,is}$ is determined by selecting an appropriate value of the nozzle loss coefficient. The pressure at the nozzle outlet, p_s is determined as a function of nozzle inlet entropy and nozzle outlet isentropic enthalpy. The other thermodynamic properties (T_2, ρ_2, $c_{2,sound}$) are then determined by calling the property function in EES as a function of pressure, p_2 and enthalpy, h_2.

$$h_2 = h_{02} - \frac{1}{2} C_2^{\,2} \tag{16.44}$$

$$\xi_s = \frac{h_2 - h_{2,is}}{h_{02} - h_2} = \frac{h_2 - h_{2,is}}{\frac{1}{2} C_2^{\,2}} \tag{16.45}$$

$$p_2 = p_{2,is} = f(s_2 = s_1 = s_{01}, h_{2,is}) \tag{16.46}$$

The turbine loss in the vaneless zone between the nozzle and the rotor is neglected, and the thermodynamic properties at the nozzle outlet are assumed the same as the thermodynamic properties at the rotor inlet. The effective flow area at the nozzle outlet and the rotor inlet are estimated using equation (5.29). The total enthalpy at the rotor outlet is determined using the Euler turbomachinery equation. The rothalpy, I is total enthalpy (or stagnation enthalpy) in rotating frame of reference. The rothalpy is constant along the streamlines of the flow path within a radial turbine [10]. The conservation of rothalpy within the rotor allows the calculation

of static enthalpy at the turbine outlet, h_2 once the velocity diagram at the turbine outlet is constructed. The static pressure at the turbine outlet is defined by user. The thermodynamic properties (T_3, ρ_3, s_3, c_{sound}) are determined as a function of static pressure, p_3 and static enthalpy, h_3. The total entropy and the static entropy at the turbine outlet is the same ($s_{03}=s_3$). The total (or stagnation) condition at the turbine outlet are determined as a function of entropy, s_3 and total enthalpy, h_{03}.

$$h_{03} = h_{01} - \Delta h_0 \tag{16.47}$$

$$I_3 = h_3 + \frac{1}{2}W_3^2 - \frac{1}{2}U_3^2 = I_2 = h_2 + \frac{1}{2}W_2^2 - \frac{1}{2}U_2^2 \tag{16.48}$$

5.2.5 Nozzle and Rotor Design

The rotor and nozzle geometry are set up based on the constructed velocity diagram and the thermodynamic properties from the previous section. The effective flow area at the rotor inlet and the outlet are calculated using equations (5.29) and (5.35). The aerodynamic blockage fraction, B is assumed as 0.02 to take account into the thin boundary layer by the fluid flow. The geometrical flow area, A_{eff} is then calculated using equation (5.49). The blade height at the rotor inlet, b_2, the rotor outlet tip diameter, $r_{3,shroud}$ and the hub diameter, $r_{3,hub}$ are determined by using a value of radius ratio, ε in the range of 0.4 and 0.7, where $\varepsilon=r_3/r_2$.

$$A_{geo} = \frac{A_{eff}}{1-B} \tag{16.49}$$

$$A_{2,geo} = 2\pi r_2 b_2 \tag{16.50}$$

$$A_{3,geo} = \pi\left(r_{3,shroud}^2 - r_{3,hub}^2\right) \tag{16.51}$$

The nozzle vane is designed and set up using the correlations presented by Glassman [25] and Aungier [11]. The nozzle vane is uncambered and the vane height is constant across the nozzle stage. The nozzle inlet-to-outlet ratio is recommended to be 1.25 [25]. Nozzle inlet flow angle is usually assumed to be radially inward in the preliminary design stage [10] but this is not the optimal case. Nozzle inlet flow angle, α_1 is calculated using the correlation by Glassman, shown in equation (52), where c_s is the chord of nozzle vane, and r_3 is the mean radius at the rotor outlet. The chord of the nozzle vane is calculated using equation (5.53), which is derived mathematically from the work by Glassman [17]. The equation is only valid

if the vane surface length is equivalent to the chord length, which is applicable for uncambered vanes.

$$\tan(\alpha_1) = \frac{\sin(\alpha_2)}{\frac{c_s}{r_2} + \cos(\alpha_2)} \tag{16.52}$$

$$c_s{}^2 + 2r_2 c_s \cos(\alpha_2) + \left(r_2^2 - r_1^2\right) = 0 \tag{16.53}$$

The correlation between minimum number of nozzle vane for zero diffusion loss, nozzle exit angle, nozzle inlet angle, and radius ratio was plotted by Northern Research and Engineering Corporation and reported by Baines [12]. The number of nozzle vane can be predicted using the aforementioned correlation chart. The pitch (or vane spacing) at the nozzle outlet is estimated given the nozzle vane number, Z_s.

$$s_2 = \frac{2\pi r_2}{Z_s} \tag{16.54}$$

The width of nozzle throat, o_s is then estimated using cosine rule [11].

$$\cos\alpha_2 = \frac{o_s}{s_2} \tag{16.55}$$

The clearance gap between the nozzle outlet and the rotor inlet correlates to the turbine efficiency. The optimal clearance gap was proposed by proposed by Watanabe as a function of nozzle blade height, b_2 and outlet flow angle, α_2 [26].

$$\Delta r = 2b_2 \cos(\alpha_2) \tag{16.56}$$

One of the challenges in turbine design is the estimation of number of blades. If the number of blade is excessive, the blade surface area is high and the frictional loss is high [15]. A minimum number of blade is necessary to avoid flow reversal [27]. There are different equations to calculate the minimum number of rotor blades developed by Jamieson [27], Glassman [16] and Whitfield [15]. Glassman suggested that Jamieson's equation provides an excessive number of rotor blades especially at high stator exit flow angles [28]. Whitfield's equation for number of blades is developed for minimum rotor inlet Mach number [15], as shown in equation (57). The empirical correlation between number of rotor blades and the nozzle outlet angle, derived by Glassman [25] in equation (5.58) is employed. The number of blades can

also be deduced using the empirical correlation by Rohlik [29] as a function of absolute flow angle in equation (5.59), as presented by Aungier [11].

$$Z_r = \frac{0.63\pi}{2\cos^2 \alpha_2} \tag{16.57}$$

$$Z_r = \frac{\pi\left(110 - \alpha_2\right)\tan\left(\alpha_2\right)}{30} \tag{16.58}$$

$$Z_r = 12 + 0.03(33 - \alpha_2)^2 \tag{16.59}$$

The mean blade pitch at the rotor outlet, s_3 and the width of throat, o_r can be estimated using the following equations [11]. If the relative Mach number at the rotor outlet, $M_{3,rel}$ is less than one (implying a subsonic expansion process), the throat width can be deduced using equation (5.61).

$$s_3 = \frac{2\pi r_3}{Z_r} \tag{16.60}$$

$$o_r = \frac{s_3 C_{m3}}{W_3} \tag{16.61}$$

5.2.6 Turbine Loss Model

The performance losses of radial turbine were categorized into stator loss, rotor loss, clearance loss, windage loss, and exit kinetic energy loss by Rohlik [29].Different breakdown of loss models were proposed and developed over the years for radial turbine, such as stator loss, incidence loss, and viscous loss within rotor by Glassman [25], profile loss, incidence loss, clearance loss, blade loading effect, hub-to-shroud loading effect, and moisture loss by Aungier [11], incidence loss, passage loss, clearance loss, trailing edge loss, and windage loss by Baines [12]. The subsequent turbine loss model was mainly adapted from the turbine loss model suggested by Baines but the passage loss model presented by Venture was applied [3].

Passage loss is defined as total loss within the blade passage, including secondary flow loss, mixing flow loss, blockage loss, and kinetic energy loss due to the growth of boundary layer along the blade surface [12]. Baines reported that the initial passage loss model by NASA cannot accurately predict the passage loss for all types of radial turbines under different operating conditions. An improved version of passage loss formula is presented in his work

based on the geometry at the throat of the impeller. However, the evaluation of the fluid flow velocity at the throat is difficult as the blade profile is usually not finalized in the preliminary design stage. The passage loss model in this study is evaluated as the average value of Musgrave loss model and Rodgers loss model [3], which considers the rotor inherent curvature and frictional effects.

$$\Delta h_{passage} = \frac{1}{2}\left(2 f_t \frac{L_h}{D_h} \overline{W}^2 + \frac{r_2 {C_2}^2}{r_c Z_r} \right) \tag{16.62}$$

The passage loss coefficient is expressed in term of enthalpy loss, where f_t is skin friction factor modified by Musgrave for curved flow inside the rotor, L_h is the hydraulic length, D_h is the hydraulic diameter, $\hat{W}$ is the averaged value of the relative fluid flow velocity evaluated at rotor inlet and outlet, r_c is the mean curvature radius and Z_r is the blade number of the impeller. The parameters in equation (5.62) are found by solving the equations (5.63) to (5.66), where f is Fanning friction factor and Re is Reynolds number. The mean curvature radius, r_c is assumed as the mean radius of the flow passage, and calculated using equation (5.67).

$$D_h = \frac{1}{2}\left[\frac{4\pi r_2 b_2}{2\pi r_2 + Z_r b_2} + \frac{\pi\left({r_{3,shroud}}^2 - {r_{3,hub}}^2 \right)}{\pi\left(r_{3,shroud} - r_{3,hub} \right) + Z_r \left(r_{3,shroud} + r_{3,hub} \right)} \right] \tag{16.63}$$

$$L_h = \frac{\pi}{2}\sqrt{\frac{1}{2}\left[\left(r_2 - r_{3,shroud} + \frac{b_2}{2} \right)^2 + \left(\frac{r_{3,shroud} - r_{3,hub}}{2} \right)^2 \right]} \tag{16.64}$$

$$f_c = f\left(1 + 0.075\,\mathrm{Re}^{0.25} \sqrt{\frac{D_h}{2r_c}} \right) \tag{16.65}$$

$$f_t = f_c \left[\mathrm{Re}\left(\frac{r_{in}}{r_c} \right)^2 \right]^{0.05} \tag{16.66}$$

$$r_c = r_2 - r_3 \tag{16.67}$$

Incidence loss occurs when the fluid approaches the rotor at an angle differs from the optimal flow angle. The optimal relative flow angle, $\beta_{2,opt}$ is determined by the empirical correlation by Whitfield in equation (5.68) [15]. The incidence loss coefficient is calculated as the change in relative flow velocity in tangential direction [30], as expressed in equation (5.69), where n is 3 at positive incidence and 2 at negative incidence angle based on the experimental result by Glassman [17] (as reported by Baines in [12]).

$$\tan\left(\beta_{2,opt}\right)=\frac{-1.98tan\left(\alpha_2\right)}{Z_r\left(1-\frac{1.98}{Z_r}\right)} \tag{16.68}$$

$$\Delta h_{incidence}=\frac{1}{2}\left[W_2\sin\left(\beta_2-\beta_{2,opt}\right)\right]^n \tag{16.69}$$

A common loss of energy in turbomachinery is the kinetic energy of the fluid flow at the rotor outlet. If the swirl angle is large at the turbine outlet, the internal energy of the fluid is converted into the kinetic energy where the magnitude of the energy is proportional to the square of the absolute flow velocity at the turbine outlet. A diffuser is commonly employed to recover the kinetic energy into the static pressure rise of the fluid at the stage outlet given that the installation space is not a design constraint. The enthalpy loss of the flow at the rotor outlet is expressed as below.

$$\Delta h_{exit}=\frac{1}{2}C_3{}^2 \tag{16.70}$$

A clearance gap exists between the rotor and the casing/housing, which is categorized as axial clearance and radial clearance. The axial clearance is the gap between the rotor and the housing at the rotor inlet whereas the radial clearance is the gap between the rotor and the housing at the outlet. The tip clearance is modelled as an orifice with shear flow inside the passage [30]. The clearance loss is expressed in term of enthalpy loss in equation (5.71). and the mathematical derivation of the equation can be found from the work by Baines [12].

$$\Delta h_{tip}=\frac{U_2{}^3Z_r}{8\pi}(K_a\varepsilon_aC_a+K_r\varepsilon_rC_r+K_{a,r}\sqrt{\left(\varepsilon_a\varepsilon_rC_aC_r\right)} \tag{16.71}$$

Where K_a is the discharge coefficient of the axial component, K_r is the discharge coefficient of the radial component, $K_{a,r}$ is the cross coupling coefficient of the axial and radial components, ε_a is the axial clearance gap, and ε_r is the radial clearance gap. The values of K_a, K_r, and $K_{a,r}$ are found as 0.4, 0.75, and -0.3, respectively, with good agreement with experimental data [12]. C_a and C_r are axial and radial coefficients for tip clearance model with the following equations.

$$C_a=\frac{1-\frac{r_{3,shroud}}{r_2}}{C_{\mathrm{m}2}\,\mathrm{b}_2} \tag{16.72}$$

$$C_r = \left(\frac{r_{3,shroud}}{r_2} \right) \frac{b_{total} - b_2}{C_{\mathrm{m3}}\, \mathrm{r_3 b_3}} \tag{16.73}$$

Windage loss is frictional loss between the back face of the rotor and the fluid flow leaked into the gap between the back face of the rotor and housing/generator. The leakage flow acts as a counter-rotating flow and generates a frictional torque on the back face of the rotor. The fluid flow behaviour in the region was investigated by Daily and Nece [31] by considering a rotating disc in an enclosed casing. The empirical equations were modified to consider the frictional torque on the rotor, and expressed in enthalpy loss, as shown in equation (5.74).

$$\Delta h_{windage} = k_f \frac{\bar{\rho} U_2^3 r_2^2}{2\dot{m}} \tag{16.74}$$

k_f denotes the empirical correlation for frictional torque by Daily and Nece [31], and ρ is the mean fluid density evaluated by rotor inlet and outlet static condition. The correlation is dependent on Reynolds number and the value is calculated for two different flow regimes, laminar flow ($\mathrm{Re}<10^5$) using equation (5.75), and turbulent flow ($\mathrm{Re}>10^5$) using equation (5.76). ε denotes the clearance gap between the back face of the rotor wheel and the housing.

$$k_f = \frac{3.7 \left(\frac{\varepsilon}{r_2} \right)^{0.1}}{\mathrm{Re}^{0.5}} \tag{16.75}$$

$$k_f = \frac{0.102 \left(\frac{\varepsilon}{r_2} \right)^{0.1}}{\mathrm{Re}^{0.2}} \tag{16.76}$$

The turbine total-to-static efficiency, η_{ts} and total-to-total efficiency, η_{tt} are then determined as below.

$$\eta_{ts} = \frac{\Delta h_0}{\Delta h_0 + \Delta h_{passage} + \Delta h_{incidence} + \Delta h_{tip} + \Delta h_{windage}} \tag{16.77}$$

$$\eta_{tt} = \frac{\Delta h_0}{\Delta h_0 + \Delta h_{passage} + \Delta h_{incidence} + \Delta h_{tip} + \Delta h_{windage} + \Delta h_{exit}} \tag{16.78}$$

5.2.7 Validation of Turbine Empirical Loss Model

The turbine loss model was developed based on a number of existing correlations for air from different authors. The passage loss model was validated by Emilie [3] and compared against the improved passage loss model by Baines [12]. However, the lack of published data with detailed measurement of properties of interest inside the blade passage makes the validation of the individual loss models difficult. Also, the other loss models (incidence loss, windage loss and tip clearance loss) are validated against the data from the radial turbines with low pressure ratio gas turbine and turbocharger [12]. At the time of writing, there were no published loss models specifically developed for refrigerants. Thus, the loss models for air were used for the performance analysis for refrigerants and validated by comparison to published turbine performance data for air [32] and R245fa [4].

The design parameters from a commercial gas turbine unit and an academic research turbo-expander unit are presented in Table 5.1 for the validation purpose. The numerical model in this study does not take into account of the losses across the nozzle. Whitfield [15] reported that the overall turbine performance is very insensitive to the nozzle loss coefficients based on the potential range of nozzle loss coefficients calculated by Benson [24] and Johnston [33]. The simulated turbine total-to-static efficiency from the turbine empirical loss model and the turbine efficiency at the design point are shown in Table 5.1. The turbine empirical loss model over-estimates the turbine performance in the range of 2 to 4%. The discrepancy is attributed to the lack of loss coefficients of the nozzle and the vaneless space between rotor and nozzle. However, the turbine model is sufficient to provide an estimation of the potentially highest turbine efficiency in this study assuming that the nozzle is designed properly with minimal losses.

Table 5.1: Operating Conditions of Selected Cases

	Sundstrand Power System T-100 (Commercial unit) [3, 32]	ORC-Turbo Expander [4]
Fluid	Air	R245fa
Rotational Speed (rev/min)	106588	20,000
Inlet temperature (K)	1056	353
Inlet pressure (kPa)	580	732
Total-to-static pressure ratio (-)	5.73	4.11
Mass flow rate (kg/s)	0.33	1.58
Rotor blade number (-)	16	12
Rotor inlet radius (mm)	58.96	70
Rotor outlet tip radius (mm)	44.18	40.6
Rotor outlet hub radius (mm)	17.69	21
Rotor inlet blade height (mm)	5.47	4.275*
Rotor height (mm)	20.65	33.67*
Rotor inlet absolute flow angle (deg)	76.7*	71.6*
Rotor inlet relative flow angle (deg)	-36.8*	-18.4*
Total-to-static efficiency (%)	86	76
Efficiency from numerical model (%)	87.8	80

**The given value is calculated from the numerical correlations for optimal operating condition due to the lack of information from the published literature.*

5.2.8 Optimization of Objective Function

The in-built optimization program in EES was applied to determine the optimal preliminary design by varying the specific speed, N_s between 0.4 and 0.6, flow coefficient, ϕ between 0.2 and 0.3, and radius ratio, ε between 0.4 and 0.7, simultaneously. Two different optimization programs are available in EES commercial package, namely conjugate direction method and variable metric optimization method [34, 35]. The conjugate direction method (also known as Powell method), utilizes one-dimensional search to locate the optimal point. One variable is manipulated and the corresponding optimal value is located while the other variables are held constant. This method, however might not be accurate in locating the true optimal point because of the non-linear relationships between variables. The second method, variable metric optimization, requires numerical derivatives in the calculation. The objective function is fitted into a number of quadratic function with all the independent variables. The optimal point is found by setting the derivative to the variables at zero as described in Kalyanmoy [36] or Klein [34, 35]. The objective function in this study is total-to-static isentropic efficiency of the turbine, assuming a diffuser is not used. Both optimization methods were applied and compared in the preliminary design phase.

5.2.9 Numerical Mathematical Model

The mathematical model of the preliminary design phase was defined and solved using Engineering Equation Solver (EES), and the numerical model is shown in Figure 5.2. The operating condition across the turbine is defined using the thermodynamic model in previous chapter, and the shaft speed and the rotor diameter are calculated using the specific speed-specific diameter chart. The design parameters (ϕ, ε) are selected using experience. An initial guess for turbine efficiency is made and iterated to a final solution. The velocity diagram is set up at the rotor inlet and rotor outlet, and the thermodynamic properties at each station are calculated. The principal turbine geometry is then determined before the performance evaluation. Two different optimization methods are then conducted by varying the specific speed, N_s, flow coefficient ϕ, and radius ratio, ε. Turbine total-to-static efficiency is defined as the objective function in the optimization program to select the best configuration of N_s, ϕ, ε for further development.

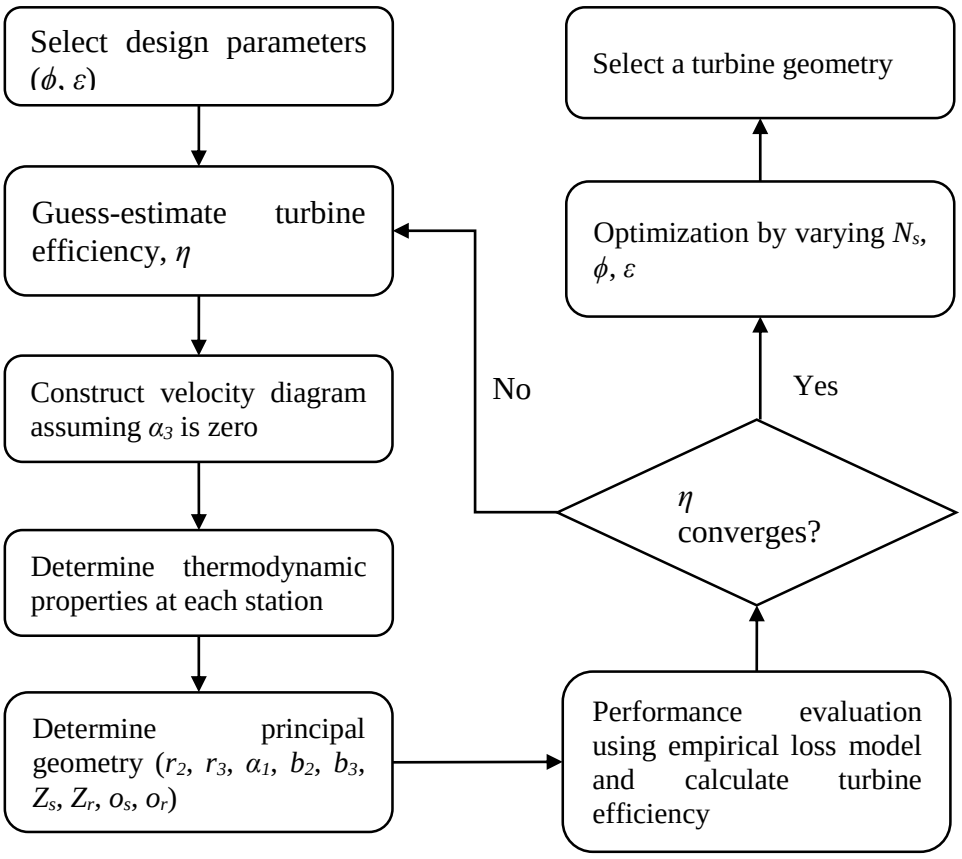

Figure 5.2: Calculation flow for turbine preliminary design process

5.3 Case Study for Low-Temperature Geothermal Brine

The turbine preliminary design process was conducted using a set of fictitious heat source and heat sink condition presented in Table 5.2. The heat source is from a low temperature geothermal reservoir with geothermal brine in liquid phase and an air-cooled condenser is employed in the cycle design. The thermodynamic cycle in the previous chapter was adapted for the heat source and heat sink condition, and the operating condition across the turbine was determined. The geothermal brine was modelled as water using the cycle design analysis approach. The cycle modelling was performed with the following constraint:

- the critical temperature/pressure of the fluids is not exceeded,
- the expansion process occurs in the superheated region, and
- the differential temperature at the pinch point in the condenser and evaporator is 5˚C or more

The system output from the thermodynamic cycle analysis was shown in Table 5.3 for three selected working fluids, R134a, n-Pentane, and R245fa at similar power output, between 330 and 340 kW. The preliminary design process of radial inflow turbine was implemented for these three working fluids with the design condition shown in Table 5.3. The averaged specific heat ratio and isobaric heat capacity were calculated using REFPROP [37], as shown in Table 5.5, and used as input in the preliminary design using perfect gas equations. The result of the preliminary design was tabulated in Table 5.4.

Table 5.2: Heat source and heat sink condition for turbine design

Heat source		
Working medium	-	Geothermal brine
Inlet pressure	kPa	1200
Inlet temperature	˚C	130
Outlet temperature	˚C	90
Flow rate	kg/s	18
Heat sink		
Working medium	-	Air
Inlet temperature	˚C	17
Outlet temperature	˚C	35

Table 5.3: Turbine operating condition using different working fluids

Parameters	Unit	Case 1	Case 2	Case 3
Working fluid	-	R134a	R245fa	n-Pentane
Turbine inlet temperature	˚C	105.0	100	98
Turbine inlet pressure	kPa	3,667	1,266	563
Degree of superheat	˚C	9	0	0
Mass flow rate	kg/s	16.3	13.7	6.8
Turbine outlet temperature	˚C	43.8	54.0	62.1
Turbine outlet pressure	kPa	1,003	238	109
Pressure ratio	-	3.7	5.3	5.2
Turbine work output	kW	330	340	333
Cycle efficiency	%	8.4	9.8	9.8

Table 5.4: Design output from the preliminary design program for three different working fluids using perfect gas equations and real gas equations

		R134a		R245fa		n-Pentane	
		Ideal	Real	Ideal	Real	Ideal	Real
$\Delta h_{ts,is}$	kJ/kg	281	25	159	31	105	61
N	rev/min	104,122	16,026	36,862	10,596	18,066	12,137
d	m	0.093	0.186	0.189	0.312	0.337	0.385
			Velocity diagram				
α_1	degree	51	51	51	51	51	51
α_2	degree	77	77	77	77	77	77
α_3	degree	0	0	0	0	0	0
β_2	degree	-29	-28	-28	-28	-30	-30
β_3	degree	-63	-63	-63	-63	-63	-63
U_2	m/s	509	156	365	173	319	245
U_3	m/s	204	62	146	69	127	98
C_2	m/s	463	143	335	158	289	222
C_3	m/s	102	31	73	35	64	49
W_2	m/s	117	35	82	39	74	56
W_3	m/s	228	70	163	78	127	109
			Thermodynamic Conditions				
T_{02}	K	378	375	373	371	371	370
T_2	K	317	345	330	349	351	353
p_{02}	kPa	3,546	3,440	1,217	1,173	538	525
p_2	kPa	2,340	1,995	726	591	289	271
M_2	-	2.2	1.1	2.0	1.2	1.4	1.1
T_{03}	K	247	317	281	327	327	335
T_3	K	244	316	279	326	326	334
p_{03}	kPa	1,032	1,027	245	246	113	113
p_3	kPa	1,003	1,003	238	238	109	109
ρ_3	kg/m^3	50	48	14	13	3	3
$M_{3,rel}$	-	1.2	0.5	1.1	0.6	0.7	0.6
			Principal Geometry				
r_1	m	0.058	0.116	0.118	0.195	0.211	0.241
r_2	m	0.047	0.093	0.095	0.156	0.168	0.193
r_3	m	0.019	0.037	0.038	0.062	0.067	0.077
$r_{3,shroud}$	m	0.032	0.062	0.067	0.103	0.112	0.127
$r_{3,hub}$	m	0.005	0.013	0.009	0.022	0.023	0.027
b_2	mm	6	9	9	13	14	16
b_{total}	mm	20	41	37	66	71	82
Z_s	-	20	20	20	20	20	20
Z_r	-	15	15	15	15	15	15
s_s	mm	15	29	30	49	53	60
s_r	mm	8	16	16	26	28	32
o_s	mm	3	6	7	11	12	13
o_r	mm	3	7	7	12	13	14
			Turbine Performance				
$\Sigma\Delta h_{loss}$	kJ/kg	49.0	3.1	38.5	3.5	11.3	6.5
η_{ts}	-	0.82	0.87	0.76	0.88	0.89	0.89
ψ	-	0.9	0.9	0.9	0.9	0.9	0.9
			Optimal configuration				
ϕ	-	0.2	0.2	0.2	0.2	0.2	0.2
ε	-	0.4	0.4	0.4	0.4	0.4	0.4
N_s		0.48	0.49	0.46	0.49	0.49	0.50

Table 5.5: Averaged specific heat ratio and isobaric heat capacity of the selected fluids with the corresponding operating range

	Unit	R134a	R245fa	n-Pentane
k	-	1.74	1.10	1.32
c_p	kJ/kg.K	1.75	2.02	1.29

The turbine rotational speed and rotor wheel size were determined by first defining the optimal specific speed and specific diameter from the specific speed-specific diameter performance chart. The isentropic enthalpy drop across the turbine was over-estimated at 72% (n-Pentane), 413% (R245fa), and 1,000% (R134a) using ideal gas equations. The rotor diameter was over-estimated at 12.5% (n-Pentane), 39% (R245fa), and 50% (R134a), and the shaft speed was over-predicted at 50% (n-Pentane), 250% (R245fa), and 550% (R134a). The velocity diagrams at the rotor inlet and rotor outlet are similar for all the working fluids despite the operating condition. The magnitude of the velocity was over-estimated when ideal gas equations are applied attributed to the over-estimated turbine rotational speed and tip speed. The high turbine tip speed and flow velocity give rise to the high values of Mach number at the nozzle outlet, M_2 and the relative Mach number at the rotor outlet, $M_{3,rel}$. The principal geometry of the turbine (*r*, *b*, *s*, and *o*) using ideal gas equations was under-estimated up to 50%. The turbine loss model was applied to estimate the losses for each design, and the turbines designed using ideal gas equations were found to have a very high enthalpy loss, at 100% (n-Pentane), 1,000% (R245fa) and 1,400% (R134a) higher than the turbines designed using real gas equations. The estimated turbine isentropic efficiency using the ideal gas equations is not accurate attributed to the large error in the isentropic enthalpy drop across the turbine. The performance parameters of the turbine designed using ideal gas equations were re-evaluated by re-calculating the isentropic enthalpy drop using equations (5.40) to (5.43), the specific speed, the loading coefficient using equation (5.2), the velocity ratio using equation (5.3), the static enthalpy at the rotor outlet using equation (5.48), the density at the rotor outlet, the mass flow rate at the rotor outlet, $\dot{m}_{outlet}$ using equation (5.35), and the turbine isentropic efficiency using equation (5.77), and tabulated in Table 5.6. The actual specific speed for the turbines designed using ideal gas equations deviates significantly from the optimal specific speed (which is in the range of 0.4 and 0.6 for radial inflow turbines). The performance of radial turbine is sensitive to the choice of specific speed. Hence, the turbines designed using ideal gas equations for R134a show the highest turbine loss, followed by R245fa, and n-Pentane. The deviation of enthalpy change for R134a using ideal gas equations is the largest. Hence, the stage loading

coefficient, the specific speed, and the velocity ratio, which are functions of enthalpy change, are deviated significantly from the optimal values. The predicted mass flow rate at the turbine outlet is 410.7 kg/s, which is deviated significantly from the design specification at 16.3 kg/s for R134a. The isentropic efficiency for the turbines designed using ideal gas equations for R134a and R245fa were not available since the enthalpy loss is much higher than the isentropic enthalpy drop. This indicates that the turbines operate as pumps and work input is required to achieve the specified rotational speed.

Table 5.6: Performance parameters for turbines designed using perfect gas equations

	Unit	R134a	R245fa	n-Pentane
N_s	-	3.2	1.7	0.7
Ψ	-	0.08	0.18	0.53
v	-	2.27	1.47	0.91
$\dot{m}_{outlet}$	kg/s	410.7	23.8	7.4
η_{ts} (%)	-	-	-	83

The thermodynamic properties, enthalpy, h, and isobaric heat capacity, c_p are independent of pressure using perfect gas equations whereas the enthalpy and the isobaric heat capacity are dependent on temperature and pressure in real fluids. Comparison was made between the distribution of enthalpy as a function of temperature and pressure in Figure 5.3. The temperature-pressure-enthalpy diagram was generated using REFPROP [37] with the multi-parameter equations of states, whereas the temperature-enthalpy diagram in Figure 5.3(b) was generated using equation (5.79). The enthalpy of the real fluids in the superheated region is between 460 and 490 kJ/kg using real gas equations, but the enthalpy of the perfect gas is between 650 and 750 kJ/kg. The change in enthalpy across the same temperature ratio is 30 kJ/kg for real gas and 100 kJ/kg for perfect gas. The large error in estimating the change in enthalpy was carried forward during the preliminary design phase, with a poor choice of turbine option as the design outcome.

$$h = C_p T \tag{16.79}$$

The estimation of isobaric heat capacity and change in enthalpy for real fluids can be performed using the following equations [38]. $C_{v,ideal}$ denotes ideal isochoric heat capacity, and V specific volume.

$$C_p = C_{v,ideal} + T\int_{\infty}^{V} \frac{\partial^2 p}{\partial T^2} dV - T\frac{\frac{\partial p}{\partial T}}{\frac{\partial p}{\partial V}} \tag{16.80}$$

$$\partial h = C_p \partial T + \left(T\frac{\partial p}{\partial T} - p \right) \partial V \tag{16.81}$$

In an ideal gas condition, the integral and the derivatives are simplified using equations (5.82) to (5.84), and the interaction between molecules are neglected.

$$\int_{\infty}^{V} \frac{\partial^2 p}{\partial T^2} dV = 0 \tag{16.82}$$

$$\frac{\partial p}{\partial T} = \frac{R}{V} \tag{16.83}$$

$$\frac{\partial p}{\partial V} = \frac{-RT}{V^2} \tag{16.84}$$

The deviation of c_p using ideal gas equations and some real gas equations was investigated and presented in the study by Lujan [38].

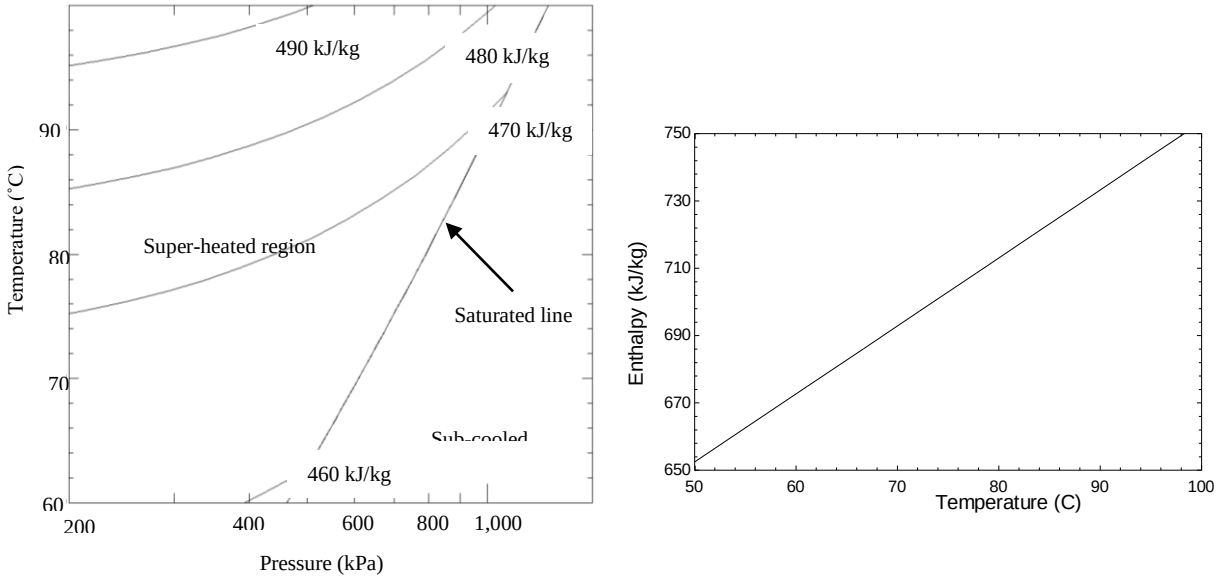

(a) (b)

Figure 5.3: Temperature-enthalpy diagram for R245fa using multi-parameters equations of states (a) and ideal gas equations (b)

Large deviation was found in turbine parameters, such as specific speed, loading coefficient, velocity ratio, from the optimal values for the turbine designed using ideal gas equations. The largest deviation was found for R134a, followed by R245fa and n-Pentane. The largest deviation was found to occur when the compressibility factor is further away from one. The compressibility factor was shown in Table 5.7. The preliminary design using ideal gas equations yields large error when the compressibility factor is low. Compressibility factor is the ratio of actual volume of a gas to the ideal volume of the gas. When the compressibility factor is low, the deviation in estimating the thermodynamic properties (including enthalpy, isobaric heat capacity, and etc.) is large.

Table 5.7: Molecular weight and compressibility factor of the selected working fluids

Fluid	Compressibility factor at inlet
n-Pentane	0.85
R134a	0.56
R245fa	0.75

The result shows that the turbine preliminary design using perfect gas equations is valid if the compressibility factor is close to one, as shown by n-Pentane with compressibility factor of 0.85. If the compressibility factor is further away from one, the high deviation in thermodynamic properties would be carried forward in the preliminary design process with a poor design choice.

5.4 Conclusion

This chapter presents the preliminary design process of radial inflow turbines using ideal gas equations and real gas equations by coupling the turbine preliminary design program to the in-built fluid database in EES. Multi-variable optimization was performed during the preliminary design phase to determine the best turbine geometry by varying the selected turbine parameters, such as specific speed, flow coefficient, and radius ratio. The turbine preliminary design program was utilized to design turbines for a geothermal binary plant using three different working fluids, namely n-Pentane, R245fa and R134a. The results show that the rotor diameter is under-estimated and the shaft speed is over-estimated for the turbines designed using ideal gas equations. The large deviation is attributed to the error in estimating the thermodynamic properties using ideal gas equations, and the deviation is larger at lower compressibility factor. The optimal flow angle and relative flow angle are independent on the type of gas model as they are function of turbine parameters, such as the user-defined flow coefficient and specific speed. The turbine preliminary design process using perfect gas equations is valid only if the compressibility factor is close to one. If the compressibility factor is deviated from one, the preliminary design using real gas equations is required to avoid the poor turbine design options. Since the turbine operating condition is usually away from one, the turbine preliminary design using real gas model is a better option to match the existing turbines to the cycle design.

5.5 References

1. Harinck, J., *Super-and Transcritical Fluid Expansions,* in *Mechanical, Maritime and Materials Engineering*. 2010, Delft University of Technology.
2. Harinck, J., et al., *Influence of thermodynamic models in two-dimensional flow simulations of turboexpanders.* Journal of turbomachinery, 2010. **132**(1): p. 011001.
3. Ventura, C., et al., *Preliminary Design and Performance Estimation of Radial Inflow Turbines: An Automated Approach.* Journal of Fluids Engineering-Transactions of the Asme, 2012. **134**(3).
4. Kang, S.H., *Design and experimental study of ORC (organic Rankine cycle) and radial turbine using R245fa working fluid.* Energy, 2012. **41**(1): p. 514-524.
5. Sauret, E. and A.S. Rowlands, *Candidate radial-inflow turbines and high-density working fluids for geothermal power systems.* Energy, 2011. **36**(7): p. 4460-4467.
6. Lemmon, E.W. and R. Span, *Short fundamental equations of state for 20 industrial fluids.* Journal of Chemical & Engineering Data, 2006. **51**(3): p. 785-850.
7. Span, R., *Multiparameter equations of state: an accurate source of thermodynamic property data*. 2000: Springer.
8. Fiaschi, D., G. Manfrida, and F. Maraschiello, *Thermo-fluid dynamics preliminary design of turbo-expanders for ORC cycles.* Applied Energy, 2012. **97**: p. 601-608.
9. Pan, L. and H. Wang, *Improved analysis of Organic Rankine Cycle based on radial flow turbine.* Applied Thermal Engineering, 2013. **61**(2): p. 606-615.
10. Dixon, S.L. and C. Hall, *Fluid Mechanics and Thermodynamics of Turbomachinery*. 2010, Butterworth-Heinemann: Burlington.
11. Aungier, R.H., *Turbine aerodynamics: axial-flow and radial-inflow turbine design and analysis*. 2006: ASME Press.
12. Moustapha, H., et al., *Axial and Radial Turbines*. 2003: Concepts Eti.
13. Khan, R.S.R.G.a.A.A., *Axial Flow and Radial Flow Gas Turbines,* in *Turbomachinery: Design and Theory*. 2003, CRC Press.
14. Japikse, D. and N.C. Baines, *Introduction to turbomachinery*. 1995: Concepts ETI.
15. Whitfield, A. and N.C. Baines, *Design of radial turbomachines.* 1990.
16. Glassman, A.J., *Turbine Design and Application. NASA SP-290.* NASA Special Publication, 1972. **290**.
17. Wasserbauer, C.A. and A.J. Glassman, *FORTRAN program for predicting off-design performance of radial-inflow turbines.* NASA Technical Paper, 1975(TN D-8063).
18. Chen, H. and N.C. Baines, *The aerodynamic loading of radial and mixed-flow turbines.* International Journal of Mechanical Sciences, 1994. **36**(1): p. 63-79.
19. Schobeiri, M., *Turbomachinery flow physics and dynamic performance*. 2005: Springer.
20. Rohlik, H.E., *Analytical determination of radial inflow turbine design geometry for maximum efficiency.* 1968.

21. Baines, N. *ENGR408-ENME 627-S1 Special Topic in Engineering: Turbomachinery*. 2014.

22. Redlich, O. and J. Kwong, *On the Thermodynamics of Solutions. V. An Equation of State. Fugacities of Gaseous Solutions.* Chemical Reviews, 1949. **44**(1): p. 233-244.

23. Hiett, G. and I. Johnston. *Paper 7: Experiments Concerning the Aerodynamic Performance of Inward Flow Radial Turbines*. in *Proceedings of the Institution of Mechanical Engineers, Conference Proceedings*. 1963. SAGE Publications.

24. Benson, R.S., *A review of methods for assessing loss coefficients in radial gas turbines.* International Journal of Mechanical Sciences, 1970. **12**(10): p. 905-932.

25. Glassman, A.J., *Computer program for design analysis of radial-inflow turbines.* 1976.

26. Watanabe, I., I. Ariga, and T. Mashimo, *Effect of dimensional parameters of impellers on performance characteristics of a radial-inflow turbine.* Journal of Engineering for Power, 1971. **93**: p. 81.

27. Jamieson, A., *The radial turbine.* Gas turbine principles and practice, 1955.

28. Whitfield, A., *The preliminary design of radial inflow turbines.* J. Turbomach, 1990. **112**: p. 50-57.

29. Rohlik, H.E., *Analytical determination of radial inflow turbine design geometry for maximum efficiency*. 1968: National Aeronautics and Space Administration.

30. Ghosh, S.K., R. Sahoo, and S.K. Sarangi, *Mathematical Analysis for Off-Design Performance of Cryogenic Turboexpander.* Journal of fluids engineering, 2011. **133**(3).

31. Daily, J. and R. Nece, *Chamber dimension effects on induced flow and frictional resistance of enclosed rotating disks.* Journal of Basic Engineering, 1960. **82**: p. 217.

32. Jones, A.C., *Design and Test of a Small, High Pressure Ratio Radial Turbine.* Journal of Turbomachinery, 1996. **118**(2): p. 362-370.

33. Benson, R., *Paper 16: An Analysis of the Losses in a Radial Gas Turbine.* Proceedings of the Institution of Mechanical Engineers, Conference Proceedings, 1965. **180**(10): p. 41-53.

34. Klein, S.A. and G. Nellis, *Mastering EES*. 2013: F-Chart Software.

35. Klein, S. and F. Alvarado, *EES manual.* Middleton, Wisconsin, USA, 1999.

36. Kalyanmoy, D., *Optimization for engineering design: Algorithms and examples*. 2004: PHI Learning Pvt. Ltd.

37. Lemmon, E.W., Huber, M.L., McLinden, M.O, *NIST Standard Reference Database 23: Reference Fluid Thermodynamic and Transport Properties-REFPROP, Version 9.1*, in *National Institute of Standards and Technology*. 2013, Standard Reference Data Program: Gaithersburg.

38. Luján, J.M., et al., *Model of the expansion process for R245fa in an Organic Rankine Cycle (ORC).* Applied Thermal Engineering, 2012. **40**(0): p. 248-257.

Components of the SMC Adaptive Strategy

6.0 Meanline Analysis of Radial Inflow Turbine

The aim of this thesis is to present the SMC-DTR approach for low temperature resources, and the main contribution of this thesis is to develop the key component, SMC analysis approach. The critical components of the SMC-DTR approach is the SMC adaptive strategy. One of the analysis techniques of the SMC adaptive strategy is the meanline analysis. This chapter aims to present the turbine performance analysis using the meanline analysis. The meanline analysis refers to the performance analysis along the mid-line (also known as mean-line or centre-line) of the fluid along the flow passage. The thermodynamic properties are determined along the meanline of the fluid flow at different locations, such as the turbine inlet and the turbine outlet. The meanline analysis model consists of the empirical loss models which have been developed by the turbine manufacturers and the researchers. The meanline analysis model in this study is made up from the loss models developed by Baines and by Sauret. The model is validated against two different turbines: an industrial gas turbine and an academic-based ORC turbine using R245fa as working fluid. The meanline analysis model in this chapter is the same as the turbine performance analysis model presented in the previous chapter. This model is integrated into the preliminary design of radial inflow turbine and the SMC adaptive strategy attributed to the accuracy and the simplicity of the analysis model with minimal computational effort.

6.1 Introduction

Numerical modelling of turbine performance can be classified into meanline analysis, two-dimensional fluid flow study, three-dimensional inviscid fluid flow analysis, and three-dimensional viscous flow study. The meanline analysis has been commonly used to model the turbine performance in turbine preliminary design process, performance evaluation process in the preliminary stage and turbine retrofit process. This analysis model is commonly applied in turbomachines, such as axial flow turbines, axial flow compressors, radial flow turbines, and centrifugal compressors. The analysis model involves a number of different loss models, involving the passage loss, incidence loss, clearance loss, moisture loss, shear loss, frictional loss, and etc. Most of the individual loss models have been developed empirically with some empirical coefficients, and validated against the experimental data. The development of the loss models requires the experiences of the engineers and researchers, referred to the field as knowledge-based engineering. Not all the loss models are required to model the turbomachines. For example, moisture loss model is applied specifically for steam turbines if the quality of the fluid is less than one during the expansion process. The moisture loss model is not required in an ORC expansion if the expansion of the fluid occurs in the superheated region. Most of the turbine loss models have been developed for axial flow turbomachines in the military application during the Second World War. Some of the loss models have then been adapted and validated for radial flow machines, such as incidence loss model. The passage loss model of axial flow machine cannot be adapted for radial flow machines due to the difference of the flow patterns for these two turbomachines.

Meanline analysis refers to the performance analysis along the centre-line of the flow passage. The end-wall effect and near the end-wall effect are usually not considered in the meanline analysis. This analysis provides the representative values for the thermodynamic properties at the critical stations in a turbine stage, including nozzle inlet, interface between nozzle and rotor, and rotor outlet. Sometimes, a volute and a diffuser analysis would be included in the meanline analysis. The meanline analysis technique in this chapter is the same as the turbine performance analysis technique presented in the previous chapter as part of the preliminary design method of radial inflow turbine. The meanline analysis approach is integrated into the preliminary design (in the previous chapter) and the SMC adaptive strategy as this analysis model can estimates the overall turbine efficiency with close agreement to the experimental data with minimal computational effort.

The objective of this chapter is to present the meanline analysis model used in the SMC adaptive strategy, and validate the model against two different turbines: one industrial radial gas turbine and an ORC radial turbine using R245fa as working fluid. This meanline analysis model in the SMC strategy is implemented only if the performance data of the selected turbines is not available.

6.2 Turbine Loss Model

The performance losses of radial turbine can be categorized into stator loss, rotor loss, clearance loss, windage loss, and exit kinetic energy loss by Rohlik [1].Different breakdown of loss models have been proposed and developed over the years for radial turbine, such as stator loss, incidence loss, and viscous loss within rotor by Glassman [2], profile loss, incidence loss, clearance loss, blade loading effect, hub-to-shroud loading effect, and moisture loss by Aungier [3], incidence loss, passage loss, clearance loss, trailing edge loss, and windage loss by Baines [4]. The subsequent turbine loss model was adapted from different turbine loss model, including the incidence loss, passage loss, clearance loss, trailing edge loss, and windage loss by Baines [4], and the passage loss model by Venture [5].

Passage loss is defined as total loss within the blade passage, including secondary flow loss, mixing flow loss, blockage loss, and kinetic energy loss due to the growth of boundary layer along the blade surface [4]. The initial passage loss model by NASA cannot accurately predict the passage loss for all types of radial turbines under different operating conditions [4]. An improved version of passage loss formula has been presented [4] based on the geometry at the throat of the rotor. However, the evaluation of the fluid flow velocity at the throat is difficult as the blade profile is usually not finalized in the preliminary design stage. The passage loss model in this study is evaluated as the average value of Musgrave loss model and Rodgers loss model [5], which considers the rotor inherent curvature and frictional effects.

$$\Delta h_{passage} = \frac{1}{2}\left(2 f_t \frac{L_h}{D_h} \overline{W}^2 + \frac{r_2 {C_2}^2}{r_c Z_r} \right) \tag{17.1}$$

The passage loss coefficient is expressed in term of enthalpy loss, where f_t is skin friction factor modified by Musgrave for curved flow inside the rotor, L_h is the hydraulic length, D_h is the hydraulic diameter, $\hat{W}$ is the averaged value of the relative fluid flow velocity evaluated at rotor inlet and outlet, r_c is the mean curvature radius and Z_r is the blade number of the impeller.

The parameters in equation (6.1) are found by solving the equations (6.2) to (6.6), where f is Fanning friction factor and Re is Reynolds number. The mean curvature radius, r_c is assumed as the mean radius of the flow passage, and calculated using equation (6.6).

$$D_h = \frac{1}{2}\left[\frac{4\pi r_2 b_2}{2\pi r_2 + Z_r b_2} + \frac{\pi\left({r_{3,shroud}}^2 - {r_{3,hub}}^2 \right)}{\pi\left(r_{3,shroud} - r_{3,hub} \right) + Z_r \left(r_{3,shroud} + r_{3,hub} \right)} \right] \tag{17.2}$$

$$L_h = \frac{\pi}{2}\sqrt{\frac{1}{2}\left[\left(r_2 - r_{3,shroud} + \frac{b_2}{2}\right)^2 + \left(\frac{r_{3,shroud} - r_{3,hub}}{2}\right)^2\right]} \tag{17.3}$$

$$f_c = f\left(1 + 0.075\,\mathrm{Re}^{0.25}\sqrt{\frac{D_h}{2r_c}}\right) \tag{17.4}$$

$$f_t = f_c\left[\mathrm{Re}\left(\frac{r_{in}}{r_c}\right)^2\right]^{0.05} \tag{17.5}$$

$$r_c = r_2 - r_3 \tag{17.6}$$

Incidence loss occurs when the fluid approaches the rotor at an angle differs from the optimal flow angle. The optimal relative flow angle, $\beta_{2,opt}$ is determined by the empirical correlation by Whitfield in equation (6.7) [6]. The incidence loss coefficient is calculated as the change in relative flow velocity in tangential direction [7], as expressed in equation (5.69), where n is 3 at positive incidence and 2 at negative incidence angle based on the experimental result by Glassman [8] (as reported by Baines in [4]).

$$\tan\left(\beta_{2,opt}\right) = \frac{-1.98tan\left(\alpha_2\right)}{Z_r\left(1 - \frac{1.98}{Z_r}\right)} \tag{17.7}$$

$$\Delta h_{incidence} = \frac{1}{2}\left[W_2 \sin\left(\beta_2 - \beta_{2,opt}\right)\right]^n \tag{17.8}$$

Where Δh_{inc} is the incidence loss coefficient expressed in term of enthalpy loss.

A common loss of energy in turbomachinery is the kinetic energy of the fluid flow at the rotor outlet. If the swirl angle is large at the turbine outlet, the internal energy of the fluid is converted into the kinetic energy where the magnitude of the energy is proportional to the square of the absolute flow velocity at the turbine outlet. A diffuser is commonly employed to recover the kinetic energy into the static pressure rise of the fluid at the stage outlet given that the installation space is not a design constraint. The enthalpy loss of the flow at the rotor outlet is expressed as below.

$$\Delta h_{exit} = \frac{1}{2}C_3^{\,2} \tag{17.9}$$

A clearance gap exists between the rotor and the casing/housing, which is categorized as axial clearance and radial clearance. The axial clearance is the gap between the rotor and the housing at the rotor inlet whereas the radial clearance is the gap between the rotor and the housing at the outlet. The tip clearance is modelled as an orifice with shear flow inside the passage [7]. The clearance loss is expressed in term of enthalpy loss in equation (6.10). and the mathematical derivation of the equation can be found from the work by Baines [4].

$$\Delta h_{tip} = \frac{U_2^{\,3} Z_r}{8\pi}\left(K_a \varepsilon_a C_a + K_r \varepsilon_r C_r + K_{a,r}\sqrt{\left(\varepsilon_a \varepsilon_r C_a C_r\right)}\right) \tag{17.10}$$

Where K_a is the discharge coefficient of the axial component, K_r is the discharge coefficient of the radial component, $K_{a,r}$ is the cross coupling coefficient of the axial and radial components, ε_a is the axial clearance gap, and ε_r is the radial clearance gap. The values of K_a, K_r, and $K_{a,r}$ are found as 0.4, 0.75, and -0.3, respectively, with good agreement with experimental data [4]. C_a and C_r are axial and radial coefficients for tip clearance model with the following equations.

$$C_a = \frac{1 - \dfrac{r_{3,shroud}}{r_2}}{C_{\mathrm{m}2}\,\mathrm{b}_2} \tag{17.11}$$

$$C_r = \left(\frac{r_{3,shroud}}{r_2}\right)\frac{b_{total} - b_2}{C_{\mathrm{m}3}\,\mathrm{r}_3\mathrm{b}_3} \tag{17.12}$$

Windage loss is frictional loss between the back face of the rotor and the fluid flow leaked into the gap between the back face of the rotor and housing/generator. The leakage flow acts as a counter-rotating flow and generates a frictional torque on the back face of the rotor. The fluid flow behaviour in the region was investigated by Daily and Nece [9] by considering a rotating disc in an enclosed casing. The empirical equation has been modified to consider the frictional torque on the rotor, and expressed in enthalpy loss, as shown in equation (6.13).

$$\Delta h_{windage} = k_f \frac{\bar{\rho} U_2^3 r_2^2}{2\dot{m}} \tag{17.13}$$

Where k_f denotes the empirical correlation for frictional torque by Daily and Nece [9], and ρ is the mean fluid density evaluated by rotor inlet and outlet static condition. The correlation is dependent on Reynolds number and the value is calculated for two different flow regimes, laminar flow ($Re<10^5$) using equation (5.75), and turbulent flow ($Re>10^5$) using equation (5.76). ε denotes the clearance gap between the back face of the rotor wheel and the housing.

$$k_f = \frac{3.7\left(\frac{\varepsilon}{r_2}\right)^{0.1}}{\mathrm{Re}^{0.5}} \tag{17.14}$$

$$k_f = \frac{0.102\left(\frac{\varepsilon}{r_2}\right)^{0.1}}{\mathrm{Re}^{0.2}} \tag{17.15}$$

The turbine total-to-static efficiency, η_{ts} and total-to-total efficiency, η_{tt} are then determined as below.

$$\eta_{ts} = \frac{\Delta h_0}{\Delta h_0 + \Delta h_{passage} + \Delta h_{incidence} + \Delta h_{tip} + \Delta h_{windage}} \tag{17.16}$$

$$\eta_{tt} = \frac{\Delta h_0}{\Delta h_0 + \Delta h_{passage} + \Delta h_{incidence} + \Delta h_{tip} + \Delta h_{windage} + \Delta h_{exit}} \tag{17.17}$$

6.3 Validation of Turbine Empirical Loss Model

The turbine loss model was developed based on a number of existing correlations for air from different authors. The passage loss model was validated by Emilie [5] and compared against the improved passage loss model by Baines [4]. However, the lack of published data with detailed measurement of properties of interest inside the blade passage makes the validation of the individual loss models difficult. Also, the other loss models (incidence loss, windage loss and tip clearance loss) are validated against the data from the radial turbines with low pressure ratio gas turbine and turbocharger [4]. At the time of writing, there were no published loss models specifically developed for refrigerants. Thus, the loss models for air were used for the performance analysis for refrigerants and validated by comparison to published turbine performance data for air [10] and R245fa [11].

The design parameters from a commercial gas turbine unit and an academic research turbo-expander unit are presented in Table 6.1 for the validation purpose. The numerical model in this study does not take into account of the losses across the nozzle. Whitfield [6] reported that the overall turbine performance is very insensitive to the nozzle loss coefficients based on the potential range of nozzle loss coefficients calculated by Benson [12] and Johnston [13]. The simulated turbine total-to-static efficiency from the turbine empirical loss model and the turbine efficiency at the design point are shown in Table 6.1. The turbine empirical loss model over-estimates the turbine performance in the range of 2 to 4%. The discrepancy is attributed to the lack of loss coefficients of the nozzle and the vaneless space between rotor and nozzle.

This turbine model provides an estimation of the potentially highest turbine efficiency with the minimal input of turbine dimension and the minimal computational effort. Hence, this analysis technique is integrated into the SMC adaptive strategy and this technique is applied to determine the turbine performance for different selected turbines/operating conditions/working fluids provided that the turbine performance map is not available. A more comprehensive performance analysis is required if the selected turbine has fallen into the acceptable range of isentropic efficiency. The comprehensive analysis is a computational fluid dynamic (CFD) analysis, which is presented in the next chapter.

Table 6.1: Operating Conditions of Selected Cases

	Sundstrand Power System T-100 (Commercial unit) [5, 10]	ORC-Turbo Expander [11]
Fluid	Air	R245fa
Rotational Speed (rev/min)	106588	20,000
Inlet temperature (K)	1056	353
Inlet pressure (kPa)	580	732
Total-to-static pressure ratio (-)	5.73	4.11
Mass flow rate (kg/s)	0.33	1.58
Rotor blade number (-)	16	12
Rotor inlet radius (mm)	58.96	70
Rotor outlet tip radius (mm)	44.18	40.6
Rotor outlet hub radius (mm)	17.69	21
Rotor inlet blade height (mm)	5.47	4.275*
Rotor height (mm)	20.65	33.67*
Rotor inlet absolute flow angle (deg)	76.7*	71.6*
Rotor inlet relative flow angle (deg)	-36.8*	-18.4*
Total-to-static efficiency (%)	86	76
Efficiency from numerical model (%)	87.8	80

**The given value is calculated from the numerical correlations for optimal operating condition due to the lack of information from the published literature.*

6.4 References

1. Rohlik, H.E., *Analytical determination of radial inflow turbine design geometry for maximum efficiency*. 1968: National Aeronautics and Space Administration.
2. Glassman, A.J., *Computer program for design analysis of radial-inflow turbines.* 1976.
3. Aungier, R.H., *Turbine aerodynamics: axial-flow and radial-inflow turbine design and analysis*. 2006: ASME Press.
4. Moustapha, H., et al., *Axial and Radial Turbines*. 2003: Concepts Eti.
5. Ventura, C., et al., *Preliminary Design and Performance Estimation of Radial Inflow Turbines: An Automated Approach.* Journal of Fluids Engineering-Transactions of the Asme, 2012. **134**(3).
6. Whitfield, A. and N.C. Baines, *Design of radial turbomachines.* 1990.
7. Ghosh, S.K., R. Sahoo, and S.K. Sarangi, *Mathematical Analysis for Off-Design Performance of Cryogenic Turboexpander.* Journal of fluids engineering, 2011. **133**(3).
8. Wasserbauer, C.A. and A.J. Glassman, *FORTRAN program for predicting off-design performance of radial-inflow turbines.* NASA Technical Paper, 1975(TN D-8063).
9. Daily, J. and R. Nece, *Chamber dimension effects on induced flow and frictional resistance of enclosed rotating disks.* Journal of Basic Engineering, 1960. **82**: p. 217.
10. Jones, A.C., *Design and Test of a Small, High Pressure Ratio Radial Turbine.* Journal of Turbomachinery, 1996. **118**(2): p. 362-370.
11. Kang, S.H., *Design and experimental study of ORC (organic Rankine cycle) and radial turbine using R245fa working fluid.* Energy, 2012. **41**(1): p. 514-524.
12. Benson, R.S., *A review of methods for assessing loss coefficients in radial gas turbines.* International Journal of Mechanical Sciences, 1970. **12**(10): p. 905-932.
13. Benson, R., *Paper 16: An Analysis of the Losses in a Radial Gas Turbine.* Proceedings of the Institution of Mechanical Engineers, Conference Proceedings, 1965. **180**(10): p. 41-53.

7.0 CFD Analysis of Radial Inflow Turbine

The aim of this thesis is to present the SMC-DTR approach for low temperature resources, and the main contribution of this thesis is to develop the key component, SMC adaptive strategy. One of the critical analysis techniques of the SMC adaptive strategy is the computational fluid dynamics (CFD) analysis for the radial flow turbines. This chapter presents the numerical method used in evaluating the aerodynamic performance of the radial inflow turbine by conducting three dimensional flow field analysis across the nozzle and rotor blade passage. The performance study uses a commercial CFD tool, namely ANSYS. The performance analysis involves five basic steps; generation of solid model, meshing, setup of physics and boundary conditions, solving Navier-Stokes equations, and post-simulation analysis. The solid models of the nozzle and rotor are generated using ANSYS Blade-Gen, or imported from another computer-aided drawing (CAD) package. Meshes are generated for the flow field across the nozzle and rotor blade passages using ANSYS-Turbo Grid. The boundary conditions and the flow domain are defined using ANSYS-CFX, and the Navier-Stokes equations are solved using the in-built numerical schemes. The velocity vector field and distribution of thermodynamic properties across the blade passage are analysed. A search of published literature reveals that only one gas turbine with sufficient geometry and data to be used in the case study. A case study is then performed on the gas turbine (which has been designed and developed for a Sundstrand Power Systems T-100 Multipurpose Small Power Unit), and the CFD model is validated by comparing the simulated performance against the experimental data.

7.1 Introduction

Numerical modelling of turbine performance can be classified into meanline analysis, two-dimensional fluid flow study, three-dimensional inviscid fluid flow analysis, and three-dimensional viscous flow study. The meanline analysis was discussed and presented in the previous chapter. Two-dimensional inviscid flow analysis in the blade-to-blade plane simplifies the complex three-dimensional fluid dynamic problem onto the blade-to-blade plane by ignoring the secondary flow. The secondary flow develops as a result of migration of low momentum boundary layer fluid across the stream surfaces [1]. The validity of this approach is questionable when the flow separation effect is significant, which is a typical phenomenon in compressors or in turbine part-load operation. This approach is less popular with the advancement in lower cost computational power. This approach is not integrated into the SMC adaptive strategy as the three dimensional flow analysis can provide a better estimation of the flow field with the similar amount of computing time and computational power.

Three-dimensional flow analysis is usually performed at the end of the turbine design process, to finalize the aerodynamic profile of the nozzle and rotor blade, and to optimize the turbine performance. The flow analysis is sometimes simplified by neglecting the viscosity effect of the fluid flow to reduce the computational effort. Current CFD packages such as ANSYS and STAR-CCM+ allow the calculation of the flow field considering the viscosity effects. The 3-D flow field analysis using a numerical scheme is able to provide the flow pattern which is difficult to measure experimentally. The onset of the separation along the suction surface within the blade passage at part-load condition, and the Coriolis's effect on the main flow that leads to the secondary flow pattern, can be studied and investigated using the CFD tools. The fluid flow field can be determined by solving the Navier-Stokes equations. The Navier-Stokes equations can be solved using two different methods: direct numerical solution (DNS) or simplification of the Navier-Stokes equations with different turbulence model. The DNS for Navier-Stokes equations is feasible for low Reynolds number with the increasing computing power in recent years. However, the DNS at high Reynolds number still proves to be a challenge, and an appropriate turbulence model has to be selected to simplify the numerical calculation process. The working fluids in ORC systems typically have a low viscosity with high Reynolds number. Hence, a turbulence model has to be selected based on the modelling requirements. For example, the k-ε model is selected to minimize the computational effort

while the RANS model is chosen to maximize the accuracy in predicting the onset of the flow separation zone.

The objective of this chapter is to present the CFD approach in predicting the flow field and stage performance of the radial inflow turbine using the commercial CFD package, ANSYS ver15.0. The CFD analysis approach is the critical component in the SMC adaptive strategy to predict the performance of the selected turbines before a turbine re-design is performed. This chapter presents the five basic steps in estimating the turbine performance: generate the solid model, mesh the flow domain, set up the boundary condition, solve the Navier Stokes equations, and analyse the simulation result. An industrial radial gas turbine is presented as the subject of the case study. The industrial gas turbine has been designed and developed for the Sundstrand Power Systems T-100 Multipurpose Small Power Unit. The turbine performance predicted using the CFD approach is compared to the experimental data in order to validate the CFD model before the numerical model can be used for extended study and analysis.

7.2 CFD Methodology

Figure 7.1 illustrates the 5 basic steps for numerical analysis of a radial inflow turbine. A commercially available single stage radial inflow turbine, originally developed for use in the Sundstrand Power Systems T-100 Multipurpose Small Power Unit with nominal power output of 37 kW with capability up to 75 kW was selected for the case study [2]. The geometry of the nozzle and rotor was published in the open literature [3]. The experimental data of the gas turbine is available from the designer in his publication [2]. The simulated performance data from the CFD model was compared to the experimental data to validate the CFD model.

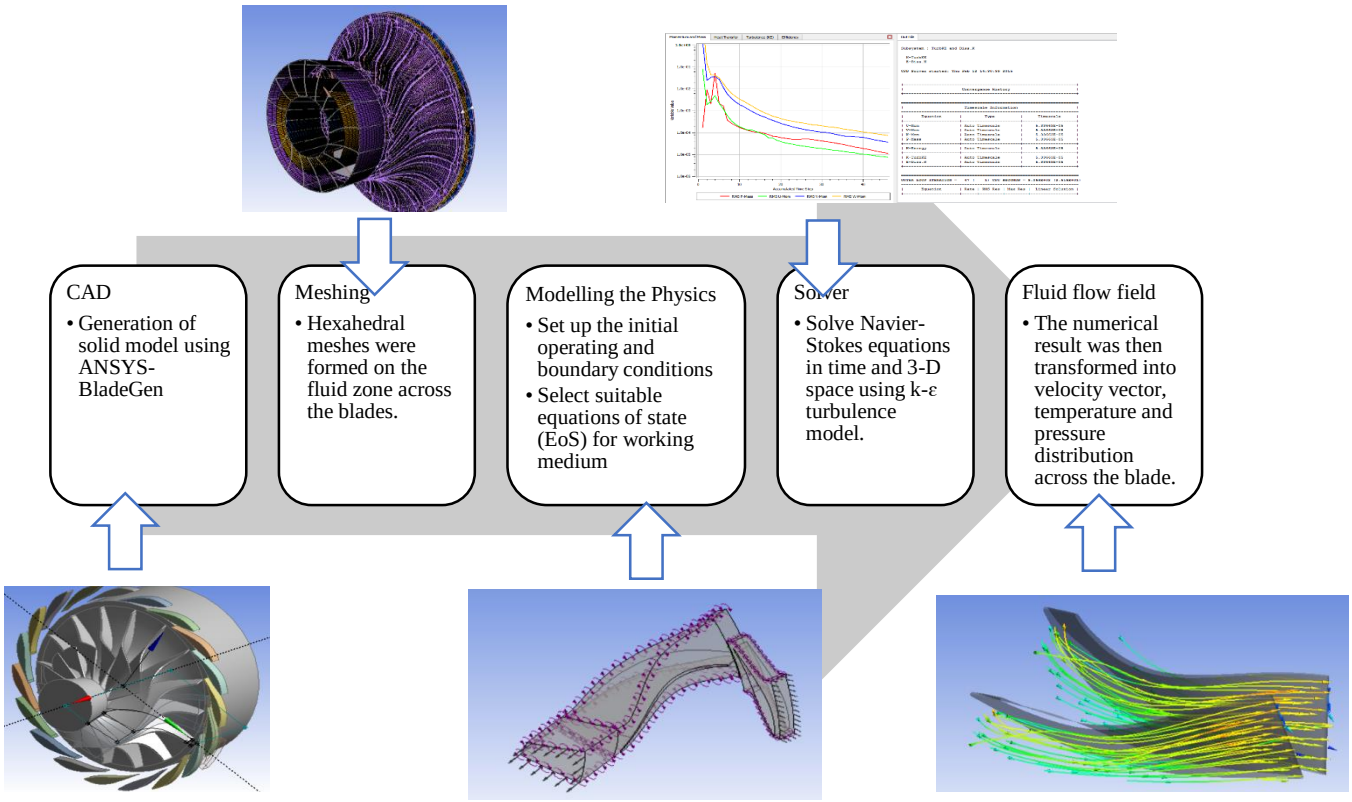

Figure 7.1: Overall procedures of CFD simulation using ANSYS Turbomachinery Package

7.2.1 Generation of Solid Models

The principal dimensions, and the distribution of blade angle, blade thickness, and wrap angle of the nozzle vanes and rotor blade are published by Emilie [3]. A solid model is required for the CFD analysis. The solid model of the rotor wheel can be developed using ANSYS Blade-Gen or the solid model can be imported from other computer aided drawing (CAD) packages. Both of the solid models of the nozzle vanes and the rotor wheel are generated using ANSYS Blade-Gen. The distribution of wrap angle, blade angle, and blade thickness were defined as a function of meridional distance from leading edge to trailing edge of the rotor blade, as shown in Figure 7.2. The leading edge and the trailing edge of the rotor blade was defined as ellipse type with elliptic ratio of 2.0 and 1.0, respectively. The same process was applied on the nozzle vanes by defining the principal dimension, distribution of blade angle, wrap angle, and thickness of nozzle vanes from the leading edge to the trailing edge. The solid model of the nozzle vanes and the rotor wheel was generated by ANSYS Blade-Gen and coupled in ANSYS Geometry, as shown in Figure 7.3.

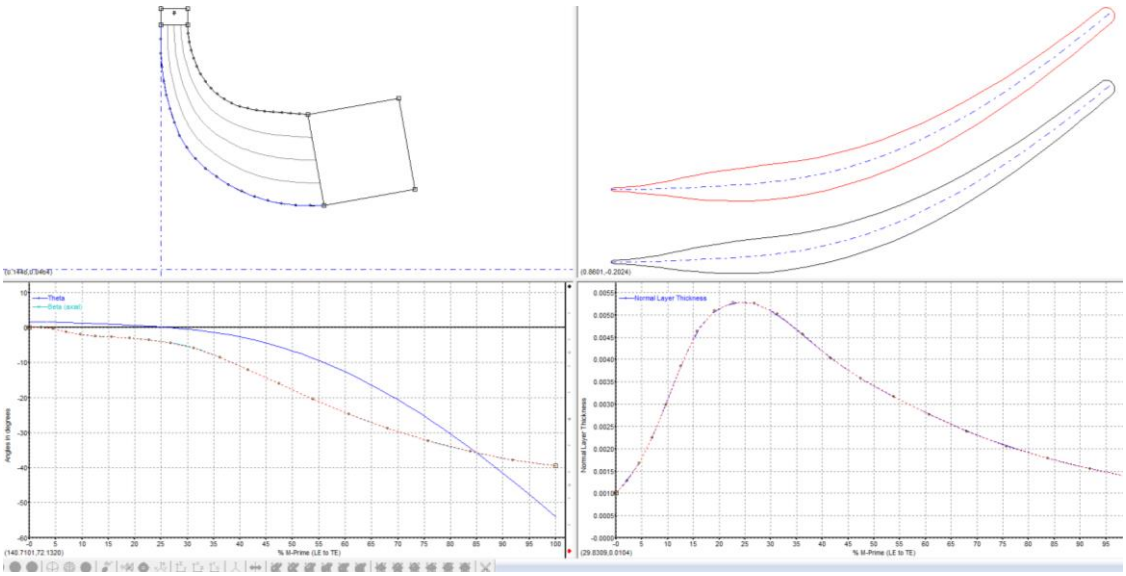

Figure 7.2: Meridional view of rotor (top left), rotor blade in blade-to-blade view (top right), distribution of blade angle and wrap angle as a function of meridional distance from leading edge (bottom left), and distribution of blade thickness from leading edge (bottom right)

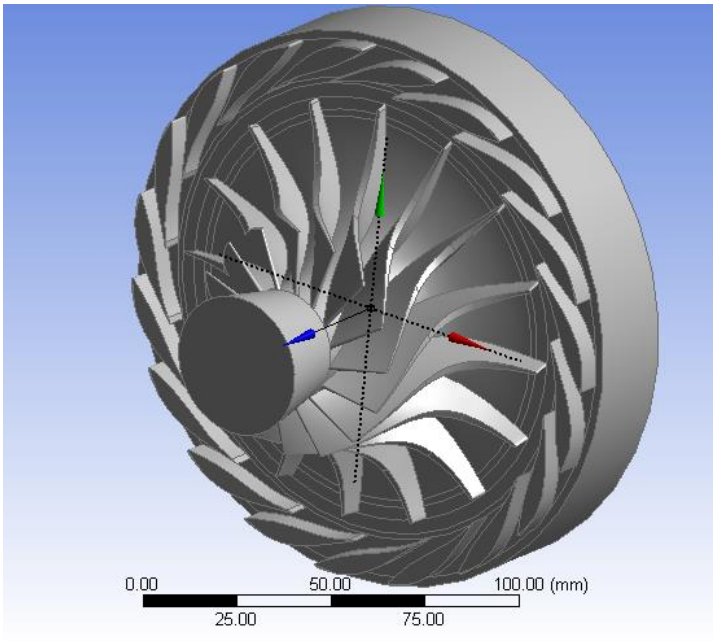

Figure 7.3: Solid model of nozzle vanes and rotor wheel in ANSYS Geometry

7.2.2 Meshing

Meshing of the flow path across the rotor blade passage is a challenging issue as the selection of the types of grids, size and geometry of the grids, placement of the grids and density of the grids determine the quality of the meshes. The quality of the meshes can be quantified by face angle, element volume ratio, mesh volume, edge length ratio and connectivity number. In this analysis, any meshes which do not fall into the recommended range for the measured parameters are considered to be ill-meshes, as the accuracy of the solution by the CFX solver would be compromised. The meshing process was conducted using ANSYS Turbo grid instead of ANSYS Meshing module. ANSYS Turbo grid provides an improved platform for automating the grid generation across the blade passage, the tip and both the leading and the trailing edges with manual control of the placement control points [4].

The solid model of the nozzle and rotor was imported from the ANSYS BladeGen. The solid zone and the fluid zone were defined in Turbo-Grid. Virtual topology was formed along three surfaces (hub, shroud, and mid-span) prior to meshing to provide virtual frameworks to position the mesh elements. The arrangement of the block elements across the topology formation determines the maximum skew of the topology blocks, which determines the maximum skew of the mesh elements in three-dimensional workspace [5]. Automatic topology and meshing (ATM Optimized) was chosen to allow the program (ANSYS Turbo-Grid) to select a suitable topology for the blade passage based on the blade angle, the presence of the splitter blades, and the type of the leading edge and the trailing edge. The inlet domain of the rotor is sometimes undetectable during the formation of the topology, which can be solved by moving the control points upstream of the rotor inlet closer or further from the rotor blade. An intermediate layer of topology was formed between the shroud layer and the hub layer to guide the meshing by providing a path for the generation of the mesh elements along the hub and the shroud. An increased number of intermediate layers is usually recommended for turbine blades with significant variations from the hub to the shroud, such as long blades in axial turbines with significant variations in the twist and reaction values along the blade. One intermediate layer of topology was found sufficient between the hub and shroud layers in this analysis. Meshing can be automated once the topology is finalized. The node count of the meshes can be pre-defined as coarse, medium, or fine, with an approximate node count of 20,000, 100,000 and 250,000 respectively. A grid t study was performed and described in the subsequent section to assure the simulation result is grid independent.

A number of settings allows the control of the generation of O-grid blocks normal to the blade surface, namely *proportional to mesh size*, *edge refinement factor*, and *first element offset*. The details of the setting can be found from the Turbo-Grid user manual [5]. *Proportional to mesh size* was chosen to maintain the similar O-grid expansion ratio based on the pre-defined node count. *Edge refinement factor* does not maintain a similar O-grid expansion rate based on the previously defined mesh size, requiring the user's input to control the edge refinement parameters for different mesh size. *First element offset* focuses on the mesh quality at the near-wall height, which is not a crucial element in determining the overall turbine performance in this study.

The distribution of the mesh elements along the blade in the spanwise direction can be controlled with different approaches, namely *element count and size*, *boundary layer*, *expansion rate*, *uniform*, *proportional* (only valid if the ATM Optimized topology was selected), and *end ratio* (valid with traditional topology setting only). The method *proportional* is the default method to automate the grid generation and distribution in the spanwise direction along the blade. Proportional factor was set at one by default and can be manually manipulated by the user to control the mesh resolution in the spanwise direction. Different configurations of proportional factor along the blade passage to generate high quality mesh elements were investigated. The optimal proportional factor along the passage was chosen to be 1.6 to result in minimum amount of ill-meshes for element volume ratio and edge length ratio across the blade passage, and minimum amount of ill-meshes in element volume ratio at the passage inlet, as shown in Table 7.1.

Table 7.1: Parametric study of proportional factor in ANSYS Turbo Grid

Proportional Factor	*1*	*1.5*	*1.6*	*1.8*
Passage				
Maximum element volume ratio	9.339	6.5	5.7	13
Number of bad elements	2.66%	1.76%	1.67%	2.30%
Maximum edge length ratio	196.4	140	140	174
Number of bad elements	0.30%	0.02%	0.02%	0.04%
Inlet				
Maximum element volume ratio	6.66	4.34	4.27	9.98
Number of bad elements	3.50%	2.90%	2.90%	3.90%

The selection of factor base and factor ratio within the *proportional to mesh size* setting determines the number of elements across the boundary layer and along the leading

edge/trailing-edge. Different configurations of the factor ratio and the factor base were investigated to minimize the skew of the mesh elements. The boundary layer refinement control was set to *proportional to mesh size*. Two factor base values, 0 and 0.5, and four factor ratios, 1.4, 1.5, 1.6, and 2.0, were investigated in Tables 4.2 and 4.3, respectively. Larger amount of bad elements was observed when the factor base is higher, at 0.5. Four factor ratios were investigated, and the factor ratio between 1.4 and 1.6 were observed to provide similar result. When the factor ratio was set at 2, higher number of bad elements was observed for element volume ratio and edge length ratio along the passage, whereas lower number of bad elements was observed for element volume ratio at the passage inlet, as shown in Table 7.3. The factor base and factor ratio were chosen as 0 and 1.6 respectively in the study. The number of nodes and the number of mesh elements were determined to be 235,773 and 213,050 respectively for a single blade row configuration.

Table 7.2: Parametric study of factor base in ANSYS Turbo Grid

Factor Base	*0*	*0.5*
Passage		
Maximum element volume ratio	5.7	14
Number of bad elements	1.67%	3.40%
Maximum edge length ratio	140	335
Number of bad elements	0.02%	0.30%
Inlet		
Maximum element volume ratio	4.27	10.66
Number of bad elements	2.90%	5.00%
Maximum edge length ratio		143
Number of bad elements		0.16%

Table 7.3: Parametric study of factor ratio in ANSYS Turbo Grid

Factor Ratio	*1.4*	*1.5*	*1.6*	*2*
Passage				
Maximum element volume ratio	5.86	5.86	5.86	5.7
Number of bad elements	1.20%	1.20%	1.20%	1.67%
Maximum edge length ratio				140
Number of bad elements				0.02%
Inlet				
Maximum element volume ratio	4.4	4.4	4.4	4.27
Number of bad elements	3.30%	3.30%	3.30%	2.90%

7.2.3 Details of Modelling the Physics

Turbomachinery mode in ANSYS CFX allows turbomachinery simulations to be quickly set up by automatically setting up the domains and boundary interfaces once the basic parameters are defined by the users. Steady state analysis is chosen over transient analysis as the overall turbine performance can be determined accurately with a steady state model while greatly reducing the computational effort. The tip clearance loss was reported to contribute up to 0.2% and 1.6% losses of total-to-total efficiency for every 1% increase in axial clearance and radial clearance, respectively [6]. Hence, the effect of the tip clearance at the shroud is included during the simulation to contain the effects of the leakage losses across the tip clearance.

The effect of the heat transfer is important to model the fluid flow temperature distribution in gas turbine due to the high inlet fluid temperature over 1,000 K. The in-built heat transfer model includes *none, isothermal, thermal energy, total energy,* and *fluid dependent* [7]. The modelling of heat transfer is neglected if the heat transfer model is set as *none*, and this mode is only applicable if the variation in temperature along the flow passage, and the temperature difference between the flow and the surface in contact is negligible. *Isothermal* mode is applied only if the fluid can be modelled as ideal gas and the fluid properties are temperature dependent. *Thermal energy* mode models the transport of enthalpy across the fluid domain but the flow kinetic energy is neglected. *Total energy* mode models the transport of enthalpy considering the flow kinetic energy, with the transport equation as below [8].

$$\frac{\partial(\rho h_t)}{\partial t} - \frac{\partial \rho}{\partial t} + \nabla \cdot (\rho U h_t) = \nabla \cdot (\lambda \nabla T) + \nabla \cdot (U \cdot \tau) + U \cdot S_M + S_E \qquad (18.1)$$

Where ρ is density, h_t is total enthalpy, t is time scale, T is temperature, U is vector of velocity in x, y, z coordinates, τ is shear stress, λ is thermal conductivity, S_M is the momentum source, and S_E is the energy source. The term $\nabla \cdot (U \cdot \tau)$ represents the internal heating or work attributed to the viscous stress of the fluid, and the term $U \cdot S_M$ represents the work attributed to the external momentum source. The transient term in equation (7.1) is omitted for the steady state analysis in this study. The in-built model - *total energy* mode was chosen for the subsequent modelling as this approach takes account of the flow kinetic energy since the investigated turbine is a high speed turbine during the operation.

A proper selection of the turbulence model is important to adequately model the formation of eddies and the separation flow behaviour, which gives rise to the secondary flow loss across the blade passage and the efficiency of the turbine. Two turbulence models are available in the steady state analysis, namely k-epsilon (k-ε) model and shear stress transport (SST) model. The k-ε model is a widely used two-equation turbulence model for industrial applications, where k represents the turbulence kinetic energy and ε represents the turbulence eddy dissipation. The values of k and ε are determined from the differential transport equations of the turbulence kinetic energy and turbulence dissipation rate. These equations are available in the ANSYS CFX Theory Guide [8]. The SST model provides a more accurate estimation of the onset of the flow separation along the blade passage with a smooth surface under adverse pressure gradients, which is commonly encountered in turbomachinery flows, especially in pump and compressors due to the strong diffusion of flow near the leading edge of the blade. The flow separation effect is, however, less significant in turbines at close-to design point as the flow acceleration thins the boundary layer. In both settings, the boundary layers are resolved with a fine mesh near the walls. A favourable pressure gradient is typically encountered in turbine flows, where the boundary layer does not grow quickly [9]. A test case was investigated using the k-ε model and the SST model to evaluate the accuracy and the required computational effort under the similar physics settings and solver setting. The simulation was performed for a flow across turbine stage (nozzle and rotor) under steady state analysis using a quad core I7 machine with 3.4GHz and 16 GB installed memory. The simulation was performed using local parallel environment with 6 partitions to accelerate the simulation process. The simulation was performed for the following test case:

- Turbine inlet stagnation temperature: 800˚C
- Turbine inlet stagnation pressure: 500 kPa
- Turbine outlet static pressure: 100 kPa
- Turbine shaft speed: 125,000 rev/min
- Assume no clearance gap at shroud and hub

Two turbine parameters were used as the benchmark to compare the simulation result, which are total-to-total isentropic efficiency, and static temperature at the rotor outlet. The result in Table 7.4 shows that both turbulence models produce a very similar result, with deviation less than 0.5%. The velocity vector of the flow field was illustrated in Figure 7.4 to compare the accuracy of both model in estimating the separation zone.

Table 7.4: Comparison of SST and k-ε models

Target node count	*Efficiency*	*Temperature (˚C)*
SST	59.79	827.20
k-ε	59.59	827.85

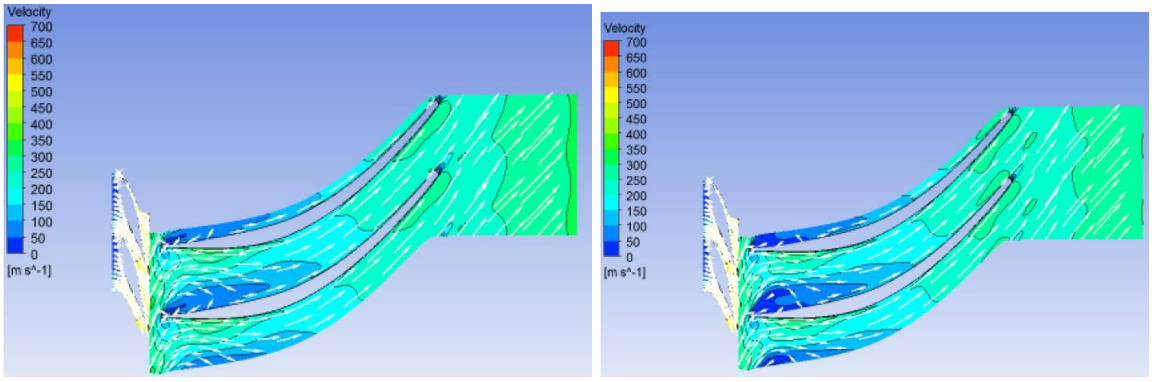

(a) (b)

Figure 7.4: Velocity vector of the turbine flow field using SST model (a) and k-ε model (b)

The result shows that the onset of the separation and the recirculation zone within the blade passage using two different turbulence models are similar. The simulation with the SST model took over 8 clock hours whereas the simulation with the *k-ε* model took less than 3 clock hours for each simulation. The *k-ε* model was selected as the model provides a highly accurate estimation of the turbine performance with fairly accurate prediction of the onset of the flow separation at off-design condition, while requiring a reasonable computational effort.

The domain interface between a stator and a rotor has to be specified to determine the type of analysis at the interface. Three mixing models are available, namely *frozen rotor, stage,* and *transient rotor-stator* [10]. The *frozen rotor* model is suitable for non-axisymmetric flow domains, mainly between the rotor and volute of a centrifugal type of machine. The model is robust and suitable for high blade counts, with less computational effort. The physics of the local flow, however, cannot be modelled accurately. The *stage* model averages the flux at the interface and provides this information for downstream analysis. The *stage* model does not predict the wake effects and the loading for tight coupling of components at the interface. The *transient rotor-stator* model is the most comprehensive model to accurately predict the physics of the transient flows at the interface. Large computational effort is the major drawback of the more comprehensive mixing models, as the required computational clock hours would be high depending on the complexity of the interface connection and the quality of the mesh elements.

The *frozen rotor* model was selected over the *transient rotor-stator* model as the local transient behaviour at the interface is not of the utmost importance and a reasonable computational effort was required for this study. The initial values and the boundary conditions for the simulation were set up in Table 7.5.

Table 7.5: Initial settings and boundary conditions for the radial turbine CFD simulation.

Parameters	*Value*
Machine type	Radial Turbine
Analysis Type	Steady State
Rotating Component	
Rotational Speed	106,588 rev/min
Wall Configuration	Tip Clearance at Shroud
Physics Definition	
Fluid	Air Ideal Gas
Model Data	0 atm
Heat Transfer	Total Energy
Turbulence Model	k-Epsilon
Boundary Templates	P-Total Inlet P-Static Outlet
Inflow Direction	Normal to Boundary
Stator-Rotor Interface	Frozen Rotor

7.2.4 Solver

The governing equations to be solved by ANSYS CFX are unsteady Navier Stokes equations. The transport equations were presented in their conservative forms, in terms of mass, momentum, and energy. The continuity equation, and the momentum equation were presented below, and the total energy equation was presented in equation (1), where $\otimes$ is cross product.

$$\frac{\partial \rho}{\partial t} + \nabla \cdot (\rho U) = 0 \tag{18.2}$$

$$\frac{\partial (\rho U)}{\partial t} + \nabla \cdot (\rho U \otimes U) = -\nabla p + \nabla \cdot \tau + S_M \tag{18.3}$$

The modelling was performed for flow across turbine stage under steady state analysis using a quad core I7 machine with 3.4GHz and 16 GB installed memory. The simulation was performed using local parallel environment with 6 partitions to accelerate the simulation process. The maximum root mean squared (RMS) residual is usually no higher than 5e-4 in the simulation. The details of the calculation of the residual values and the convergence criteria can be found in the CFX user's guide [11]. Convergence was achieved, and the residual values for the mass, momentum, energy, and the coefficients of turbulence model were shown in Figure 7.5.

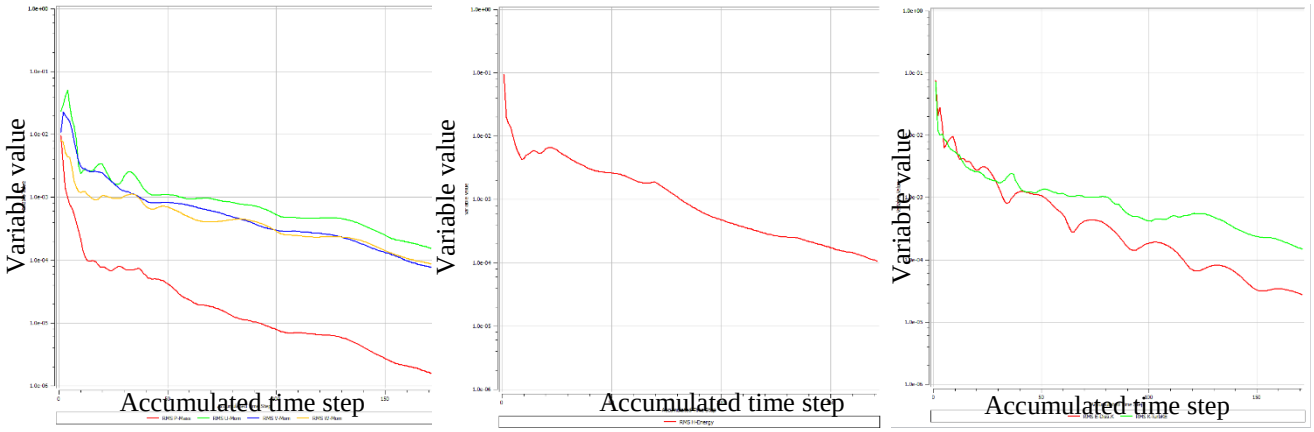

(a) (b) (c)

Figure 7.5: Residual plotting for mass balance and momentum (a), energy (b), and dissipation value and coefficient of turbulence model (k-ε) (c)

7.3 Grid Independence Study

A grid study was performed to assure that the simulation result is independent of the number of grids. The default target passage size is coarse (target node count of 20,000), medium (target node count of 100,000), and fine (target node count of 250,000). The grid study was performed using the following conditions:

- Turbine inlet stagnation temperature: 800˚C
- Turbine inlet stagnation pressure: 500 kPa
- Turbine outlet static pressure: 100 kPa
- Turbine shaft speed: 100,000 rev/min
- Assume no clearance gap at shroud and hub

The study was performed at different target node counts and the result was presented in Table 7.6. Two turbine parameters were used as the benchmark to compare the simulation result, which are total-to-total isentropic efficiency, and static temperature at the rotor outlet. The correlation between the target node counts and the turbine parameters was plotted in Figure 7.6. The result shows that the result is independent of the target node count once the target node count is over 150,000. Hence, the CFD simulation for the subsequent chapters is performed using the 'fine' target passage size with target node count of 250,000 for the nozzle vanes and the rotor blade passage.

Table 7.6: Grid independent study

Target node count	*Efficiency*	*Temperature (˚C)*
20,000	84.85	734.84
50,000	84.56	735.93
100,000	84.14	737.51
150,000	83.84	738.62
250,000	83.80	738.80
350,000	83.80	738.80

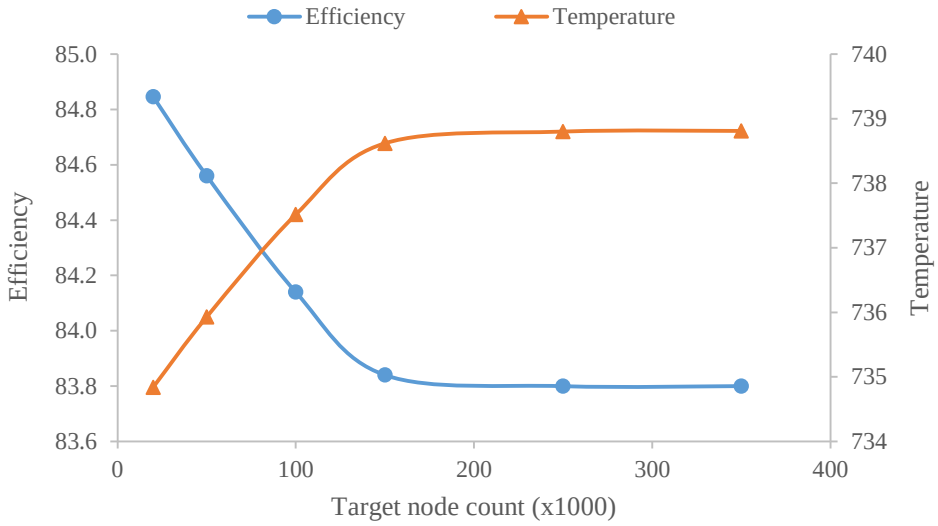

Figure 7.6: Residual plotting for mass balance and momentum (a), energy (b), and dissipation value and coefficient of turbulence model (k-ε) (c)

7.4 Validation of the CFD Model

The performance of the gas turbine was compared to the experimental data by A. C. Jones [2] to validate the CFD model with the aforementioned settings. The experimental data of the turbine efficiency was published by Jones as a function of total-to-static pressure ratio. Two types of turbine efficiency were available, total-to-total efficiency and total-to-static efficiency. The definition and the differences between the total-to-total efficiency and the total-to-static efficiency can be found in the turbomachinery text by Baines [9]. Both types of efficiency would be considered in this section. The experimental data by Jones was conducted in a test rig at an operating condition different than the design condition, in which the total temperature and the total pressure at the inlet are 477.6 K and 413.6 kPa respectively. The outlet static pressure was set at 72.4 kPa in the CFD model to determine the performance curve at the design pressure ratio, where the design pressure ratio is 5.7. The inlet condition was imposed at a distance equivalent to 50% of the inlet blade height and the outlet condition was imposed at the diffuser outlet. The total-to-static efficiency and the total-to-total efficiency from the numerical simulation was compared to the experimental data in Figure 7.7.

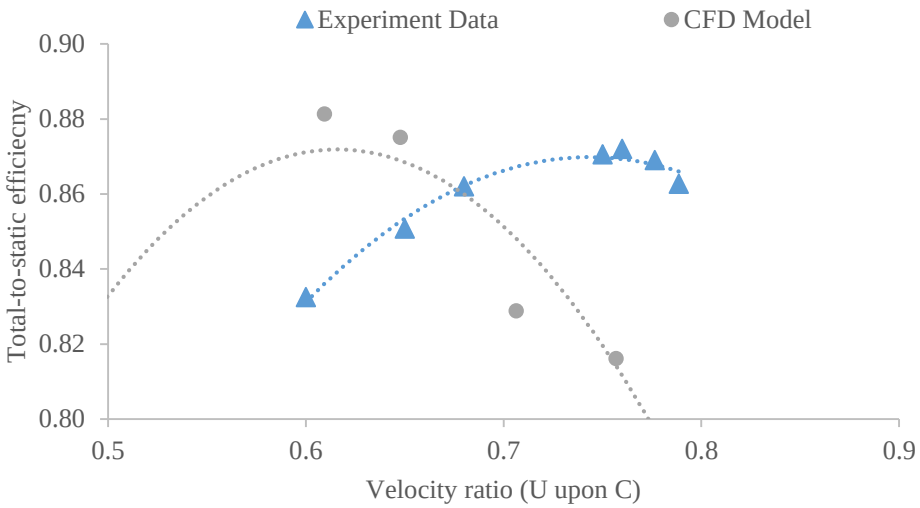

Figure 7.7: Comparisons of isentropic efficiency of the gas turbine from CFD simulation and experimental data in term of total-to-static efficiency

The general performance trend was reproduced in the CFD model, with the curve shifted to a lower velocity ratio. A very close agreement was observed for the peak efficiency and the off-design efficiency, where the error is less than 1%. The location of the peak

efficiency was estimated by the numerical simulation at velocity ratio of 0.6 whereas the experimental data shows the peak efficiency at the velocity ratio of 0.76. The shift might be attributed to the lack of details in the geometry of the trailing edge of the rotor wheel. The pressure recovery factor of the diffuser from the CFD model deviates slightly from the experimental data, and this further contributes to the deviation. The use of k-ε turbulence model might not predict the onset of the flow separation behaviour along the diffuser accurately, further reducing the efficiency in the numerical simulation. However, the shift in the optimal velocity ratio does not affect the SMC-DTR strategy, as the purpose of the CFD model is to estimate the turbine efficiency. The turbine performance map is integrated into the cycle analysis. The subsequent analysis was then conducted with the corrected CFD model assuming the absence of the diffuser.

7.5 Conclusion

The three-dimensional fluid flow analysis approach was presented with five basic steps, with solid modelling, meshing, modelling the physics, solving Navier Stokes equation, and result analysis. The proposed CFD approach was showcased using an industrial gas turbine, and the CFD model with the aforementioned settings was validated against the experimental data with agreement less than 1% in term of total-to-static efficiency. The proposed CFD model is then applied to investigate the turbine performance behaviour using different working fluids with real gas behaviour in the subsequent chapters.

7.6 References

1. Aungier, R.H., *Turbine aerodynamics: axial-flow and radial-inflow turbine design and analysis*. 2006: ASME Press.
2. Jones, A.C., *Design and Test of a Small, High Pressure Ratio Radial Turbine.* Journal of Turbomachinery, 1996. **118**(2): p. 362-370.
3. Sauret, E. *Open design of high pressure ratio radial-inflow turbine for academic validation*. in *Proceedings of the ASME 2012 International Mechanical Engineering Congress and Exposition*. 2012. Houston, Texas: American Society of Mechanical Engineers (ASME).
4. Patange, S. *ANSYS Turbomachinery CFD System - 14.5 Update (BladeModeler, TurboGrid, Vista, Vista-TF, CFD Solver, Turbo Post-processing).* in *ANSYS UK Convergence Conference*. 2013. UK.
5. *ANSYS TurboGrid User's Guide, Release 14.5*. 2012, ANSYS, Inc.: Canonsburg, PA 15317. p. 168.
6. Moustapha, H., et al., *Axial and Radial Turbines*. 2003: Concepts Eti.
7. *ANSYS CFX-Solver Modeling Guide, Release 14.5*. 2012, ANSYS, Inc: Canonsburg.
8. *ANSYS CFX-Solver Theory Guide, Release 14.5*. 2012, ANSYS, Inc. Release 14.5: Canonsburg. p. 372.
9. Japikse, D. and N.C. Baines, *Introduction to turbomachinery*. 1995: Concepts ETI.
10. *ANSYS CFX Reference Guide, Release 14.5*. 2012, ANSYS, Inc: Canonsburg. p. 328.
11. *ANSYS CFX-Solver Manager User's Guide, Release 14.5*. 2012, ANSYS, Inc.: Canonsburg. p. 190.

8.0 Similarity Analysis

The aim of this thesis is to present the SMC-DTR approach for low temperature resources, and the main contribution of this thesis is to develop the key component, SMC adaptive strategy. One of the critical analysis techniques in the SMC adaptive strategy is the similarity analysis approach. The known similarity analysis approach allows the prediction of the performance of turbomachines at rotor size and operating condition different from the original design. However, the known similarity approach is not capable to predict the turbomachines performance for working fluid different than the original design. The objective of this chapter is to investigate a number of parameter sets for the similarity analysis approach, and present the most feasible similarity analysis approach with suitable parameter set to scale a radial inflow turbine for working fluid different than the original design. Three different variable parameter sets were established for the similarity study, namely perfect gas, variable pressure ratio, and constant specific speed approach. These parameter sets were applied on a radial inflow turbine (originally designed and developed using air as working fluid) to establish the performance curves for two refrigerants: R134a and R245fa. The result from these parameter sets was compared to the performance map generated using the CFD analysis tools. The most feasible similarity model to predict the turbine performance at the optimal operating point and the non-optimal operating points for different working fluid was selected. The result shows that complete similarity cannot be achieved using two different working fluids, even at the best efficiency point. The differences in the fluid properties and the expansion ratio lead to the deviation in turbine performance parameters, velocity diagram, turbine's exit swirl angle, and entropy generation. A radial flow turbine performance correction chart was generated for R245fa to estimate the turbine's performance at higher expansion ratio as a function of volumetric ratio.

8.1 Introduction

The adaptation of an existing turbine for the ORC application using a different working medium is fundamentally subjected to the similitude of the design analysis of turbomachinery, which is also known as similarity concept. Non-dimensional parameters of turbomachines for similarity concept have been derived using the Buckingham Pi theorem. In turbomachinery there are numerous dimensionless groups possible from the seven fundamental variables, such as flow coefficient, head coefficient, power coefficient, and Reynolds number. These non-dimensional groups serve as fundamental parameters for turbomachines handling compressible or incompressible fluids. A number of other important turbine parameters include specific speed, specific diameter, and loading coefficients. The introduction of specific speed allowed the rapid development in the experimental testing of hydraulic turbines in the 1900s [1] and facilitated the selection of turbomachines' types for different applications [2]. The performance mapping using flow coefficient and loading coefficient has facilitated the preliminary design process for both axial flow turbines [3] and radial inflow turbines [4]. These parameters also allow turbomachinery designers to scale a turbine from one application to another application, with different wheel size, different inlet operating conditions, and different working mediums [5, 6].

Scaling of turbomachines using the previously discussed non-dimensional parameters is feasible if the machine is geometrically similar, which implies that the number of blades, blades thickness, blade angle, machine size, radii and operating clearance are scaled proportionally [6]. Scaling from large sizes to small sizes imposes some difficulties, attributed to the surface finish, the manufacturing limit and the increased cost for increased geometrical tightness at small size. The Reynolds number imposes the next major constraint, in which a correction factor has to be applied. A number of correction charts are recommended to take into account of the Reynolds number effect in the laboratory testing of centrifugal compressors at different operating conditions [7, 8]. The geometrical scaling of turbomachinery from one size to another requires the tip speed to be constant to maintain similar effects from windage loss, tip clearance loss, external losses and mechanical effects [6].

Scaling of turbomachines for different operating conditions within the same working fluid is a common practice in turbomachinery testing. The inlet operating condition is scaled to reduce the pressure and temperature into the compressor or the turbine during the performance test. This practice can reduce the operational cost and the capital cost of the testing

equipment. The Reynolds number cannot be scaled and a correction factor is required either from the published literature or based on in-house knowledge.

The increasing interest in Organic Rankine Cycles has prompted the need for ORC turbines that can operate with various working mediums. The most common working fluid in existing commercial installations is n-Pentane (working fluid patented by ORMAT) [9]. Other working fluids are actively proposed and recommended under different conditions for a better thermodynamic cycle efficiency [10] and a more cost-efficient design of heat exchanger [11]. The testing of the turbine, however, is not a simple task. A full scale ORC set-up is favorable for turbine performance test but it imposes high design, development, and installation cost and efforts in the concerns of system layout, pump, heat exchanger and piping. Refrigerants typically introduce some side effects to either the environment, atmosphere, and health and safety issues. The refrigerants have to be sealed properly with minimal leakage, which further increases the operational cost of the test facility. A simple compressed air test bench is favorable as the compressed air is safe to be released to the atmosphere without any environmental issues. The testing via compressed air, however, might introduce some important deviations, as the real gas effects cannot be accounted accurately. The variation of density of real gas across blade passage during the expansion process and the machine Reynolds number cannot be scaled precisely from one fluid to another, which further limits the similitude using real gas. The lack of published correction chart for Mach number and Reynolds number for different working mediums has further limited the application of the similarity concept. These issues make it difficult for the turbomachinery designers or the engineers to apply the turbine performance curve generated using compressed air to an application using real gas, such as n-Pentane.

This chapter explores the feasibility of utilizing the similarity concept to estimate the turbine performance using real gas. Three different approaches using the similarity concept were proposed to scale air performance data to generate performance curves for two refrigerants, namely R134a and R245fa. A full computational fluid dynamic (CFD) analysis was then performed to generate the performances curves for the selected refrigerants. The approaches using the similarity concept were then compared to the result from the CFD analysis. The most feasible approach in scaling a turbine from air to refrigerants was selected. The accuracy of the performance prediction through the similarity analysis of the ORC turbomachine was estimated. The deviation in turbine's performance for different working fluids was presented and discussed.

8.2 Methodology

An industrial gas turbine with published turbine geometry [12] was selected for this study. The selected gas turbine was initially designed for Sundstrand Power Systems (SPS) T-100 Multipurpose Small Power Unit (MPSPU) with a single-shaft configuration to accommodate the ground-based auxiliary power application [13]. The nominal power of the selected turbine is 37 kW with a growth capability up to 75 kW [13]. A CFD model was previously conducted on the gas turbine using air as the working medium and the result from the numerical modelling was compared to the experimental data in Chapter 4 [13, 14]. The result from the CFD model agreed with the experimental data with less than 1% error in term of total-to-static efficiency. The CFD method was employed in this Chapter to generate the performance curve using two selected refrigerants, namely R134a and R245fa to validate the precision and accuracy of three different approaches of similarity concept in scaling the gas turbine from one working medium with ideal gas behavior to another working medium with real gas behavior.

The first part of this chapter re-generated the performance map of the selected gas turbine using air as the working medium and the performance curve served as a benchmark to determine the turbine performance using R134a and R245fa via similarity concept. The fluid properties of air were estimated using polytropic ideal gas equations. Three different approaches for similarity analysis were applied in this study. The performance curve scaled from the air data was plotted as a function of velocity ratio and specific speed for comparison.

The second part utilized the CFD methodology as outlined in Chapter 7 to generate the performance map of the selected gas turbine using R134a and R245fa. The performance map generated from the CFD tools was compared to the scaled performance map. The fluid properties of the refrigerants were extracted from REFPROP developed by National Institute of Standards and Technology [15], and the details of the mathematical expressions to represent the real gas behavior of the selected refrigerants should be referred to the work by Lemmon [16]. The three different approaches were compared to the performance map by CFD tools, and the accuracy of each method was discussed.

The third part discusses the deviation in the turbine's performance using different working fluids at the best efficiency point. The fluid flow field and the blade loading across the blade passage, the velocity diagram at the turbine inlet and the outlet, and the Reynolds number effect on the turbine's performance were investigated. The limitation of the selected

approach was presented, and a correction factor was generated to predict the best efficiency point of the turbine at higher expansion ratio (including super-sonic expansion).

8.2.1 Similarity Analysis

Similarity analysis, or similitude, provides a quick solution to scale a fluid machine for different operating conditions and different incompressible fluids without resorting to the full scale three-dimensional CFD methods. The performance of a turbomachine is dependent on the machine size, machine speed, and the fluid properties. Turbomachines are designed to handle either compressible or incompressible flow. Two extra terms are employed for turbomachines handling compressible flow, compared to the fluid machines handling incompressible flow, to take account of the compressible flow properties and the change of density during the expansion/compression process [3]. The performance parameters of a compressible flow turbomachine is expressed as a function of some variables, as listed in equation (1).

$$\Delta h_{0s}, P, \eta = f(N, D, \dot{m}, \rho_{01}, a_{01}, \gamma, \mu) \tag{19.1}$$

Where Δh_{0s} is the total-to-static enthalpy drop of the fluid across the turbine at the designed pressure ratio, P is the shaft power, η is the isentropic efficiency, and the efficiency is evaluated using the inlet stagnation and outlet static condition in this study, N is the rotational speed of the shaft, D is the diameter of the turbine wheel, $\dot{m}$ is the inlet mass flow rate, ρ_{01} is the density evaluated using the inlet stagnation condition, a_{01} is the sonic velocity at the inlet, γ is the specific heat, and μ is the dynamic viscosity. Buckingham π theorem was applied in equation (1) and three variables, density, ρ_{01}, shaft speed, N, and wheel diameter, D were selected to reduce the original expression into five dimensionless groups, as presented in equation (2). The full mathematical derivation should be referred to the work by Dixon [3].

$$\frac{\Delta h_{0s}}{a_{01}^2}, \eta, \frac{P}{\rho_{01} a_{01}^3 D^5} = f\left\{\frac{\dot{m}}{\rho_{01} N D^3}, \frac{\rho_{01} N D^2}{\mu}, \frac{ND}{a_{01}}, \gamma\right\} \tag{19.2}$$

The current dimensionless group is not an explicit formulation where the parameters, such as density and sonic velocity, cannot be measured directly. The dimensionless groups can be reduced to a number of variables which allows direct measurement from the experiments if the

compressible flow is modelled as a perfect gas. The dimensionless parameters were then reduced to a function of temperature and pressure at both inlet and outlet stations of the turbine, as listed in equation (3).

$$\frac{p_{02}}{p_{01}}, \eta, \frac{\Delta T_0}{T_{01}} = f\left\{\frac{\dot{m}\sqrt{\gamma R T_{01}}}{p_{01} D^2}, \mathrm{Re}, \frac{ND}{\sqrt{\gamma R T_{01}}}, \gamma\right\} \tag{19.3}$$

Where p is pressure, T is temperature, Re is machine Reynolds number, and R is the gas constant. The mathematical simplification of the dimensionless groups using perfect gas model are available from the works by Baines, Aungier, and Dixon [3, 5, 6]. Complete similarity can be achieved when

1) complete geometrical similarity is achieved [5, 6], in which the turbine is scaled up or scaled down proportionally, *and*
2) dynamic similarity is achieved, in which the velocity components and forces are equal [5].

8.2.2 Scaling Approach for Different Compressible Fluids

Three different approaches are trialed to scale the performance data using air into the performance map using refrigerants. The scaled performance curve from each approach was compared to the performance curve from CFD analysis and the accuracy for each method was evaluated.

The *perfect gas approach* assumes that the selected refrigerants, R245fa and R134a are perfect gas. Three non-dimensional groups are hold constant, which are pressure ratio, blade speed coefficient in equation (4), and mass flow coefficients in equation (5). The outlet static pressure of the refrigerants is determined given the pressure ratio of the turbine using air. Equation (4) is employed to calculate the shaft's rotational speed whereas equation (5) is applied to determine the mass flow rate at the turbine inlet.

$$\frac{ND}{a_{01}} = \text{constant} \tag{19.4}$$

$$\frac{\dot{m}}{\rho_{01} N D^3} = \text{constant} \tag{19.5}$$

The *variable pressure ratio approach* is similar to the perfect gas approach, but the pressure ratio does not remain constant. The pressure ratio using the selected refrigerants is determined using the correlation in equation (6). Equation (4) and equation (5) are then employed to determine the shaft speed and the mass flow rate, respectively.

$$\frac{\Delta h_{0s}}{a_{01}^2} = \text{constant} \tag{19.6}$$

The *constant specific speed approach* assumes constant pressure ratio, velocity ratio, υ and the specific speed, N_s for the selected working medium. The optimal velocity ratio and specific speed of a turbomachine typically fall in a narrow range of operation for maximum efficiency. Both are hold constant to determine the shaft speed and the mass flow rate by using equations (7) and (8), respectively.

$$\nu = \frac{U}{C_{is}} = \frac{U}{\sqrt{2\Delta h_{0s}}} \tag{19.7}$$

Where U is turbine inlet tip speed, and C_{is} is the fictitious velocity when the fluid is expanded in an isentropic process across a nozzle, with the pressure ratio equals to the pressure ratio of the turbine stage.

$$N_s = \frac{\omega\sqrt{\dot{m}/\rho_{exit}}}{\Delta h_{0s}^{\,0.75}} \tag{19.8}$$

Where ρ_{exit} is the density at the turbine outlet.

8.2.3 Evaluation of Aerodynamic Performance using CFD Analysis

CFD analysis was conducted on the gas turbine to determine the overall performance of the turbine stage and evaluate the fluid dynamics across the blade passage. The detail of the CFD approach was presented in Chapter 4. The following discussion in this section restates the application of the CFD approach for the case study in this chapter. The CFD analysis was

performed using ANSYS CFX version 15.0 and the overall procedure is illustrated in Figure 8.1. The solid models of both nozzle and rotor blades were constructed in ANSYS Blade Gen by providing the principal geometry and the distribution of the wrap angle along the meridional position. Hexahedral meshes were then applied on the fluid zone across both the nozzle and turbine blades. A two-dimensional topography was generated on the hub surface, mid span and close-to-shroud surface as a framework to smoothen the formation of meshes. The mesh quality was controlled by refining the mesh size and manipulating the number of elements across the boundary layer of the blade surface. The skew meshes were eliminated to avoid ill-meshes. The operating condition and the boundary condition were then set up at each stations (nozzle inlet, interface between nozzle and turbine rotor, and rotor outlet). A suitable working fluid was selected from the in-built fluid database or the fluid properties can also be imported from the external fluid database. *k-ε* model was selected to model the turbulence across the blade passage. The Navier-Stokes equations were solved numerically and the result was evaluated as velocity vector field and distribution of thermodynamics properties across the blade passage.

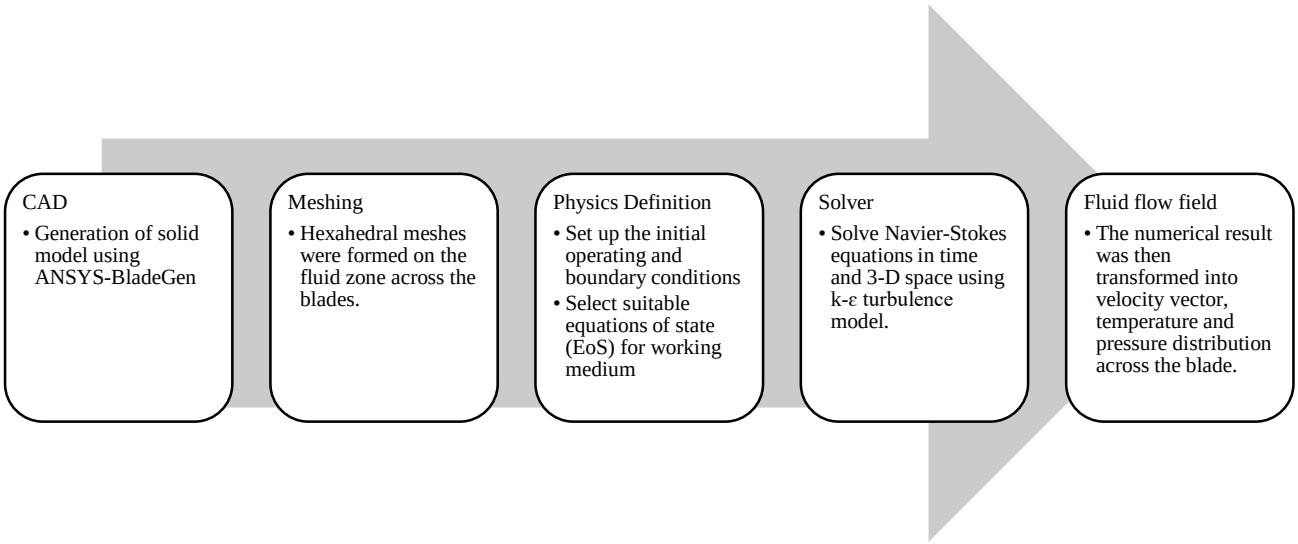

Figure 8.1: Overall procedures of CFD simulation using ANSYS Turbomachinery Package

8.3 Result

The three different approaches were applied to scale the performance curve from air to R134a and R245fa with the operating conditions in Table 8.1.

Table 8.1: Operating condition of air and selected refrigerants

	Unit	Air	R134a	R245fa
Molecular weight, M	g/mol	28.97	102.03	134.05
Inlet total temperature	K	1056.5	386	406.1
Inlet total pressure	kPa	580.4	2380	2334
Compressibility factor at inlet	-	1	0.786	0.630
Speed of sound at inlet	m/s	635	153.4	108.6
Outlet static pressure	kPa	101.3	420	420
Compressibility factor at outlet	-	1	0.931	0.904

R134a was superheated up to 35 degree before entering the turbine to avoid the formation of moisture at the end of the expansion process since it is a wet fluid. The scaled performance curves of R134a using the three approaches were compared to the result from the CFD analyses, in terms of velocity ratio in Figure 8.2, and specific speed in Figure 8.3. The three similarity approaches and the CFD analyses were compared in term of specific speed for R134a in Figure 8.3, and R245fa in Figure 8.4.

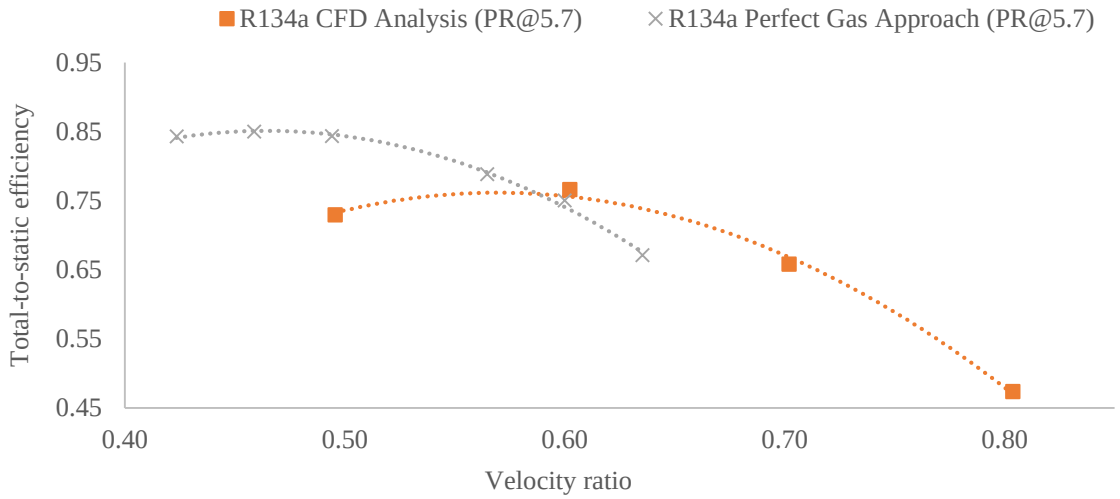

(a)

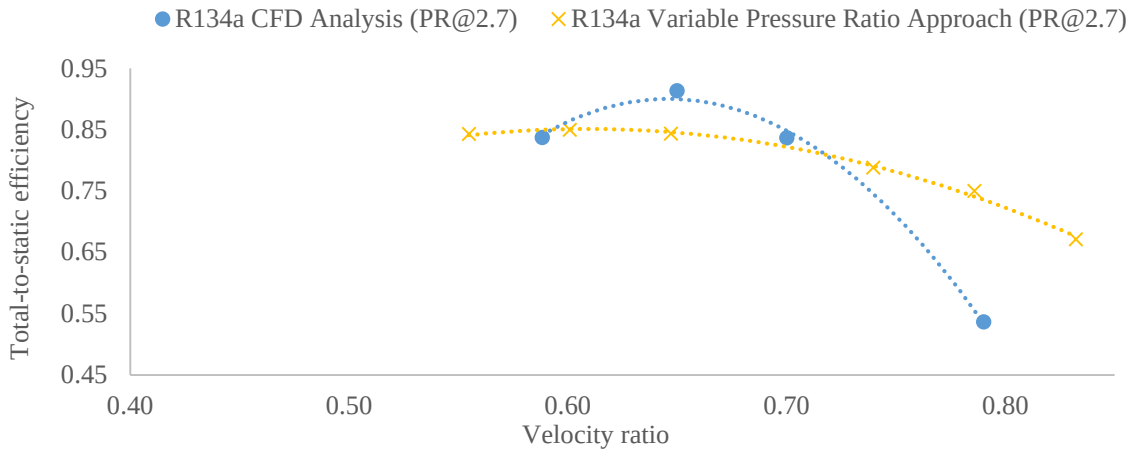

(b)

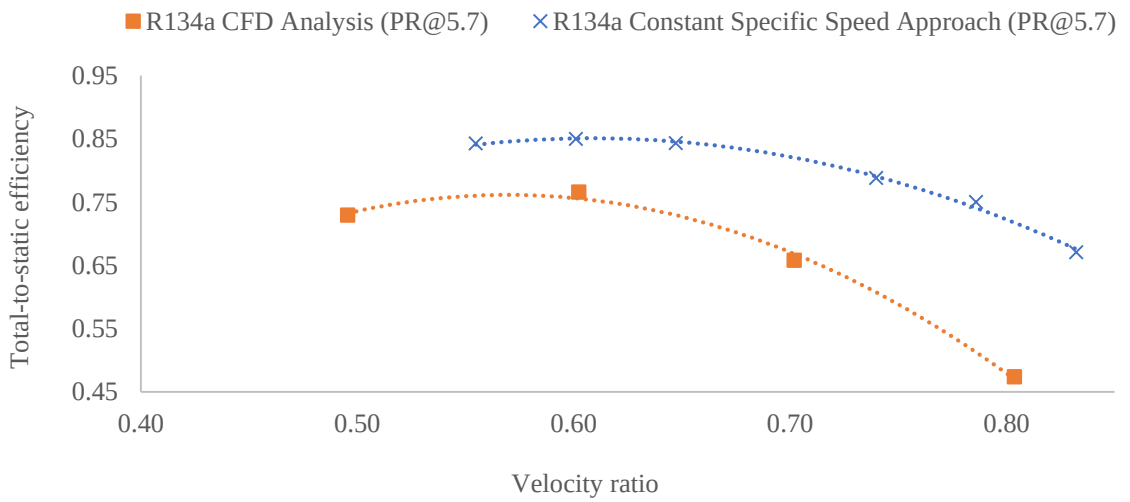

(c)

Figure 8.2: Comparisons of the three similarity approaches and the CFD analysis in term of velocity ratio for R134a

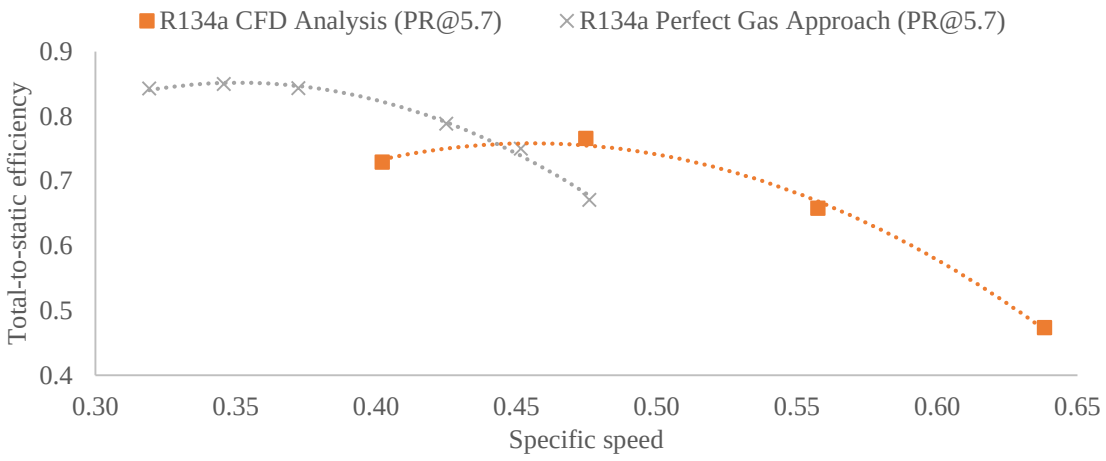

(a)

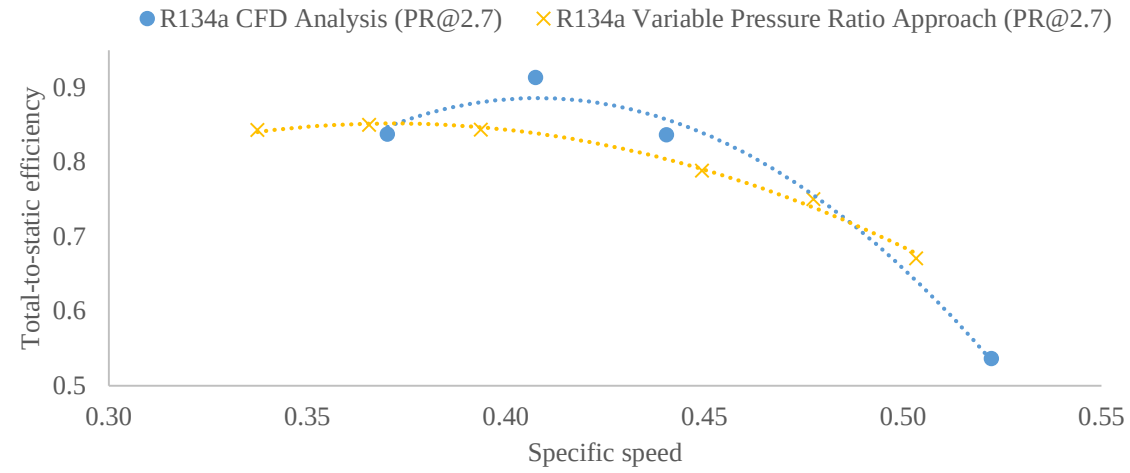

(b)

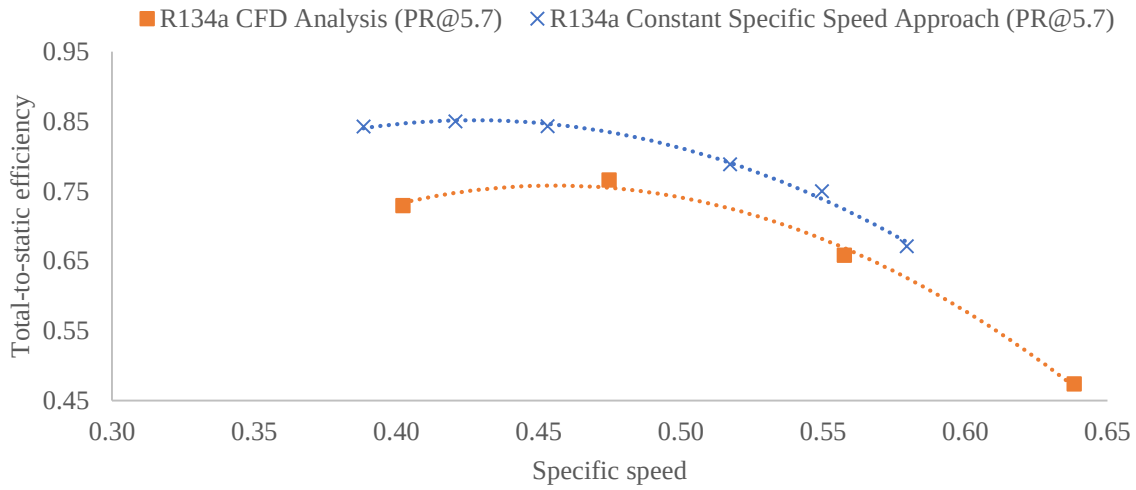

(c)

Figure 8.3: Comparisons between the three similarity approaches and the CFD analysis in term of specific speed for R134a

The *perfect gas approach* shows that the optimal velocity ratio is under-estimated. The optimal value from the *perfect gas approach* is 0.48, whereas the estimated value from the CFD analysis is 0.60. The optimal velocity ratio from the *variable pressure ratio approach* and the *constant specific speed approach* agrees closely to the estimated values from the CFD analysis, with an error less than 10%, as illustrated in Table 8.1. The optimal operating shaft speed would be predicted incorrectly if the *perfect gas approach* was applied.

The overall trend of the turbine performance is similar between the CFD analysis and the *constant specific speed* approach, but the trend is different for the *variable pressure ratio*

approach. The *variable pressure ratio* approach shows fairly flat efficiency for the range of velocity ratio between 0.55 and 0.70, and the range of specific speed between 0.33 and 0.42. However, the CFD analysis shows that the turbine is very sensitive to the operating point, as shown in Figure 8.2 (b) and Figure 8.3 (b). The turbine performance drops significantly at the operating points away from the best efficiency point. The best efficiency point is defined as the point with the maximum total-to-static isentropic efficiency at certain pressure ratio. The result shows that the *variable pressure ratio* approach provides a good prediction of optimal velocity ratio, optimal specific speed, and maximum efficiency. However, the approach does not provide a good estimation of performance for the operating points away from the best efficiency point, as presented in Table 8.2.

The *constant specific speed* approach assumes constant pressure ratio, specific speed and velocity ratio. The trend of the performance is similar between the *constant specific speed* approach and the CFD analysis for R134a and R245fa, based on Figure 8.3 and Figure 8.4. However, the turbine efficiency was over-estimated with errors between 10 and 20%, for the investigated range of velocity ratio and specific speed. This approach provides a better estimation in the turbine performance away from the best efficiency point, compared to another two approaches. However, the *constant specific speed* approach yields over 10% error in estimating the optimal velocity ratio, optimal specific speed, and maximum turbine efficiency, whereas the *variable pressure ratio* approach yields an error between 7% and 8%, as listed in Table 8.2.

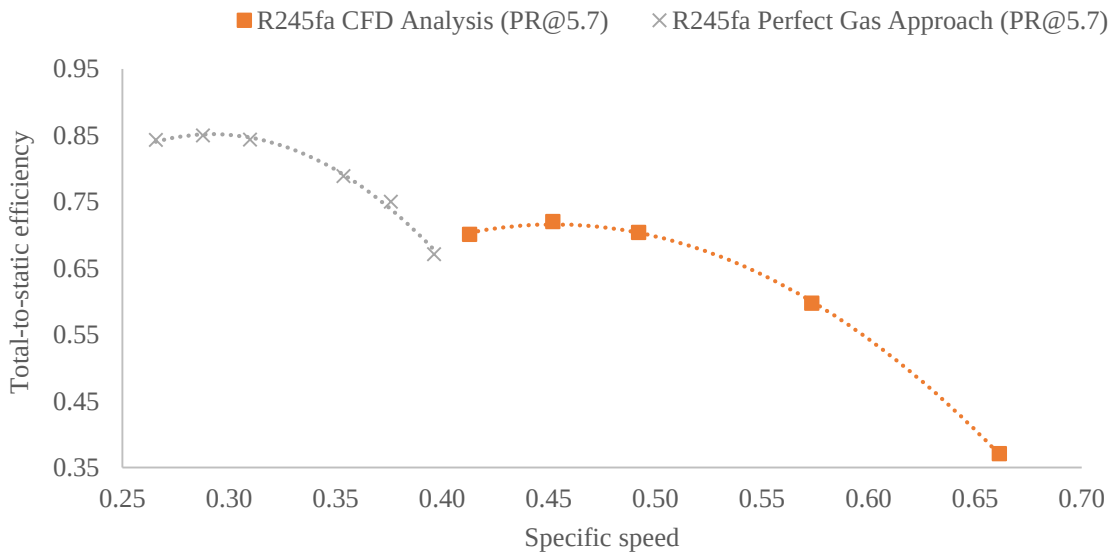

(a)

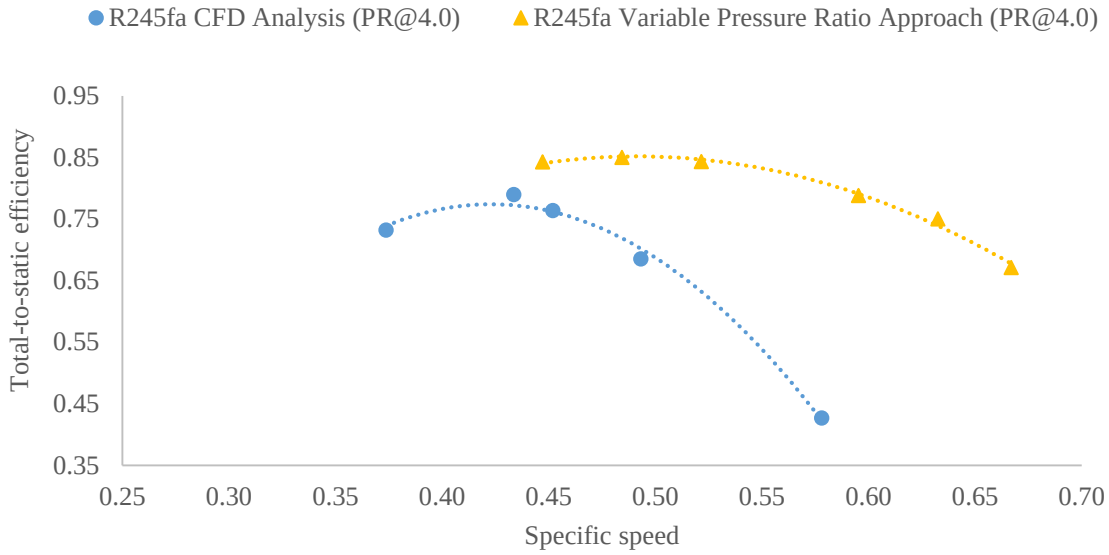

(b)

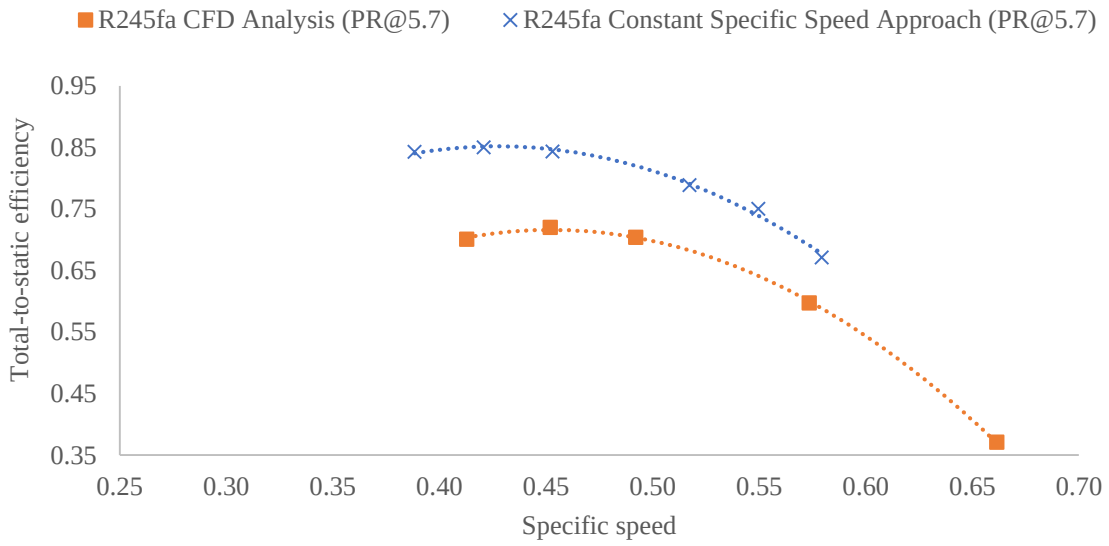

(c)

Figure 8.4: Comparisons of scaled performance from air data and CFD result for R245fa as a function of specific speed

The estimation of the inlet mass flow rate by the three similarity approaches and the CFD analysis was compared. The *perfect gas* approach and the *variable pressure ratio* approach utilize the mass flow coefficient in equation (5) whereas the *constant specific speed* approach uses the specific speed correlation in equation (8) to estimate the inlet mass flow rate. The result in Table 8.2 shows that the mass flow rate was under-estimated using all three approaches. The mass flow coefficient predicts the inlet mass flow rate with a better accuracy,

with an error less than 10%, as opposed to the specific speed correlation, with error in the range of 15 and 25%. Hence, the *perfect gas* approach and the *variable pressure ratio* approach provide better estimations in the inlet mass flow, compared to the *constant specific speed* approach.

Table 8.2: Numerical error for different scaling analysis approaches

	Working medium	Pressure ratio	Optimal velocity ratio	Optimal specific speed	Maximum total-to-static efficiency	Mass flow rate (kg/s)	Average Error (%)
Benchmark	Air	5.7	0.6	0.42	0.85	0.29	
Approach 1	R134a	5.7	0.46	0.35	0.85	3.46	
	Error (%)		23.3	25.5	11.8	4.6	16.3
	R245fa	5.7	0.38	0.29	0.85	3.75	
	Error (%)		31.9	35.9	18.4	9.0	23.8
Approach 2	R134a	2.7	0.6	0.37	0.85	3.46	
	Error (%)		7.7	9.8	6.6	4.7	7.2
	R245fa	4.0	0.6	0.48	0.85	3.75	
	Error (%)		2.9	13.5	9.4	9.0	8.7
Approach 3	R134a	5.7	0.6	0.42	0.85	2.99	
	Error (%)		0.0	10.6	11.8	17.6	10.0
	R245fa	5.7	0.6	0.42	0.85	3.15	
	Error (%)		7.5	7.2	18.4	23.5	14.1
CFD	R134a	2.7	0.65	0.41	0.91	3.63	
		5.7	0.60	0.47	0.76	3.63	
	R245fa	4.00	0.58	0.42	0.78	4.12	
		5.7	0.56	0.45	0.72	4.12	

8.4 Discussion

The discrepancy in the turbine efficiency if a turbine stage is scaled from one operating condition into another is attributed to the variation in machine Reynolds number and Mach number. Various Reynolds number corrections were proposed for centrifugal compressors, such as ASME PTC-10 [17] and the efficiency-deficiency chart by Pampreen [18]. The machine Reynolds number, however, does not have significant effect on the change in efficiency in this study as the effects of viscosity and thermal conductivity can be neglected at high Reynolds number [19]. Reynolds number, $Re=\rho UD/\mu$ is a function of density, ρ, tip speed, U, wheel diameter, D, and dynamic viscosity, μ. The dynamic viscosity of the refrigerants is much smaller, rendering a higher value in the Reynolds number, in the magnitude of 100 x 10^6, as opposed to the Reynolds number of steam, air, and water in the magnitude of 1 x 10^6. The turbine inlet condition was varied using the CFD analysis to investigate the correlation between the machine Reynolds number and the turbine performance, as illustrated in Figure 8.5. The turbine's performance is fairly consistent in a wide range of Reynolds number, between 10 and 90. Hence, the Reynolds number effect can be neglected in this study.

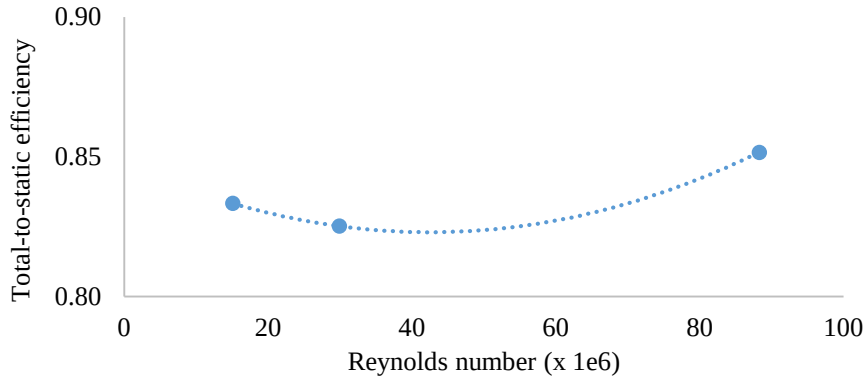

Figure 8.5: Effect of machine Reynolds number on turbine's performance using R134a

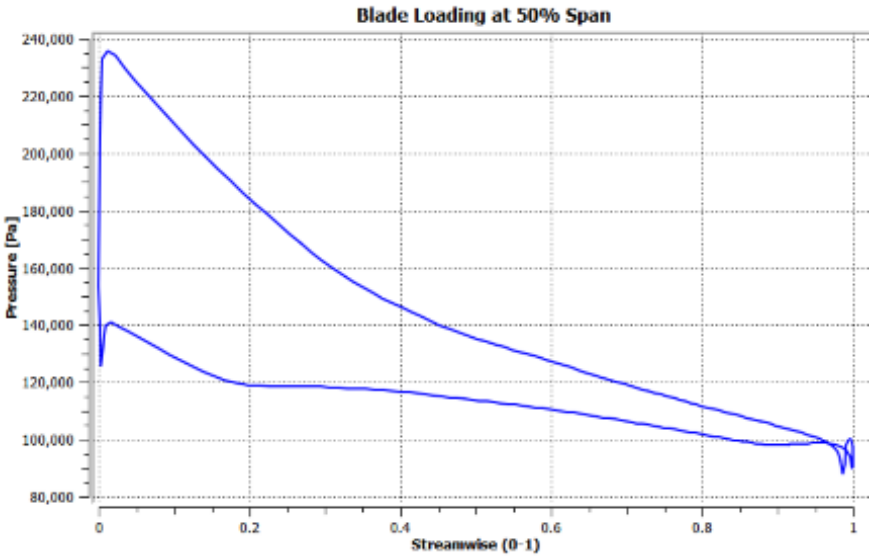
Blade Loading at 50% Span
240,000
220,000
200,000
180,000
160,000
140,000
120,000
100,000
80,000
Pressure [Pa]
0
0.2
0.4
0.6
0.8
1
Streamwise (0-1)

(a)

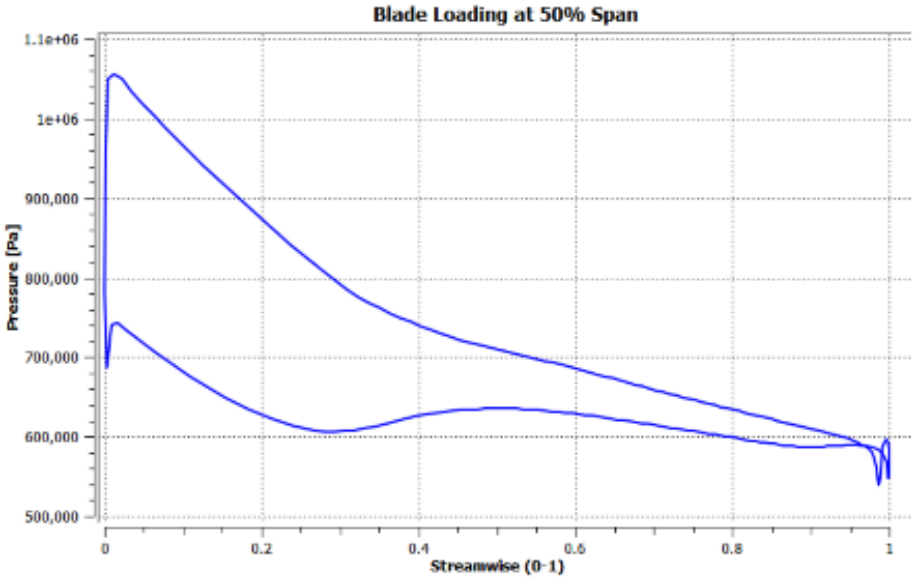
Blade Loading at 50% Span
1.1e+06
1e+06
900,000
800,000
700,000
600,000
500,000
Pressure [Pa]
0
0.2
0.4
0.6
0.8
1
Streamwise (0-1)

(b)

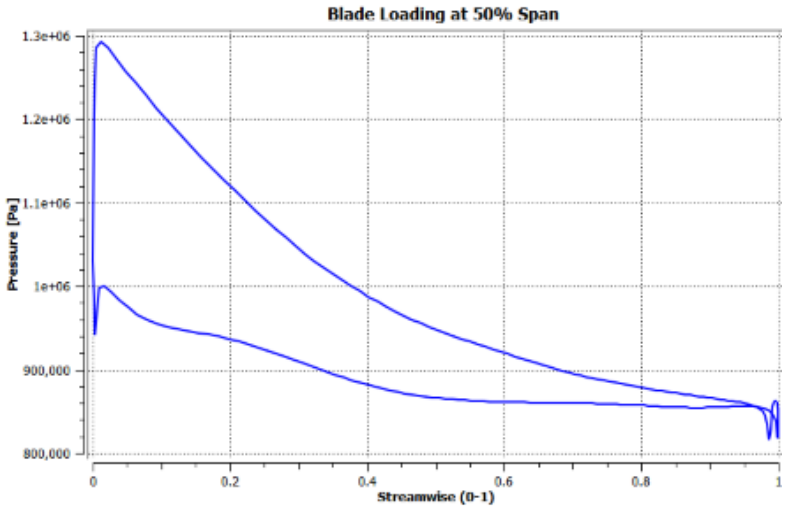

(c)

Figure 8.6: Blade loading and density at blade surface using air at pressure ratio of 5.7 (a), R245fa at pressure ratio of 4.0 (b) and R134a at pressure ratio of 2.7 (c)

The blade loading along the pressure and suction surfaces at optimal specific speed using the *variable pressure ratio* approach are similar for all three working fluids; air, R134a and R245fa. Constant pressure drop was observed for air (modelled as ideal gas), R134a and R245fa (modelled as real gas) along pressure surface, but pressure fluctuation was observed for R245fa along the suction surface. The fluctuation is related to the adverse pressure gradient near the leading edge of the suction surface, which forms a vortex and local backpressure downstream of the vortex, as illustrated by the velocity vector in Figure 8.7. The flow re-attaches downstream of the vortex with gradual pressure drop along the blade passage.

The maximum isentropic efficiency for air, R134a and R245fa is different although the pressure loading along the blade passage at the optimal specific speed is similar. The highest turbine efficiency is achieved by R134a, followed by air, and R245fa. The deviation can be explained as a function of compressibility effect. The compressibility factor is a ratio of actual specific volume to the ideal volume of selected fluids. The compressibility effect of the expansion process across the turbine was measured qualitatively by volumetric flow ratio [20]. Macchi and Perdichizzi found that the increase in the volumetric flow ratio gives rise to a reduction in the turbine efficiency at optimal specific speed [20], and the volumetric flow ratio has to be less than 50 to achieve a high turbine stage efficiency greater than 0.80 [21]. The volumetric flow ratio is different for different working fluid using the *variable pressure ratio*

approach. The volumetric flow ratio was determined as 5.7 for air, 4.9 for R245fa, and 2.7 for R134a. The use of equation (9) justifies the highest efficiency using R134a at low pressure ratio. Equation (9) is the change of entropy of a perfect gas in a closed system.

$$\Delta s = c_v \ln\left(T_3 / T_1\right) + R \ln\left(v_3 / v_1\right) \tag{19.9}$$

Where Δs denotes the entropy generation, c_V isochoric heat capacity, R specific gas constant, T temperature, and v specific volume. The increase in volumetric flow ratio generates a larger entropy difference. The larger the entropy differences, the larger the irreversibility of the system and the lower the turbine's efficiency. Hence, the highest efficiency is achieved by R134a with the lowest pressure ratio among all three working fluids. However, the turbine's efficiency using R245fa (expansion ratio of 4.9) is 78%, which is lower than air at 85% (expansion ratio of 5.7). This shows that the volumetric flow ratio is not the sole contributor to the drop in turbine performance using different fluids.

Table 8.3: Performance parameters for different working fluids using Variable Pressure Ratio Approach

Fluids	Air	R134a	R245fa
Velocity triangle	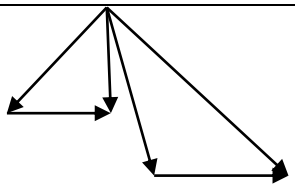	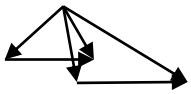	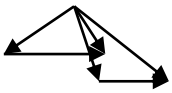
Pressure ratio	5.7	2.7	4.0
Volumetric flow ratio	3.7	2.7	4.9
Degree of Reaction	0.42	0.47	0.44
Flow coefficient	0.245	0.172	0.249
Stage loading coefficient	1.040	0.974	0.995

The differences in the volumetric flow ratio also gives rise to the change in a number of turbine parameters. Optimum degree of reaction decreases whereas optimal flow coefficient increases with increasing expansion ratio. These yield some changes in the velocity diagram at the turbine exit, as shown in Table 8.3. The complete similarity is not achieved as the velocity vector at the turbine exit is not conserved. Hence, the *variable pressure ratio* approach does

not achieve complete similarity, and this gives rise to the error in estimating the velocity ratio, specific speed, and turbine performance.

The flow field diagrams of R245fa, R134a, and air using the *variable pressure ratio* approach were compared in Figure 8.7. The flow undergoes turning from axial direction to tangential direction, and gives rise to Coriolis effect in the radial direction [22]. The flow undergoes a non-uniform velocity distribution in the spanwise direction, with lowest velocity near the end wall surface of the hub. The radial gradient of the flow velocity in the spanwise direction gives rise to the imbalance in the pressure gradient in the spanwise direction. The end result of the Coriolis effect and the non-uniform velocity give rise to a complex flow field, which is illustrated in Figure 8.7 in term of flow angle. The bulk flow moves from suction surface near the shroud to pressure surface near the hub. The flow is compensated by a number of passage vortices, and the flow vector diagram can be found in Kitton's work (also presented by Baines in his work [22]). This phenomena exists in the best efficiency point, attributed to the turning of the flow from axial to tangential direction. The distribution of the swirl angle at the trailing edge was averaged and the flow angle was determined as 1˚ for air, 33° for R134a and 37° for R245fa. The result implies that the turbine exit swirl angle might increase monotonically with the molecular weight of the working fluids, with the highest by R245fa and the lowest by air. Positive swirl angle is non-favorable as the fluid internal energy would be lost as kinetic energy. The specific work output would decrease with a positive swirl angle, based on Euler turbomachinery equation.

$$W_x = U_2 C_{\theta 2} - U_3 C_{\theta 3} = U_2 C_{m2} \tan \alpha_2 - U_3 C_{m3} \tan \alpha_3 \qquad (19.10)$$

Where W_X is specific work output, U_2 is rotor inlet tip speed, U_3 is rotor outlet tip speed, C_θ is tangential velocity component, C_m is meridional velocity component, and α is swirl angle.

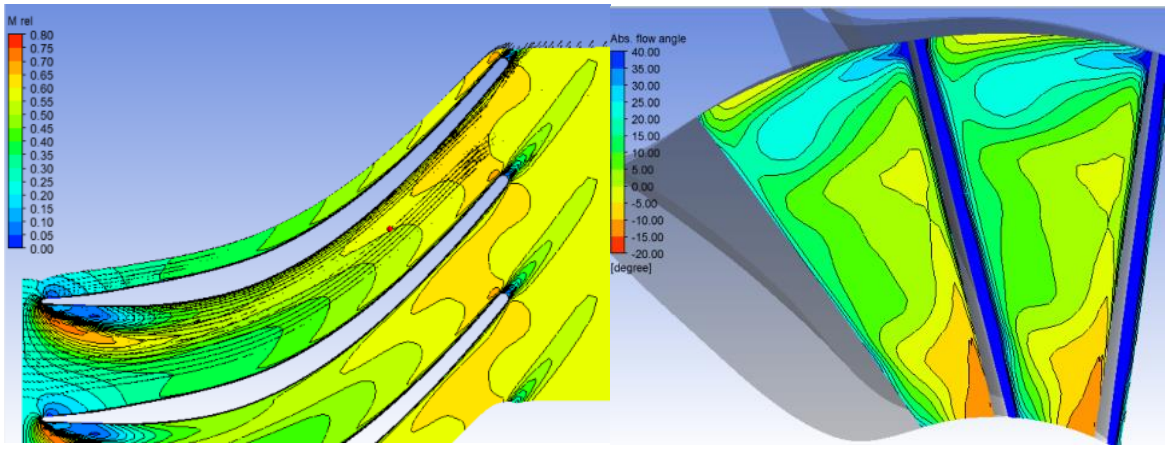

(a) (b)

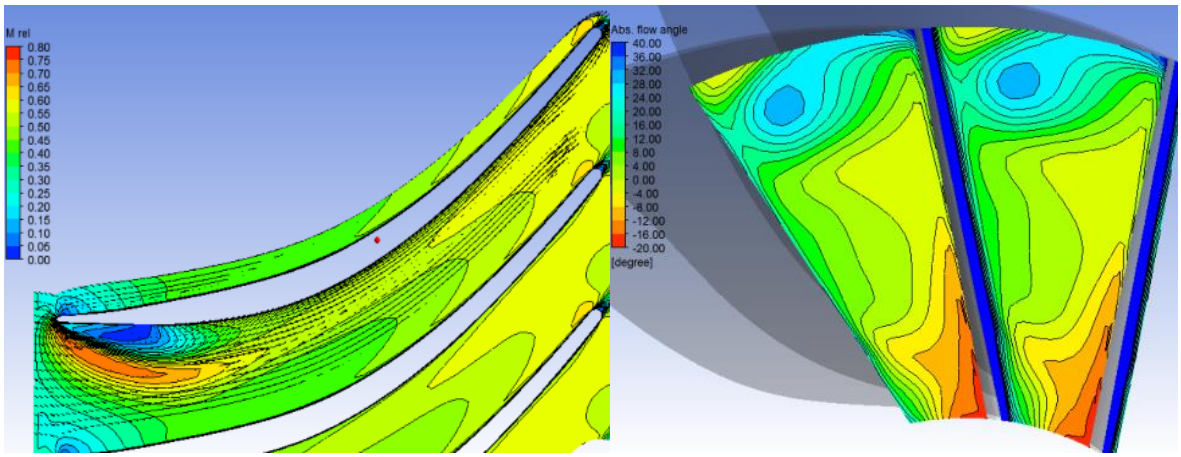

(c) (d)

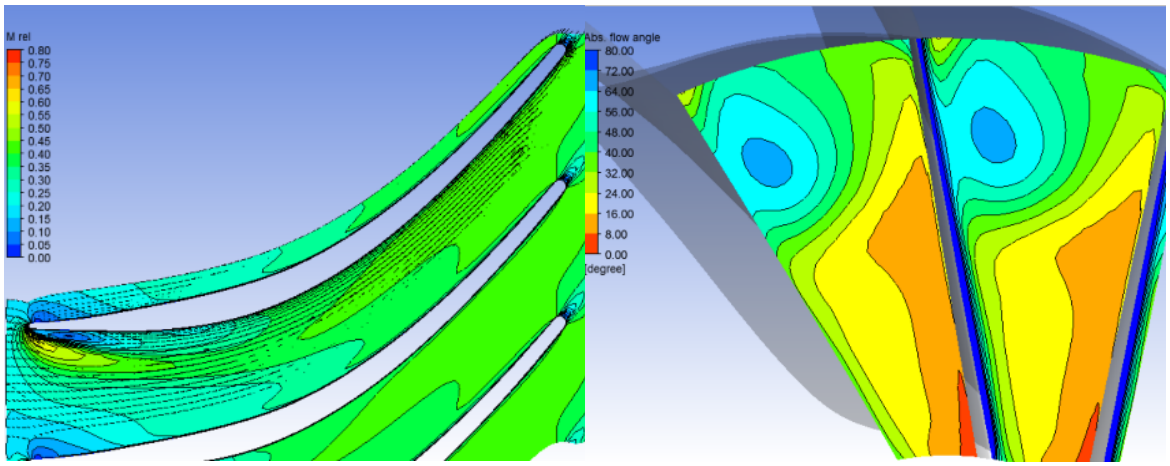

(e) (f)

Figure 8.7: Distribution of relative Mach number in the meridional plane and distribution of absolute flow angle at the trailing edge using air at pressure ratio of 5.7 (a-b), R245fa at pressure ratio of 4.0 (c-d) and R134a at pressure ratio of 2.7 (e-f)

The conventional radial inflow turbine is typically designed for low pressure ratio application, which is between 1.2 and 3.0 for automotive turbochargers, and less than 10 for single stage gas turbines to avoid choking and shock waves in supersonic expansion. The selected gas turbine has a design pressure ratio of 5.7. Different pressure ratio was determined for R134a and R245fa assuming constant value of $\Delta h_{0s}/a_{01}^2$ (using the *variable pressure ratio* approach) and plotted in Figure 8.8. The limiting line on the left represents the saturation lines of the refrigerants. The calculated pressure ratio for the selected refrigerants is less than 5.7, which is the pressure ratio imposed on the turbine using air. The local sound speed of refrigerants with heavier molecular weight is less than the local speed of sound using air. The local speed of sound is between 90 and 190 m/s for R134a and between 75 and 160 m/s for R245fa for the temperature range of 300 and 450 K, and pressure range of 0.5 and 4.0 MPa, which is less than the local speed of sound of air at 635 m/s with the given operating condition in Table 8.1. The smaller the local speed of sound, the smaller the isentropic enthalpy drop and the smaller the pressure ratio across the turbine. Hence, the *variable pressure ratio* approach is limited to a pressure ratio less than the design pressure ratio using air. This limits the applicability of the approach in ORC application, which is characterized for high pressure ratio expansion.

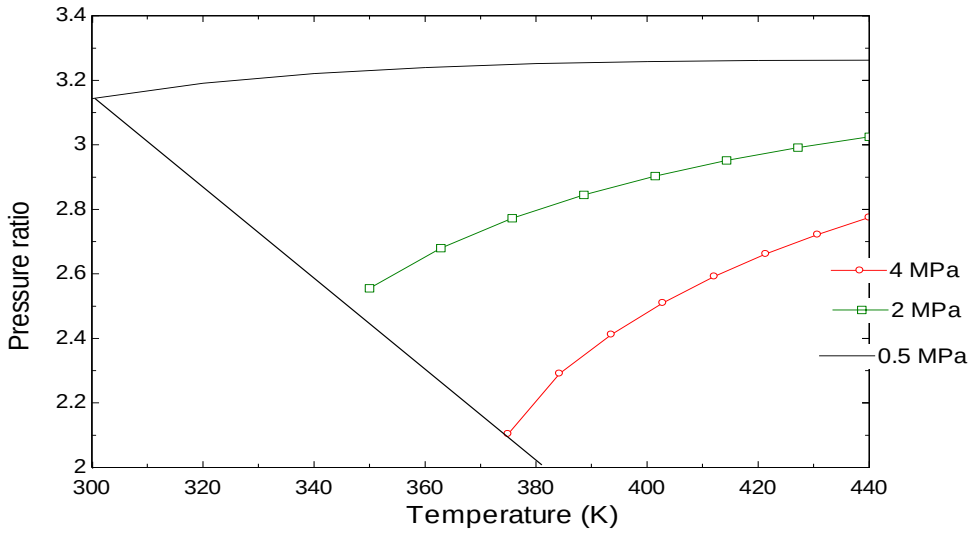

(a)

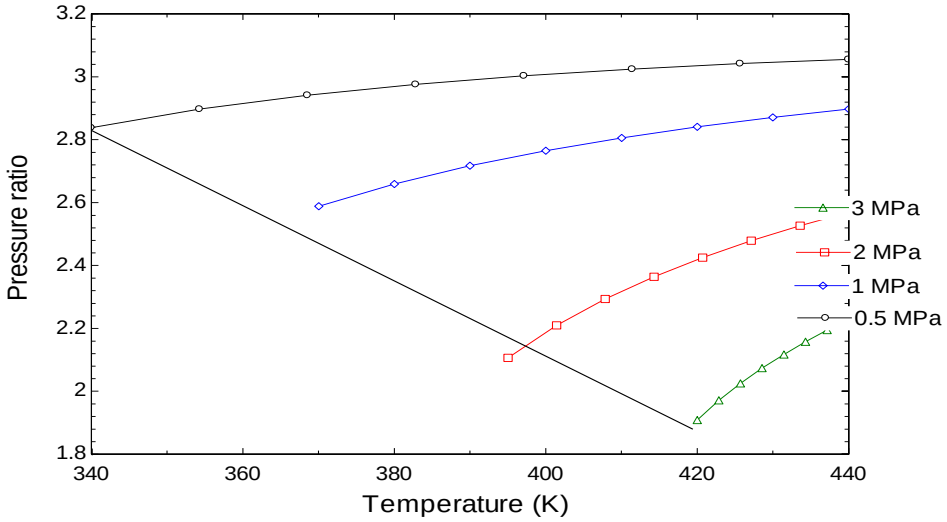

(b)

Figure 8.8: Range of applicability using equation (6) for R134a (a) and R245fa (b)

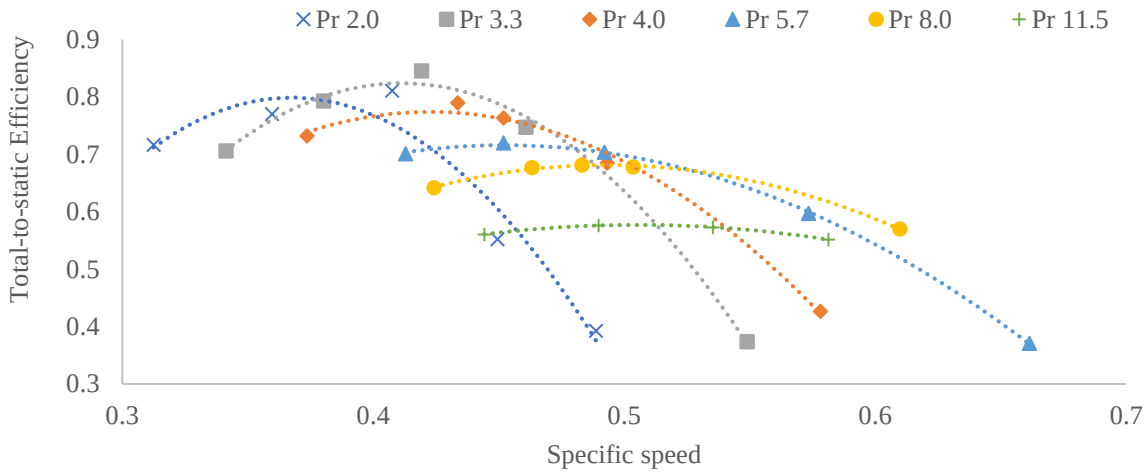

Figure 8.9: Performance map of R245fa at different specific speed and pressure ratio

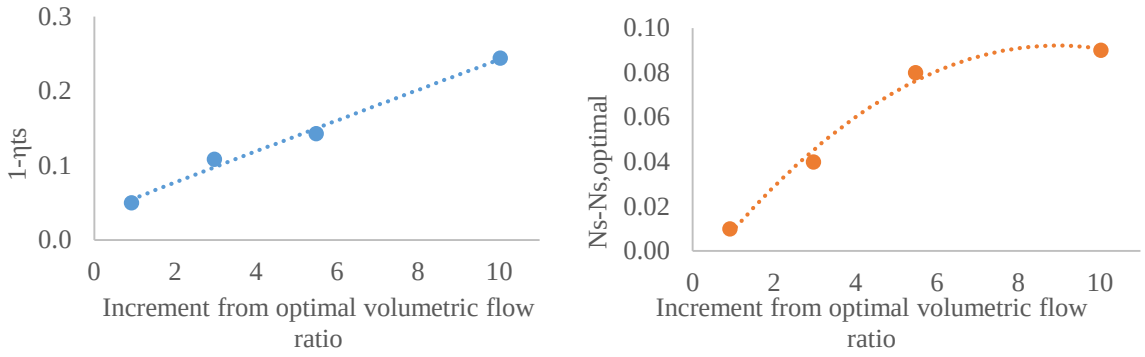

(a) (b)

Figure 8.10: Deviation of best efficiency point and the corresponding specific speed at increasing volumetric flow ratio

The prediction of the turbine performance at higher pressure ratio or expansion ratio is required for ORC application. A correction chart for R245fa at different expansion ratio was developed using Figure 8.9. The turbine's performance map for R245fa was generated for different pressure ratio (2 – 11.5) and specific speed (0.3 – 0.7), and plotted in Figure 8.9. The result shows that the maximum turbine performance was achieved at a pressure ratio of 3.3 (equivalent to volumetric flow ratio at 4.0). The maximum efficiency point at the pressure ratio of 3.3 iss used as a benchmark to calculate the deficiency in efficiency and deviation of optimal specific speed at higher volumetric flow ratio. The turbine losses increases linearly with increasing volumetric flow ratio as shown in Figure 8.10(a). The location of the specific speed for the best efficiency point at increasing volumetric ratio is increasing, as shown in Figure 8.9. The deviation in the optimal specific speed is plotted as a function of volumetric flow ratio in Figure 8.10. The result shows that the deviation in optimal specific speed increases with increasing volumetric flow ratio until the blade passage is choked (with the relative Mach number around 1). The further increment in volumetric flow ratio does not have any effect on the value of N_s-$N_{s,optimal}$, as illustrated in Figure 8.10.

8.5 Conclusion

Three different approaches using the similarity concept were proposed and investigated to scale the selected gas turbine from air to R134a and R245fa in this study. The *perfect gas* approach assuming the real gas as perfect gas provides the largest error in terms of optimal velocity ratio, optimal specific speed, and maximum efficiency. The *variable pressure ratio* approach shows the highest averaged accuracy in predicting the optimal velocity ratio, optimal specific speed, maximum efficiency and mass flow rate. The *constant specific speed* approach is recommended to estimate the turbine's performance away from the best efficiency point.

Constant value of $\Delta h_{0s}/a_{01}^2$ was imposed in the *variable pressure ratio* approach to achieve the similarity but a number of deviations was observed, including swirl angle at the turbine outlet, volumetric flow ratio, best efficiency point and the corresponding specific speed. The Reynolds number effect does not influence the scaling using refrigerants as the effect of viscosity is negligible at high Reynolds number using refrigerants with low viscosity. The swirl angle at the turbine outlet was observed as a function of molecular weight, in which the increment in molecular weight increases the swirl angle and reduces the specific work output. The *variable pressure ratio* approach does not ensure a constant volumetric flow ratio, hence the complete similarity cannot be achieved. The *variable pressure ratio* approach is limited to pressure ratio less than the design pressure ratio using air, which is not suitable to scale an ORC turbine. Therefore, a correction chart was developed to scale the performance of the gas turbine for higher volumetric ratio using R245fa. The deficiency in turbine efficiency is linearly correlated to the increased volumetric flow ratio. The correction chart provides a good estimation in selecting a suitable turbine for a particular ORC application. However, the correction chart has to be validated against the experimental data for better accuracy.

8.6 References

1. Meher-Homji, C.B. *'The Historical Evolution of Turbomachinery*. in *Proceedings of the 29th Turbomachinery Symposium, Texas A&M University, Houston, TX*. 2000.
2. Balje, O.E., *Turbomachines: A Guide to Design Selection and Theory*. 1981: Wiley.
3. Dixon, S.L. and C. Hall, *Fluid Mechanics and Thermodynamics of Turbomachinery*. 2010, Butterworth-Heinemann: Burlington.
4. Chen, H. and N.C. Baines, *The aerodynamic loading of radial and mixed-flow turbines.* International Journal of Mechanical Sciences, 1994. **36**(1): p. 63-79.
5. Aungier, R.H., *Turbine aerodynamics: axial-flow and radial-inflow turbine design and analysis*. 2006: ASME Press.
6. Japikse, D. and N.C. Baines, *Introduction to turbomachinery*. 1995: Concepts ETI.
7. Strub, R.A., et al., *Influence of the Reynolds Number on the Performance of Centrifugal Compressors.* Journal of Turbomachinery, 1987. **109**(4): p. 541-544.
8. Casey, M.V., *The Effects of Reynolds Number on the Efficiency of Centrifugal Compressor Stages.* Journal of Engineering for Gas Turbines and Power, 1985. **107**(2): p. 541-548.
9. Quoilin, S. and V. Lemort. *Technological and economical survey of Organic Rankine Cycle systems*. in *5th European Conference Economis and Management of Energy in Industry*. 2009. Algarve, Portugal.
10. Bao, J. and L. Zhao, *A review of working fluid and expander selections for organic Rankine cycle.* Renewable and Sustainable Energy Reviews, 2013. **24**: p. 325-342.
11. Quoilin, S., et al., *Thermo-economic optimization of waste heat recovery Organic Rankine Cycles.* Applied Thermal Engineering, 2011. **31**(14–15): p. 2885-2893.
12. Sauret, E. *Open design of high pressure ratio radial-inflow turbine for academic validation*. in *Proceedings of the ASME 2012 International Mechanical Engineering Congress and Exposition*. 2012. Houston, Texas: American Society of Mechanical Engineers (ASME).
13. Jones, A.C., *Design and Test of a Small, High Pressure Ratio Radial Turbine.* Journal of Turbomachinery, 1996. **118**(2): p. 362-370.
14. Wong, C.S. and S. Krumdieck. *Energy and Exergy Analysis of an Air-Cooled Geothermal Power Plant with Fixed Nozzle Turbine in Subsonic Expansion and Supersonic Expansion via CFD Analysis*. in *36th New Zealand Geothermal Workshop* 2014. Auckland University.
15. Lemmon, E.W., Huber, M.L., McLinden, M.O, *NIST Standard Reference Database 23: Reference Fluid Thermodynamic and Transport Properties-REFPROP, Version 9.1*, in *National Institute of Standards and Technology*. 2013, Standard Reference Data Program: Gaithersburg.
16. Lemmon, E.W. and R. Span, *Short fundamental equations of state for 20 industrial fluids.* Journal of Chemical & Engineering Data, 2006. **51**(3): p. 785-850.
17. PTC, A., *PTC 10-1997, Performance test code on compressors and exhausters.* American Society of Mechanical Engineers, New York, 1997. **3**.

18. Pampreen, R., *Small turbomachinery compressor and fan aerodynamics.* Journal of Engineering for Gas Turbines and Power, 1973. **95**(3): p. 251-256.

19. Harinck, J., A. Guardone, and P. Colonna, *The influence of molecular complexity on expanding flows of ideal and dense gases.* Physics of Fluids (1994-present), 2009. **21**(8): p. 086101.

20. Macchi, E. and A. Perdichizzi, *Efficiency prediction for axial-flow turbines operating with nonconventional fluids.* ASME Journal of Engineering for Power, 1981. **103**: p. 718e24.

21. Angelino, G., C. Invernizzi, and E. Macchi, *Organic Working Fluid Optimization for Space Power Cycles*, in *Modern Research Topics in Aerospace Propulsion*, G. Angelino, L. De Luca, and W.A. Sirignano, Editors. 1991, Springer New York. p. 297-326.

22. Moustapha, H., et al., *Axial and Radial Turbines*. 2003: Concepts Eti.

Application of the SMC-DTR Approaches

9.0 Application of the SMC-DTR using Meanline Analysis

The aim of this thesis is to present the SMC-DTR approach for low temperature resources, and the main contribution of this thesis is to develop the key component, SMC adaptive strategy. The following chapters present the application of the SMC-DTR approach for different resources' characteristics.

This chapter presents the application of the SMC-DTR approach by adapting nozzle-less automotive turbochargers for a resource condition with constant heat source and heat sink condition. The SMC-DTR approach was utilized to design an ORC bottoming cycle in a petroleum refining plant in New Zealand. The meanline analysis technique was applied as the performance map of the given turbochargers is not available. The geometry of the turbine wheels was measured, and the data was fed into the SMC adaptive strategy to evaluate the turbine performance. The selected automotive turbocharges are not equipped with nozzle vanes. Hence, a preliminary design of nozzle vanes was performed, and the turbine performance was evaluated assuming the turbine is equipped with the designed nozzle vanes. The thermal efficiency of the ORC model was optimized using the two automotive turbochargers and four different working fluids (n-Pentane, R134a, R245fa, and isobutane). The selected turbocharger was modified and adapted as an ORC turbine and the mechanical system design of the ORC turbo-generator set was presented. This chapter aims to present the SMC-DTR approach using automotive turbochargers as the core test subjects. This chapter presents the cycle design and fluid selection, the calculation of turbine specification, the SMC adaptive strategy using meanline analysis technique, and the mechanical system design of the ORC turbine.

The result shows that the adaptation of the automotive turbochargers as ORC turbine is feasible but the optimal range of pressure ratio is less than 3.0. If the pressure ratio is above this value, the turbine performance would drop significantly.

9.1 Introduction

The capital cost of an ORC unit is dependent on the development scheme of the system. The cost for an ORC power plant is averaged at $2,700 NZD/kW ($1,890 USD/kW) for a 20 MW to 50 MW power plant [1]. The cost of hybrid plant (steam plant and ORC binary plant) is lower. The total installation cost for Rotokawa I plant is about $2,600 NZD/kW (in 1995) and the Mokai II plant is around $2,200 NZD/kW (in 2000) [1]. An indicative installation cost of ORC plant is presented in Figure 9.1 [2] as a function of target application and net electrical power. The installation cost tends to be higher at small nominal output power. The development of a new turbine expander would incur high design and manufacturing cost [3]. For example, the 1 kW scroll expander with generator from a scroll supplier, Air Squared, used in the experimental work in our lab costs nearly $5,000 USD (equivalent to 7,700 NZD) provided for academic research at-cost by the manufacturer. The conversion of an automotive scroll compressor into a scroll expander costs less than $2,000 USD (equivalent to 3,100 NZD) [4], but the cost per kWh for the scroll expander is higher than the turbo-generator due to the low capacity of the scroll machines.

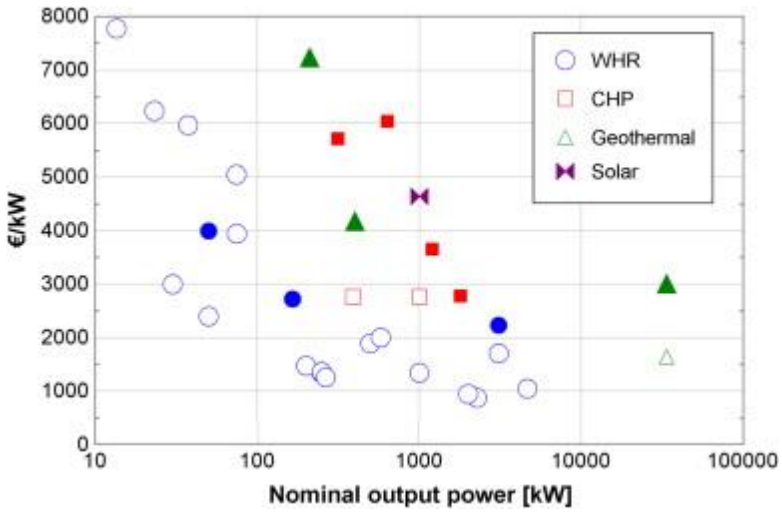

Figure 9.1: Unit cost (without considering the labour cost for the installation - empty dots) and total cost (unit cost plus labour cost for system installation - plain dots) of ORC systems as a function of target application and net electrical power [2]

The cost of an ORC unit is between $1,300 NZD/kW and $1,350 NZD/kW if a refrigeration chiller is converted as an ORC unit [5]. A 250 kW ORC system has been designed by retrofitting a refrigeration chiller, changing the working fluid from R245fa into R134a for

better thermal match of the heat source and heat sink condition, and replacing the centrifugal compressor into a radial inflow turbine [5]. The cost of an ORC unit can range from 3,000 €/kW to 7,000 €/kW (correspond to 5,000 and 11,500 NZD/kW) between 100 and 1,000 kW, based on Figure 5.1. The authors believe that the cost of an ORC unit between 100 and 1,000 kW could be reduced if an existing turbine technology is adapted. An ORC system for waste heat recovery was developed by converting an automotive turbocharger by ABB Schweiz AG Switzerland [6]. The conversion process and the cost, however, are not published. The radial turbines from the automotive turbocharges are believed to be the best candidates for the small-scale ORC applications due to the high volume manufacturing in a wide range of size at relatively low cost.

This chapter presents the SMC-DTR approach (shown in Figure 9.2) using automotive turbochargers as the ORC turbine for a petroleum refining plant in New Zealand. Four different working fluids were considered, namely n-Pentane, isobutane, R245fa, and R134a. The fluids were chosen as they are commonly used in commercial ORC units;

- R134a in Chena binary plant [7],
- Isobutane in Otake pilot plant in Japan [8] and the plant operated by ENEL [9], and
- n-Pentane in ORMAT Energy Convertor in Brady [8], and Rotokawa [10].
- R245fa was reported as the most suitable candidate in geothermal application with geothermal brine temperature over 167°C when thermodynamic First-Law efficiency is the objective function [5].

The performance of two given automotive turbochargers were evaluated using the SMC adaptive strategy. The meanline analysis technique was applied as the performance map of the turbine is not available. The thermodynamic cycle was designed based on the heat source and heat sink condition, the turbine specification was defined, and the turbine performance map using the four different working fluids was generated. The turbine performance map was fed into the cycle analysis model to determine the best configuration of turbine and working fluid. The selected turbine was modified and adapted as an ORC turbine, and the mechanical design process was presented.

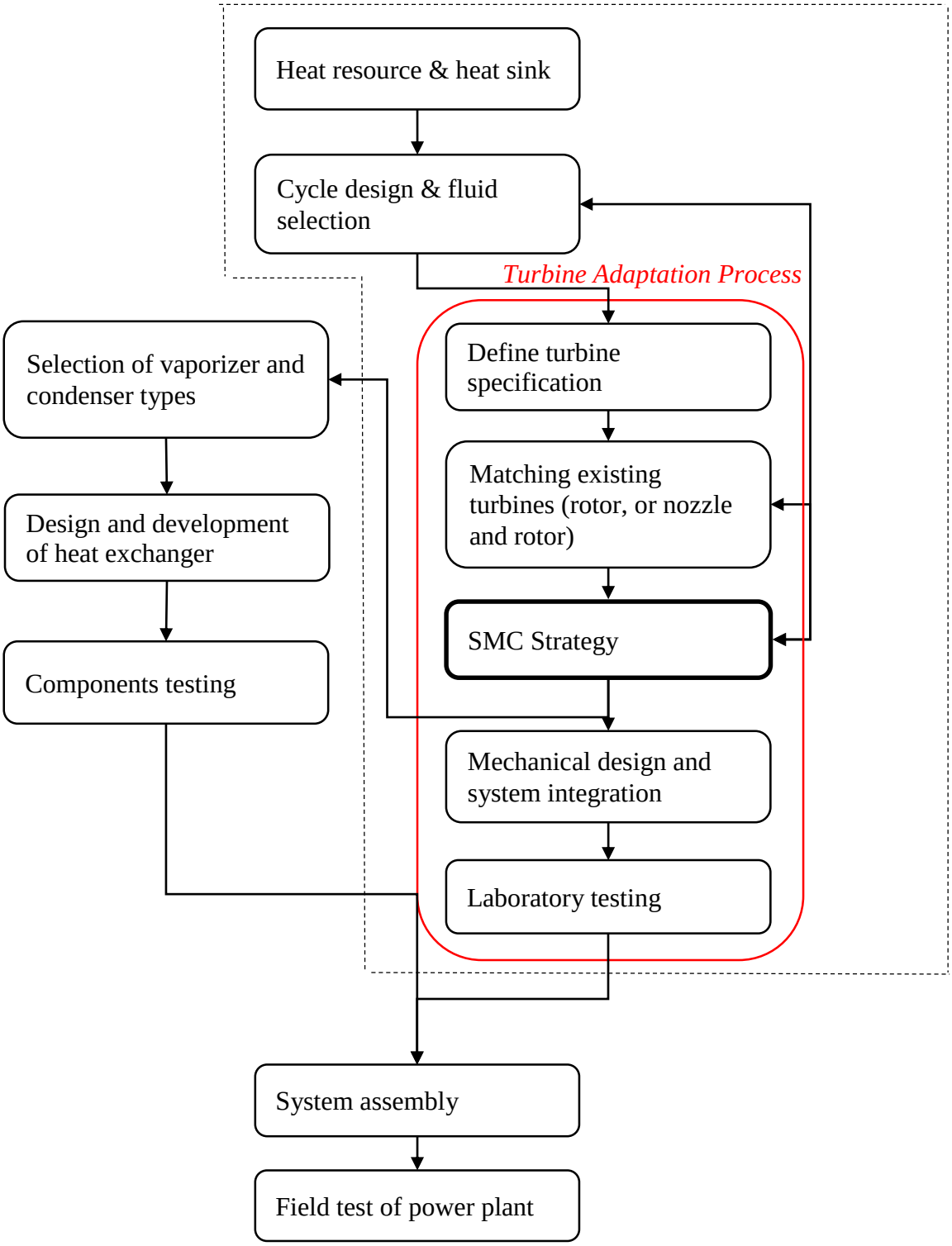

Figure 9.2: The SMC-DTR approach for LT-ORC

9.2 Application of the SMC-DTR approach in a waste heat recovery (WHR) system

9.2.1 Heat source and heat sink:

An ORC bottoming cycle has been planned for a petroleum refinery plant in New Zealand [11]. The planned ORC bottoming cycle utilizes the kerosene stream as the heat source, with the estimated thermodynamic properties of the kerosene flow tabulated in Table 9.1.

Table 9.1: The thermodynamic properties of the kerosene flow [11]

	Evaporator Inlet	Evaporator outlet
Temperature (C)	115	70
Pressure (kPa)	740	740
Enthalpy (kJ/kg)	227.9	134.0

Water has been selected as the cooling medium in the condenser. The cooling water at the condenser inlet is set at 24˚C and the cooling water is discharged at 35˚C at the condenser outlet.

9.2.2 Cycle design and fluid selection:

The design and analysis model of the thermodynamic cycle in Chapter 3 was applied on the heat source and the sink. The turbine efficiency was assumed 85% in the cycle design. The pinch point temperature different at the evaporator and the condenser were set between 5 and 20˚C to allow a feasible heat transfer within the heat exchangers. Four different working fluids were selected for the cycle design: n-Pentane, isobutane, R134a and R245fa. The cycle analysis model was coupled to an optimization code (variable metric method) to optimize the cycle performance using the overall cycle thermal efficiency as the objective function. The numerical calculation was performed using Engineering Equation Solver (EES) and the details of the mathematical model could be found in Chapter 3. The result from the cycle design and analysis model was tabulated in Table 9.2.

Table 9.2: The optimal operating condition of the planned ORC bottoming cycle using four different working fluids

Fluid	-	n-Pentane	R134a	R245fa	Isobutane
Inlet total temperature	C	74.9	86.2	76.5	78.2
Inlet total pressure	kPa	322	2821	724	1294
Outlet static pressure	kPa	114	1020	245	523
Total-to-static pressure ratio	-	2.8	2.8	3.0	2.5
Mass flow	kg/s	18.5	43.3	36.7	21.2
Cycle thermal efficiency	%	7.7	8.2	7.9	8.0

9.2.3 Define turbine specification:

The turbine shaft speed and rotor diameter were determined using the specific speed-specific diameter performance chart, presented in Chapter 4. The number of stages was calculated using the flow chart illustrated in Figure 4.3, and the result was presented in Table 9.3.

Table 9.3: The turbine shaft speed, rotor diameter and number of stages for four different working fluids

Fluid	-	n-Pentane	R134a	R245fa	Isobutane
Specific speed	-	0.5	0.5	0.5	0.5
Specific diameter	-	4	4	4	4
Shaft speed	rev/min	5314	8429	4781	9653
Tip speed	m/s	387	277	281	378
Rotor diameter	cm	139	62.8	112	74.8
Number of stages	-	1	1	1	1

Where station 1 is the nozzle inlet, station 2 is the interface of the nozzle and the rotor, and station 3 is the rotor outlet in this chapter.

9.2.4 Matching existing turbines:

This step was not performed in this case study as there are only two available automotive turbochargers for the evaluation of the adaptation process. The turbine wheels of the turbochargers were shown in Figure 9.3.

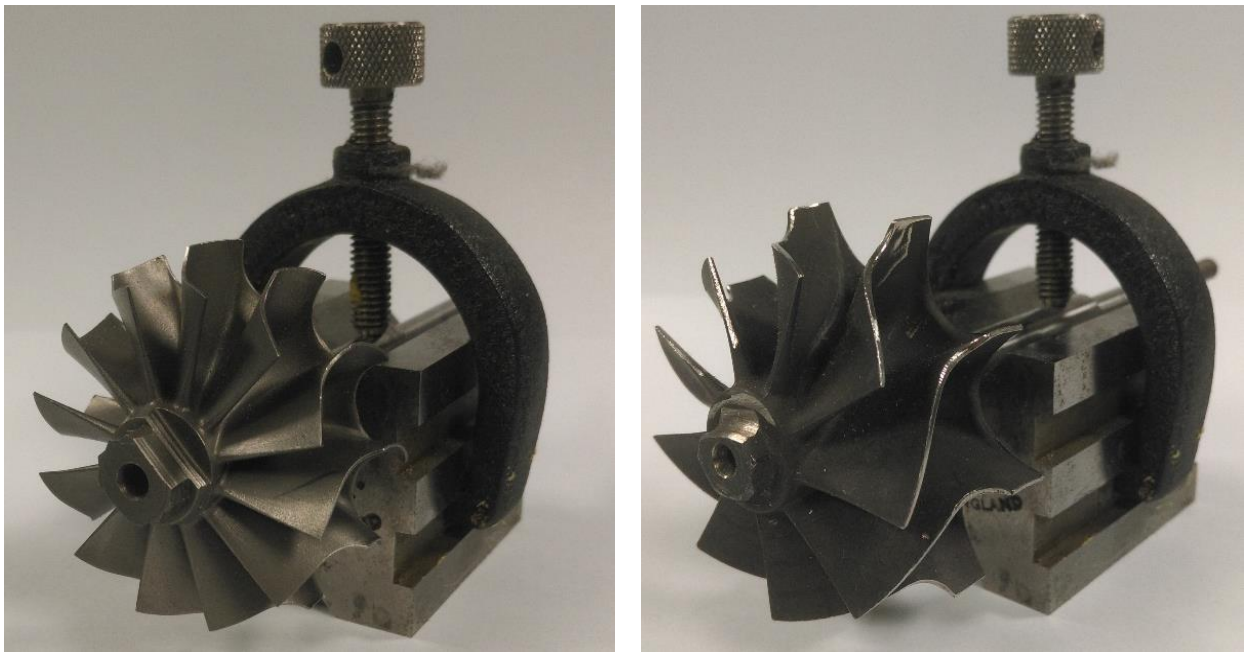

Figure 9.3: Turbine wheels of two given automotive turbochargers, TC-12 (on the left) and TC-9 (on the right)

The 12-blade and 9-blade turbine wheels were identified as TC-12 and TC-9 respectively in this study. The geometry information for the turbochargers was unavailable. Hence the basic geometry of the turbine wheels was measured manually using a Vernier caliper and a protractor, and the measurements were shown in Table 9.4. The given turbine wheels are not similar to the optimal design when the turbine wheels diameter was compared to the result in Table 9.3. Thus, the following section aims to showcase the application of the DTR-SMC approach rather than determining the optimal design for the proposed heat resource.

Table 9.4: Basic Dimensions Value of Available Turbochargers (TC-9 and TC-12)

		Unit	TC-9	TC-12
Inlet radius	r_2	mm	22.3	19.6
Outlet tip radius	$r_{3,tip}$	mm	19.3	17.6
Outlet hub radius	$r_{3,hub}$	mm	6.5	6.1
Inlet blade height	b_2	mm	6	6.6
Total blade height	b_{total}	mm	18.5	14.2
Blade number	Z	-	9	12
Inlet blade angle	$\beta_{2,b}$	deg.	0	0
Outlet blade angle at tip	$\beta_{3t,b}$	deg.	-55	-70
Outlet blade angle at hub	$\beta_{3h,b}$	deg.	-45	-50

9.2.5 Design of Nozzle Vanes:

The selected turbine wheels are not equipped with nozzles. A preliminary design of the nozzle vanes was performed for the selected turbochargers using the method outlined in Chapter 5. The nozzle vane is designed and set up using the correlations presented by Glassman [12] and Aungier [13]. The nozzle vane is uncambered and the vane height is constant across the nozzle stage. The nozzle inlet-to-outlet ratio is recommended to be 1.25 [12]. The nozzle outlet flow angle was determined using the empirical correlation by Glassman between number of rotor blades and nozzle outlet flow angle [12], as shown in equation (9.1).

$$Z_r = \frac{\pi(110-\alpha_2)\tan\alpha_2}{30} \tag{20.1}$$

Where Z_r is number of rotor blades, and α_2 is the nozzle outlet flow angle. Nozzle inlet flow angle is usually assumed to be radially inward in the preliminary design stage [14] but this is not the optimal case. Nozzle inlet flow angle, α_1 was calculated using the correlation by Glassman, shown in equation (9.2), where c_s is the chord of nozzle vane, and r_3 is the mean radius at the rotor outlet. The chord of the nozzle vane was calculated using equation (9.3), which is derived mathematically from the work by Glassman [15]. The equation is only valid if the vane surface length is equivalent to the chord length, which is applicable for the uncambered vanes.

$$\tan(\alpha_1) = \frac{\sin(\alpha_2)}{\frac{c_s}{r_2} + \cos(\alpha_2)} \tag{20.2}$$

$$c_s^{\,2} + 2r_2 c_s \cos(\alpha_2) + (r_2^2 - r_1^2) = 0 \tag{20.3}$$

The correlation between minimum number of nozzle vane for zero diffusion loss, nozzle exit angle, nozzle inlet angle, and radius ratio was plotted by Northern Research and Engineering Corporation and reported by Baines [16]. The number of nozzle vane can be predicted using the aforementioned correlation chart. The pitch (or vane spacing) at the nozzle outlet was estimated using equation (9.4) given the nozzle vane number, Z_s.

$$s_2 = \frac{2\pi r_2}{Z_s} \tag{20.4}$$

The width of nozzle throat, o_s was then estimated using cosine rule [13].

$$\cos\alpha_2 = \frac{o_s}{s_2} \tag{20.5}$$

The clearance gap between the nozzle outlet and the rotor inlet correlates to the turbine efficiency. The optimal clearance gap was proposed by proposed by Watanabe as a function of nozzle blade height, b_2 and outlet flow angle, α_2 [17].

$$\Delta r = 2b_2 \cos(\alpha_2) \tag{20.6}$$

The result of the design of the nozzle vanes for TC-9 and TC-12 was tabulated in Table 9.5.

Table 9.5: Principal geometry of the design of the nozzle vanes

Parameters	Units	TC-12	TC-9
Nozzle inlet angle	deg	49	43
Nozzle outlet angle	deg	71	58
Chord length	mm	10	9
Minimum number of nozzle vanes	-	18	13
Number of nozzle vanes	-	20	15
Pitch (or spacing of vanes)	mm	6	9
Width of nozzle throat	mm	2	5
Clearance between nozzle and rotor	mm	4.2	6.4

9.2.6 Application of the SMC adaptive strategy

The SMC adaptive strategy was applied to evaluate the performance of the selected turbine wheels for the ORC bottoming cycle. The meanline analysis technique was applied as the turbine performance map is not available. The overall calculation flow to evaluate the performance of the design point (from the cycle design mode) was presented in Figure 9.4. The calculation flow in Figure 9.5 shows the prediction of the performance at the non-design points (also known as part-load analysis).

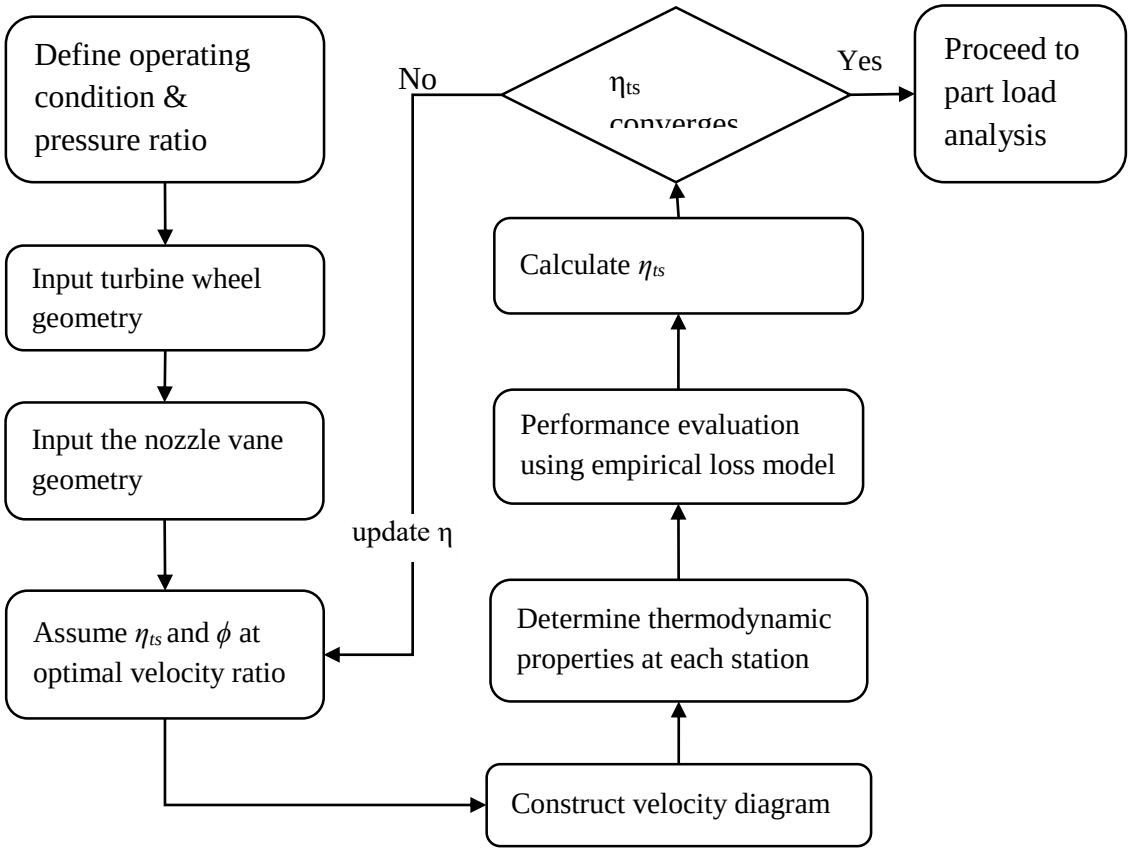

Figure 9.4: Meanline analysis of the turbochargers at optimal velocity ratio

The meanline analysis at the optimal velocity ratio was performed. The turbine operating condition and the geometry of the designed nozzle vanes and the turbine wheel were fed into the meanline analysis programme developed in EES. Velocity diagram was constructed and the thermodynamic properties were determined at each station, where station 1 is the nozzle inlet, station 2 is the nozzle outlet/rotor inlet, and station 3 is the rotor outlet. The turbine performance using the selected refrigerants was evaluated using the meanline analysis model outlined in Chapter 6. The calculated total-to-static isentropic efficiency was compared to the

assumed efficiency. If the error converges to a threshold value (1e-5 in this study), the numerical calculation proceeds to the next section, part load analysis. If the error does not fall within the range of the threshold value, the value of the assumed efficiency would be updated with the calculated value, until the convergence was achieved.

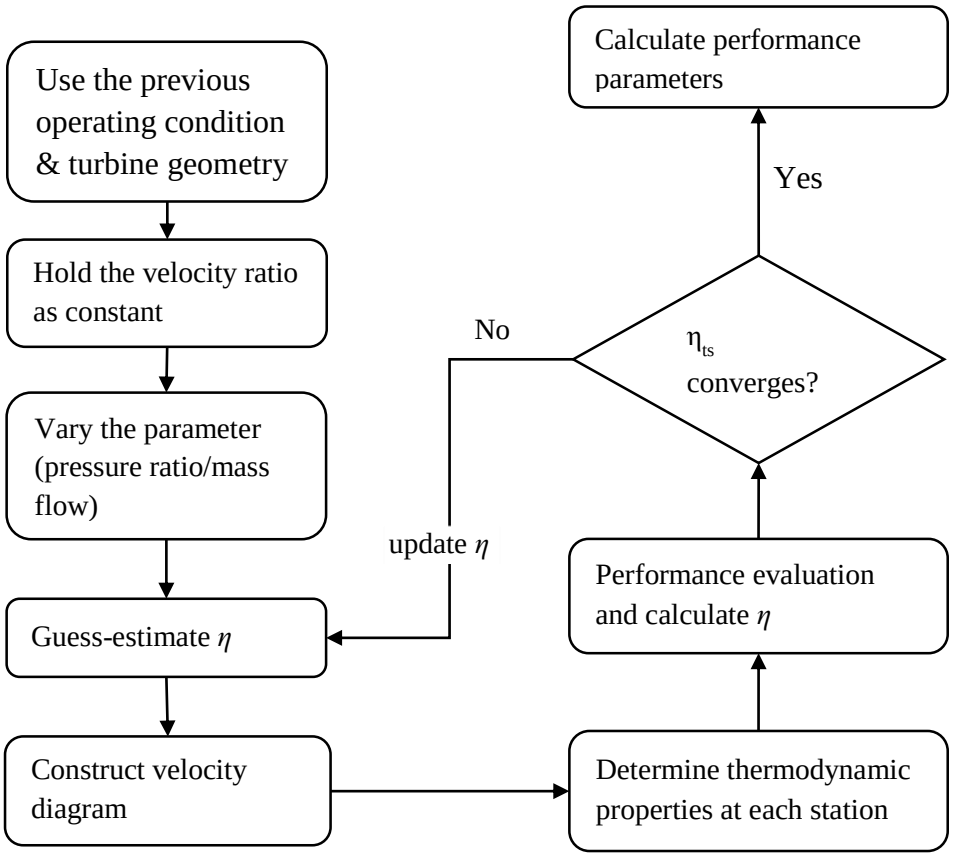

Figure 9.4: Evaluation of turbine performance at part-load operating conditions using meanline analysis

The performance analysis at the part load conditions (at different rotational speed/velocity ratio) was evaluated using Figure 9.5. The operating condition, and the geometry of the designed nozzle vanes and the turbine wheel were fed into the meanline analysis programme. The mass flow rate, $\dot{m}$ determined from Figure 9.4 was held constant. The velocity ratio was varied between 0.4 and 1.0. The efficiency was estimated, the velocity diagram was constructed, and the thermodynamic properties at each station was determined. The calculated efficiency was compared to the estimated value of the efficiency to check the convergence. The estimated value would be updated with new value of the efficiency, until the convergence was achieved. The turbine performance parameters, such as loading coefficient, and power output, were calculated subsequently.

Table 9.6: The performance of TC-9 and TC-12 at the optimal velocity ratio

		n-Pentane	R134a	R245fa	isobutane
TC-9					
Velocity ratio	-	0.7	0.7	0.7	0.7
Loading coefficient	-	0.7	0.7	0.7	0.7
Specific speed	-	0.76	0.76	0.76	0.76
Shaft speed	rev/min	81,688	59,094	60,173	80,751
Mass flow	kg/s	0.18	2.09	0.55	0.72
Power	kW	4.7	26.8	7.6	17.7
Isentropic efficiency (total-to-static)	-	0.69	0.66	0.68	0.67
Isentropic efficiency (total-to-total)	-	0.77	0.73	0.76	0.75
TC-12					
Velocity ratio	-	0.7	0.7	0.7	0.7
Flow coefficient	-	0.3	0.3	0.3	0.3
Specific speed	-	0.79	0.79	0.79	0.79
Shaft speed	rev/min	92,941	67,660	68,462	91,875
Mass flow	kg/s	0.15	1.73	0.46	0.60
Power	kW	4.6	27.2	7.5	17.5
Isentropic efficiency (total-to-static)	-	0.81	0.80	0.81	0.80
Isentropic efficiency (total-to-total)	-	0.85	0.84	0.85	0.84

The performance of TC-9 and TC-12 at the optimal velocity ratio was presented in Table 9.6. The optimal velocity ratio was assumed 0.7 for radial section blades [16]. The result shows that TC-12 is a better candidate for the planned ORC bottoming cycle with higher isentropic efficiency at 80%, compared to TC-9 with the isentropic efficiency in the range of 66 and 69%. The isentropic efficiency using TC-12 is similar for all four working fluids at the optimal velocity ratio. R134a was selected attributed to the highest shaft power among the four working fluids.

A part-load analysis was subsequently performed on TC-12 using R134a as the working fluid. Two scenario was considered: the first scenario is the mass flow was held constant and the pressure ratio was varied; the second scenario is the mass flow was varied and the pressure ratio was held constant.

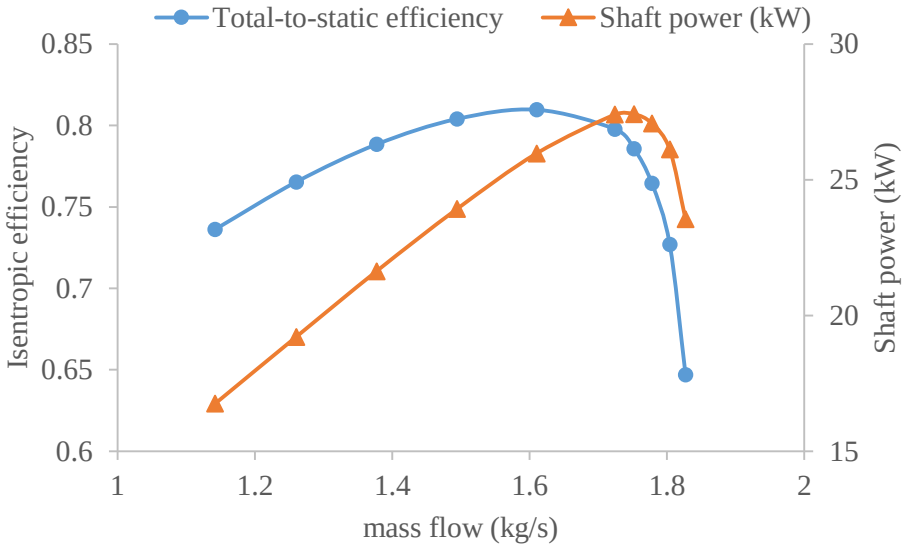

Figure 9.6: Performance of TC-12 using R134a at varying mass flow and constant pressure ratio of 2.8

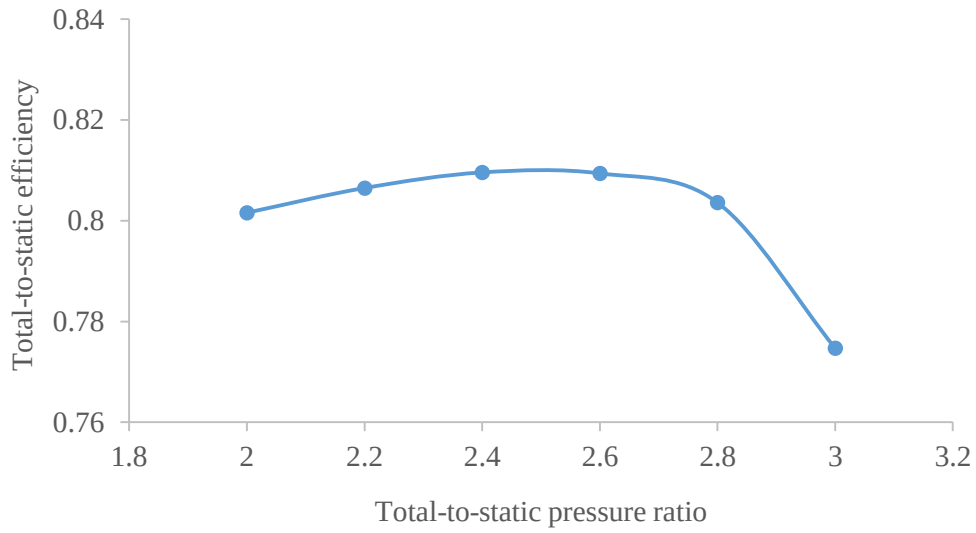

Figure 9.7: Performance of TC-12 using R134a at varying pressure ratio and constant mass flow

The performance of TC-12 was plotted in Figure 9.6 and Figure 9.7. The optimal mass flow to achieve maximum isentropic efficiency occurs at 1.6 kg/s whereas the optimal mass flow to achieve the maximum shaft power occurs at 1.8 kg/s. If the temperature of the cooling medium varies due to the seasonal variations, the pressure ratio across the turbine would be varied. The pressure ratio was varied between 2.0 and 3.0 to investigate the correlation between the pressure ratio and the turbine efficiency if the mass flow is held constant. The efficiency of TC-12 is fairly constant between the pressure ratio of 2.0 and 2.8. If the pressure ratio of the system is over 2.8, the turbine performance drops significantly.

The CFD analysis technique was not performed for the selected turbocharger as this unit was not suitable for the given heat resource. The design mass flow of the working fluid within the ORC loop is 43.3 kg/s (from Table 9.2) but the optimal mass flow of the selected turbine is between 1.6 and 1.8 kg/s. It implies that around 24 to 27 of the selected turbine wheels are required to be converted into single stage ORC turbines for the proposed heat resource. This solution is not cost efficient and the required space of installation is large, defying the original requirement of a small yet cost effective waste heat recovery system.

The performance map of TC-12 using R134a as the working fluid was fed into the cycle analysis model to evaluate the thermal efficiency of the overall system. The correlation between the cycle efficiency, the turbine efficiency and the temperature of the heat sink was illustrated in Figure 9.8. The efficiency of the selected turbine wheel is fairly constant at higher heat sink temperature. When the heat sink temperature is high, the temperature difference between the evaporator and the condenser is low. The pressure ratio across the turbine is low and the turbine efficiency is high as the selected turbine operates in optimal performance in a low pressure ratio range (based on Figure 9.7). When the heat sink temperature is low, the pressure ratio across the turbine is high, and the turbine efficiency is low. The performance map in Figure 9.8 also shows that the overall cycle efficiency is very sensitive to the temperature of the heat sink. The cycle efficiency drops significantly when the heat sink temperature is away from the optimal heat sink temperature.

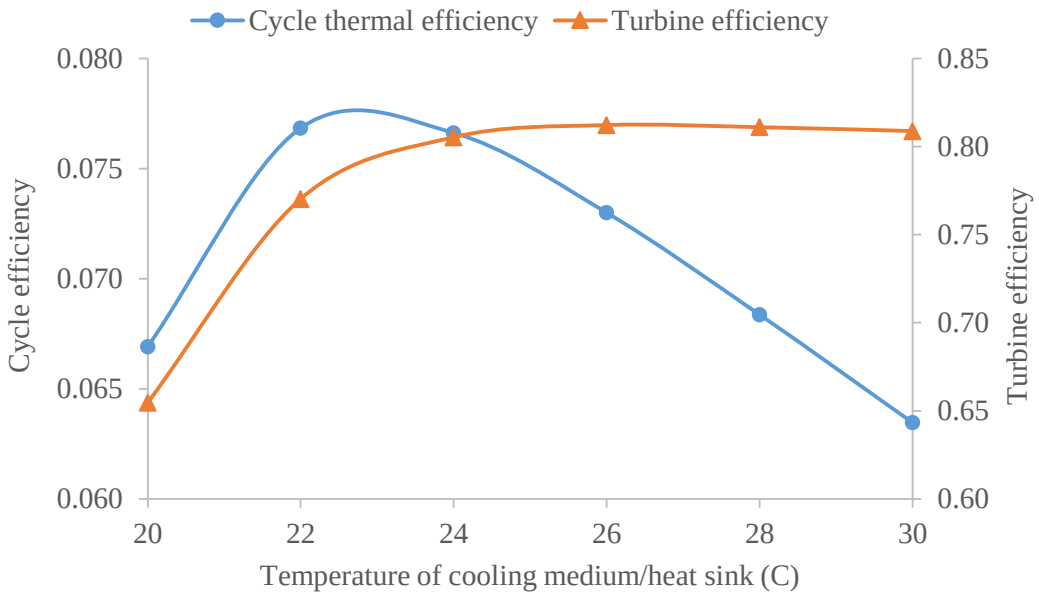

Figure 9.8: Performance of TC-12 using R134a at varying pressure ratio and constant mass flow

9.2.6 Mechanical design and system integration:

TC-12 shows a higher potential turbine efficiency compared to TC-9. The weight of TC-12 is smaller than TC-9, in which the transient performance of TC-12 is better during the start-up and shut-down procedure. However, the required rotational speed to achieve optimal velocity ratio using TC-12 is higher than TC-9 in the range of 4,000 and 11,000 rev/min at the similar pressure ratio. The objective of this thesis is to demonstrate the application of the SMC-DTR approach, instead of optimizing the power generation with the particular heat resource. Hence, a simple prototype design with direct coupling is preferable option to showcase the design process of the turbo-generator. Hence, TC-9 was selected to demonstrate the mechanical design and system integration of the SMC-DTR approach.

9.2.6.1 Functional testing

Turbochargers cannot be directly applied into the ORC system due to a number of issues, which are excessive leakage, poor sealing, unsuitable housing geometry and lubrication issues. The chosen turbocharger was tested in the research laboratory in University of Canterbury, as shown in Figure 9.9. The performance of the turbocharger, however, was not tested due to the constraint of the flow rate of the compressed air of the test facility. The test aims to investigate the required modification of the turbochargers for ORC application, as the potential leakage of refrigerants into environment would give rise to health and safety issues of the plant operators, and the environmental contamination.

Figure 9.9: Laboratory Leak Test Rig of Turbocharger TC-9

Leakages

Excessive leakage was found through the turbo gasket which is sandwiched between the turbine casings. The second major leak site was the bypass valve which is originally used to limit the pressure ratio across the turbine section and prevent over-speed of the shaft. The third leak site was along the shaft from the turbine side to the compressor side. Proper seal is not required in the automotive turbocharger as the exhaust gas could be safely released to the atmosphere. However, leakage is not tolerated in an ORC system depending on the working fluids.

Housing Geometry

The chosen turbocharger does not have a nozzle to direct and accelerate the flow into the turbine wheel, thus reducing the overall turbine efficiency. Hence, a new housing was designed with stationary vanes to redirect the flow into the turbine rotor.

Lubrication System

Oil-based lubricant was applied to lubricate the bushing and shaft in the selected turbocharger. This type of lubrication system is not suitable in the ORC turbine due to high differential pressure between evaporator outlet and condenser inlet. A separate oil pump with an external oil circuit is required for the ORC turbine. However, the mixture of oil and refrigerant will reduce the lubricating film thickness on the bearing and shaft which would be discussed in the following section. The proposed design would use working R245fa as direct lubrication which was described in the subsequent section.

9.2.6.2 Conceptual Design: Modification of Turbocharger into ORC Turbine

This section discusses the modification required to convert a turbocharger into an ORC turbine. The laboratory testing of the turbocharger determined the necessary modifications for the turbine wheel to be adapted, but the casing would need to be re-designed and the bearing would need to be re-selected. The turbine casing must be re-designed to a fully enclosed model to avoid leakage through open drive shaft. The turbine shaft would be coupled with a magnetic coupling which facilitates the coupling with an external high speed generator. O-rings would be installed between the turbine casings to prevent leakage of high pressure working fluid through the casing's gap. The proposed design of an ORC turbine by retrofitting the turbocharger is shown in Figure 9.10. Modular block design is proposed in the design of a prototype in order to simplify the manufacturing process.

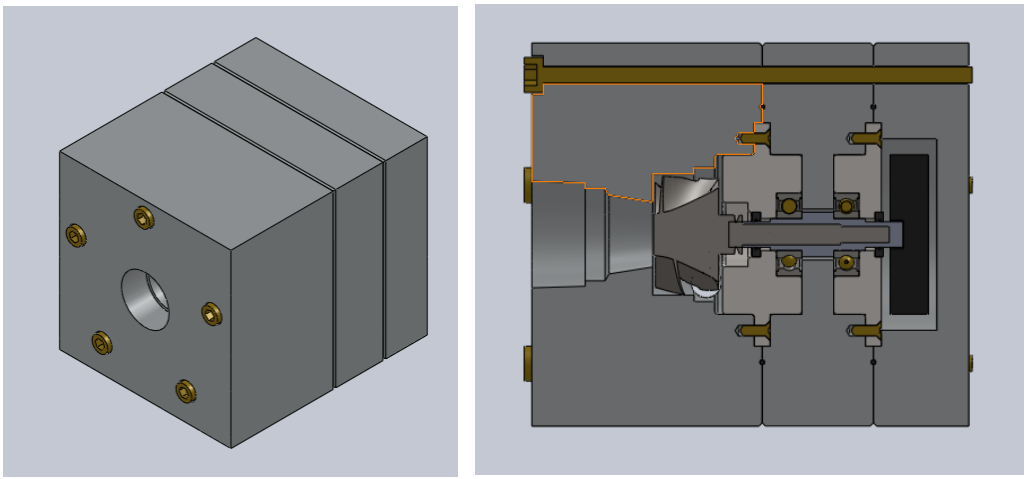

(a) (b)

Figure 9.10: Isometric view and cross-sectional view of proposed design of ORC turbine

Selection of Bearings

Bearings are required to support a rotor shaft in the turbine assembly. The turbine assembly commonly requires radial bearings and thrust bearings to support both the radial load and axial thrust. Literature review on steel bearings and hybrid bearings shows that hybrid bearings are the most suitable bearings for ORC application. In a study by Molyneaux, hybrid bearings were found to be more suitable than steel bearings in an ORC turbine [18]. The application of hybrid bearings for refrigerants has also been suggested by Jacobson as the hybrid bearings have optimal raceway topography to ensure the maximum elastic deformation of the asperities in Hertzian contact as compared to steel bearings [19]. The optimization of the raceway allows an effective separation of the mating surfaces, further allowing the bearing to withstand pure refrigerant lubrication for long periods [19]. The proposed design of the ORC turbine would be equipped with a pair of hybrid bearings to provide a longer life under lubrication from pure refrigerants.

Selection of Lubricants

The bearings for steam turbines are usually lubricated by oil lubricants with an external or separate oil circuit and oil pump [20] whereas the bearings in the ORC application are lubricated by the working fluid [21]. Two journal bearings and a thrust bearing were lubricated with R134a in an 18 kW oil-free compressors investigated by Molyneaux [18], and journal bearings and thrust bearings were lubricated by toluene in a 25 kW solar-powered ORC system investigated by Nesmith [22]. Common issues in bearing failures by using refrigerants include

the attack of bearing surfaces by some refrigerants such as ammonia [19]. Many refrigerants tend to dissolve into lubricants, such as R134a in ester oil. The mixture reduces the initial lubricant viscosity and pressure viscosity coefficient thus reducing the film thickness during lubrication process. Furthermore, the boiling point of the refrigerant-oil mixture is reduced at the local pressure [23]. The reduction in boiling point allows vaporization of lubricant on the bearing surface when the bearing surface temperature is higher than the boiling point of the mixture, thus reducing the lubricant film thickness [19]. The ORC turbine would use the working fluid as lubricant for the bearings to reduce the cost and complexity of the external lubrication system.

The rheology of three working fluids, R245fa, R134a and R123 has been studied to select an optimal lubricant for the bearing. Among the three working fluids, R245fa has been found as a better lubricant for rolling bearings followed by R134a, and lastly R123 [19]. Though R134a is a relatively poor lubricant compared to R245fa, R134a has been employed as the lubricant in an oil-free compressor [18] as the pressure viscosity coefficient of R134a is very similar to the pressure viscosity coefficient of poly alpha olefin oil [19]. The proposed design of turbo-expander in Figure 9.9 was designed to be lubricated by R134a.

Casing Design and Seal Selection

The turbine casing can be categorized into enclosed and open-drive designs. In an open drive design, the turbine shaft is coupled to an external generator for power generation. The working fluid would leak into atmosphere due to high differential pressure between the fluid inside the turbine and the atmosphere. The most common sealing system for an open drive design is a dry gas seal and a mechanical seal which are not suitable for small size turbo-generators. The need for an extra gas buffer system and lubrication system to the seal increases the cost of the turbo-generator. In a fully enclosed design, the turbine shaft is coupled to a high speed generator within the enclosed casing. Due to the scarcity of off-the-shelf high speed generators, the proposed design of ORC turbine would be connected to a magnetic coupling which facilitates the coupling to an external generator. The casing surrounding the magnetic coupling would be made from aluminium to allow the operation of magnetic coupling.

9.3 Conclusion

This chapter presents the application of the SMC-DTR approach on two nozzle-less automotive turbochargers, named TC-9 and TC-12 in a planned waste heat recovery (WHR) system for a petroleum refining plant in New Zealand with constant heat source and heat sink temperature. The objective of this chapter is to present the SMC-DTR approach. A thermodynamic cycle of an ORC system was designed for the kerosene flow in the refinery plant. The SMC turbine adaptive strategy was applied to evaluate the performance of two turbochargers with four different working fluids (n-Pentane, R134a, R245fa, and isobutane). The meanline analysis technique was applied as the performance map of the selected turbine is not available. TC-12 and R134a were determine as the best solution as they show the maximum turbine efficiency and the shaft power compared to other options. However, the selected turbocharger was found not cost-effective for the proposed heat resource. Hence, the CFD analysis in the SMC-DTR approach was not applied. The performance map of TC-12 with R134a was fed into the cycle analysis model to evaluate the correlation between the cycle performance and the temperature of the cooling medium (or heat sink). Turbocharger cannot be converted directly as an ORC turbine. Hence, a mechanical concept design was presented in modifying and adapting the turbocharger as an ORC turbine. This chapter presents the key steps in the SMC-DTR approach: designing the thermodynamic cycle, evaluating the turbine performance with different working fluids, optimizing the cycle efficiency with different turbine options and different working fluids, investigating the performance of the selected turbine as a function of the heat sink temperature, and the modification and adaption of the turbocharger into an ORC turbine.

One important lesson from this study is the feasibility of adapting a nozzle-less automotive turbocharger in an ORC application. However, nozzle has to be designed to direct the flow into the turbine rotor at an optimal flow angle to yield the optimal turbine performance. Another lesson is the same turbine wheel can be applied for different working fluid to produce different amount of work output; TC-12 is expected to produce 4.6 kW using n-Pentane, 27.2 kW using R134a, or 17.5 kW using isobutane. The difference is attributed to the mass flow into the turbine wheel, which is affected by the specific volume of each working fluid. Lastly, the performance of the adapted turbocharger is optimal at low pressure ratio less than 3.0. If the pressure ratio increases, the turbine performance drops significantly.

9.4 References

1. Merz, S.K. *Assessment of Current Costs of Geothermal Power Generation in New Zealand (2007 Basis)*. 2009.
2. Quoilin, S., et al., *Techno-economic survey of Organic Rankine Cycle (ORC) systems.* Renewable and Sustainable Energy Reviews, 2013. **22**(0): p. 168-186.
3. Qiu, G., H. Liu, and S. Riffat, *Expanders for micro-CHP systems with organic Rankine cycle.* Applied Thermal Engineering, 2011. **31**(16): p. 3301-3307.
4. Orosz, M., et al., *Small Scale Solar ORC system for distributed power.* Proc. of the SolarPaces Conference, 2009.
5. Holdmann, G., *The Chena Hot Springs 400kW geothermal power plant: experience gained during the first year of operation.* Chena Geothermal Power Plant Report, Chena Power Plant, Alaska, 2007: p. 1-9.
6. Buerki, T., et al., *Use of a Turbocharger and Waste Heat Conversion System*. 2010, EP Patent 2,092,165.
7. Aneke, M., B. Agnew, and C. Underwood, *Performance analysis of the Chena binary geothermal power plant.* Applied Thermal Engineering, 2011. **31**(10): p. 1825-1832.
8. DiPippo, R., *Second law assessment of binary plants generating power from low-temperature geothermal fluids.* Geothermics, 2004. **33**(5): p. 565-586.
9. Ghasemi, H., et al., *Modeling and optimization of a binary geothermal power plant.* Energy, 2013. **50**(0): p. 412-428.
10. Legmann, H. and P. Sullivan. *The 30 MW Rotokawa I geothermal project five years of operation*. in *International Geothermal Conference*. 2003.
11. Jung, H.C., S. Krumdieck, and T. Vranjes, *Feasibility assessment of refinery waste heat-to-power conversion using an organic Rankine cycle.* Energy Conversion and Management, 2014. **77**(0): p. 396-407.
12. Glassman, A.J., *Computer program for design analysis of radial-inflow turbines.* 1976.
13. Aungier, R.H., *Turbine aerodynamics: axial-flow and radial-inflow turbine design and analysis*. 2006: ASME Press.
14. Dixon, S.L. and C. Hall, *Fluid Mechanics and Thermodynamics of Turbomachinery*. 2010, Butterworth-Heinemann: Burlington.
15. Wasserbauer, C.A. and A.J. Glassman, *FORTRAN program for predicting off-design performance of radial-inflow turbines.* NASA Technical Paper, 1975(TN D-8063).
16. Moustapha, H., et al., *Axial and Radial Turbines*. 2003: Concepts Eti.
17. Watanabe, I., I. Ariga, and T. Mashimo, *Effect of dimensional parameters of impellers on performance characteristics of a radial-inflow turbine.* Journal of Engineering for Power, 1971. **93**: p. 81.
18. Molyneaux, A. and R. Zanelli, *Externally pressurised and hybrid bearings lubricated with R134a for oil-free compressors.* 1996.
19. Jacobson, B.O. and G.E.M. Espejel, *High Pressure Investigation of Refrigerants HFC245fa, R134a and R123.* 2006.

20. Couchman, R., K. Robbins, and P. Schofield, *GE Steam turbine design philosophy and technology programs.* GE Company, Schenectady, NY, Report No. GER-3705, 1991.

21. David Japikse, F.D.B., Maxwell Hurgin, Keith Patch. *Development of a 300 kWe Integrated Axial Turbine and Generator for ORC Applications*. in *2nd Internal Seminar on ORC Power Systems: Turbo Expanders II*. 2013. De Doelen, Rotterdam, The Netherlands: American Society of Mechanical Engineers (ASME).

22. Nesmith, B., *Bearing development program for a 25-kWe solar-powered organic Rankine-cycle engine*. 1985, Jet Propulsion Lab., Pasadena, CA (USA).

23. Yamamoto, Y., S. Gondo, and J. Kim, *Solubility of HFC134a in Lubricants and Its Influence on Tribological Performance.* Tribology transactions, 2001. **44**(2): p. 209-214.

10.0 Application of the SMC-DTR using CFD Analysis on Turbine with Fix Nozzle Vane

The aim of this thesis is to present the SMC-DTR approach for low temperature resources, and the main contribution of this thesis is to develop the key component, SMC analysis approach. This chapter presents the application of the SMC-DTR approach by adapting a radial gas turbine with fixed nozzle vanes for a resource condition with constant heat source temperature and varying heat sink temperature. This approach was utilized to design an air-cooled binary plant for a geothermal reservoir in Rotokawa, New Zealand. The selected turbine is a 37 kW radial flow gas turbine with fix nozzle vanes, and the turbine is originally designed for the Sundstrand Power Systems T-100 Multipurpose Small Power Unit. The CFD analysis technique was applied as there is only one available radial gas turbine for this study. The geometry of the turbine is available from the published literature, and the 3D model was re-generated using the one of the modules in the ANSYS Turbomachinery package, Blade-Gen. Both the thermal efficiency and the exergy efficiency (also known as utilization efficiency) are the objective functions of the cycle design in this chapter. A binary plant model was designed and developed for the geothermal heat source condition using the ambient air as the heat sink. The performance was interpreted as overall stage performance and detailed flow field analysis. The overall stage performance was fed into the cycle analysis model to optimize the cycle performance at different air temperature, whereas the flow behaviour in the radial gas turbine was presented via the detailed flow field analysis. The effect of the air temperature on the condenser temperature, and thus on the operation of the turbine was studied.

The result shows that the adaptation of a radial gas turbine with fixed nozzle vanes is feasible to produce an acceptable range of turbine performance in an ORC application. The turbine performance changes if the working fluid is changed from one into another. One lesson from this study is that the radial gas turbine was originally designed and developed for subsonic expansion process. If the selected working fluid requires high expansion ratio across the turbine for the supersonic expansion, the turbine performance drops significantly due to the mismatch to the blade passage design to the expansion behaviour. Another lesson is the performance of the turbine and the binary cycle changes within 1 to 2% when the heat sink temperature changes from 10 to 23˚C. Hence, a radial turbine with fixed nozzle vanes can provide an acceptable cycle performance at both design and off-design points for the resource condition with varying heat sink temperature.

10.1 Introduction

The turbine technologies suitable for a geothermal binary plant are the multiple stage axial turbine and the single stage radial inflow turbine. The geothermal binary plant in Ngatamariki, New Zealand is powered by a two-stage axial turbine whereas the binary plant in Still Water, Nevada, US, is powered by a single stage radial inflow turbine. The concept of adapting a gas turbine for binary plant was proposed by the author to reduce the design and development cost of the turbine for binary plant. This concept facilitates the new entrants to the ORC market without the decades of engineering development required for new turbine design. The application of the radial gas turbines into a binary plant provides an alternative turbine solution, which would assist the development of Organic Rankine cycle (ORC) in geothermal, waste heat recovery, and biomass applications. However, the application of the market available gas radial turbines using refrigerants has not been investigated and no relevant open literature was found.

The application of the radial gas turbines into a binary plant still imposes a number of questions, including:

- Does the turbine stage provide the similar efficiency using the working fluids different from the original design? And
- Is the adapted turbine sensitive to the change in operating condition?

The performance of an air-cooled binary plant is susceptible to the change in ambient temperature. For example, the net power output of the air-cooled geothermal plant was reduced by up to 40% from winter to summer in northern Nevada [1]. The change in ambient temperature affects the pressure ratio and the mass flow across the turbine. A turbine is usually designed for a set of mass flow rate and pressure ratio. If the pressure ratio and the mass flow change, the turbine efficiency drops. Hence, an accurate turbine off-design model is crucial in predicting the performance of an air-cooled binary plant across the life cycle. Several researchers have investigated the off-design effects of the ORC. The change in ambient temperature contributes to off-design performance of the turbo-generator. Greg [2] has modelled the turbine off-design performance as a deviation from the velocity ratio using the corrections chart from Balje [3]. The turbine correlation chart developed by Balje, however, is limited to incompressible fluids [3]. The turbine-generator efficiency was assumed to be constant by Cengel [1] and Marco [4] in modelling the binary geothermal plant. Mitsos modeled the turbine performance with isobutane as a function of the design isentropic

efficiency, ratio of enthalpy drop and ratio of volumetric flow rate [5]. None of the model has utilized the CFD analysis in modelling an ORC system due to the high computational cost. One advantage of utilizing the SMC-DTR approach is the performance of the adapted (or selected) turbine has to be fed back into the cycle model to determine the turbine performance at both design point and the off-design points. This step allows an engineer or a financial analyst to predict the earnings and the financial benefits of the design more accurately.

This chapter aims to showcase the application of the SMC-DTR approach (illustrated in Figure 10.1) by adapting a radial gas turbine with fixed nozzle vanes to design an air-cooled geothermal binary plant for resources with varying heat sink temperature. The SMC adaptive strategy was applied to evaluated the turbine performance, and the CFD analysis technique was applied (based on the criteria selection presented in Figure 10.2) as there is only one available turbine option in this case study. The turbine performance map was fed into the cycle analysis model to evaluate the performance of the turbine and the binary cycle at varying heat sink temperature.

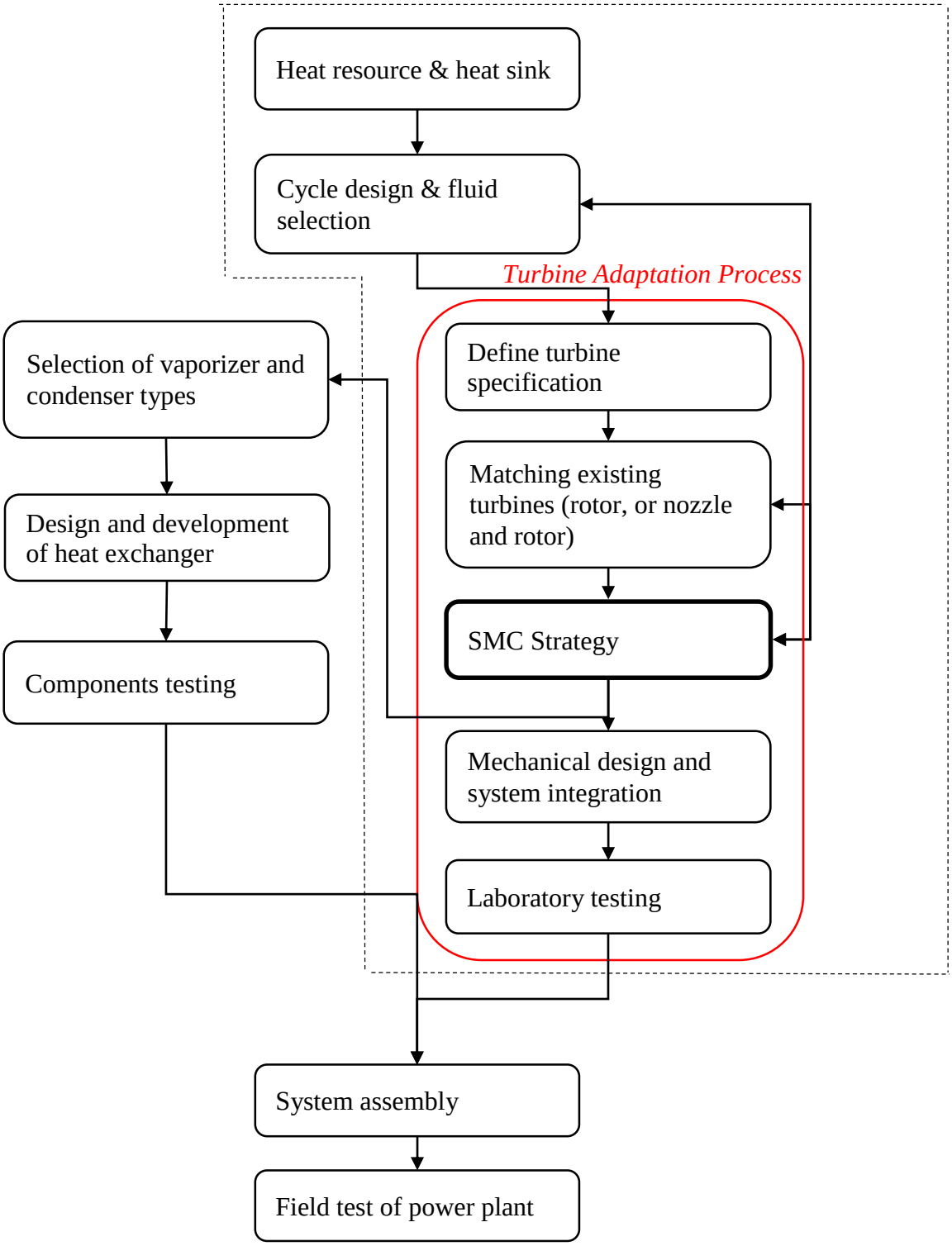

Figure 10.1: The SMC-DTR approach for LT-ORC

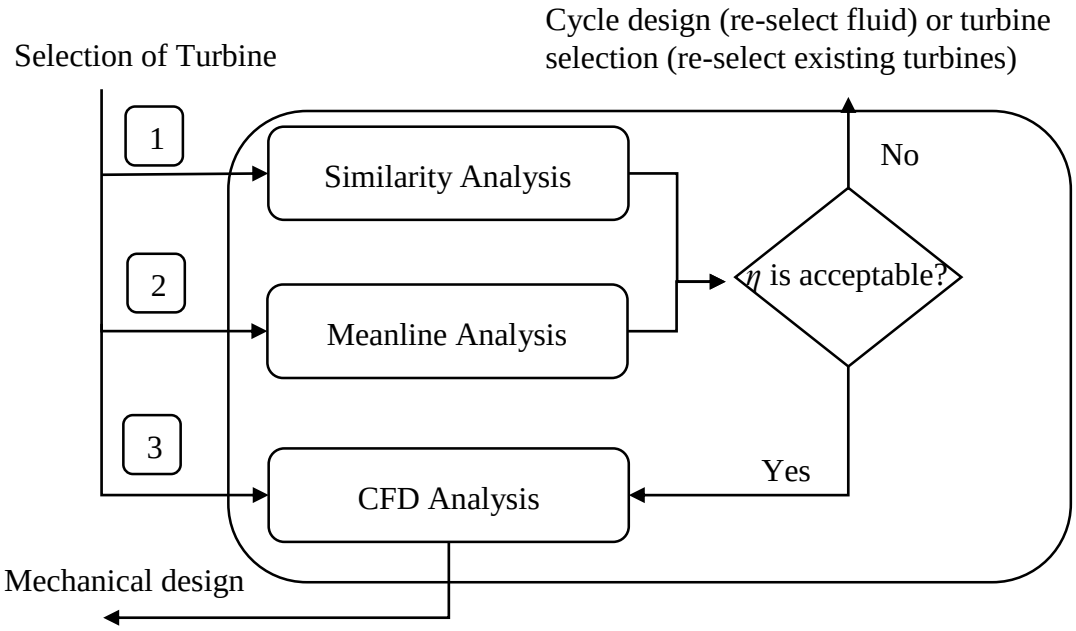

1: Turbine performance map (using air as working medium) is available.
2: Turbine performance map is not available.
3: Only one existing turbine is available.

Figure 10.2: SMC adaptive strategy

10.2 Application of the SMC-DTR Approach to Design an Air-Cooled Binary Plant

The SMC-DTR approach was presented to design an air-cooled geothermal binary plant based on an industrial radial gas turbine. The selected gas turbine was originally designed and developed for the Sundstrand Power Systems model T-100 Multipurpose Small Power Unit with nominal power output of 37 kW, with capability up to 75 kW [6]. A binary plant model was designed using four different working fluids (R134a, R245fa, n-Pentane, and isobutane) was developed using the heat source and heat sink condition in Rotokawa. The turbine specification and the matching to the existing turbines were not performed as there is only one available radial gas turbine with published geometry for use in this study. The performance of the selected radial gas turbine was evaluated using the SMC adaptive strategy. The performance curve of the radial turbine using different working fluids was generated. The performance map of the selected turbine was fed into the cycle analysis model to predict the overall cycle performance at different ambient temperature. The mechanical design process was not performed as the process would be very similar to the adaptation process in chapter 9.

10.2.1 Heat source and heat sink

A case study was performed using the Rotokawa geothermal reservoir as the heat source and the ambient air as the heat sink. The Rotokawa geothermal steam field is one of the largest geothermal reservoir in use for power generation in New Zealand. Steam power plants and binary plants have been installed using the Rotokawa geothermal reservoir to produce over 100 MW. The temperature of the geothermal brine of the binary plant was used as the case study in this chapter. The temperature of the brine fed into the evaporator (also known as vaporizer) is 217.5°C and the injection well temperature is 150°C [7].

The designed geothermal plant is proposed to have the same cooling mechanism as the actual binary plant installed in Rotokawa, which is air-cooled condenser. The design ambient temperature is set at 12°C and the mean temperature across the year was plotted in Figure 10.3. The distribution of the ambient temperature 11 km from Rotokawa (latitude at -38.68°, longitude at 176.07°, and height at 385m) was extracted from the climate database [8]. The temperature includes mean monthly, mean daily maximum, and mean daily minimum air temperature shown in year 2012. The mean monthly temperature was applied in the binary plant model in the later section to investigate the binary plant behavior across the year.

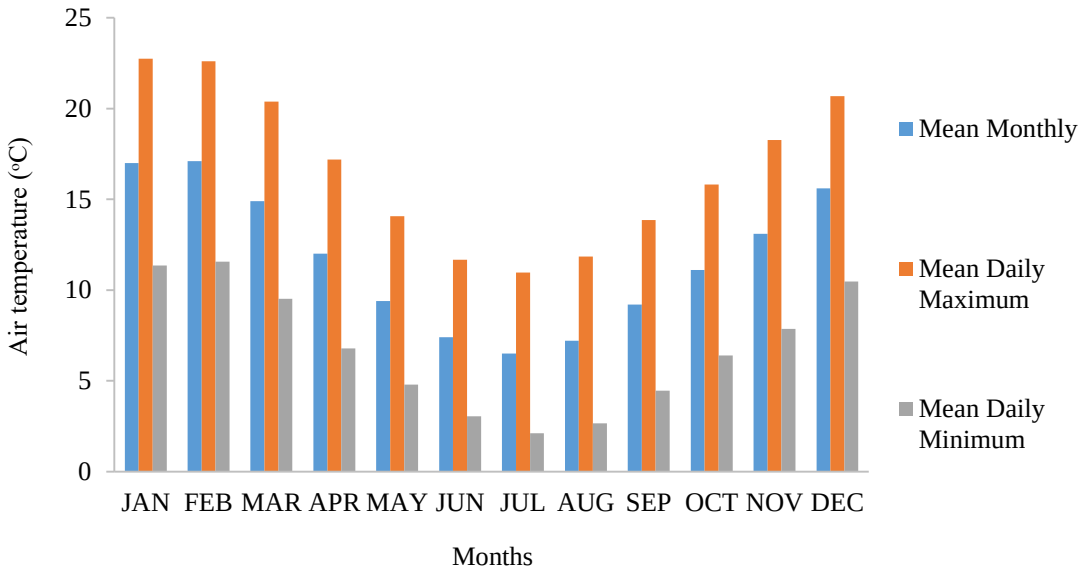

Figure 10.3: Average air temperature in Taupo in year 2012

10.2.2 Cycle design and fluid selection

The thermodynamic model of the cycle analysis in Chapter 3 was applied with the following assumptions:

- Negligible pressure loss across the heat exchangers and pipe fittings
- Ideal heat transfer across the heat exchangers without losses into the atmosphere
- Pressure loss across the piping is negligible
- Air side pressure drop in the air cooled-condenser is 170 Pa [9]
- Degree of sub-cooling: 0^{o}C
- Differential temperature at the condenser pinch: 5^{o}C
- Fan efficiency: 80%
- Generator efficiency: 95%
- Pump efficiency: 80%

Four different working fluids were applied in the cycle design and analysis model: n-Pentane (also known as normal pentane), R134a, R245fa, and isobutane. R134a is a wet fluid, R245fa is an isentropic fluid, and n-Pentane and isobutane (R600a) are dry fluid [10]. A large amount of superheat is required for wet fluid to avoid the formation of liquid droplet at the turbine outlet and prevent the damage of the turbine rotor from cavitation effects. R134a is superheated up to 10^{o}C to avoid wet expansion. Superheat for dry fluid and isentropic fluid is not required as the superheat would reduce the overall cycle efficiency [10]. However, if the evaporator is sized at the design point with zero degree of superheat, the fluid might end up in the saturated state at the off-design operating points. Hence, the evaporator has to be oversized and the degree of superheat was set at 3^{o}C for the three working fluids.

The installation cost and the operational cost of a plant is affected by the maximum allowable pressure. High pressurized piping has to be installed if the working pressure is over 25 bar (equivalent to 2,500 kPa), and the capital cost would be increased. Hence, the maximum allowable pressure was limited below 2,500 kPa to avoid the application of high-pressurized piping and equipment in this chapter. The turbine operating requirements (the inlet condition and the pressure ratio) were determined assuming a constant turbine efficiency at 80%, and tabulated in Table 10.1.

Table 10.1: Turbine inlet condition

Fluid	R134a	n-Pentane	Isobutane	R245fa
Type	Wet	Dry	Dry	Isentropic
T_{in} (C)	85	178	113	133
P_{in} (kPa)	2,366	2,427	2,381	2,339
Pressure ratio	2.4	25	4.7	10.2

Degree of superheat (C)	10	3	3	3
η_{cycle}	5.9 %	15.4%	10.0 %	12.1%
Nominal Power (kW)	55 kW	300 kW	80 kW	135 kW

There is a significant difference in the predicted plant performance (especially the potential power output) for the same configuration, the same turbine efficiency, and the same temperatures attributed solely to the working fluid thermodynamic behavior. The maximum cycle efficiency was achieved by n-Pentane, in line with the maximum cycle temperature. However, the required pressure ratio using n-Pentane is too high for the selected radial gas turbine in a single stage configuration. A multi-stage axial turbine is required to achieve the required pressure ratio in subsonic expansion process within the turbine passage. Hence, the CFD analysis was performed using the other three working fluids, R134a, R245fa and isobutane.

The theoretical maximum thermal efficiency of a thermodynamic cycle is usually estimated using Carnot efficiency assuming an isothermal heat addition at the heat source temperature and an isothermal heat rejection at the heat sink temperature. However, the brine does not serve as an isothermal heat source since the brine temperature decreases during the heat transfer process. DiPippo has proposed a triangular cycle efficiency with an isobaric heat addition process to better represent the possible maximum cycle efficiency for the binary plant [11].

$$\eta_{TRI} = \frac{T_H - T_L}{T_H + T_L} \tag{21.1}$$

Where η_{TRI} is the triangular cycle efficiency (also known as theoretical maximum efficiency of a binary plant), T_H is the heat source temperature, the brine inlet temperature, and T_L is the heat sink temperature, the ambient air temperature. This efficiency serves as a benchmark to the cycle performance for different working fluids in this chapter.

10.2.3 Define turbine specification:

This step was not performed as this chapter aims to investigate the potential turbine efficiency and power output of adapting the radial gas turbine for the given heat resource.

10.2.4 Matching existing turbines:

This step was not performed since there is only one available radial gas turbine with published geometry for use in this study. Hence, it is not necessary to select a suitable turbine from a pool of options using this method.

10.2.5 Application of the SMC Adaptive Strategy

The SMC adaptive strategy was applied to evaluate the performance of the selected radial gas flow turbine for the air-cooled binary plant. The CFD analysis technique was applied as there is only one existing turbine available for the given heat source. The gas turbine was designed and developed originally for air at high speed operation, at 106,588 rev/min with nominal power of 37 kW. A number of modification is required to adapt the radial gas turbine into an ORC turbine, including the replacement of the high speed generator to a lower speed generator, re-design the casing and re-design the mechanical system to contain the refrigerants from leaking into the atmosphere. This section presents the CFD analysis technique of the SMC adaptive strategy to evaluate the turbine performance before proceeding to the mechanical system design. The CFD analysis aims to predict the turbine performance and determine the optimal turbine operating condition. The process flow of applying the CFD analysis was presented in Figure 10.4. The detail of the CFD analysis was discussed and presented in Chapter 7.

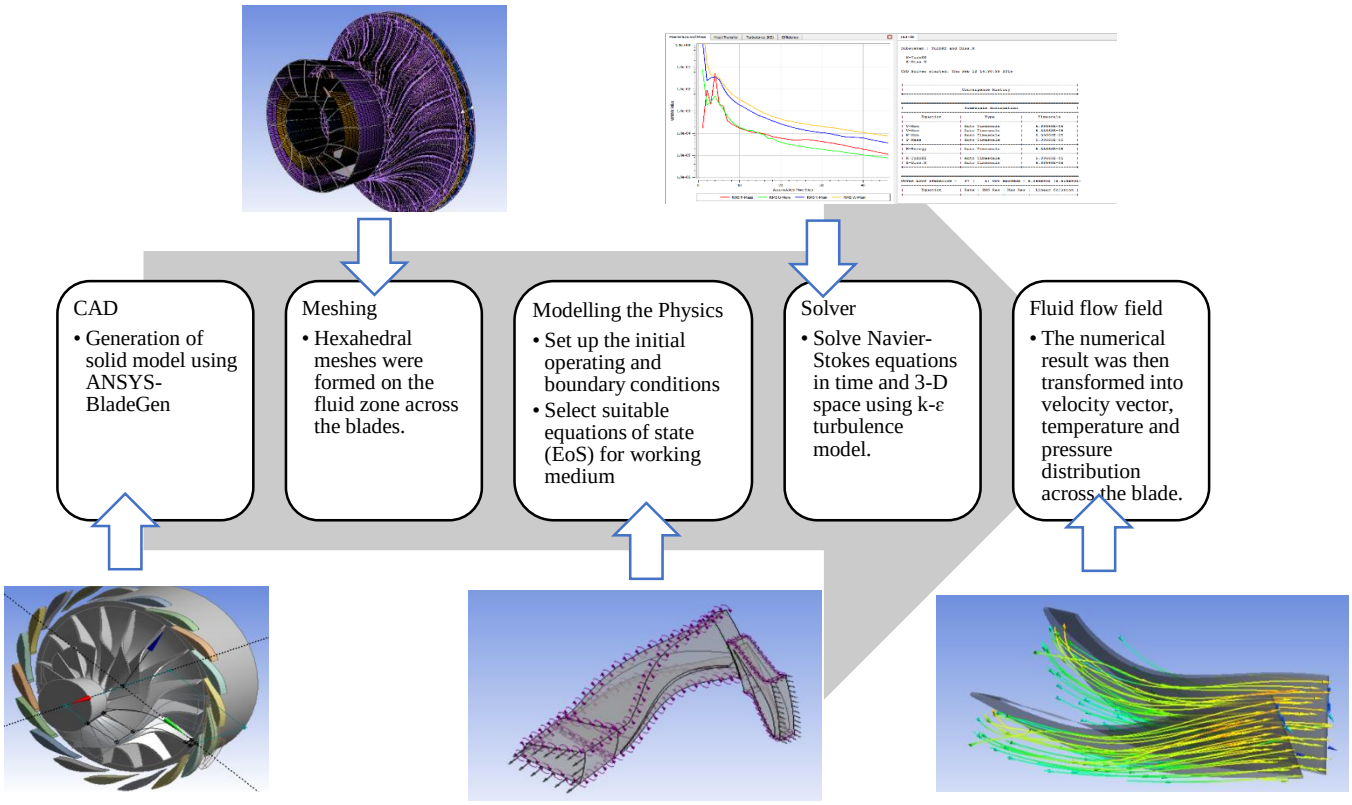

Figure 10.4: Process flow of applying CFD analysis technique

The CFD analysis technique involves a number of critical steps: generate the 3D model, mesh the flow domain, set up the boundary condition, solve the Navier-Stokes equations, and analyze the data. The 3D model of the turbine nozzle and rotor was re-generated using ANSYS Blade-Gen and the flow domain was meshed using ANSYS Turbo Grid. Steady state analysis was performed via ANSYS-CFX 14.5 to determine the overall performance of the radial turbine, as detailed in Chapter 7. *Frozen rotor* was defined at the interface between the nozzle and rotor in ANSYS-CFX to take account of the non-axisymmetric flow at the interface. The model was first validated using air as the working fluid with the published experimental data [6]. The result of the CFD model agrees with the experimental data with error less than 1% in the efficiency, and the detail was presented in Chapter 7.

The operation of the gas turbine using other working fluids, refrigerant and hydrocarbon with heavy molecular weight, requires a lower rotational speed, in which the rotational speed can be determined at the optimal velocity ratio.

$$\frac{U_2}{C_{is}} = \frac{U_2}{\sqrt{2\Delta h_{is}}} \tag{21.2}$$

Where U_2 is the tip speed at the rotor inlet, C_{is} is the velocity of the fluid if the fluid is expanded in an ideal nozzle with the equivalent pressure ratio, and Δh_{is} is the isentropic enthalpy drop at the given pressure ratio. The performance of the turbine is characterized using the thermal efficiency (thermodynamic First-Law efficiency) and exergy efficiency (thermodynamic Second-Law efficiency) [11].

$$\eta_{I,turbine} = \frac{h_{01} - h_{03}}{h_{01} - h_{3,is}} \tag{21.3}$$

Where $\eta_{I,turbine}$ is the thermal efficiency of the turbine, h_{03} and h_{03} are the total enthalpy (stagnation enthalpy) at the turbine nozzle inlet and the turbine rotor outlet, and $h_{3,is}$ is the isentropic enthalpy at the turbine rotor outlet.

$$\eta_{II,turbine} = \frac{h_{01} - h_{03}}{\left(h_{01} - h_{03}\right) + T_0(\mathrm{s}_3 - \mathrm{s}_1)} \tag{21.4}$$

Where $\eta_{II,turbine}$ is the exergy efficiency of the turbine, T_0 is the dead state temperature, where the dead state temperature of the air-cooled binary plant is the ambient temperature (or dry bulb temperature of the air), s_1 is the entropy at the turbine nozzle inlet and s_3 is the entropy at the turbine rotor outlet.

10.2.5.1 Integration of Fluid Properties from Fluid Database into ANSYS CFX

This section presents the method to develop the real fluid database in ANSYS CFX using the fluid database by National Institute of Standards and Technology (NIST). ANSYS CFX version 14.5 has inbuilt fluid properties for R134a but it does not have the fluid properties for R245fa and isobutane. The fluid information has to be manually set up to allow the generation of the table of fluid properties during the simulation. The in-built Aungier Redlich Kwong model would be applied to determine the fluid properties for the selected fluids, R245fa and isobutane [12].

$$p = \frac{RT}{v - b + c} - \frac{a(T)}{v(v + b)} \tag{21.5}$$

Where p is the pressure, R is the specific gas constant, T is the temperature, v is the specific volume, a, b, and c are model coefficients. The model coefficients can be calculated using the equations below.

$$a = a_0 \left(\frac{T}{T_c} \right)^{-n} \tag{21.6}$$

$$a_0 = \frac{0.42747 R^2 T_c^{\,2}}{p_c} \tag{21.7}$$

$$n = 0.4986 + 1.1735\omega + 0.4754\omega^2 \tag{21.8}$$

Where T_c is critical temperature, p_c is critical pressure, ω is acentric factor.

$$b = \frac{0.08664 R T_c}{p_c} \tag{21.9}$$

$$c = \frac{R T_c}{p_c + a_0 / v_c (v_c + b)} + b - v_c \tag{21.10}$$

Where v_c is critical specific volume. The enthalpy and the entropy has to be determined by the flow solver to evaluate the enthalpy change and the irreversibility effect across the turbine stage. The enthalpy is determined from the internal energy equation as below.

$$du = c_v dT + \left[T \left(\frac{dp}{dT} \right)_v - p \right] dv \tag{21.11}$$

$$h = u + pv \tag{21.12}$$

Where c_v is isochoric specific heat, u is internal energy, and h is enthalpy of the fluid.

The entropy change is evaluated using integral below, where c_{p0} is zero pressure ideal gas specific heat capacity.

$$s(T,v) - s(T_{ref}, v_{ref}) = \int_{v_{ref}}^{\infty} \left(\frac{dp}{dT} \right)_v dv_{T_{ref}} + \int_{T_{ref}}^{T} \frac{c_{p0}}{T} dT - R \ln \left(\frac{p}{p_{ref}} \right) - \int_{v}^{\infty} \left(\frac{dp}{dT} \right)_v dv_T \tag{21.13}$$

The zero pressure ideal gas specific heat capacity is expressed as a fourth order polynomial equation as a function of temperature [13].

$$\frac{C_{p0}}{R} = a_1 + a_2 T + a_3 T^2 + a_4 T^3 + a_5 T^4 \tag{21.14}$$

The correlation of C_{p0}/R and temperature of isobutane and R245fa was plotted in Figure 10.5. A curve fitting algorithm in Microsoft Excel was applied to determine the values of the coefficients. The required user's inputs for the selected fluids, R245fa and isobutane, such as

the thermodynamic properties, the reference state, and the coefficients for the specific heat capacity, were shown in Table 10.2.

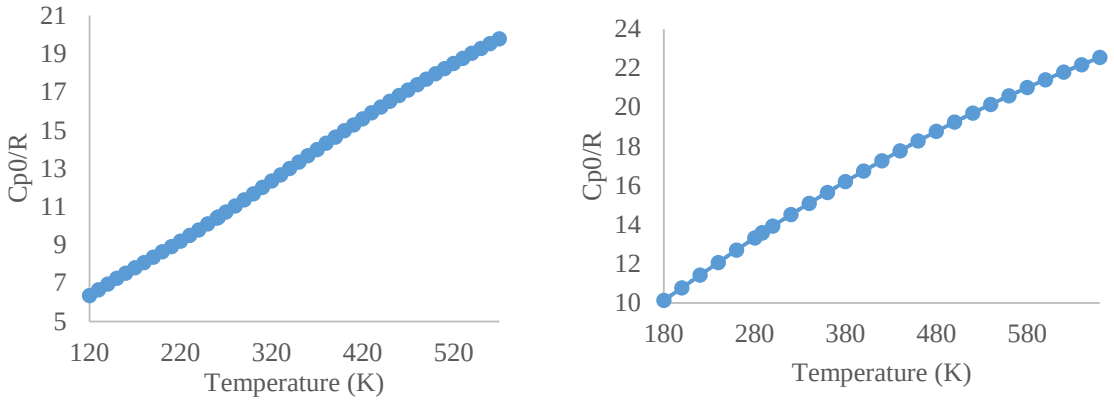

(a) (b)

Figure 10.5: Correlation of C_{p0}/R and temperature for isobutane (a) and R245fa (b)

Table 10.2: Fluid information for R245fa and Isobutane

Fluid		R245fa	isobutane
	Fluid Information		
Molar mass	kg/kmol	134.05	58.12
Critical temperature	K	427.16	407.81
Critical pressure	MPa	3.651	3.629
Critical volume	cm3/mol	259.7	257.7
Acentric factor	-	0.378	0.184
Boiling temperature	K	288.3	261.4
	Specific Heat Capacity		
a1	-	3.504	3.764
a2	K^{-1}	0.040	0.019
a3	K^{-2}	-2.0E-05	3.0E-05
a4	K^{-3}	4.0E-09	9.0E-09
a5	K^{-4}	-3.0E-12	-5.0E-11
Lower limit	K	171	113
Upper limit	K	440	575
	Reference State		
Reference temperature	K	298.2	298.2
Reference pressure	MPa	0.101	0.101
Reference specific enthalpy	J/kg	424,610	598,029
Reference specific entropy	J/kg.K	1,780	2,510

10.2.5.2 Turbine stage performance

The CFD analysis was performed on the radial turbine for the given operating condition from Table 10.1. The turbine performance was modeled for each working fluid, except n-Pentane, at different velocity ratio to determine the optimal rotational speed of the turbine, as shown in Figure 10.6.

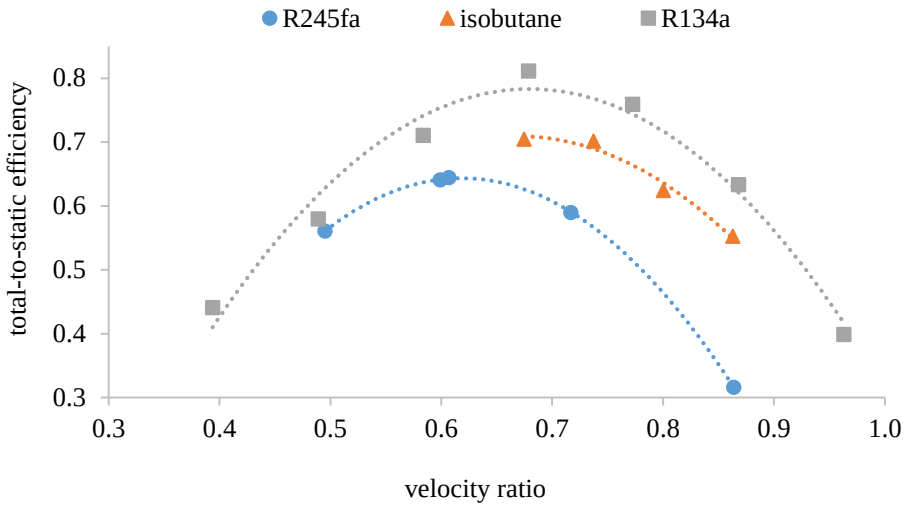

Figure 10.6: Performance analysis of gas turbine using refrigerants at different velocity ratio

The optimal velocity ratio was determined to be in the range of 0.6 and 0.7 from Figure 10.6, which corresponds to the experimental data of by Jones for the selected gas turbine [6] and the analytical study by Baines for radial inflow turbines with radial section blades [14]. The optimal rotational speed of the turbine with the corresponding pressure ratio, and the gear ratio to couple the turbines to a 60 Hz generator, were presented in Table 10.3.

Table 10.3: Optimal rotational speed of single stage gas turbine with different working fluids

Fluids	Pressure Ratio	Gear ratio	Rotational Speed (rev/min)	U/C
R245fa	10.2	8	28,800	0.607
Iso-butane	4.7	11	39,600	0.675
R134a	2.4	6	21,600	0.710

The turbine performance was then simulated at different pressure ratios using the rotational speed and velocity ratio in Table 10.3, and the turbine performance map was presented in Figure 10.7. R134a shows a higher total-to-static efficiency, followed by R245fa and isobutane. A low pressure ratio is preferable for the selected radial turbine for optimal performance for all three fluids as the turbine was originally designed for subsonic expansion with low pressure ratio.

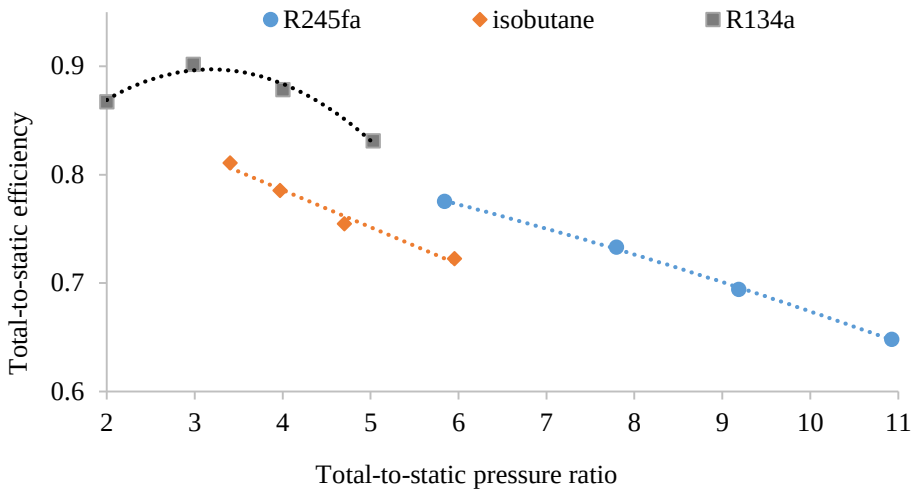

Figure 10.7: Performance analysis of gas turbine as a function of pressure ratio using different working fluids at optimal velocity ratio

10.2.5.3 Flow Field Analysis

A complete solution of the flow field was generated for the gas turbine using different fluids, R134a, isobutane and R245fa. R134a and isobutane operating in subsonic expansion show a higher turbine efficiency than R245fa in supersonic expansion process. The discrepancy in the efficiency is attributed to the design of the turbine rotor blade passage. The gas turbine was originally designed for subsonic expansion using air as the working fluid [6]. A minimum cross-sectional area, known as the throat, exists near the trailing edge of the blade passage. The throat area determines the flow capacity across the blade passage and allows proper diffusion of flow at the trailing edge of the blade. Diffusion is required to control the swirl angle of the flow near the turbine outlet and recover the kinetic energy of the flow, which in turn controls the specific work output, W_x from the turbine, based on Euler turbomachinery relation.

$$W_x = U_2 C_{m,2} \tan\alpha_2 - U_3 C_{m,3} \tan\alpha_3 \tag{21.15}$$

Where U is the tip speed of the turbine, C_m is the absolute meridional flow velocity, and α is the absolute flow angle, at the assigned station. Station 2 represents the turbine rotor inlet and station 3 represents the turbine rotor outlet. The velocity vector of R134a in Figure 10.8 shows a smooth flow pattern along the blade passage with minimal secondary flow losses. The low flow velocity at the turbine outlet increases the specific work output of the turbine using the Euler turbomachinery equation.

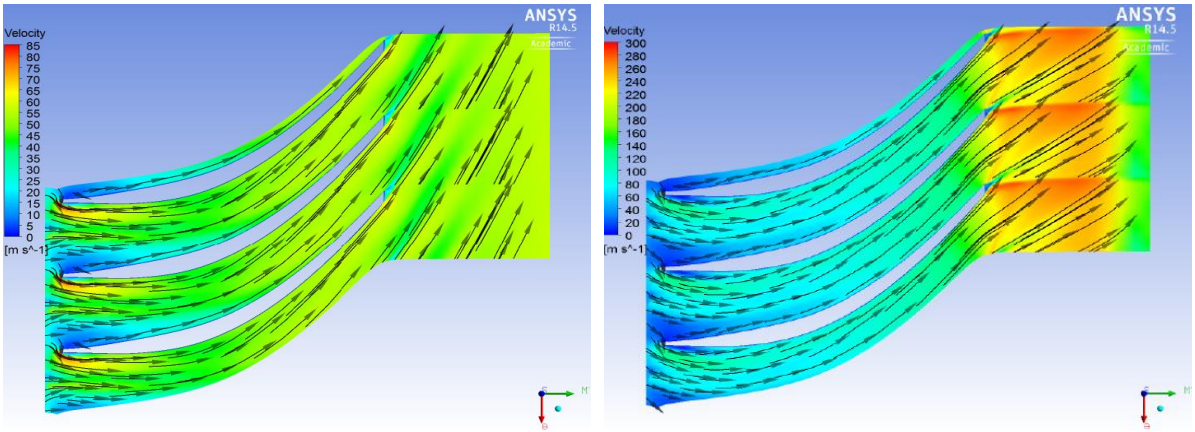

Figure 10.8: Velocity vector of R134a (on the left) and R245fa (on the right) along the blade passage

The high pressure ratio across the turbine using R245fa produces a supersonic expansion process in the turbine. The flow accelerates up to the throat along the blade passage, similar to the subsonic expansion. The flow continues to accelerate downstream of the throat and the absolute flow velocity increases significantly up to 280 m/s, as shown in Figure 10.8 The over-acceleration of the flow at the downstream of the throat reduces the specific work output of the turbine stage, based on the Euler turbomachinery equation. The mismatch between the blade profile and the characteristics of supersonic expansion reduces the turbine stage efficiency and contributes to the discrepancy of the turbine efficiency between R134a, isobutane and R245fa.

10.2.5.4 Energy and Exergy Analysis on Turbine and Binary Plant

The turbine performance varies across the year at different ambient temperature, and the performance across the year was plotted in Figure 10.9. The thermal efficiency and the exergy efficiency of the turbine using different fluids are fairly constant at different ambient temperature across the year. R245fa shows the lowest total-to-static efficiency, attributed to the supersonic expansion across the turbine. It is interesting to note that the turbine using R245fa shows the highest exergy efficiency although the thermal efficiency is the lowest among the three fluids. The high exergy efficiency using R245fa is attributed to the lowest entropy drop during the expansion across the turbine at different pressure ratio, as shown in Figure 10.10.

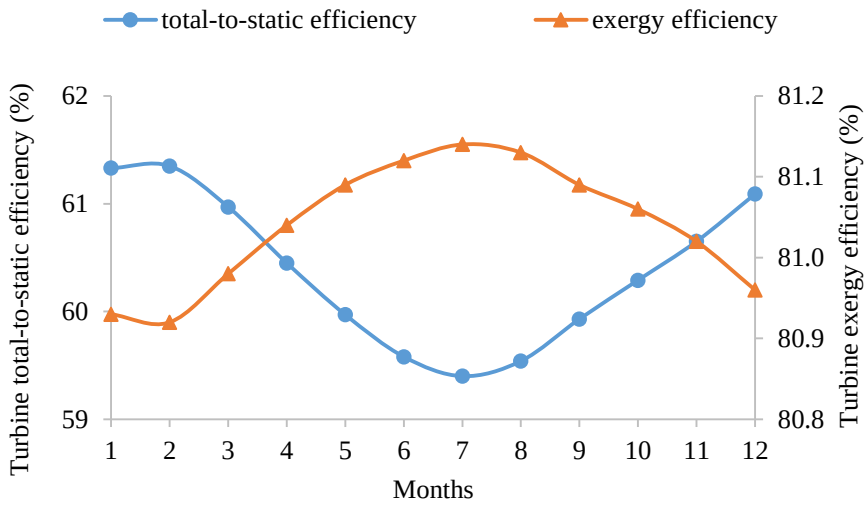
total-to-static efficiency
exergy efficiency
Turbine total-to-static efficiency (%)
Turbine exergy efficiency (%)
62
61
60
59
81.2
81.1
81.0
80.9
80.8
1 2 3 4 5 6 7 8 9 10 11 12
Months

(a)

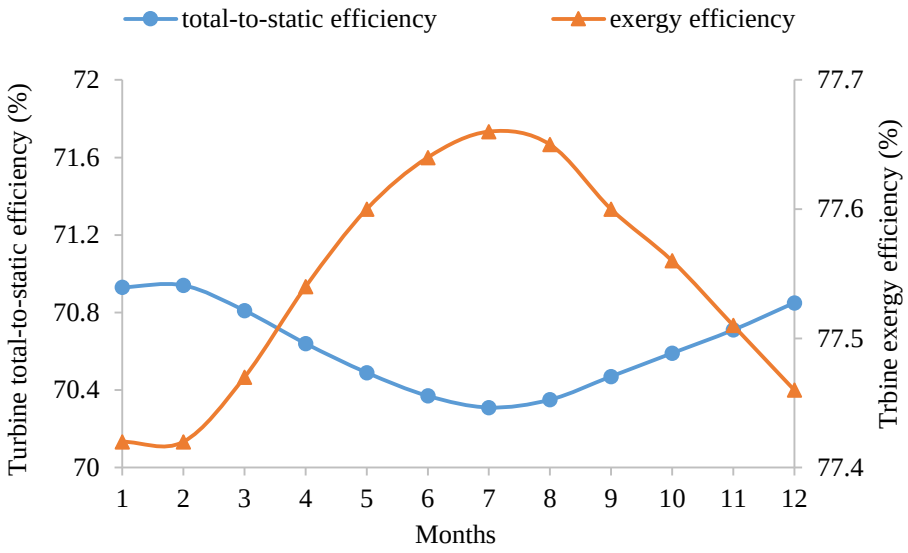
total-to-static efficiency
exergy efficiency
Turbine total-to-static efficiency (%)
Trbine exergy efficiency (%)
72
71.6
71.2
70.8
70.4
70
77.7
77.6
77.5
77.4
1 2 3 4 5 6 7 8 9 10 11 12
Months

(b)

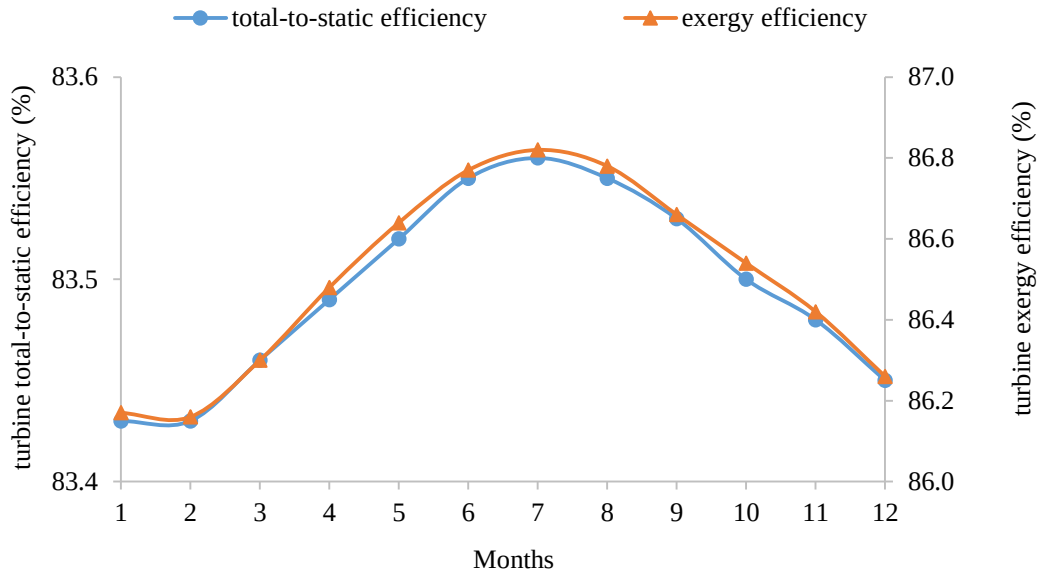

(c)

Figure 10.9: Thermal efficiency and exergy efficiency of the gas turbine using R245fa (a), isobutane (b), and R134a (c) across the year

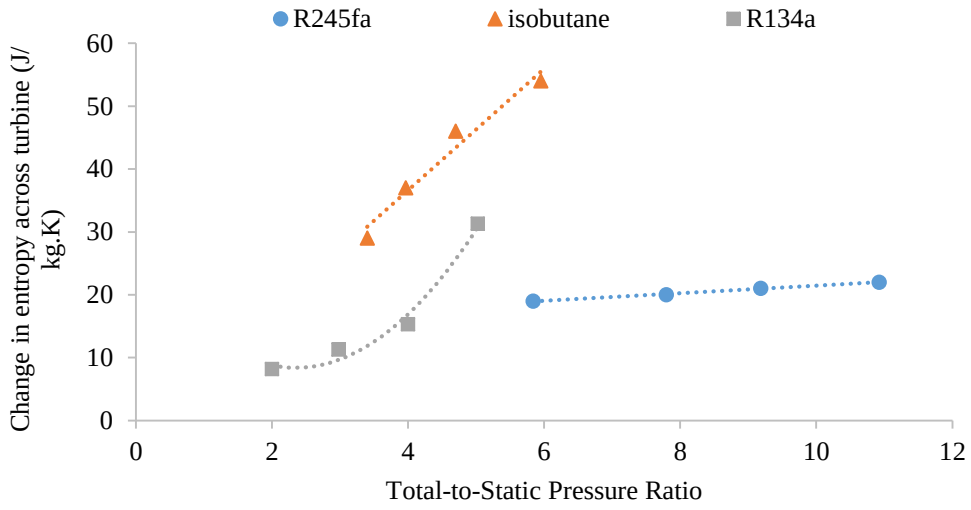

Figure 10.10: Change in entropy across the turbine at different pressure ratio

The turbine performance map was fed into the cycle analysis model to predict the thermal efficiency and exergy efficiency at different ambient temperature. The thermal efficiency and the exergy efficiency of the binary cycle were plotted as a function of ambient temperature in Figure 10.11 and Figure 10.12 respectively.

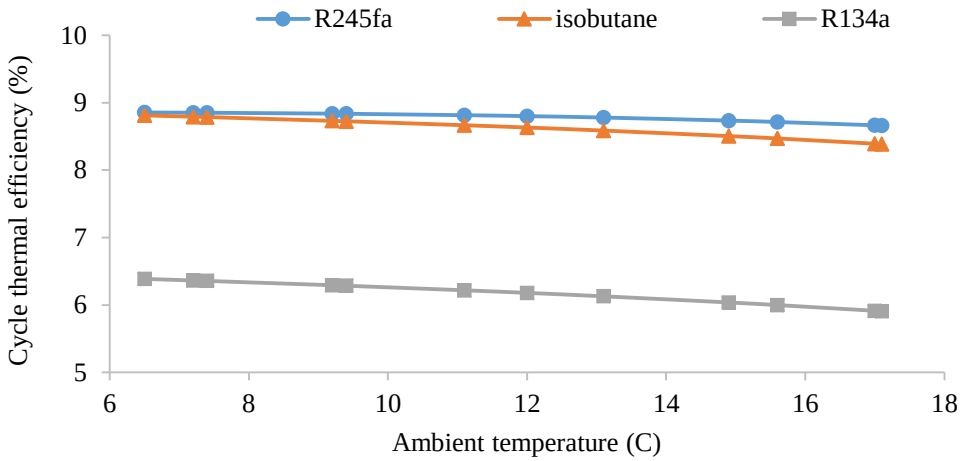

Figure 10.11: Thermal efficiency of the binary cycle as a function of ambient temperature

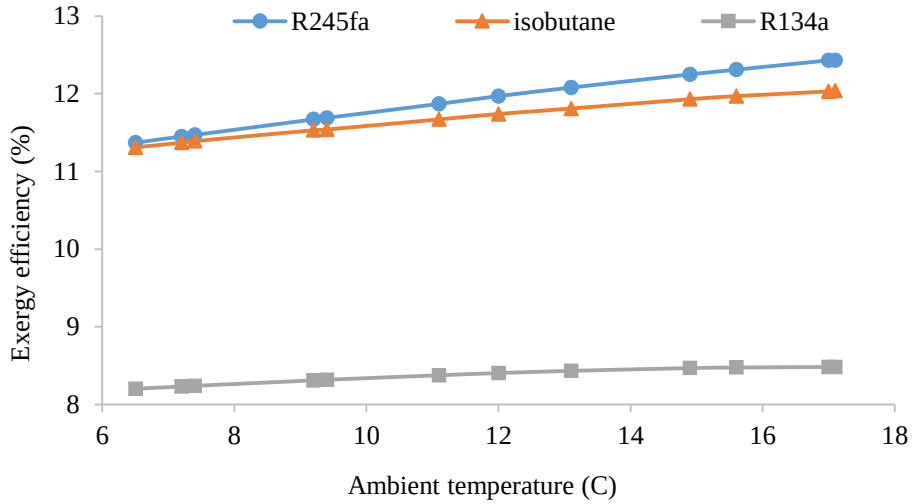

Figure 10.12: Exergy efficiency of the binary cycle as a function of ambient temperature

The thermal efficiency of the binary cycle decreases with the rise in ambient temperature. At higher ambient temperature, the differential temperature between the heat sink and the heat source is lower, and the cycle thermal efficiency is reduced. However, the thermal efficiency of the turbine increases with the rise in ambient temperature. The selected radial gas turbine would perform optimally with higher total-to-static efficiency and lower entropy change over the summer with lower pressure ratio. The exergy efficiency of the binary plant increases with respect to the ambient temperature, as the available maximum theoretical work output from the cycle reduces with increase in ambient temperature, as presented in Figure 10.12. The overall cycle efficiency was compared to the theoretical maximum efficiency of the binary plant present in Figure 10.13. The cycle thermal efficiency is much lower than the theoretical maximum efficiency.

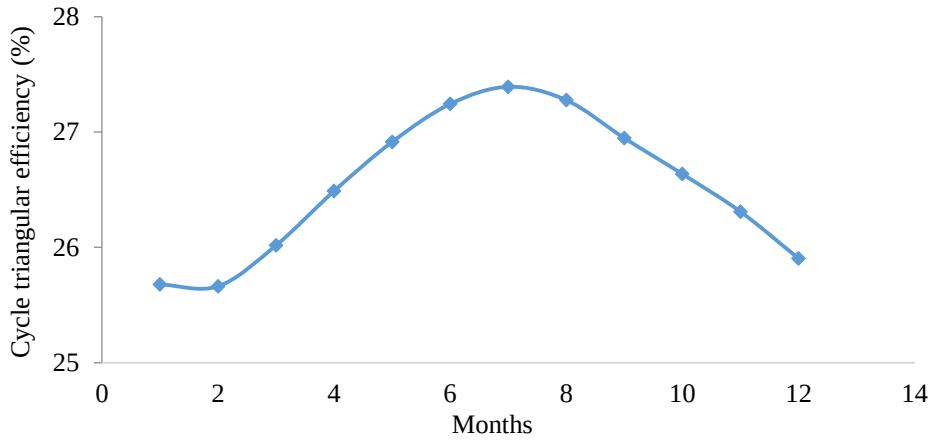

Figure 10.13: Triangular efficiency across the year

The discrepancy in the cycle performance might be attributed to the following factors.

1. The low evaporating temperature within the vaporizer using R245fa, isobutane and R134a contributes to a large degree of differential temperature at the pinch of the vaporizer as shown in Figure 10.14. The larger the pinch point differential temperature, the smaller the cycle thermal efficiency [15].

2. The heating curve of the working fluid within the vaporizer does not match with the heat source as phase change occurs within the vaporizer for a sub-critical ORC system, as shown in Figure 6.13. The mismatch increases the irreversibility during the heat transfer across the vaporizer. A more thorough explanation of this phenomena can be found in reference [16].

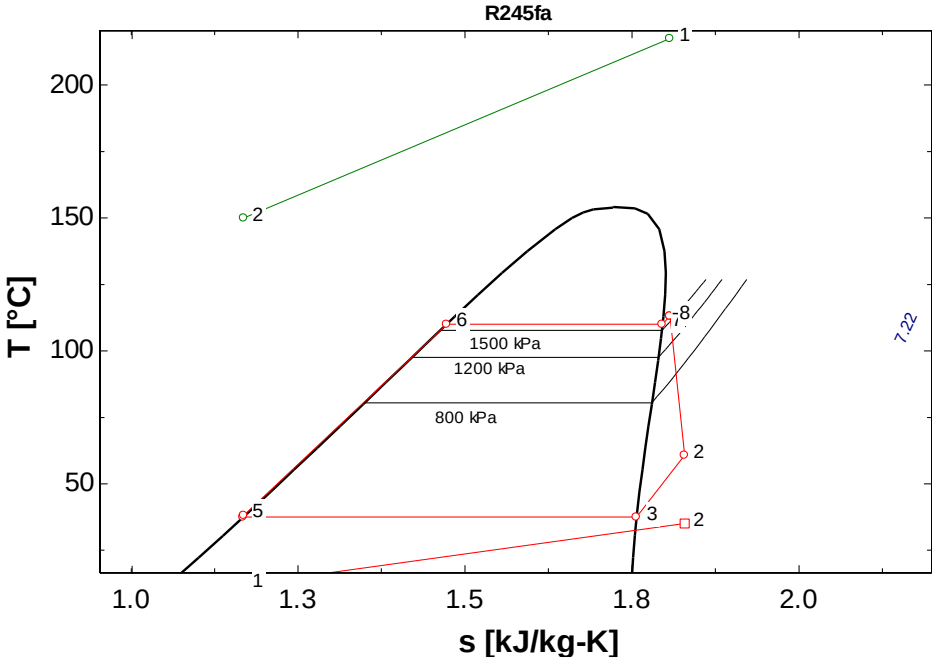

Figure 10.14: Simulation of binary plant using R245fa

The exergy efficiency and the thermal efficiency of the binary plant are dependent on the working fluids and the degree of superheat. Both isobutane and R245fa show a similar trend of the cycle thermal efficiency and exergy efficiency, with the same degree of superheat despite the difference in the maximum temperature of the working fluids within the cycle. R134a shows a similar trend of efficiency as a function of ambient temperature, with the curve shifted downwards at 2.5% and 3.5% for the thermal efficiency and the exergy efficiency, respectively, as shown in Figure 10.12. The following correlations were approximated from Figure 10.11 and Figure 10.12 for the cycle thermal efficiency and exergy efficiency as a function of ambient temperature.

$$\eta_{I,cycle} = -0.04T_{amb} + \eta_{I,cycle,0} \tag{21.16}$$

Where $\eta_{I,cycle,0}$ is the cycle thermal efficiency when the ambient temperature is 0°C, and T_{amb} is the air ambient temperature for any ACC binary plant, in degree Celsius.

$$\eta_{II,cycle} = -0.0018\left(T_{amb}\right)^2 + 0.1\left(T_{amb}\right) + \eta_{II,cycle,0} \tag{21.17}$$

Where $\eta_{II,cycle,0}$ is the cycle exergy efficiency when the ambient temperature is 0°C. These equations could be applied to predict the off-design performance of an air-cooled geothermal binary plant in a preliminary design phase.

10.3 Conclusion

This chapter presents the SMC-DTR approach by adapting a radial gas turbine with fixed nozzle vanes to design an air-cooled geothermal binary plant for resource condition with varying heat sink temperature. The CFD analysis technique from the SMC adaptive strategy was applied as there is only one available turbine option for this case study. This chapter shows that the adaptation of an existing gas turbine as an ORC turbine is feasible. The rotational speed of the turbine is much lower when the working fluid is changed from air to refrigerants such as R134a, R245fa, n-pentane and isobutane. The generator must be modified or replaced to accommodate the new rotational speed of the turbine.

One of the lessons learned in this chapter is the change in turbine efficiency if the working fluid is replaced from air into the refrigerants. One of the reasons is attributed to the original design of the turbine blade passage. The adapted gas turbine was originally designed

for sub-sonic expansion process. Hence, the turbine shows a higher isentropic efficiency using R134a and isobutane in subsonic expansion process and a lower isentropic efficiency using R245fa in supersonic expansion process.

Another lesson is that the change in the ambient temperature from 10 to 23˚C in Rotokawa, NZ across the year does not provide any significant effect on the thermal efficiency and the exergy efficiency of the turbine and the binary cycle. The turbine thermal efficiency changes up to 2%, and the exergy efficiency up to 1% at the given condition. The efficiency of the binary cycle changes less than 2% for this temperature range. Hence, the adaptation of a radial gas turbine with fixed nozzle vanes is suitable to the resource condition with varying heat sink temperature, with the efficiency changes in less than 2%.

10.4 References

1. Kanoğlu, M. and Y.A. Çengel, *Improving the Performance of an Existing Air-Cooled Binary Geothermal Power Plant: A Case Study.* Journal of Energy Resources Technology, 1999. **121**(3): p. 196-202.
2. Mines, G.L., *Evaluation of the impact of off-design operation on an air-cooled binary power plant.* Transactions - Geothermal Resources Council, 2002: p. 701-706.
3. Balje, O.E., *Turbomachines: A Guide to Design Selection and Theory*. 1981: Wiley.
4. Astolfi, M., et al., *Binary ORC (organic Rankine cycles) power plants for the exploitation of medium–low temperature geothermal sources – Part A: Thermodynamic optimization.* Energy, 2014. **66**(0): p. 423-434.
5. Ghasemi, H., et al., *Modeling and optimization of a binary geothermal power plant.* Energy, 2013. **50**(0): p. 412-428.
6. Jones, A.C., *Design and Test of a Small, High Pressure Ratio Radial Turbine.* Journal of Turbomachinery, 1996. **118**(2): p. 362-370.
7. Legmann, H. and P. Sullivan. *The 30 MW Rotokawa I geothermal project five years of operation*. in *International Geothermal Conference*. 2003.
8. NIWA, *The National Climate Database*. 2014: National Institute of Water and Atmospheric Research.
9. Lukawski, M., *Design and optimization of standardized organic Rankine cycle power plant for European conditions.* 2010.
10. Chen, H., D.Y. Goswami, and E.K. Stefanakos, *A review of thermodynamic cycles and working fluids for the conversion of low-grade heat.* Renewable and Sustainable Energy Reviews, 2010. **14**(9): p. 3059-3067.
11. DiPippo, R., *Geothermal power plants: principles, applications, case studies and environmental impact*. 2012: Butterworth-Heinemann.
12. *ANSYS CFX-Solver Theory Guide, Release 14.5*. 2012, ANSYS, Inc. Release 14.5: Canonsburg. p. 372.
13. *ANSYS CFX-Solver Modeling Guide, Release 14.5*. 2012, ANSYS, Inc: Canonsburg.
14. Moustapha, H., et al., *Axial and Radial Turbines*. 2003: Concepts Eti.
15. Guo, T., H. Wang, and S. Zhang, *Selection of working fluids for a novel low-temperature geothermally-powered ORC based cogeneration system.* Energy Conversion and Management, 2011.
16. Stijepovic, M.Z., et al., *On the role of working fluid properties in Organic Rankine Cycle performance.* Applied Thermal Engineering, 2012. **36**: p. 406-413.

11.0 Application of the SMC-DTR using CFD Analysis on Turbine with Variable Nozzle Vane

The aim of this thesis is to present the SMC-DTR approach for low temperature resources, and the main contribution of this thesis is to develop the key component, SMC analysis approach. The objective of this chapter is to utilize the SMC adaptive strategy to evaluate the performance of an automotive turbocharger with variable nozzle vanes and design an ORC system for a heat source with fluctuating mass flow.

The first section presents the control strategy to optimize the turbine performance for varying mass flow using air as working fluid. The CFD analysis technique was applied, and the performance of the turbine was generated at different velocity ratio, specific speed, mass flow, and nozzle vane position. The result shows that the inlet mass flow at the turbine inlet is linearly proportional to the vane angle. The vane angle has to be adjusted to the corresponding mass flow to optimize the turbine performance.

The second section presents the SMC-DTR approach to design and optimize an ORC system for a heat source with fluctuating mass flow using the selected turbocharger with the control strategy from the first section. The cycle design, fluid selection, set up of turbine specification, matching to the existing turbines, and the mechanical system design were not performed in this chapter as the previous two chapters have presented the applications of these steps. This section models the performance of the turbine using air and refrigerants, compares the turbine performance, and feeds the turbine performance into the cycle analysis model to evaluate the cycle thermal efficiency for heat sources with varying mass flow. The case studies in this chapter are the Chena geothermal hot spring in Alaska, USA, and the petroleum refining plant in New Zealand.

11.1 Introduction

The previous two chapters demonstrate the application of the SMC-DTR approach to design ORC system for low temperature resources, using the off-the-shelf nozzle-less automotive turbochargers and a radial gas turbine with fix nozzle vanes. The turbines are adapted assuming that the mass flow of the heat source is constant over the life cycle of the ORC system. However, this assumption is not applicable in geothermal application. The productivity of a geothermal well would decline over the time, attributed to the pressure decline as a result of the fluid extraction from the well [1]. The flow data of 18 wells at The Geysers steam field in California, USA was analysed by Dykstra [2]. The study shows that there was a 50% reduction in the flow rate extracted from the well after 8 years of the production. Subir reported that the production rate of The Geysers steam field reduces at 4.8% per year between 1987 and 1995, 2.9% per year between 1998 and 2004, and 2% per year between 2004 and 2011 [3]. The production rate of one of the geothermal wells in Turkey was reported to decline at nearly 40% per year between year 2012 and 2013 [4]. The flow rate of the brine declined from 590 tonne/hour to 540 tonne/hour between December 2012 and April 2013. The application of the radial inflow turbine would provide a low turbine efficiency for the geothermal resources with declining productivity over the time. The established turbine performance map (specific speed-specific diameter chart by Balje [5], and specific speed chart by Dixon [6]) shows that the radial inflow turbine is sensitive to the operating condition. Reza compared the performance of two radial inflow turbines: one with variable nozzle vanes, and one with fixed nozzle vanes for a geothermal plant in Nevada, USA. The result shows that the radial inflow turbine with variable nozzle vanes provides a better efficiency than the turbine with fixed nozzle vanes at off-design points. Hence, an off-the-shelf turbine with variable nozzle vanes would be studied to design an ORC system using a heat source with varying mass flow.

The objective of this chapter is to utilize the SMC-DTR approach to design and optimize an ORC system for the heat source with varying mass flow, using an automotive turbocharger with variable nozzle vanes. The first section defines the strategy to optimize the turbine performance using variable nozzle vanes. The second section models the performance of the turbine with fixed nozzle vanes and variable nozzle vanes using different working fluids. The performance of the ORC system using the turbines with fixed nozzle vanes and variable nozzle vanes was compared. The last part of this chapter investigates the losses within the flow

domain across the variable nozzle vanes in order to predict the optimal vane angle for ORC application.

11.2 Test Subject – Automotive Turbocharger with Variable Nozzle Vanes

The test subject for this chapter is an automotive turbocharger with variable nozzle vanes (also known as variable nozzle turbocharger and abbreviated as VNT). The smallest VNT from Garrett Honeywell with an inbuilt ball bearing cartridge was chosen for the study in this chapter. The model number of the turbocharger is GTB2060VKLR. The variable nozzle turbocharger by Garrett is classified into different generations, which can be identified from the model number. GT is the first generation, GTA is the second generation, GTB is the third generation, and GTC is the optimized version of third generation [7]. Each letter or digit of the model number gives the information of the type of the system and the geometry of the components:

20	turbine wheel diameter
60	compressor wheel size
V	variable inlet guided vanes
K	hydraulically controlled system
L	water lubrication
R	ball bearing system

This turbine was selected as the turbine equipped with ball bearings requires less amount of lubrication compared to a turbine equipped with journal bearings. Hence, a VNT equipped with ball bearings would be a better candidate to be adapted as an ORC turbine. The modification and adaptation of a turbocharger into an ORC turbine was detailed in Chapter 9.

Figure 11.1: The selected variable nozzle turbocharger from Garrett Honeywell with turbine casing removed

11.3 Performance Optimization using Variable Nozzle Vanes

This section aims to investigate the control strategy to optimize the performance of the automotive turbocharger using variable nozzle vanes. A CFD model (with details outlined in chapter 7) was applied on the turbine and the performance was predicted at different parameters: mass flow, velocity ratio, and pressure ratio. The modelling was performed using air as the working fluid to reduce the computational power and computing time.

One of the challenges in evaluating the performance of the turbochargers for ORC application is to obtain the 3D model (also known as solid model), which would be imported into the CFD tools to solve for the potential fluid flow field across the turbines. A number of approaches are available to obtain the 3D model, including a number of 3D scanning devices, co-ordinate measurement machines (CMM), and photo-modelling technology. This section use a portable 3D scanner by Artec to obtain the cloud points and generate the solid model. The turbine rotor and the nozzle vanes were scanned using a portable 3D scanner from Artec, known as Artec Spider. A series of linear patterns of blue LED light was projected onto the scanned object. The distance from the scanner and the object's surface was determined by the scanner to obtain the cloud points. The selected 3D scanner is able to capture the details of the scanned model and textures with an accuracy up to 50 microns, and a resolution up to 100 microns. The scanned data was processed by the corresponding software, known as Artec Studio, to form the point cloud using the in-built algorithm. The noise from lighting condition was filtered manually to avoid the inaccuracy in predicting the object structure. The point cloud was processed using a parametric solid modelling software, named Geomagic Design X. The point clouds were connected with tri-angular meshes and the generated surface was smoothened, as shown in Figure 11.2.

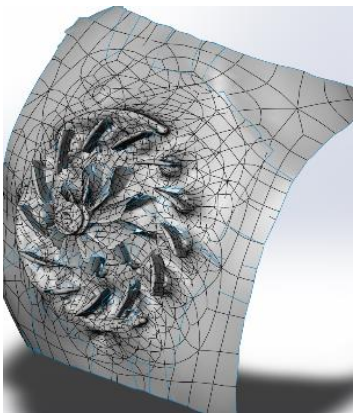

Figure 11.2: Meshed data of the scanned model from Geomagic Design X

A 3D model is required to perform the CFD analysis on the turbine. However, the solid model from the Geomagic Design X cannot be imported directly into ANSYS CFX for the CFD analysis. A solid model was re-generated in ANSYS Blade-Gen and compared to the solid model generated from Geomagic Design X. Three solid models were generated at three different vane positions, namely position 1, position 2, and position 3, as shown in Figure 11.3. At position 1, the vane was adjusted to a fully open position; at position 2, the vane was adjusted nearly half of the open position; at position 3, the vane was adjusted to a nearly closed position.

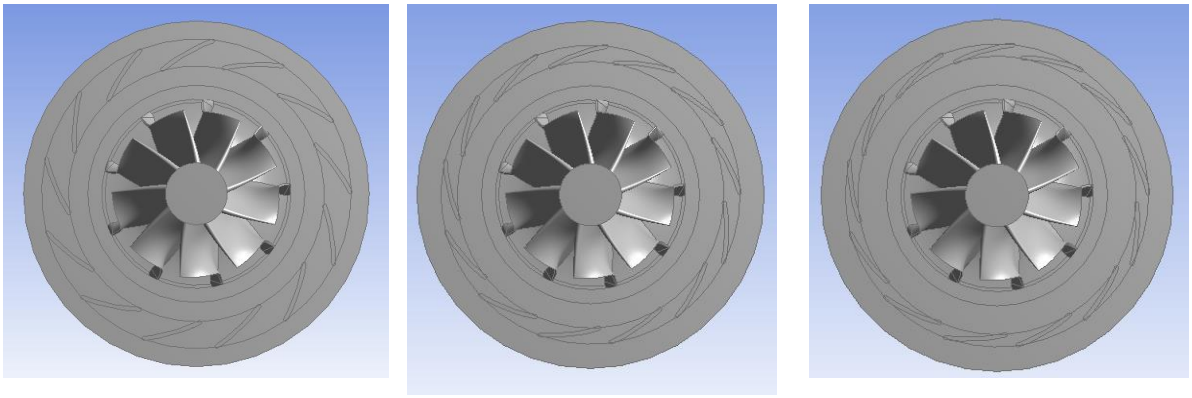

(a) (b) (c)

Figure 11.3: Solid model of the turbine wheel and nozzle generated in ANSYS Blade-Gen, with position 1 (a), position 2 (b), and position 3 (c)

Meshing was performed in ANSYS Turbo-Grid. O-grids were automated across the fluid zone, and 116,288 nodes and 104,940 meshes were generated for a single rotor blade, whereas 167,292 nodes and 154,440 meshes were generated for a single nozzle blade, as illustrated in Figure 11.4.

The domains, interfaces and boundary conditions of the nozzle and the rotor were set up in ANSYS CFX. A steady state analysis was selected rather than a transient analysis as the computational effort would be greatly reduced while providing an accurate result for the overall turbine stage performance. The interface between the nozzle outlet and the rotor inlet was defined using the in-built settings – 'Stage'. The setting averages the interaction effects across the boundary between the nozzle outlet and the rotor inlet without considering the transient behavior across the interface. The working fluid, air, was modelled as an ideal gas to reduce the computing time.

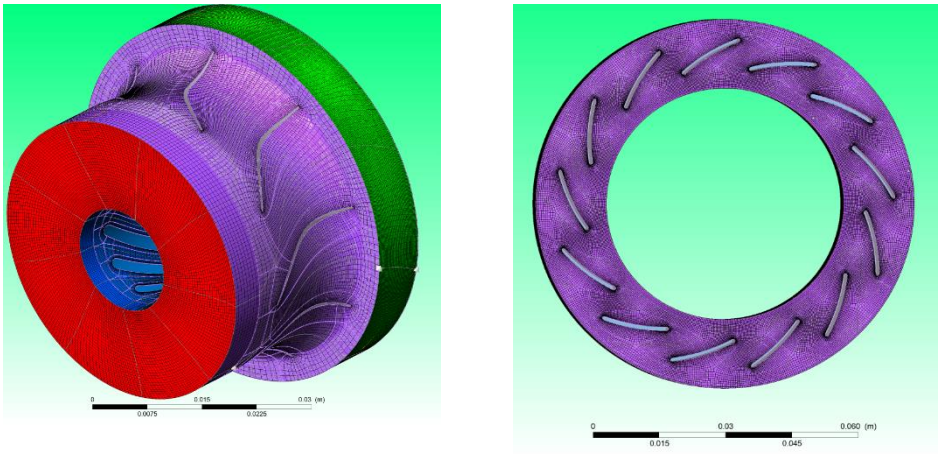

Figure 11.4: Meshing of rotor wheel and nozzle vanes at position 1

The performance of the turbine was simulated at different vane positions, including position 1, position 2, and position 3. The turbine performance was evaluated at different velocity ratio, and the correlation between the turbine total-to-static efficiency and velocity ratio was plotted in Figure 11.5. The pressure ratio across the turbine was set at two to generate the turbine performance in Figure 11.5.

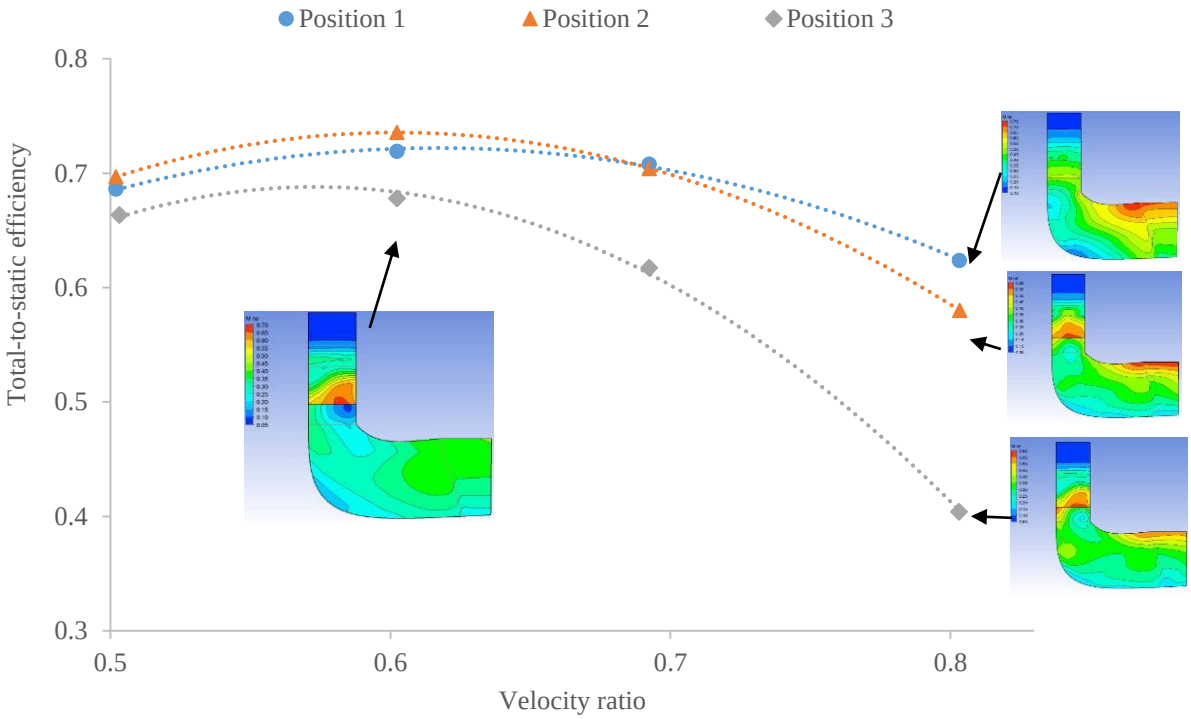

Figure 11.5: Performance analysis of the turbine stage at different vane positions as a function of velocity ratio, using air as working medium

The optimal velocity ratio is at 0.6 for all three vane positions, showing that the location of the optimal velocity ratio is independent of the vane position. The turbine performs at the peak efficiency when the vane position is set at position 2. The lowest peak efficiency was found when the vane position is near to the fully closed position (position 3). The contour of circumferentially area-averaged relative Mach number was included in the performance map in Figure 11.5. Highest relative Mach number was achieved at the outlet of the nozzle as the flow was accelerated along the nozzle before entering the rotor. The highest relative Mach number is well below 1 and choke does not occur at the nozzle outlet. If the relative Mach number is above 1 at the interface between the nozzle and the rotor, shock wave forms at the interface, and the fluid potential and kinetic energy would be dissipated as the turbine losses. Another source of the turbine losses is the secondary flow. The secondary flow effect becomes significant at high rotational speed (when the velocity ratio is 0.8) and the turbine efficiency suffers a significant drop due to the secondary flow loss.

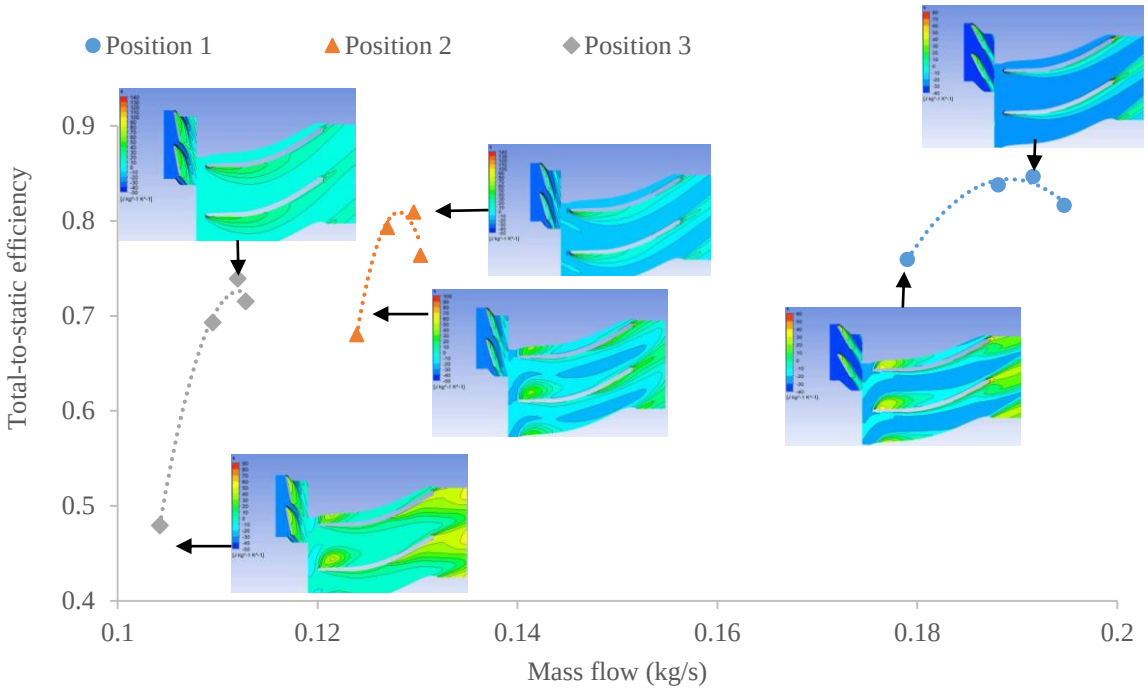

Figure 11.6: Performance analysis of the turbine stage at different vane positions as a function of mass flow

The turbine performance analysis was performed at different mass flow rate, and the correlation between the turbine performance and the mass flow was plotted in Figure 11.6. The result shows that the turbine performance is sensitive to the inlet mass flow rate, when the pressure ratio and the vane position is fixed. The turbine efficiency drops significantly if the

inlet mass flow is different from the optimal mass flow when the vane position is fixed. The distribution of entropy across the nozzle and rotor blade passage was also included in Figure 11.6, for the maximum efficiency point and the non-optimal operating point. At the non-optimal operating point, high irreversibility was found at two positions; near the leading edge of the rotor, and downstream of the trailing edge of the rotor. The phenomena can be explained as below.

Near the leading edge: Adverse pressure gradient occurs, which gives rise to the flow reversal and generate vortex flow.

Downstream of trailing edge: The irreversibility is attributed to the mixing of the secondary flow and the bulk flow across the blade passage, which gives rise to the wake further downstream from the throat.

The turbine performance was plotted as a function of specific speed in Figure 11.7. When the vane position was adjusted from position 1 to position 3, the cross sectional area across the nozzle vane passage was reduced, and the mass flow rate at the turbine inlet was reduced. The optimal specific speed was reduced from 1.0 at position 1 to 0.7 at position 3.

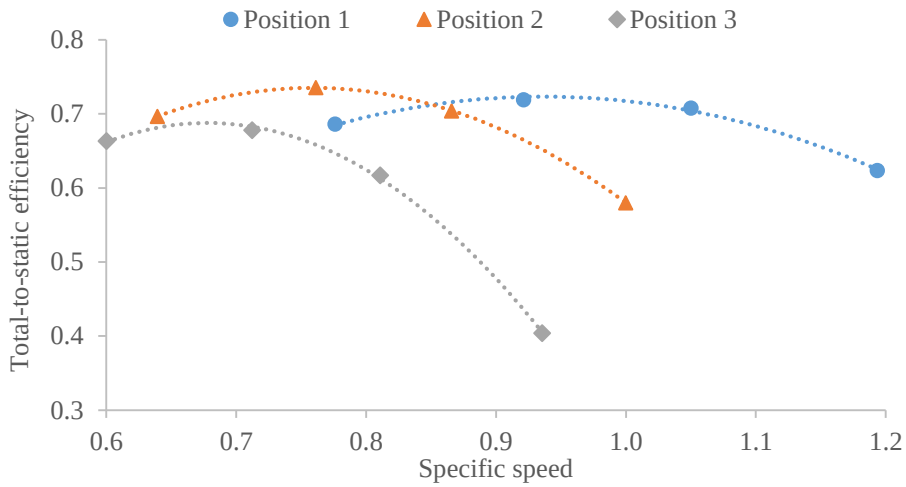

Figure 11.7: Performance analysis of the turbine stage at different vane positions as a function of specific speed, using air as working medium

The correlation between the turbine performance, velocity ratio, and pressure ratio was plotted in Figure 11.8 to determine the optimal velocity ratio at different pressure ratio. The total-to-static efficiency of the turbine using air was set at pressure ratio of 2 and 4. The contour of entropy at the highest efficiency point was included in the performance map. The optimal

velocity ratio was found at 0.6 for both pressure ratio, indicating that the location of the optimal velocity ratio is unchanged for different pressure ratio, if the same working medium is applied. The generation of entropy is higher at higher pressure ratio, especially at the downstream of the trailing edge of the rotor, which gives rise to lower turbine's efficiency.

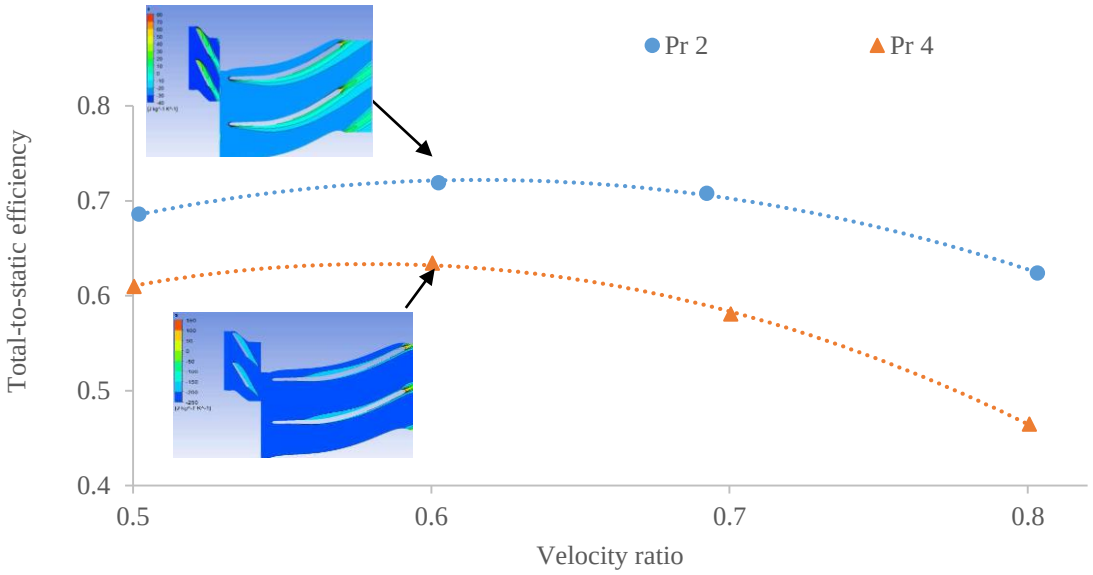

Figure 11.8: Performance analysis of the turbine stage at different pressure ratio using air as working medium, when the vane was adjusted to position 1 (fully open)

The performance analysis presents the fundamental information to control a variable nozzle turbine for optimal performance, which are summarized below.

- The location of the optimal velocity ratio of a turbine stage is independent of the vane position and the pressure ratio.
- The turbine performance is sensitive to the inlet mass flow rate at different vane positions.

Hence, the optimal velocity ratio is set by fixing the turbine rotational speed for a given pressure ratio.

$$\nu = \frac{U_2}{C_s} = \frac{2\pi r_2 N}{60\sqrt{2\Delta h_{ts,is}}} \tag{22.1}$$

Where υ is velocity ratio, U_2 is rotor inlet tip speed, C_s is the fluid velocity when the fluid is expanded in an ideal nozzle with the same pressure ratio of the turbine stage, r_2 is radius at the rotor inlet, and N is turbine shaft speed in rev/min.

An example was showcased using the air as working medium, at total-to-static pressure ratio of 2. The optimal velocity ratio was found at 0.6 from the performance analysis, and the turbine shaft speed is adjusted at 87,000 rev/min. The vane position has to be adjusted accordingly to the inlet mass flow rate; position 1 at 0.19 kg/s, position 2 at 0.13 kg/s, and position 3 at 0.11 kg/s, as shown in Figure 11.6. The vane position could be adjusted either by defining a set of positions (as shown above), or manipulating the vane angle. The correlation between the mass flow at the turbine inlet and the vane angle can be approximated by a linear correlation, as shown in Figure 11.9 using air as the working fluid. The vane position was adjusted accordingly using the position approach or the vane angle-mass flow correlation in Figure 11.9 for air, to determine the VNT performance. The performance of the VNT and the turbine at the fixed vanes was simulated using the CFD approach, and compared in Figure 11.10 as a function of mass flow. The variable nozzle turbine (VNT) shows better efficiency in a wide range of mass flow rate, between 0.10 and 0.20 kg/s, whereas the turbine performance at fixed vane position is sensitive to the change in mass flow rate. The application of VNT allows the turbine to accommodate different mass flow of the working medium, to match with variable demand in power supply across the day, or to match the variable geothermal heat source condition. The change in pressure ratio across the turbine stage, however, has to be matched with different rotational speed, using the velocity ratio parameter for optimal performance.

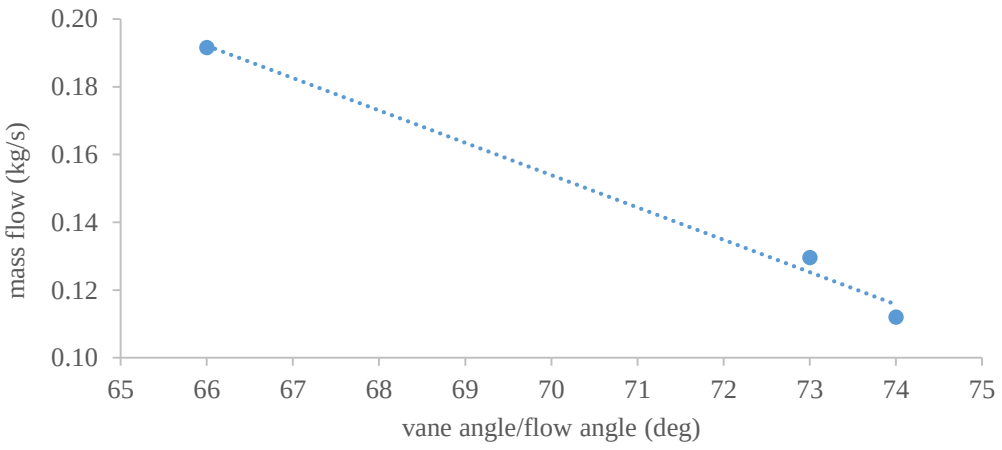

Figure 11.9: Correlation between inlet mass flow rate of the turbine stage and the vane angle (or absolute flow angle) at the nozzle outlet

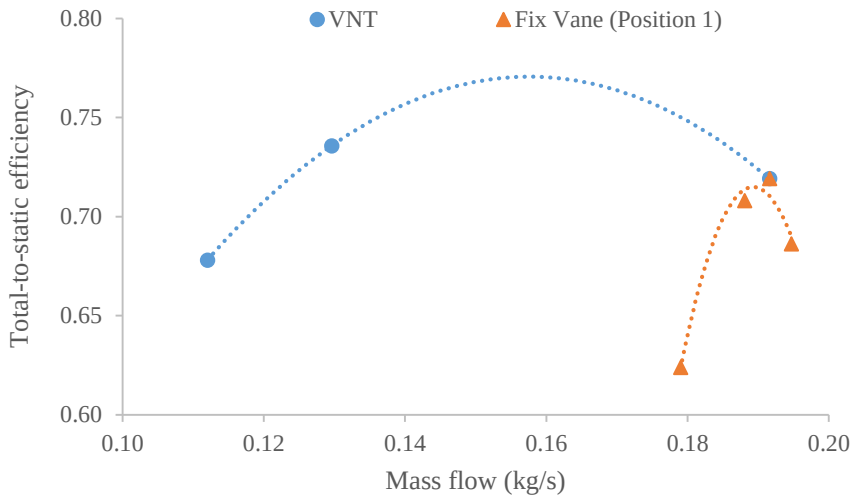

Figure 11.10: Comparison of turbine performance using variable nozzle vanes and fixed vanes at position 1 using air as working medium, at pressure ratio of 2

11.4 Application of the SMC-DTR Approach in Heat Source with Variable Mass Flow

This section aims to present the application of the SMC-DTR approach to design an ORC system using a heat source with variable mass flow. The SMC adaptive strategy was applied to evaluate the turbine performance using refrigerants, compare the turbine performance using air and using refrigerants, and evaluate the ORC performance by feeding the turbine performance map into the cycle analysis model.

11.4.1 ORC System

The selected automotive turbocharger was applied on two different case studies; the geo-fluid from the Chena geothermal hot spring in Alaska [8] and the kerosene flow in a petroleum refining plant in New Zealand [9]. There are two ORC units installed in the Chena hot spring producing over 500 kW. An ORC system has been proposed and planned as a bottoming cycle for the refinery plant. The ORC operating condition was extracted from the design condition of the binary plant in Chena hot spring [8] and the design condition of a planned ORC system for the refinery plant [9], as shown in Table 11.1. The planned waste heat recovery (WHR) system and the binary plant in Chena utilizes R245fa and R134a as the working fluid respectively. Assumption was made on the mass flow of the heat sources to allow the study of heat source with variable mass flow in this chapter. The mass flow of the geo-fluid was assumed to vary from 5 to 10 kg/s, and the mass flow of the kerosene flow was assumed to vary from 2 to 4 kg/s during the operation.

Table 11.1: Resource characteristics and operating parameters of the selected case studies

Application	Waste heat recovery	Low temperature geothermal
Site	Refining NZ, New Zealand	Chena Hot spring, Alaska, US
	Heat Source	
Heat source medium	Kerosene flow	Hot spring water
Heat source inlet temperature (°C)	115	73.3
Heat source outlet temperature (°C)	70	54.4
	Heat sink	
Cooling medium	Water	Water/Air
Cooling medium temperature (°C)	24	4.44
	ORC system	
Working medium	R245fa	R134a
Density at turbine outlet (kg/m^3)	13.17	20.84
Inlet pressure (kPa)	725	1600
Inlet temperature (°C)	78.6	64.2
Outlet pressure (kPa)	244.7	439
Pressure ratio	3	3.6

11.4.2 Application of the SMC Adaptive Strategy

The SMC adaptive strategy was applied to evaluate the performance of the selected turbocharger for the ORC system with the inlet condition from Table 11.1. The CFD analysis technique was applied since there is only one turbine option for this chapter. The CFD model for this turbocharger was presented in the previous section. The total-to-static pressure ratio was set at 4, since a higher pressure ratio is favorable for ORC application. The correlation between the turbine performance and the velocity was plotted in Figure 11.11 for vane position 1. A comparison was made on the performance of the selected turbocharger using air and refrigerants. The result shows that the application of refrigerants in the automotive turbocharger deteriorates the turbine performance up to 20% in the total-to-static efficiency given the same pressure ratio. The turbine efficiency was dropped from over 60% to over 40% by replacing the air with refrigerants as working medium, for the velocity ratio between 0.5 and 0.8. The location of the optimal velocity ratio was found to shift to a lower velocity ratio, from 0.6 for air to 0.5 for R134a and R245fa.

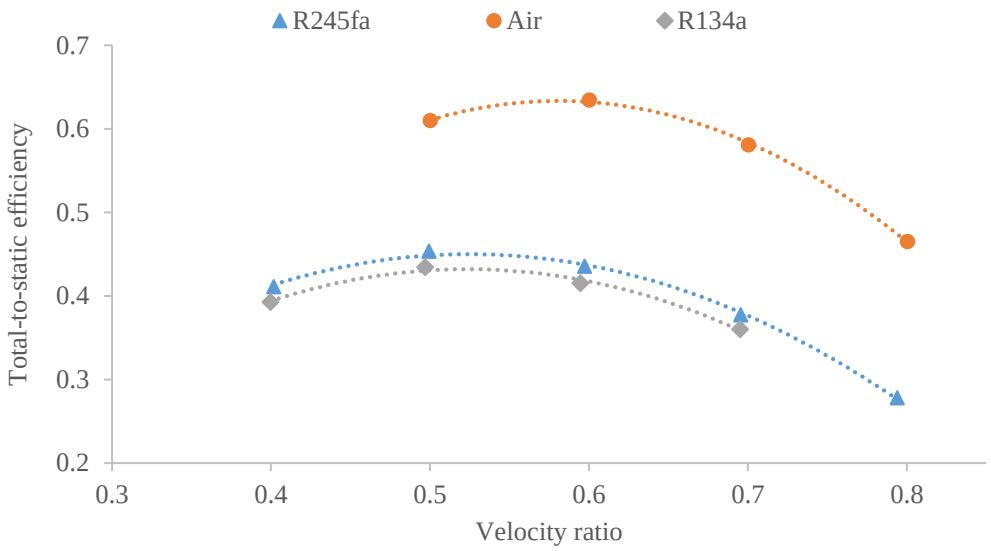

Figure 11.11: Comparison of turbine performance for air, R134a and R245fa at pressure ratio of 4, when the vane was adjusted to position 1 (fully open)

The performance of the VNT using refrigerants was predicted using the control strategy from the previous section. The correlation between the inlet mass flow and vane angle for R134a and R245fa was plotted in Figure 11.12. The vane position has to be adjusted accordingly to the mass flow rate to optimize the VNT performance using R134a and R245fa. The

performance of the VNT and the turbine at the fixed vane position (at position 1) was compared in Figure 11.13.

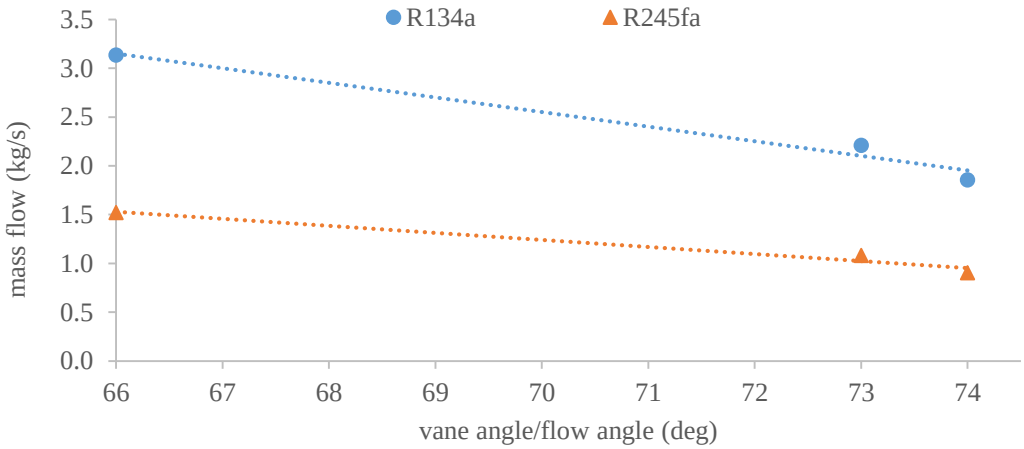

Figure 11.12: Correlation between inlet mass flow and vane angles for R134a and R245fa

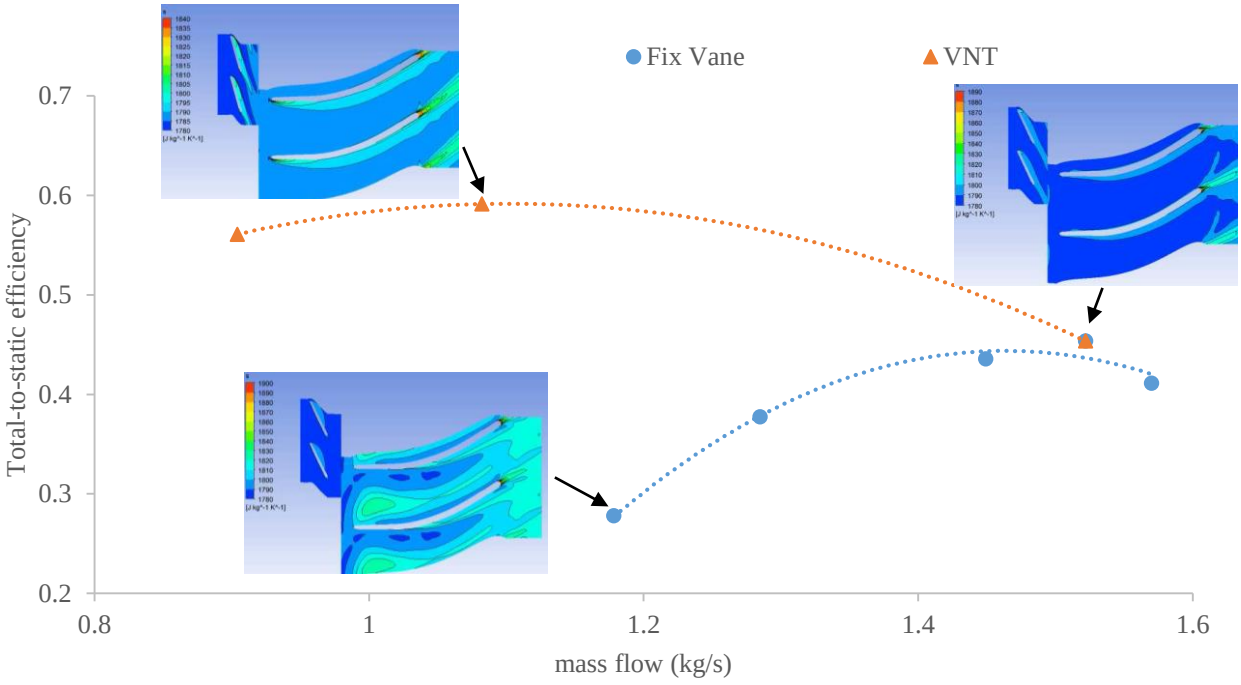

(a)

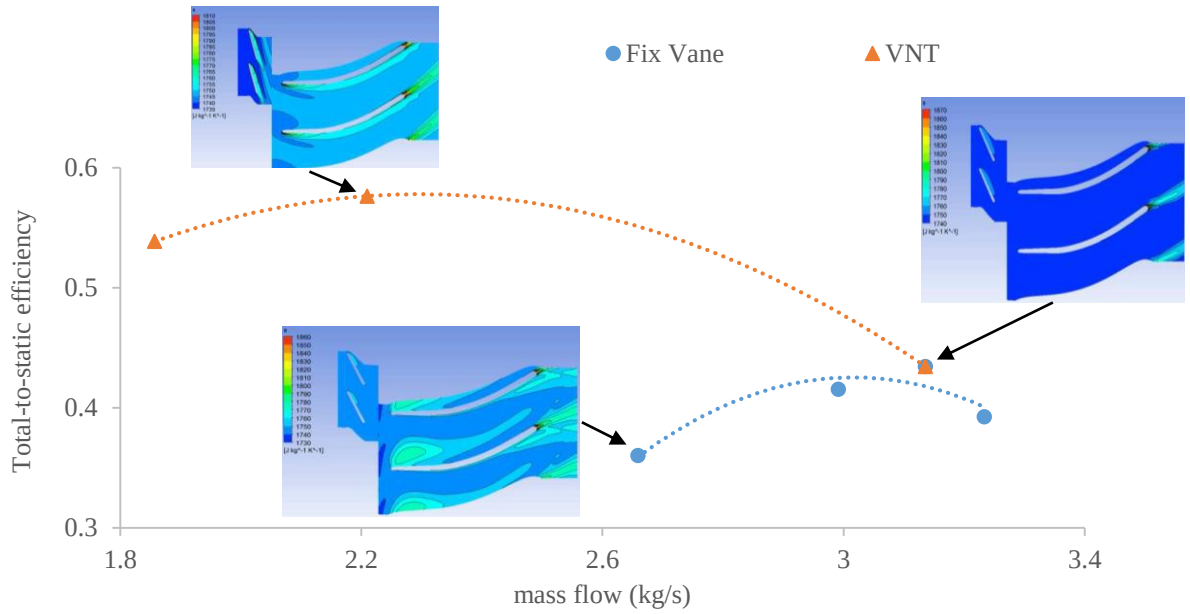

(b)

Figure 11.13: Comparison of turbine performance between variables nozzle vanes and fixed vanes for R245fa (a) and R134a (b) at pressure ratio of 4, was a function of mass flow and specific speed

The performance behavior using refrigerants is very similar to the turbine performance using air. The application of variable nozzle vanes allows the optimized turbine performance at a wider range of mass flow rate, between 0.8 and 1.6 kg/s for R245fa, and between 1.8 and 3.2 kg/s for R134a. The performance of the turbine using fixed nozzle vanes drops significantly when the inlet mass flow is deviated from the optimal mass flow. This situation has limited the application of the radial inflow turbines with fixed nozzle vanes in heat source with variable/fluctuating mass flow, such as geothermal heat source with decreasing reservoir pressure/mass flow. The contour plots of the entropy for R134a and R245fa was included in the performance map. The use of variable nozzle vanes allows a wider range of mass flow without giving rise to flow separation within the blade passage. Flow separation and flow reversal occur at non-optimal points if the fixed vane nozzle is used, as shown in Figure 11.13.

The turbine performance was fed into the cycle analysis model, and the cycle performance using the turbine with fixed nozzle vanes (at vane position 1 – fully open position) and the turbine with variable nozzle vanes was plotted in Figure 11.14. The result shows that the ORC system shows a nearly flat efficiency when the turbine with the variable nozzle vanes was used, despite the significant change of the mass flow of the heat source (2 to 4 kg/s for the kerosene flow and 5 to 10 kg/s for the geo-fluid). The performance of the overall ORC system

would drop significantly if the mass flow of the heat source deviates from the optimal mass flow. This section successfully shows that the application of variable nozzle vanes in turbine would maintain the turbine performance and the overall ORC system performance at a wide range of mass flow of the heat source.

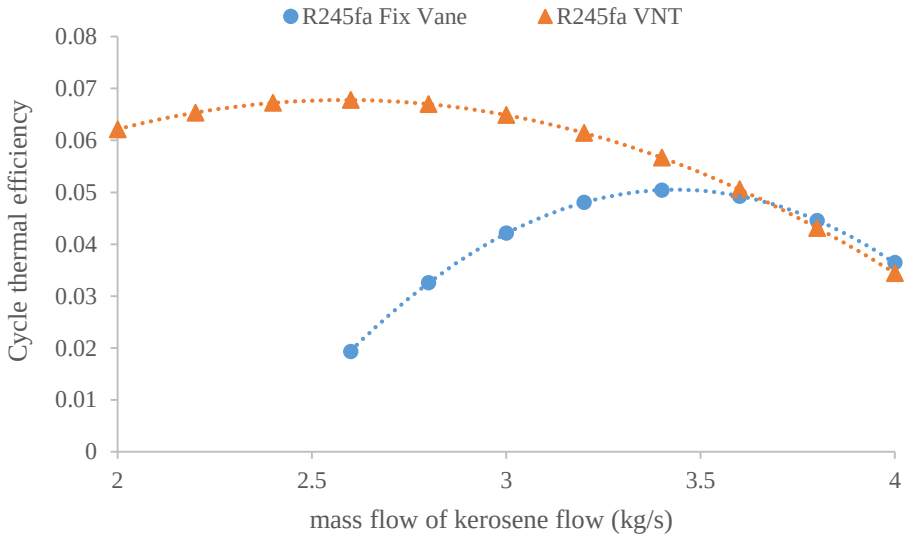

(a)

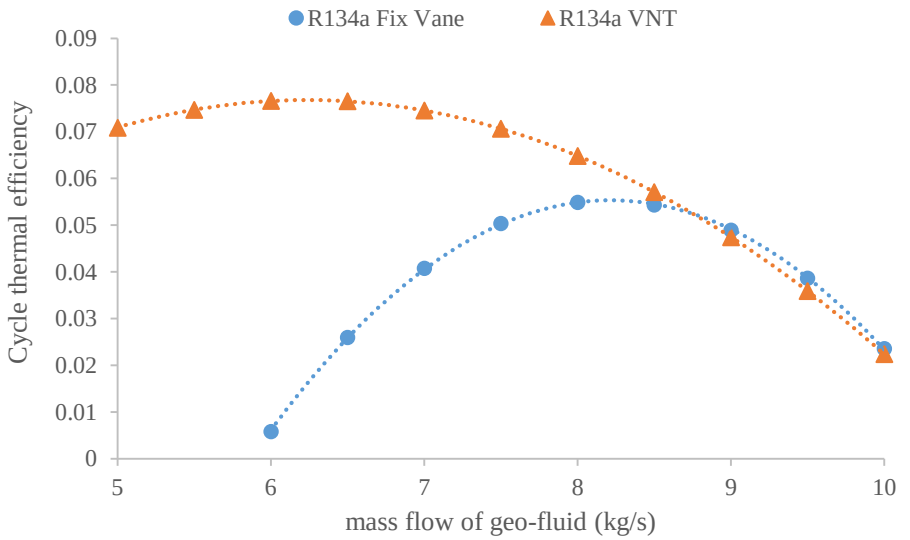

(b)

Figure 11.14: Comparison of the thermal efficiency of the ORC system between a turbine with fixed nozzle vanes and a turbine with variable nozzle vanes

11.5 Discussion – Performance Evaluation of Variable Nozzle Vanes

This section aims to study the losses in the flow passage of variable nozzle vanes at different vane positon (or different vane angle). The nozzle loss was quantified as total pressure loss in this chapter.

$$K_s = \frac{p_{01} - p_{02}}{p_{02} - p_2} \tag{22.2}$$

Where K_s is the total pressure loss coefficient of the nozzle (the subscript s represents the stator/nozzle), p_{01} is the stagnation/total pressure at the nozzle inlet, p_{02} is the total pressure at the nozzle outlet, and p_2 is the static pressure at the nozzle outlet. The correlation between the nozzle loss coefficients and the velocity ratio of the nozzle vanes using air at different vane positions was plotted in Figure 11.15.

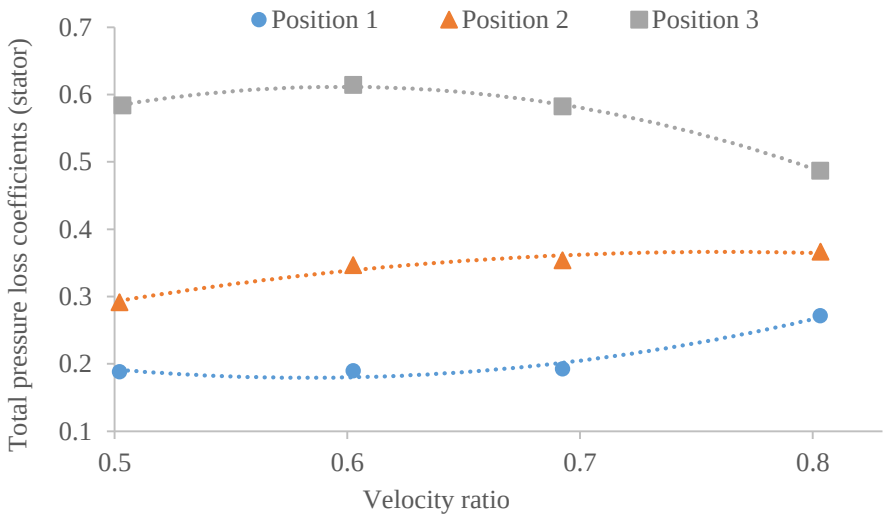

Figure 11.15: Total pressure loss coefficients of nozzle vanes at different vane position and velocity ratio, using air as the working medium

The nozzle loss coefficient was found to fall between 0.20 and 0.28 at position 1, between 0.30 and 0.37 at position 2, and between 0.50 and 0.60 at position 3. The nozzle loss coefficient is fairly constant if the vane position is fixed, and the loss coefficient is not affected by the velocity ratio of the turbine.

The nozzle loss coefficient with different working fluids was compared in Figure 11.16. The vane position 1 (fully open position) corresponds to the vane angle at 66˚, the vane position 2 (intermediate position) corresponds to the vane angle at 73˚, and the vane position 3 (nearly close position) corresponds to the vane angle at 74˚. When the vane angle is low (vane is

positioned at the fully open position), the loss coefficient is similar despite the type of the working fluid. When the vane angle is high (vane is positioned at nearly close position), the loss coefficient with air is higher than the loss coefficient with refrigerants. The nozzle loss coefficients were found to monotonically increase with increasing vane angle for all three working fluids. The velocity vector of the fluid flow across the flow domain within the nozzle vane passage was illustrated in Figure 11.17 to understand the flow behaviour and the source of the losses.

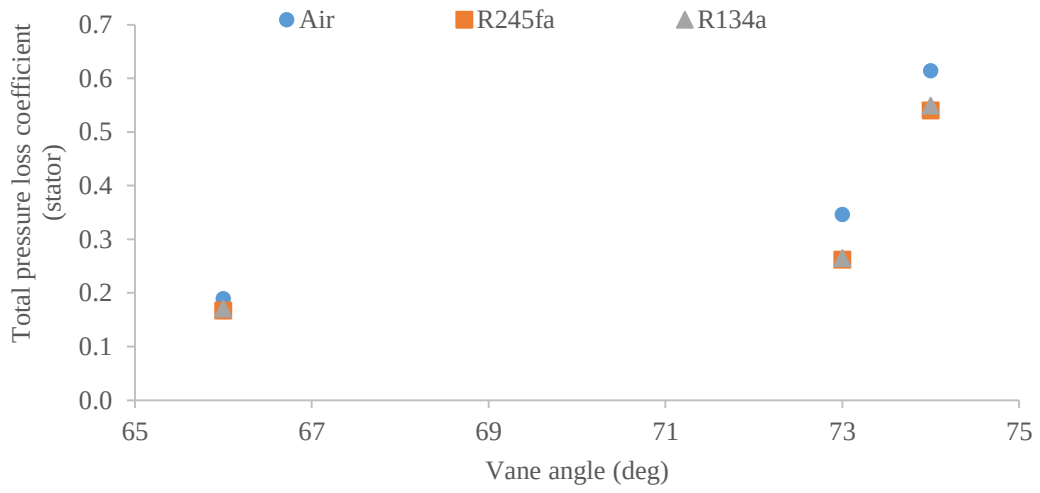

Figure 11.16: Total pressure loss coefficients of turbine stage with variable nozzles for air, R134a and R245fa as a function of vane angle

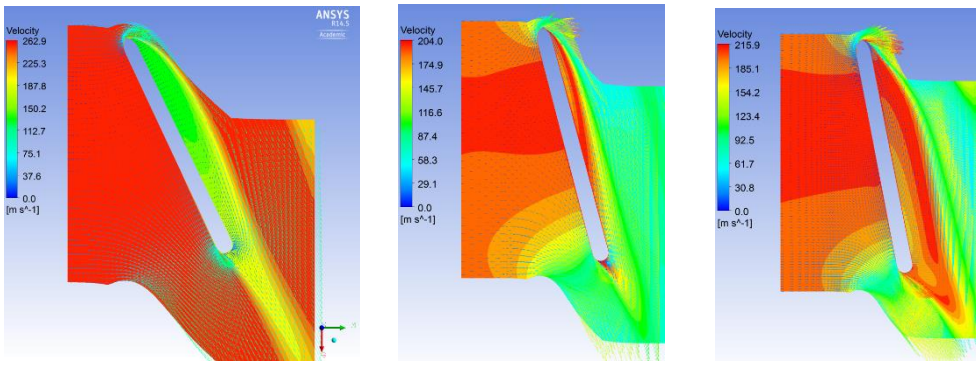

(a) (b) (c)

Figure 11.17: Distribution of velocity and the velocity vector of fluid flow across the nozzle vane at different vane position using R134a as working fluid; (a) position 1, (b) position 2, and (c) position 3

The distribution of the flow velocity and the velocity vector of the fluid flow across the flow domain within the vane passage was shown in Figure 11.17 using R134a as the working

fluid, at different vane position. A large circulation zone was observed along the suction surface of the nozzle vane, for all three vane positions. The larger the vane angle, the larger the circulation zone, and the larger the nozzle loss coefficients. This phenomena is similar to the stall of an aircraft. The angle of attack of an aircraft is increased to increase the lift coefficient during a take-off. The larger the angle of attack, the higher the lift coefficient. However, the flow separates on the top of the airfoil when the angle of attack is high, creating a large zone with separated flow and recirculated flow. If the angle of attack is too high, and a threshold value known as critical angle of attack is exceeded, the separated flow is dominant. The drag coefficient is dominant and stall occurs. The same explanation can be applied in the variable nozzle vanes. The increase in the vane angle allows the increase in blade loading across the nozzle vanes, with a larger pressure ratio across the vanes. The flow, however, separates near the leading edge of the suction surface, creating a flow circulation zone. The further increase in the vane angle worsens the separation effect along the suction surface, hence increasing the nozzle loss coefficients. The increase in the vane angle also limits the throat area and reduces the allowable volume of the flow across the nozzle vanes. The throat area would be further reduced attributed to the separation zone formed along the suction surface. The flow fluid in Figure 11.17 also shows a strong circulation flow at the trailing edge of the vanes, especially at the vane position 3 (near to the close position). The circulation flow at the trailing edge would mix with the downstream flow near the rotor inlet, hence contributing to the mixing loss or passage loss of the flow across the rotor.

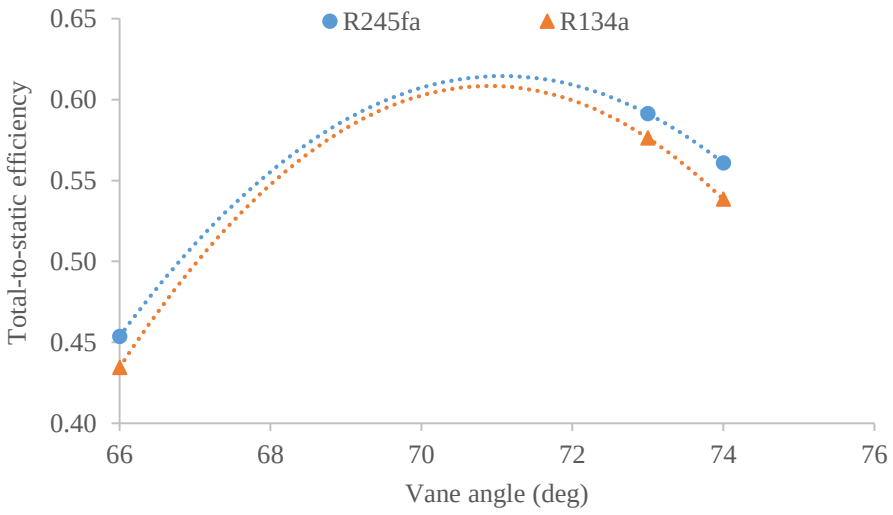

Figure 11.18: Performance of turbine with variable nozzle vanes as a function of vane angle, for R134a and R245fa

The performance of the turbine with variable nozzle vanes was plotted in Figure 11.18 to showcase the correlation between the turbine performance and the vane angle. Even though the nozzle loss coefficient increases with the vane angle attributed to the formation of a larger flow recirculation zone, the turbine provides the highest efficiency at a specific vane angle between the fully open and fully close vane position. The optimal point can be determined mathematically once the turbine performance map was generated using the CFD analysis approach.

11.6 Conclusion

The objective of this chapter is to present the SMC-DTR approach to design and optimize an ORC system for a heat source with fluctuating mass flow by using an automotive turbocharger with variable nozzle vanes.

The first section presents the control strategy to optimize the performance of the selected automotive turbocharger using air as the working fluid. The turbine rotational speed has to be defined using the optimal velocity ratio and the system pressure ratio. The nozzle vane angle has to be adjusted as a function of the mass flow of the ORC working fluids (or the mass flow of the heat source) during the operation to maintain the optimal performance of the turbine.

The second section compares the performance of the turbine and the ORC system between the turbine with fixed vane position and the turbine with variable nozzle vanes. The findings are summarized below:

1. The performance of the selected automotive turbocharger deteriorates up to 20% if the working fluid was changed from air into R134a or R245fa.
2. If the same turbine rotor is used, the use of the variable nozzle vanes provides a better efficiency for a wider range of mass flow, compared to the use of the fixed nozzle vanes.
3. The thermal efficiency of the ORC with VNT remains between 50 and 70% even if the mass flow varies from 2 to 3.5 kg/s for the kerosene flow. The thermal efficiency of the ORC with the turbine with fixed nozzle vanes changes from 50% to 20% when the mass flow varies from 3.5 to 2.5 kg/s. Hence, the thermal efficiency of the ORC with VNT provides a better efficiency to match with the heat source with varying mass flow.
4. The nozzle loss coefficient is not affected by the velocity ratio. The loss coefficient increases when the vane angle is increased. However, an optimal vane angle exists between the fully open and fully close vane position for maximum efficiency of the turbine stage. If an existing turbine (or off-the shelf turbine) is used, the optimal vane angle can be determined using the CFD analysis, as outlined in this chapter.

The result of this chapter provides the valuable information into the SMC-DTR approach that a turbine with variable nozzle vanes has to be selected if the heat source shows varying mass flow across the proposed life cycle of the planned power plant.

11.7 References

1. Ripperda, M. and G. Bodvarsson, *Decline curve analysis of production data from The Geysers geothermal field*. 1987: Lawrence Berkeley Lab.
2. Thomas, R.P., et al., *A reservoir assessment of The Geysers geothermal field*. 1981, Californina Department of Conservation, Division of Oil and Gas.
3. Sanyal, S.K. and S.L. Enedy. *Fifty years of power generation at the Geysers geothermal field, California–the lessons learned*. in *36th workshop on geothermal reservoir engineering, Stanford, California*. 2011.
4. KARADAS, M., U. SERPEN, and N. AKSOY, *Some Investigations on Decline in Dora-1 Brine Flow Rate, Case Study: AS-1 Production Well.*
5. Balje, O.E., *Turbomachines: A Guide to Design Selection and Theory*. 1981: Wiley.
6. Dixon, S.L. and C. Hall, *Fluid Mechanics and Thermodynamics of Turbomachinery*. 2010, Butterworth-Heinemann: Burlington.
7. *Garrett Performance Turbochargers*. [cited 2015 27th May]; Available from: http://www.turbobygarrett.com/turbobygarrett/turbochargers.
8. Aneke, M., B. Agnew, and C. Underwood, *Performance analysis of the Chena binary geothermal power plant.* Applied Thermal Engineering, 2011. **31**(10): p. 1825-1832.
9. Jung, H.C., S. Krumdieck, and T. Vranjes, *Feasibility assessment of refinery waste heat-to-power conversion using an organic Rankine cycle.* Energy Conversion and Management, 2014. **77**(0): p. 396-407.

12.0 Conclusion

12.1 Summary

This thesis presents the strategy to design and optimize an ORC system for low temperature resources by adapting the off-the-shelf radial inflow turbines, named SMC-DTR approach. This strategy is of primary importance in developing a cost-effective energy conversion system without having the knowledge-based engineering (KBE) in turbine technology. The motivation of this research work stems from the limited available research funding in the development of the KBE in turbine technology for the ORC turbine design. To this purpose, this thesis addresses the research question of how the energy conversion system is designed using the off-the-shelf turbines for the working fluid different from the original design. This thesis work is divided into four major sections, each serving different contribution to develop, validate, and apply the SMC-DTR approach.

12.1.1 Background

The first section presents the background of the ORC system and the fundamental modelling of the DTR approach.

Conclusions:

The literature review provides the information of the major parameters for use in the SMC-DTR approach: the type of turbine. The radial inflow turbine is selected to be adapted in the SMC-DTR approach. The radial inflow turbine is a better candidate of turbine option for low temperature resources, as compared to other turbine options, such as axial turbines, and positive displacement machines for the following reasons:

- The radial inflow turbine operates optimally in the pressure range suitable for the low temperature resources.
- The radial inflow turbine can be up-scaled to produce a few megawatts shaft power or down-scaled to produce as little as a few kilowatts shaft power.
- The radial inflow turbine is commercially available in different diameter and in large volume as automotive turbochargers and gas turbines.
- The radial inflow turbine is cheaper to be sourced from the automotive turbochargers, compared to axial turbine from steam turbines.

Secondly, the thermodynamic model of an ORC system, and the method to define the turbine specification were presented as part of the SMC-DTR approach. The inclusion of these information is important if the SMC-DTR approach has to be performed or repeated.

12.1.2 Investigative Study

This part presents the turbine preliminary design method coupled with the real gas model to match the existing turbines to the heat source.

Conclusions:

The selected gas model affects the turbine design outcome during a turbine preliminary design process. The ideal gas model under-estimate the turbine diameter up to 50% and over-estimate the turbine shaft speed up to 550%, depending on the compressibility factor of the working fluid at the turbine inlet. The design outcome using the ideal gas model provides a poor choice of turbine geometry and turbine operating condition, which might lead to a power consuming operation (behaving as a pump) instead of a power generation process (operating as a turbine). Hence, the real gas model has to be coupled into the turbine preliminary design process to provide an optimal configuration of turbine geometry and operating condition.

Implications:

This section emphasizes the disadvantage of using the conventional turbine preliminary design approach with ideal gas model for refrigerants and real gases, and presents the numerical flow process that can be imitated by ORC turbine manufacturers to perform the turbine preliminary design process using the real gas model.

12.1.3 Components of the SMC Adaptive Strategy

This section develops the analysis techniques of the SMC adaptive strategy: similarity approach, meanline analysis, and CFD method.

Conclusions:

The similarity analysis approach utilizes the similarity concept to scale a turbine from one working fluid into different working fluid. Different parameter sets were established and validated against the CFD model to determine the best parameter set to scale the radial inflow turbine. The variable pressure ratio approach is proposed at the best efficiency point, and the

constant specific speed method is used at the operating points away from the best efficiency point. A turbine correction chart was developed to scale the turbine for different volumetric flow rate at the best efficiency point.

The meanline analysis technique is developed using the empirical loss model. The meanline analysis model consists of five different losses: passage loss, secondary flow loss, incidence loss, clearance loss, and windage loss. Each loss model has been validated against the experimental data of the radial turbines using air as working fluid. The empirical loss model of the meanline analysis was validated against two turbines: an industrial radial gas turbine using air as working fluid, and a research prototype unit of ORC turbo-generator using R245fa as working fluid. The meanline analysis is applied when the performance map of the turbine is not available.

The CFD method provides the most accurate result of the turbine performance compared to other modelling approaches. The CFD analysis method consists of five main steps: generate 3D model, mesh the flow domain, set up the boundary condition and select the turbulence model, solve the Navier-Stokes equation, and analyse the flow field. The CFD model was developed and validated against the experimental data of an industrial radial gas turbine using air as working fluid.

Implications:

The three proposed methods (similarity, meanline, and CFD) provide the analytical tools to analyse the turbine performance at different level of accuracy and computational effort. These methods were integrated into the SMC adaptive strategy to analyse the turbine performance using working fluid different from the original design.

The similarity analysis allows the engineer to conduct a preliminary evaluation of the turbine performance for different working fluid (which cannot be performed prior to this study) given the performance map of the turbine using air as working fluid. This analysis approach allows the experimental evaluation of the turbine performance using a compressed air test bench. The compressed air test bench is simple with low level of hazard, and low installation and operation cost compared to a full scale turbine test facility using refrigerants as the working fluids. The turbine can be scaled from air to refrigerants using the similarity analysis approach. This approach also allows a preliminary screening of the suitability of the off-the-shelf turbines to be retrofitted or adapted for application with different working fluids.

The proposed meanline analysis can be useful in predicting the turbine performance for ORC application as the model was validated against the experimental data of the ORC turbine. This analysis model is useful when the information of the turbine, such as the model number and the performance map, is not available. This approach is simple without the need of a comprehensive measurement on the turbine.

The proposed CFD model serves as a guideline to analyse and validate radial turbine performance. The mesh setting in the model can be used for different radial turbine to produce good, if not best, quality of meshes across the flow domain. This model was refined by the author to produce the accurate estimation of the turbine performance with the minimal amount of computational power and computing time.

12.1.4 Application of the SMC-DTR Approaches

This section presents the application of the SMC-DTR approach using three different turbine technologies; a nozzle-less automotive turbocharger, a fixed vane radial gas turbine, and an automotive turbocharger with variable nozzle vanes, named variable nozzle turbocharger (VNT).

Conclusions:

The adaptation of the off-the-shelf radial turbines to design an ORC system is feasible, with the trade-off of the turbine efficiency. The automotive turbocharger is typically designed for the pressure ratio between 1.0 and 3.0, whereas the industrial radial gas turbine is designed for a higher range of pressure ratio, between 3.0 and 5.0. The turbine efficiency deteriorates up to 20% when the working fluid of the automotive turbocharger is replaced from air into the real gases or refrigerants. The efficiency of the industrial radial gas turbine changes within the range of 10% when the working fluid is changed from air into refrigerants. The automotive turbochargers and the gas turbines are mostly designed for sub-sonic expansion with the pressure ratio barely goes beyond 5.0. Hence, the application of these turbines in ORC has to be handled with care to ensure that the expansion process is within the range of sub-sonic expansion. A supersonic expansion on these turbine leads to low turbine efficiency. For example, the industrial radial gas turbine in this thesis shows the highest efficiency when the pressure ratio is between 3.0 and 4.0, and shows the deterioration in efficiency between 20 to 30% at the pressure ratio between 6.0 and 10.0. The rotor flow passage is designed to allow flow diffusion downstream of the throat, to control the swirl angle at the turbine outlet and

recover the kinetic energy of the flow in a subsonic expansion process. The flow behaviour is different in a supersonic expansion. The flow accelerates downstream of the throat, and increases the kinetic energy as the loss at the turbine outlet. As a result, the turbines originally designed for subsonic expansion performs poorly with a large deterioration in the efficiency in the supersonic expansion.

The SMC-DTR approach was applied in three different type of resource condition: constant resource condition, constant heat source condition with varying heat sink temperature, and constant heat sink condition with varying heat source flow rate. The thermodynamic cycle and the turbine performance can be optimized easily at constant resource condition. However, a nozzle has to be designed if the nozzle-less turbine is adapted. The design of the nozzle aims to provide a better guidance of the flow into the turbine rotor for optimal performance. The performance of the turbine and the thermodynamic cycle does not change significantly when the heat sink is varied based on the seasonal variation in Rotokawa, New Zealand. The efficiency of the turbine with fixed nozzle vanes efficiency shows the change in efficiency up to 2% when the cooling air is varied between 10 and 23˚C. The performance of the turbine with fix nozzle vanes changes significantly if the flow rate of the heat source deviates from the design value. For example, the result of the case study shows that the turbine efficiency with fix nozzle vanes drops from over 70% to below 50% when the mass flow of the ORC fluid changes from 0.15 to 0.10 kg/s. The thermodynamic cycle efficiency drops from over 5% to nearly 1% when the mass flow of the heat source is reduced up to 25% off the design mass flow. The turbine with variable nozzle vanes has to be selected for the heat source with varying mass flow. The performance of the turbine and the thermodynamic cycle maintains at an acceptable range of value even if the mass flow of the heat source is reduced or increased from the design mass flow.

A mechanical system design has to be performed if a turbine originally designed and developed for air is adapted into a turbine for refrigerants. The bearing is lubricated by the working fluid instead of oil-based lubricants. The hybrid bearing was found more suitable than standard steel bearing for the refrigerant lubrication. The casing has to be re-designed to contain the working fluid from leaking into the atmosphere. A hermetic design is recommended over the open-drive shaft configuration.

Implications:

These conclusions provide the information regarding the implication on the turbine performance if the off-the-shelf turbines are used in different operating condition and different working fluid than the original design. The information provides a guidance to the ORC manufacturers if an off-the-shelf turbine has to be selected. These conclusions also provide a framework on the turbine adaptation strategy when a thermodynamic cycle is designed to the resource condition. The strategy allows the development of the ORC turbine using the existing technologies in the local or global market, and significantly reduces the developmental cost.

12.2 Perspectives

The research in this work provides the framework to design an organic Rankine cycle based on the resource condition by adapting the off-the-shelf radial inflow turbine. It has led to the new design and development strategy for the energy conversion system with a lower engineering cost compared to the conventional design approach.

There are two major limitations in this thesis work. This thesis is written for the low temperature resources which usually require a low pressure ratio between 3 and 6. Hence, the radial inflow turbine is selected as the test subject for the SMC-DTR approach. If the SMC-DTR approach is to be extended for high temperature resources, the implication of adapting multiple stage axial turbines has to be investigated. The second limitation is the lack of experimental validation of the adapted ORC turbine attributed to the limited funding. To further the application of the SMC-DTR approach, there are a number of potential researches to refine the current SMC-DTR strategy:

- The adapted turbine has to be tested, and the performance has to be compared against the modelling result from the SMC adaptive strategy.
- The long term operation issues can only be found from the experimental testing of the adapted turbine, which is beyond the scope of the current study.

Finally, this SMC-DTR approach should be performed by the existing or potential ORC manufacturers as a framework in developing the next generation low cost ORC system. The lessons learned from the application of the approach can be used to refine the approach from time to time, as part of the knowledge-based engineering (KBE) for the turbine development program.